Site CM1: layered gabbros, crustal ultramafic rocks, and mantle harzburgite[1]

Kelemen, P.B., Matter, J.M., Teagle, D.A.H., Coggon, J.A., and the Oman Drilling Project Science Team[2]

Keywords: Oman Drilling Project, OmanDP, Site CM1, Hole CM1A, Hole CM1B, Wadi Zeeb, Samail ophiolite, Crust–Mantle Transition Zone, CMTZ, lower crust, mantle, layered gabbros, harzburgite, ultramafic, layered gabbros

Chapter contents

Site CM1 introduction

Site CM1 (22.90724°N, 58.33582°E) is situated in the northern end of Wadi Zeeb and hosted in layered gabbros of the lowermost crust of the Samail ophiolite (see Fig. F1 in the **Introduction to Science Theme 1A** chapter). Hole CM1A (22.90726°N, 58.33582°E) is situated a few meters above the wadi (see Fig. F2 in the **Introduction to Science Theme 1B** chapter), and Hole CM1B (22.90722°N, 58.33581°E) is ~10 m to the south, closer to the active wadi channel.

Based on extensive mapping of the area, described in the **Introduction to Science Theme 1B** chapter, a 400 m diamond-cored hole (CM1A) was designed to be drilled at an inclination of 60° (30° deviation from vertical) on a trend of 000 (due north), perpendicular to the gabbro layering and lithologic boundaries. As predicted, Hole CM1A successfully sampled the layered gabbros and the transition through dunites of the Crust–Mantle Transition Zone (CMTZ) and into the harzburgites of the uppermost mantle of the Samail Ophiolite. Hole CM1B was sited adjacent to Hole CM1A as a result of this successful drilling across the target lithologies. This wider diameter rotary well was designed to facilitate geophysical logging across the lithologic contacts, using downhole tools that are not deployable in slimline wells. Unfortunately, the target depth of 400 m could not be reached in this vertical borehole because of geological issues that terminated the well at 237 m depth. The data derived from these cores, cuttings, and boreholes will be used to investigate the nature of the CMTZ in the Samail Ophiolite and to study hydrothermal alteration in the lowermost crust and the CMTZ.

Geological setting

Site CM1 is situated on a gentle slope above an active wadi channel that cuts through southward-dipping layered gabbros of the lowermost oceanic crust of the Samail Ophiolite (Fig. F1). The geology is described in more detail in **Geology of Sites CM1 and CM2** in the **Introduction to Science Theme 1B** chapter.

Drill pad preparation was necessary at this site because of its slope. Existing access to the wadi via a track from the paved road to the south required significant improvement (mainly building up with local wadi gravels) to facilitate access for the diamond coring drill rig and associated vehicles. The CM1 site also required leveling to create a stable drill pad. Local gravels were used to build up a platform on the side of the wadi for this purpose.

[1] Kelemen, P.B., Matter, J.M., Teagle, D.A.H., Coggon, J.A., and the Oman Drilling Project Science Team, 2021. Site CM1: layered gabbros, crustal ultramafic rocks, and mantle harzburgite. *In* Kelemen, P.B., Matter, J.M., Matter, J.M., Coggon, J.A., and the Oman Drilling Project Science Team, *Proceedings of the Oman Drilling Project*: College Station, TX (International Ocean Discovery Program). https://doi.org/10.14379/OmanDP.proc.110.2020
[2] OmanDP Science Team affiliations.

MS OmanDP-110
Published 6 May 2021

Operations: Hole CM1A

All times are reported as local time in Oman (UTC + 4 h).

An overview of all holes drilled is given in Table T3 in the **Methods** chapter. Drilling operations and core curation information are reported in Table T1.

Six samples were taken for microbiology at this site after normal core flow was complete. Gloves were worn during handling of these cores in an effort to minimize contamination of the samples. The microbiology samples comprise four ~20 cm intervals of whole-round core and two 5 cm intervals of the working half for thin section production.

Drilling summary

- Spud-in: 15 Nov 2017, 10:08 h
- First core on deck: 15 Nov 2017, 10:20 h
- Surface casing (HW) installed: 15 Nov 2017, 6 m
- Surface casing (HW) extended: NA
- NW casing installed: 04 Dec 2017, 274.75 m
- Final core on deck: 13 Dec 2017, 16:15 h
- Total depth (TD) of borehole: 404.15 m

Geology summary

- Primarily layered gabbros at 0–160 mbgl (m below ground level), followed by serpentinized dunite.
- Lowermost ~20 m of borehole is dominated by serpentinized harzburgite.

Technical issues

The main technical issue was encountered at ~274 mbgl (collapsing borehole, highly fractured rocks), which was stabilized by installing NW temporary casing. Drilling continued with NQ drill bit assembly.

Operations summary

- 14 Nov 2017: mobilize rig, equipment, and accessories to site. Set up rig.
- 15 Nov 2017: start drilling Hole CM1A. After Core 2Z, install HW surface casing in increments using casing shoe to ream borehole to prevent deviation of HQ at the top of hole.
- 16 Nov 2017: drill with HQ drill bit assembly 11.25–44.25 mbgl.
- 17 Nov 2017: no drilling (Friday); scientists catch up work, describe, and curate core.
- 18 Nov 2017: core with HQ drill bit assembly to 77.25 mbgl. Drone airborne survey of Sites CM1 and CM2.
- 19 Nov 2017: core with HQ drill bit assembly to 109.75 mbgl. Wireline damaged while pulling core barrel; fixed using a special tool.
- 20–22 Nov 2017: core with HQ drill bit assembly to 183.75 mbgl.
- 23 Nov 2017: slow drilling due to fault zone. Replace HQ drill bit (hardness 11) with fresh HQ bit (hardness 7). Pull out of hole (POOH) and run in hole (RIH) with new drill bit. Restart drilling; blockage at the bottom of hole. Clean hole with heavy flush of drilling fluid. Resume drilling to 188.25 mbgl.
- 25–28 Nov 2017: drill with HQ drill bit assembly to 269.25 mbgl.
- 29 Nov 2017: drill with HQ drill bit assembly to 274.75 mbgl. Observe high torque and increasing water pressure. POOH to check drill bit and because of fractured material higher in the borehole. Drill bit blocked but in good condition. Clean drill bit; change worn stabilizer and landing ring. RIH to 196 mbgl; encounter backfill. Start to clean borehole by heavy water circulation and reaming to 200 mblg.
- 30 Nov 2017: drill with HQ drill bit assembly to 247 mbgl. System pressure decrease from 200 to ~140 kg/cm^2.
- 2 Dec 2017: after hole reaming and clearing on 30 Nov, (1) hole collapsed 196–212 mbgl, (2) cavity at 232–235 mbgl, and (3) another cavity 247–250.25 mbgl. It is not possible to reach bottom of the hole because of problems clearing cuttings. Wali proposed to either cement the hole and redrill or case the hole with HW casing and continue with NQ drill bit assembly. Jude and Nehal decided to go with the casing and change to NQ coring.
- 3 Dec 2017: POOH HQ drill bit assembly and start to install NW temporary casing with shoe bit.
- 4 Dec 2017: continue to install NW casing 30–274.65 mbgl. RIH NQ drill bit assembly to 273.50 mbgl.
- 5–6 Dec 2017: drill with NQ drill bit assembly to 296.15 mbgl. RIH to drill further but found backfill due to borehole wall collapse. Pull out 4 drill pipes, clean backfill, and continue drilling to 296.65 mbgl.
- 7–10 Dec 2017: drill with NQ drill bit assembly to 353.15 mbgl.
- 11 Dec 2017: drill with NQ drill bit assembly to 371.15 mbgl. 40 GU Tech students visited the drill site and spent the day learning about coring and core characterization/description.
- 12–13 Dec 2017: drill with NQ drill bit assembly to 404.15 m (TD). Visit from Sultanate of Oman Ministry of Regional Municipalities and Water Resources (MRMWR) representative.
- 14 Dec 2017: wrap up, describe last core from 13 Dec, and prepare site for demobilization and mobilization to Site CM2.

- 16 Dec 2017: demobilize Site CM1 (coring rig) and Site CM2 (rotary drill rig).
- 17 Dec 2017: move coring rig and equipment to CM2 site.

Igneous petrology: Hole CM1A

Macroscopic core description

Summaries of all units and subunits, their depths, and descriptions are provided Supplemental Tables **ST1**, which contains all data recorded from the igneous petrology description team, and **ST2**, which contains information related to individual lithologic units extracted from supplemental Table **ST1**.

The main lithologic units logged in Hole CM1A are dunite, olivine gabbro, gabbro, harzburgite, and wehrlite, with minor gabbronorite, troctolite, websterite, anorthosite, and chromitite. Table T2 lists the abundance of the principal rock types in unit count percentages and cumulative thickness and Figure F2 shows the graphical representation. Lithologic units are divided by contacts such as changes in mineral assemblage, modal abundance, structural, and other textural variations. The evolution of lithologies with depth including mineral modes and grain sizes are shown in Figure F3.

Lithologic sequences

The lithologic units identified and described in Hole CM1A were organized into larger igneous groups named "sequences" based on the predominant rock type. Four major sequences are identified in Hole CM1A (Table T3):

I – Layered Gabbro Sequence,
II – Dunite Sequence,
III – Dunite with Gabbro Sequence, and
IV – Mantle Sequence.

Table T3 lists the abundance of the rock types in each sequence, both in terms of the number of units (percent) and cumulative thickness percent, and Figure F4 presents a graphical representation. Major rock types occurring in each sequence and primary features are described below.

Layered Gabbro Sequence

Depth: 1.50–160.23 m
Interval: CM1A-2Z-1 through 63Z-4
Units: 1d–55e

The ~159 m thick Layered Gabbro Sequence is composed of a layered series of gabbroic and ultramafic rocks probably formed by crystal accumulation in the lowermost crust directly above the mantle. Layering is mostly defined by modal variations, commonly in combination with changes in grain size. Contacts between individual layers are typically sutured. Most common in this sequence are layered gabbroic rocks (olivine gabbro 68.4%, gabbro 18.7%, anorthosite 0.1%, and troctolite 0.01% based on the thickness of the corresponding units) exceeding by far ultramafic cumulates (wehrlite 7.6%, dunite 2.2%, and websterite 0.02%). Dunites are more common in the lower part of this sequence, and in several places dunites intrude the gabbros (e.g., interval 6Z-4, 2–10 cm; see **Reactions between gabbro and dunite in the Layered Gabbro Sequence**). In some olivine gabbros in this sequence, centimeter-sized olivines with skeletal shapes occur, indicating fast crystal growth (e.g., interval 17Z-1, 18–22 cm; see **Rapid crystal growth of olivine**). Orthopyroxene-bearing rocks are extremely rare in this interval and are restricted to a few gabbronorite intrusions cutting the main layered sequence.

Dunite Sequence

Depth: 160.23–249.99 m
Interval: 63Z-4 through 107Z-3
Units: 56a–56u

The Dunite Sequence is ~90 m thick and is nearly completely composed of dunite (99.7% by thickness). The remaining rocks (0.3%) are olivine gabbro, gabbro, and chromitite, forming a few millimeter-thin layers. Although totally altered to serpentinite, these dunites display relict primary magmatic textures including fine- to medium-grained equigranular granular textures and interstitial spinel (generally <1%). This, together with the observation that the dunites do not bear relics of deformed orthopyroxene (as is typical for mantle rocks) or any relic porphyroclastic textures (which record plastic flow within the uppermost mantle), provides strong evidence that the dunites are of magmatic origin. Examples of dunites with typical equigranular texture, characteristic for this sequence, are shown in Figure F5. See **Textures in massive dunites** for a more detailed description of the dunite textures.

Dunite with Gabbro Sequence

Depth: 249.99–310.99 m
Interval: 107Z-3 through 142Z-4
Units: 56v–64b

The Dunite with Gabbro Sequence is in principle a continuation of the Dunite Sequence, except that in this sequence a layered series of gabbroic rocks was emplaced. In contrast to the Layered Gabbro Sequence, massive dunites are the dominant rock type (85.3% by thickness) with minor gabbroic or wehrlitic rocks (gabbro 8.5%, olivine gabbro 3.9%, troctolite 0.6%, and wehrlite 1.7%, based on thickness). The contact relationships between dunite and gabbroic rocks and the observation of xenoliths of dunite within the gabbroic rocks imply that the gabbroic rocks intruded into the dunites (see **Magmatic contacts**; Fig. F53A). As in the Dunite Sequence, nearly all dunites are totally altered to serpentinites, except one sample that shows a few tiny relics of olivine (thin section [TS] Sample 142Z-1, 84–88 cm; see below). The dunites of the sequence show the same (relict) textural features as dunites in the Dunite Sequence (see also **Textures in massive dunites** for a closer view of the dunite textures.).

Mantle Sequence

Depth: 310.99–404.21 m
Interval: 142Z-4 through 179Z-4
Units: 64c–64ch

This ~93 m thick sequence is characterized by the presence of mantle harzburgite (36.8% based on thickness) and orthopyroxene-bearing dunite (62.3%), both with typical characteristic porphyroclastic mantle textures. The remaining 0.8% of the sequence consists of websterite, gabbro, gabbronorite, troctolite, anorthosite, and chromitite. In general, the dunites bear relics of orthopyroxene showing features of typical porphyroclasts, as characteristic of mantle rocks. This suggests that most dunites of this sequence, together with the harzburgites, belong to the mantle. This is in contrast to the textural features observed in dunites from the three sequences above, where magmatic textures dominate (see also **Textures in massive dunites** for a closer view of the dunite textures). Magmatic activity in this sequence is mostly restricted to a few thin (mostly < 1 cm thick) layers of troctolite, gabbro, gabbronorite, and websterite (Subunits 64m, 64aj, 64al, 64an, 64aq, 64as, and 64au) in harzburgites, which are oriented subparallel to the layering observed in the layered sequences above. Some of these are deformed (see **Structural geology: Hole CM1A**).

Principal rock types

Here we present detailed descriptions of the principal rock types and corresponding core images, in the order of abundance (according to the accumulated thickness; Table T2).

Dunite

Dunite is a minor lithology in the Layered Gabbro Sequence but is the most abundant rock type in all other sequences. In the Layered Gabbro Sequence dunite forms centimeter-thick layers with fine- to medium-grained granular textures and equigranular grain size distribution. These characteristics are interpreted as cumulate textures, in accord with the textures of the associated gabbroic rocks of this sequence. In the Layered Gabbro Sequence, 20 igneous units have dunite as the principal lithology. Very commonly the dunite bears interstitial plagioclase and/or clinopyroxene, some with poikilitic or interstitial habits (see also **Poikilitic clinopyroxene vs. poikilitic plagioclase in dunite**), in the following intervals:

- 18Z-2, 14–71.5 cm,
- 18Z-3, 53–55 cm, and 83–90 cm,
- 18Z-4, 0–25.5 cm,
- 20Z-4, 45–48 cm,
- 59Z-1, 0–56 cm.

The Dunite Sequence directly underlies the Layered Gabbro Sequence and consists nearly entirely of dunite. This sequence is ~90 m thick and encompasses the interval from Section 63Z-4, 26.5–63 cm, to 142Z-4, 0–32.5 cm (Subunits 56a–56u; see Supplemental Table ST2). These dunites are very homogeneous and are composed mainly of olivine (99.9%) with traces of spinel on the grain boundaries (~0.1% volume). Although olivine is totally altered in the sequence, relict magmatic texture is generally preserved. Grain size is mainly fine to medium grained; texture is granular with equigranular grain size distribution. The texture is very similar to that of the dunites in the Layered Gabbro Sequence. Moreover, neither orthopyroxene nor relics of porphyroclastic texture (as characteristic of mantle peridotites) are present, implying that this type of dunite is of magmatic origin, more related to the crust than to the mantle. A few thin chromitite bands ranging 0.5–1.5 cm thick occur in the following dunite intervals (Fig. F5):

- 89Z-1, 76–76.5 cm, and 78.5–79 cm,
- 96Z-3, 9.5–10 cm,
- 99Z-2, 49–49.5 cm,
- 101Z-2, 4.5–5 cm,
- 101Z-3, 22.5–23.5 cm.

Dunites are the dominant rock type in the Dunite with Gabbro Sequence (85.28%; based on thickness). As in the Dunite Sequence, nearly all dunites are totally altered to serpentinites, except one sample that shows a few tiny relics of olivine (TS Sample 142Z-1, 84–88 cm; see below). The dunites of this sequence show the same (relict) textural features as dunites in the Dunite Sequence, including the presence of poikilitic plagioclase (see above; Subunit 58a; see also **Poikilitic clinopyroxene vs. poikilitic plagioclase in dunite** and **Textures in massive dunites**), a feature implying a pure magmatic origin of this type of dunite. A close-up of this texture is shown in Figure F5.

In contrast to the dunites from all upper sequences, the dunites in the Mantle Sequence commonly include relics of orthopyroxene porphyroclasts. These rocks show medium-grained, granular textures with equigranular grain size distribution. Modal olivine in these dunites is 94%–98% with up to 3% orthopyroxene. This type of dunite occurs in 23 individual units (for details see Supplemental Table ST2). The presence of porphyroclastic orthopyroxene and the observation that the dunites commonly alternate with tectonized mantle harzburgites imply these dunites can be regarded as mantle components. In places, dunites of the Mantle Sequence are associated with chromitite patches (e.g., interval 155Z-1, 48–58 cm; Subunit 64bn; see below).

Typical images from textures of dunites from all 4 sequences are shown and discussed in **Textures in massive dunites**.

Olivine gabbro

Olivine gabbro is the main rock type in the Layered Gabbro Sequence (~70% of this sequence thickness; see Fig. **F4**) but represents only a minor proportion of the other sequences, where is mainly present as layers and patches in ultramafic host rocks.

In the Layered Gabbro Sequence, olivine gabbros are almost always medium grained with grain sizes of 1–5 mm. Exceptions to this include interval 9Z-4, 86 cm, to 11Z-3, 54 cm, which is fine grained (grain size < 1 mm), and the following coarse-grained intervals (grains > 5 mm) (Fig. **F6D**):

- 11Z-4, 0–84 cm,
- 14Z-2, 49 cm, to 14Z-3, 48 cm,
- 15Z-1, 0 cm, to 15Z-3, 9 cm,
- 16Z-3, 77 cm, to 17Z-1, 24 cm,
- 37Z-3, 75–81 cm,
- 38Z-2, 80 cm, to 38Z-3, 6.5 cm.

Equigranular cumulate textures are the most common in fine- and medium-grained olivine gabbros (Fig. **F6B, F6C**). Poikilitic clinopyroxene or plagioclase may appear near ultramafic layers, but adcumulate texture suggesting co-crystallization of olivine, clinopyroxene, and plagioclase is generally observed. Varitextured coarse-grained intervals containing skeletal olivine are present at 33 m right below a fracture subparallel to the layering between Sections 16Z-2 and 16Z-3 (Fig. **F6D**).

The modal compositions of the olivine gabbros vary significantly, with large variations of mineral proportions from one unit to another and within a single unit with modal layering. Averaged over each layered unit, olivine gabbros contain 10%–60% olivine, 35%–80% plagioclase, 5%–70% clinopyroxene, no orthopyroxene, and traces of sulfides and Cr-spinel. The modal variation within one single unit can be large and may define modal layering. Cr-spinel is relatively abundant (close to 1%) in some olivine-rich layers containing >60% olivine.

Modal layering is almost ubiquitous in all layered gabbroic series. The layering is generally planar and parallel to the major foliation (Fig. **F6A**). In rare cases, it is curved together with the foliation (interval 27Z-2, 0–44 cm). Strongly layered olivine gabbros are present in Sections 29Z-4 through 30Z-3 and 51Z-3 through 52Z-1, which show <2 cm thick cryptic modal variations (Fig. **F6A**). However, layering thickness is more commonly moderate (2–10 cm thick layers) to absent with cyclic repetitions <10 cm thick of strongly foliated olivine-rich gabbro and repetitions >40 cm thick of weakly layered to isotropic gabbros (Fig. **F6C**).

Contacts with other lithologies such as gabbros, wehrlites, or anorthosites are most commonly related to sharp or gradational modal evolution and are parallel to the layering and foliation. However, rare intrusive contacts crosscut the layering and foliation (see below).

Outside of the Layered Gabbro Sequence, olivine gabbros are present as minor layers in the Dunite Sequence but are completely altered. Olivine gabbro is also present as a ~2 m layered series in the Dunite with Gabbro Sequence (interval 113Z-1, 65 cm, to 113Z-4, 39 cm) where the petrographic features are very similar to those of the Layered Gabbro Sequence.

Gabbro

Gabbros make up ~19% of the Layered Gabbro Sequence (by thickness; see Fig. **F4**). They are commonly present as olivine-poor or olivine-free layers a few centimeters to a few meters thick within layered olivine gabbros (Fig. **F6A**) or as olivine-poor gabbroic patches cutting the layering within the layered section (Fig. **F6F**). Gabbros comprise 40%–70% plagioclase, 30%–60% clinopyroxene, and <3% olivine and <2% orthopyroxene. Trace proportions of sulfides and Fe-Ti oxides are regularly present.

Most gabbros have medium- to fine-grained, equigranular adcumulate texture (Fig. **F6E**). A coarse-grained interval at 36Z-2, 31–43 cm, shows cumulate equigranular texture with elongate grains defining strong foliation.

Layering is clearly weaker than in olivine gabbros. Medium-grained gabbros are isotropic or weakly layered with slight olivine or clinopyroxene modal variations. Fine-grained intervals (1Z-1, 59–68 cm, and 53Z-1, 0 cm, to 54Z-2, 60 cm) are strongly layered with a succession of anorthositic and gabbroic layers.

Gabbros are very rare in other sequences than the Layered Gabbro Sequence: 1 in the Dunite Sequence (Subunit 56l) that is anorthositic and totally altered, 3 in the Dunite with Gabbro Sequence (Units 60, 61b, 62) with similar features as those of the Layered Gabbro Sequence, and 1 occurrence in the Mantle Sequence (Subunit 64aj) that is totally altered to rodingite.

Harzburgite

Harzburgite first occurs in Section 142Z-4 (Subunit 64c) as a domain marking the base of the Dunite with Gabbro Sequence and the beginning of the Mantle Sequence. Further intervals in contact with dunite continue until the bottom of Hole CM1A. In total, 36 subunits are defined in the Mantle Sequence (see supplementary Table **ST2**). The harzburgite is medium grained, equigranular, with subhedral to anhedral grain shapes. Orthopyroxene occurs as characteristic porphyroclasts.

Olivine abundance is 59%–95% with a maximum grain size of 7 mm (mode = 1–3 mm). Olivine habit is granular. Orthopyroxene occurs with prismatic habit and ranges 5%–40% in modal abundance with a maximum grain size of 10 mm (mode = 1–3 mm). Spinel is present in small amounts ranging 0.5%–2% with a maximum grain size of 2 mm (mode = 0.1–1 mm). Spinel habit is granular or interstitial. Close-up photographs of typical mantle harzburgites with porphyroclastic texture are shown in Figure F7.

Wehrlite

Medium-grained, mostly equigranular wehrlites occur in several units in Hole CM1A. Most units with wehrlite as principal rock type occur in the Layered Gabbro Sequence (17 units), with only 1 unit in the Dunite with Gabbro Sequence. Wehrlite intervals typically have gradational contacts with adjacent intervals of gabbroic or dunitic rocks in the Layered Gabbro Sequence. In the Dunite with Gabbro Sequence, wehrlite occurs in a 10 m thick zone of interlayered gabbro, wehrlite, and minor troctolite (Subunit 56ab; see supplemental Table ST2).

In the Layered Gabbro Sequence, medium-grained, equigranular plagioclase-bearing wehrlites (Fig. F8, Subunits 1aa, 1ac, 1aj, 1ak, 1am, 1at) and wehrlites (Subunits 1aq, 1av) are interlayered with olivine gabbros and clinopyroxene-bearing dunites at 5.65–9.61 m in Hole CM1A. The subunits generally show moderate to weak modal layering with euhedral–subhedral olivine (50–80 vol%), subhedral clinopyroxene (10–48 vol%), and interstitial or poikilitic plagioclase (<10 vol%). Unit 1 overall is a layered series characterized by centimeter-scale modal variations of olivine, plagioclase, and clinopyroxene resulting in anorthosite, gabbro, dunite, and wehrlite lithologies in the topmost 17.29 m of the hole.

Medium-grained poikilitic plagioclase-bearing wehrlites occur in Units 16, 17b, 32, 38d, 50d, 50f, 50h, 53a, and 53c (see supplemental Table ST2). These rocks are characterized by variably foliated olivine with poikilitic patches of plagioclase and clinopyroxene. The intervals consist of olivine (30–80 vol%), clinopyroxene (10–60 vol%), plagioclase (5–15 vol%), and trace amounts of spinel and sulfide. Plagioclase-bearing wehrlites are generally interlayered with olivine gabbros with modally defined gradational or anastomosing contacts.

The deepest occurrence of wehrlite layers is found in Subunit 56ab (see supplemental Table ST2) in the Dunite with Gabbro Sequence. This subunit is weakly foliated plagioclase-bearing wehrlite in gradational contact with dunite above and below. It contains 70% olivine, 27% clinopyroxene, 2% plagioclase, and 1% spinel.

Gabbronorite

Gabbronorite is a rare lithology in the Layered Gabbro Sequence (Units 11, 20, 26b, and 26d). Here, they it forms pegmatitic intrusions in the layered gabbros (interval 29Z-3, 82–93 cm, through 29Z-4, 1–48 cm; Fig. F9), but it also forms thin magmatic veins in the Mantle Sequence (Subunits 64al, 64an). In both locations, the gabbronorites are late intrusions. Coarse-grained gabbronoritic intrusions bearing some brown hornblende cut layers in the Layered Gabbro Sequence. They have typical isotropic textures, whereas the host gabbroic rocks show foliation parallel to the layering. They contain 40%–55% plagioclase and 30%–50% clinopyroxene; orthopyroxene is a minor phase (<10%) with coronas of hornblende. These gabbronorite intrusions are varitextured with coarse-grained domains in the central part of the intrusion; regions at the contact with the host rock are finer grained.

Troctolite

Troctolite is rare in Hole CM1A. In the Layered Gabbro Sequence, medium-grained, equigranular clinopyroxene-bearing troctolite occurs in the 2 cm thick Subunit 15b (interval 18Z-3, 53–55 cm). The modal composition of this troctolite is 59% equant, subhedral olivine, 40% poikilitic, anhedral plagioclase, and 1% interstitial, anhedral clinopyroxene. The troctolite is bounded by sharp, planar upper and lower contacts with the host olivine gabbro.

Clinopyroxene-bearing troctolite appears in the Dunite Sequence in Subunit 56y (Fig. F10; interval 109Z-1, 42.5–79 cm, through 109Z-2, 0–14.5 cm) in tectonized contact with rodingitized dunite above (Subunit 56x) and rodingitized wehrlite below (Subunit 56z). Modal ratios for olivine:plagioclase:clinopyroxene are 60:20:20.

A thin spinel-rich troctolite vein in the Mantle Sequence in Subunit 64m (interval 143Z-4, 8–9 cm) contains 79% plagioclase, 20% olivine, and 1% spinel.

Websterite

Websterites occur as thin veins (maximum thickness = 14 cm) either in the Layered Gabbro Sequence (Subunit 53b) or in the Mantle Sequence (Subunits 64aq, 64as, 64au). A core photo for illustration is shown in Figure F11). They comprise medium-grained pyroxene clusters containing minor olivine and/or plagioclase. Websterite veins are parallel to the host rock layering, and the pyroxenes are slightly deformed.

The websterites contain >80% clinopyroxene and <20% orthopyroxene with minor Cr-spinel, olivine, or interstitial plagioclase. They show equigranular textures with equant, anhedral grains.

Anorthosite

Medium-grained equigranular olivine-bearing anorthosite occurs in Subunits 1e (interval 2Z-1, 53–63.5 cm) and 1ae (Fig. F12; interval 6Z-1, 69–73 cm) of the Layered Gabbro Sequence. Subunit 1e has a sharp, foliated, curved upper contact and an indistinct lower contact. It is weakly banded and consists of 99% subequant, subhedral plagioclase and 1% disseminated subequant, subhedral olivine. Subunit 1ae has a gradational, modal, planar upper contact and a sharp, modal, planar lower contact. It is foliated and consists of 95% subequant, subhedral plagioclase and 5% disseminated subequant, subhedral olivine.

A 1 cm thick anorthosite in the uppermost part of the Mantle Sequence at 317.09 m (Subunit 64v; 144Z-4, 71–71.5 cm) cuts a gabbroic band in surrounding harzburgite and is 98.5% plagioclase, 1% clinopyroxene, and trace sulfides.

A 2 cm thick anorthosite vein bounded by a dunite layer in the Mantle Sequence at 346.51–346.53 m depth (Subunit 64bk; 154Z-3, 78.5–80.5 cm) consists of 94.5% plagioclase, 5% orthopyroxene, and minor 0.5% olivine.

Chromitite

Thin intervals with chromitite are mostly found in the Dunite Sequence (Subunits 56h, 56j, 56n, 56p, 56r, 56t; supplementary Table ST2; see Fig. F5). They form together with olivine granular domains arranged in layers subparallel to the overall layering, and some are associated with interstitial plagioclase (now totally altered) and clinopyroxene. Contacts with the host dunite are sharp and anastomosing. The general grain size of the chromitite is fine.

One chromitite unit occurs in the Mantle Sequence (Unit 64bn; interval 155Z-1, 48–50 cm). Chromite associated with olivine occurs as fine-grained, granular patches in brecciated domain with tectonic contact to the surrounding dunite.

Downhole evolution with depth

Mode

Details of the changing mineral modal proportions with depth are shown in Figure F3. Modal variations in the Layered Gabbro Sequence relate to the igneous layering. Orthopyroxene appears only in some intervals, mainly where gabbronoritic intrusions occur. Olivine modal abundance increases and decreases over ~50 m intervals downhole, whereas clinopyroxene is relatively low in the uppermost 50 m but then remains present at more or less constant values. Plagioclase modes are approximately constant in the top 120 m, then vary strongly in the lowest 50 m as a result of intervals of wehrlite and more leucocratic gabbroic rocks.

The Dunite Sequence is homogeneous with respect to mineral modes. Orthopyroxene is absent, and there is <1% interstitial plagioclase and clinopyroxene. Higher modal proportions of plagioclase, clinopyroxene, and Cr-spinel occur in rare gabbroic and chromitite veins.

Modal variation in the Dunite with Gabbro Sequence reflects lithologic variability resulting from mutual intrusions of dunites and gabbros. The dunitic intrusions contain a few percent interstitial plagioclase, but clinopyroxene and orthopyroxene are absent. The Cr-spinel modal content is generally low (<1%).

The Mantle Sequence comprises alternating intervals of harzburgite and dunite. These ultramafic rock types are devoid of clinopyroxene and plagioclase, and these minerals appear only in minor gabbroic veins and patches. Cr-spinel is more abundant than in the dunites of the Dunite and Dunite with Gabbro Sequences and represents as much as 2% of the peridotite modal composition. A chromitite patch at 348 m contains >50% of this Cr-spinel.

Grain size

Details of the grain size evolution with depth are shown in Figure F3. A limited degree of grain size variation related to grain size layering is observed in intervals in the Layered Gabbro Sequence. Larger grain size variations in the Layered Gabbro Sequence occur where coarse-grained gabbros intrude into the abundant medium-grained layered gabbros. In the Dunite Sequence, grain size variations are minor; mostly the textures are medium grained, or less commonly, fine grained. Most textures in the Dunite with Gabbro Sequence are medium grained; some dunites show a fine-grained texture, whereas some coarser grained textures are related to gabbros of the layered series. In the Mantle Sequence, grains are homogeneously medium sized; coarse- and fine-grained gabbroic intrusions are entirely responsible for grain size variations.

Igneous layering

Igneous layering occurs in most of the lithologic units in all 4 sequences. The intensity of the layering ranges from weak to strong depending on the intervals at which the layers were observed. The layering is demarcated by changes in modal or grain size distribution or combined changes in both parameters. The contacts within the layers are either sharp or gradational with planar, curved, or anastomosing geometry.

Modal layering showing planar and anastomosing contacts is the most prevalent type of layering, particularly in the gabbroic units of the Layered Gabbro and the Dunite with Gabbro Sequences. Examples of weak (interval 18Z-1, 0–30 cm) and strong (interval 20Z-4, 50–70 cm) layering are shown in Figure F13A, F13B. This figure also shows typical examples for layered gabbros with a wide range in modal variations both for the Layered Gabbro Sequence (interval 6Z-1, 45–80 cm) as well as the Dunite with Gabbro Sequence (interval 113Z-2, 58–89 cm) (Fig. F13C, F13D).

Variation of the thickness of the gabbro layering in the Layered Gabbro and Dunite with Gabbro Sequences with depth is shown in Figure F3. The minimum thickness is <1 cm, and maximum thickness is 80 cm at the transition to the Dunite Sequence. For further information, see **Structural geology: Hole CM1A**.

Contacts

The contacts between units and subunits were identified by changes in modal abundance, grain size, or color. Tectonic, foliated, and intrusive contacts are also observed. These contacts are either sharp or gradational, with irregular, planar, curved, or anastomosing geometry. Figure F14A–F14F shows representative contacts commonly observed in Hole CM1A.

Contacts between (sub)units within the sequences

Within the Layered Gabbro Sequence, contacts between the subunits are generally due to changes in mineral modes and/or grain size. These contacts are sharp to gradational with planar geometry (Fig. F14B). Intrusive, sharp, and anastomosing contacts are less common but occur where gabbro (e.g., interval 25Z-4, 46–62 cm) or dunite (e.g., interval 51Z-3, 56–76 cm) intrudes into older lithologies (Fig. F14C, F14D). Tectonic and foliated contacts are rare within the Layered Gabbro Sequence (Fig. F14E, F14F).

The lowermost subunit of olivine-bearing gabbro (interval 63Z-4, 0–26.5 cm; Subunit 55e) of the Layered Gabbro Sequence has a tectonic, sharp, and anastomosing contact at 160.23 m with the underlying dunite (interval 63Z-4, 26.5–63 cm; Subunit 56a) of the Dunite Sequence. The olivine-bearing gabbro in contact with the dunite is altered and deformed, with thin mylonitic bands subparallel to the sharp contact. This is a zone of intense deformation and hydrothermal alteration (see **Alteration: Hole CM1A** and **Structural geology: Hole CM1A**)

Compared to the Layered Gabbro Sequence, few contacts are observed in the Dunite Sequence. Intrusive, sharp, and planar contacts occur where olivine gabbro and gabbro intrude into the dunite in the following intervals:

- 83Z-1, 0–6 cm,
- 83Z-2, 66–76 cm,
- 87Z-3, 61.5–64.5 cm,
- 95Z-2, 50–53 cm.

Modal, sharp, and anastomosing contacts are also observed between the chromitite bands and the dunite in the following intervals:

- 89Z-1, 76–76.5 cm, and 78.5–79 cm,
- 96Z-3, 9.5–10 cm,
- 99Z-2, 49–49.5 cm,
- 101Z-2, 4.5–5 cm,
- 101A-3, 22.5–23.5 cm.

The homogeneous dunite (interval 107Z-3, 19–86 cm; Subunit 56u) of the Dunite Sequence overlies rodingitized dunite (interval 107Z-3, 19–86 cm; Subunit 56v) that marks the top of the Dunite with Gabbro Sequence at 249.99 m. This is demarcated by an anastomosing, gradational tectonic contact (Figure F43A, F43B).

Within the Dunite with Gabbro Sequence, the subunits show tectonic, modal, and intrusive contacts. Tectonic contacts that are either gradational or sharp are common between the different rock types in the sequence and commonly display planar or anastomosing geometry, for example at the following sections:

- 108Z-1, 59 cm
- 109Z-1, 8.5 cm, and 42.5 cm
- 109Z-2, 14.5 cm
- 113Z-1, 77.5 cm
- 133Z-1, 9.5 cm, 24 cm, and 56 cm

Modal, gradational, and planar contacts are observed where there is an increase in olivine abundance from plagioclase-bearing wehrlite to dunite (e.g., interval 111Z-2, 0–78 cm). Modal, gradational, and anastomosing contacts are also noted between plagioclase-bearing dunite and dunite (e.g., interval 115Z-1, 0–13 cm [Subunit 58a], through 115Z-1, 13–97 cm [Subunit 58b]). Intrusive, gradational–sharp, planar, and anastomosing contacts are observed between olivine gabbro and gabbro and between plagioclase-bearing dunite and dunite (intervals 113Z-4, 39 cm; 123Z-1, 61.5 cm; 124Z-1, 45 cm; and 133Z-4, 27 cm).

The harzburgite and dunite subunits of this sequence generally show modal, sharp–gradational, and planar contacts (e.g., Sections 142Z-4, 32.5 cm, and 35.5 cm, and 143Z-1, 2.5 cm). A few intrusive, sharp, and planar–gradational contacts occur where gabbronorite, websterite, or anorthosite intrude the harzburgite, for example, at the following sections:

- 143Z-4, 8 cm, and 71 cm,
- 147Z-2, 57 cm,
- 148Z-1, 73 cm,
- 148Z-2, 16 cm,
- 148Z-3, 72 cm,
- 154Z-3, 78.5 cm.

Contacts between lithologic sequences

The contact between the Layered Gabbro and the Dunite Sequences is at Section 63Z-4, 26.5 cm, where the upper part of the section marks the lowermost olivine gabbro unit of the Layered Gabbro Sequence (olivine gabbro, Subunit 55e), whereas the lower part represents the beginning of the ~90 m long Dunite Sequence (Unit 56). This boundary is a ~30 cm long, steeply dipping fault (see also **Alteration: Hole CM1A** and **Structural geology: Hole CM1A**). The dunite is completely serpentinized, showing only a relict primary fine- to medium-grained granular texture. From 10 to 20 cm, the dunite is intruded by fine-grained troctolite forming a 5–10 mm thick irregular boudinaged band. The olivine gabbro at the contact is totally replaced by alteration phases and shows subparallel, slightly curved to wavy lamination, probably representing brittly deformed mylonite bands (for a core photo and details, see **Structural geology: Hole CM1A**).

The contact between the Dunite Sequence and the Dunite with Gabbro Sequence occurs at Section 107Z-3, 19 cm. This is a faulted contact where the dunite (Subunit 56u) has been hydraulically brecciated and a centimeter-thick, steeply dipping band of rodingitized dunite is emplaced (Subunit 56vw), interpreted as the first appearance of a gabbroic intrusion, features that are the characteristic magmatic feature of the Dunite with Gabbro Sequence, and become more common downhole. The first "true" gabbro occurs about 2 m deeper in the hole (Subunit 56y, clinopyroxene-bearing troctolite).

Section 142Z-4, 32.5 cm, marks the boundary between the Dunite with Gabbro Sequence and the Mantle Sequence, which is defined by the first occurrence of harzburgite with relict orthopyroxene porphyroclasts, characteristic of tectonized mantle rocks. Figure **F15** shows a core photo and close-up of a typical harzburgite near the sequence boundary. Characteristic of these rocks are millimeter-sized augen-like deformed orthopyroxenes with disrupted grain boundaries. In contrast, the dunites in the same section do not show any typical mantle deformation but display textural features very similar to those of the dunites further upsection (fine to medium grained, granular texture, with equigranular grain size distribution, no relics of porphyroclastic minerals; see Fig. **F15**).

Thin section descriptions

Principal lithologies

The following descriptions of the principal lithologies are based on individual thin section descriptions (see **Supplementary material** > **B_Thin_section descriptions**).

Dunite

Typical dunite from the Dunite Sequence or from the Dunite with Gabbro Sequence shows uniform characteristics of anhedral olivines forming a dense network of equant grains with fine- to medium-grained, granular texture and with equigranular grain size distribution (Fig. **F16**). No relict porphyroclastic orthopyroxene is present, nor are there any textural relics of porphyroclastic texture, as would be diagnostic of typical mantle rocks. Primary olivine contents in these rocks are mostly >99%, with remaining mineral content being trace spinel.

TS Sample 142Z-1, 84–88 cm, is of special interest because it is the only one of several thin sections with relict grains of olivine that are of probable magmatic origin (Fig. **F16**). In all other sections, olivine is completely replaced by serpentine.

Olivine gabbro

Most units of olivine gabbro are fine to medium grained and exhibit equigranular textures. Figure **F17** shows representative equigranular olivine gabbro with granular texture and moderately developed planar foliation parallel to the layering.

Olivine in olivine gabbro ranges 5%–15% in abundance and is mostly subhedral with elongate habit, with elongation parallel to the foliation. Partial alteration to serpentine is present in all investigated sections. In moderately to highly altered olivine gabbros, olivine is mostly completely replaced by serpentine and magnetite. Clinopyroxene in olivine gabbros is present in abundances ranging 22%–47%. Shape is mostly subhedral, and habit is prismatic. Plagioclase is variable in abundance (38%–70%) with generally tabular habit and subhedral shape.

Gabbro

The majority of gabbro shows granular texture and most are medium grained; a few gabbros are fine grained. Grain size distribution is mostly equigranular. Most rocks classified as gabbros have planar foliation, in general parallel to the layering of the gabbro, which can be generally observed in thin section (Fig. **F18**). Plagioclase abundance in gabbro ranges 20%–60%, and clinopyroxene abundance ranges 36%–80%.

Plagioclase is typically subhedral with tabular habit and generally unzoned. Clinopyroxene varies in shape and texture, mostly presenting subhedral shape with prismatic habit. Anhedral olivine, mostly elongated parallel to the foliation, is present in most gabbros (modal abundance < 5%).

Harzburgite

Typical harzburgites from Hole CM1A contain olivine, orthopyroxene, and small amounts of Cr-spinel and display texture defined by porphyroclastic orthopyroxene surrounded by olivine neoblasts, resulting in a bimodal grain size distribution (e.g., Fig. **F19**). Olivine abundance ranges 70%–90%. The olivine typically shows subhedral shapes and equant habits. Grains of spinel are always present, making up 1%–3% of the mode. Orthopyroxene abundance ranges 10%–27%, and most exhibit subhedral shapes. Characteristic sigmoidal crystal-plastic deformation of orthopyroxene and the presence of porphyroclastic texture are direct indicators of mantle flow and evidence that these harzburgites represent mantle residues (Fig. F19).

Wehrlite

Wehrlite was defined from TS Sample 6Z-3, 26–30 cm (Fig. F20). The modal composition of this sample is 81% olivine, 15% clinopyroxene, and 4% plagioclase. The grain size distribution is equigranular, grain size is medium, and texture is granular. Planar foliation fabric is parallel to the layering visible in thin section.

Approximately 80% of the olivine is replaced by serpentine and magnetite and the relics that remain occur as small ~100 µm sized isometric residual grains in originally millimeter-sized grains. Plagioclase is only slightly altered and is anhedral and elongate subparallel to the layering. Clinopyroxene is mostly unaltered and subhedral, occurring as subrounded isolated grains (Fig. F20).

Troctolite

Troctolite was described from TS Sample 9Z-3, 27–33 cm, where a contact between troctolite and gabbro was sampled (Fig. F21). The troctolite is composed of 10% plagioclase and 90% olivine. Olivine is strongly replaced (~55%) by serpentine displaying typical mesh texture. Most of the plagioclase is partially replaced by hydrothermal low-temperature phases (saussurite, clay minerals). The texture is medium grained and granular with interstitially emplaced plagioclase.

Anorthosite

Anorthosites are rare and occur only as thin layers (maximum of a few centimeters thick) in the Layered Gabbro and the Mantle Sequences. Only one thin section of an anorthosite presently exists, from the Layered Gabbro Sequence (Sample 9Z-3, 51–55 cm). The thin section shows a contact between anorthosite and olivine gabbro (Fig. F22). The rock shows granular plagioclase with equigranular grain size distribution. Its modal content is 100% plagioclase. Moderate planar foliation of the plagioclase grains is visible parallel to the layering. The plagioclase shows euhedral shape and has tabular habit. A few grains of elongated olivine occur (mode < 1%).

Detailed observations and special features

Reactions between gabbro and dunite in the Layered Gabbro Sequence

In the Layered Gabbro Sequence, dunite intrudes the gabbroic rock types in several places (e.g., interval 6Z-4, 2–10 cm; Fig. F23). In TS Sample 6Z-4, 4–8 cm, anhedral olivine infiltrates the gabbro with the tendency to include grains from the gabbroic mush, which is clearly an intrusive feature. Unfortunately, the olivine is up to 100% replaced by serpentine such that details of the individual olivine grains are not preserved. Away from the intrusive contact, the olivine progressively becomes more interstitial, resulting in "poikilitic" structure with inclusions of plagioclase and clinopyroxene from the gabbro mush (Fig. F23). This implies a pseudocrystallization order of olivine after plagioclase/clinopyroxene, which is in fact a product of the dunite infiltration process. Directly at the contact, smaller interstitial grains of olivine exist, resulting in a thin domain of olivine gabbro. Some millimeters away from the contact the intruded host rock is pure gabbro, lacking olivine. Very probably the observed situation is the result of mixing between dunitic and gabbroic crystal mush, implied by the sutured grain boundaries and the lack of any reaction between the two lithologies.

Rapid crystal growth of olivine

At some places in the olivine gabbros from the Layered Gabbro Sequence, large (centimeter-sized) olivines with dendritic to skeletal textures are present. The best example is in interval 17Z-1, 3–22 cm (see Fig. F24A). The corresponding TS Sample 17Z-1, 18–22 cm, shows centimeter-sized anhedral skeletal olivine with disrupted grain boundaries enclosing plagioclase with interstitial habit and some smaller clinopyroxene grains. The olivine is up to 100% replaced by serpentine such that details of the individual olivine grains forming the skeletal domain are not observable (Fig. F24B–F24E).

This observation is of importance because such textures imply fast crystal growth. These types of textures have been reported from layered intrusions (Isle of Rhum) and were interpreted as indicative of magmatic undercooling (O'Driscoll, 2007; Donaldson, 1982). Other reasons for such textures could be extreme cooling rates due to strong thermal or compositional gradients (see Koepke et al., 2011). The presence of tectonic fractures invaded by hydrothermal fluids a few meters above the interval where these specific textures were observed may be evidence for local rapid cooling of the mush in this precise location. Importantly, the local presence of these olivine textures shows that deformation subsequent to crystallization of the grains was locally minimal; otherwise, these delicate structures would be destroyed.

Poikilitic clinopyroxene vs. poikilitic plagioclase in dunite

In several core sections within the dunites of the Layered Gabbro and the Dunite with Gabbro Sequence, roundish, <1 cm domains of poikilitic crystals are present. Most of these poikilitic domains are formed by plagioclase (for details see supplemental Table ST1), for example,

- 18Z-3, 83–90 cm,
- 20Z-4, 45–48 cm,
- 113Z-4, 39–53 cm,
- 114Z-1, 0–74.5 cm,
- 114Z-2; 0–66.5 cm,
- 115Z-1; 0–13 cm,

or by both plagioclase and clinopyroxene, for example,

- 18Z-2, 14–71.5 cm,
- 18Z-3, 53–55 cm,
- 18Z-4, 0–25.5 cm,
- 59Z-1, 0–56 cm.

In terms of rock type, the poikilitic crystals form troctolitic (plagioclase + olivine) or wehrlitic (clinopyroxene + olivine) domains. In the following section, we focus on one spectacular example from the Layered Gabbro Sequence, where both troctolitic and wehrlitic domains coexist in a single thin section (Sample 18Z-2, 62–67 cm; Fig. F25A). The thin section displays 6 troctolitic and 2 wehrlitic domains (Figs. F25B, F26A–F26D), where up to 8 mm sized plagioclase or clinopyroxene crystals enclose 0.5–1 mm olivine grains. The texture of the matrix dunite (Fig. F26E, F26F) is undeformed, forming an equigranular fine-grained granular network that is characteristic of the dunites from this sequence, which were formed very probably by crystal accumulation, in contrast to crystal-plastic deformed dunites from the Mantle Sequence.

The formation of these poikilitic patches can be explained by cooling of pure olivine mush to temperatures where saturation of either plagioclase or clinopyroxene was produced, forcing the remaining melt to crystallize interstitially and enclosing the olivine grains of the mush. For mid-ocean-ridge basalt (MORB) crystallization in a dry system (as is typical for basalts from mid-ocean ridges in major ocean basins) clinopyroxene crystallizes at ~50°C, after plagioclase saturation (e.g., Elthon, 1991). So, how can plagioclase and clinopyroxene crystallize more or less simultaneously after the saturation of the liquidus olivine? This crystallization sequence can be attributed to elevated water activity and its well-known effect of suppression of plagioclase saturation during the main-stage crystallization of MORB melts (e.g., Gaetani, et al., 1993; Feig et al., 2006). As recently shown by two independent papers, the water content of the primary melts of the Wadi Tayin massif of the Oman paleoridge is estimated to be 0.4–1 wt% or higher (MacLeod et al., 2013; Mueller et al., 2017) with the potential of delaying plagioclase crystallization. Thus, we infer elevated water activity in primary melts of the Oman paleoridge drove the system into a region of the phase diagram near the crossing point of the plagioclase and clinopyroxene saturation curves. Local variation in water activity resulted in crystallization of either plagioclase or clinopyroxene (see Fig. F27).

Brown amphibole-bearing gabbros

Magmatic amphibole is typically a late-stage phase in oceanic gabbros, providing information on the latest stage of magmatic differentiation at temperatures <1050°C, and of the properties of the ambient fluid, because amphibole can incorporate OH, F, and Cl. Typical magmatic amphiboles in oceanic gabbros are brown, resulting from relatively high TiO_2 contents. However, brown amphiboles can also be formed at high temperatures by metamorphic reactions (generally >700°C). Consequently, it is often difficult to determine petrographically whether an individual amphibole is of magmatic or metamorphic origin. Here, textural features may help, as euhedral crystal shapes imply magmatic origin from a melt, whereas overgrowth textures may indicate a metamorphic formation mechanism.

In Hole CM1A, amphibole was described in a few sections of hornblende-bearing gabbros and gabbronorites of the Layered Gabbro Sequence, partly in pegmatitic varieties (Subunits 26a, 26c, 30b, 30d, 36b, 37d). Thin section Sample 16Z-2, 35–48 cm, shows such an amphibole-bearing rock type (Fig. F28). This rock is heterogeneous gabbro in which patches of coarse-grained hornblende-bearing gabbro interfinger with medium-grained gabbro without hornblende. The amphibole is brown and pleochroic and occurs as <1.2 mm subhedral, prismatic to interstitial crystals. The largest crystal is prismatic and trapped within clinopyroxene with sharp grain boundaries with no replacement reaction, implying magmatic origin. Smaller grains were probably grown interstitially, as is typical for late-stage amphiboles. Because large parts of the matrix adjacent to the amphiboles are totally replaced by hydrothermal alteration, we are unable to provide a detailed description (see Fig. F28).

Additional brown amphibole was observed in TS Sample 17Z-1, 18–22 cm. Here, in medium-grained gabbro, brown hornblende overgrowths replace clinopyroxene. In this sample, amphibole can also form coherent large (5 mm) anhedral, poikiloblastic crystals with brownish cores that grade to green at the rim (Fig. F28). Along contacts with adjacent clinopyroxene, diffuse reaction zones occur. Although the environment of the amphibole is strongly altered, the observed textural features suggest a metamorphic origin for this amphibole. The brownish color in the core indicates a higher metamorphic grade, at least at amphibolite facies, which contrasts with the typical hydrothermal alteration in the gabbros of Hole CM1A, which indicate lower temperature greenschist facies conditions (see Alteration: Hole CM1A).

Textures in massive dunites

To better understand the formation of the massive dunites in the Dunite and Dunite with Gabbro Sequences, we investigated in detail the corresponding thin sections. With the exception of one thin section in the Dunite with Gabbro Sequence (Sample 142Z-1, 84–88 cm), all other massive dunites are completely altered so that only relic textural features of the original rocks can be observed. In Figure F29 we compiled microphotographs of representative textures from dunites from the Dunite and Dunite with Gabbro Sequences and compared these with dunites from the Mantle Sequence. We included also one dunite from the Layered Gabbro Sequence (Sample 18Z-2, 62–67 cm) as reference texture for magmatic formation by crystal accumulation, as this dunite forms a layer within a series of layered gabbro, generally assumed to have formed by crystal accumulation. Moreover, this dunite bears undeformed poikilitic crystals of plagioclase and clinopyroxene, supporting the hypothesis that these dunites were formed by a magmatic accumulation process rather than any reaction process between peridotites and MORB melt (for details on the formation of the poikilitic domains see also Reactions between gabbro and dunite in the Layered Gabbro Sequence). The texture of this dunite shows a dense regular network of equant olivine grains with equigranular grain size distribution. The average grain size is 1 mm. Tiny Cr-spinels (maximum = 0.1 mm grain size) form inclusions within the olivine grains or interstitial growth on grain boundaries. Because this dunite also contains relics of olivine (red arrows in Fig. F29), the grain size and shape of the original olivine grains can be clearly determined.

In Figure F29 we compare this texture with those representative of massive dunites, both from the Dunite and from the Dunite with Gabbro Sequences (5 and 3 images for each), revealing a high grade of similarity between all these textures, also with respect to details on chromite features, which forms either tiny inclusions in the olivine or has crystallized on grain boundaries between the olivine crystals (yellow arrows in Fig. F29). Primary olivine contents in these rocks are generally > 99%; remaining mineral content is spinel. This comparison implies that the massive dunites formed by a similar process, which was probably crystal accumulation in a melt, as derived from the example for dunites from the Layered Gabbro Sequence.

These textures are significantly different from those of mantle dunites as shown also in Figure F29 (images of 3 samples). These typically show relics of former pyroxene porphyroclasts (not clear whether orthopyroxene or clinopyroxene), and the matrix is in general diffuse and blurred, lacking the presence of a regular equigranular network of olivine grains, as demonstrated in Figure F29. In addition, chromite grains show distinct characteristics, forming up to 1 mm sized individual grains.

To summarize, the main conclusion of this comparison is that the relict textures of massive dunites in the Layered Gabbro, Dunite, and Dunite with Gabbro Sequences formed by a similar magmatic process that is probably related to crystal accumulation at the base of the crust rather than processes within the mantle. This assessment is also supported by the absence of any relics of crystal-plastic deformed minerals or of typical porphyroclastic texture, as would be diagnostic of typical mantle rocks.

Below the contact between the Dunite with Gabbro and the Mantle Sequences, the undeformed equigranular texture typical of the massive dunites above becomes less and less common and is finally replaced by dunite with porphyroclastic relics alternating with porphyroclastic harzburgite. The lowermost dunite with undeformed equigranular texture is observed in interval 145Z-4, 38–43 cm, implying that this is the lowermost site of pure magmatic activity, probably due to crystal accumulation. Downhole, only dunite with porphyroclastic orthopyroxene relics occur. Large chromite grains as well as relict porphyroclasts (now completely altered) clearly imply that these rocks belong to the Mantle Sequence (see the last row of images in Fig. F29).

Alteration: Hole CM1A

Hydrothermal alteration occurs throughout Hole CM1A, and the rocks have undergone multiple phases of fluid infiltration and water-rock reactions. Hydrothermal alteration in Hole CM1A is reflected by secondary mineral replacements of primary phases identified as (1) background alteration of the host rocks, (2) isolated alteration patches, (3) halos surrounding veins or at lithologic contacts, and (4) as alteration zones related to deformation. In addition, fluid pathways and hydrothermal alteration are marked by precipitation of secondary minerals in multiple generations of veins. Alteration is highly variable in terms of types and intensity on the scale of a single ~1 m section, and the alteration mineral assemblages vary depending on the host rock lithology. All four of the above categories as well as various generations of hydrothermal veins were logged during core description and document a complex history of fluid-rock interaction in the lower crust and upper mantle. Alteration reactions and secondary mineral precipitation occurred under a range of temperature conditions and fluid compositions throughout the lifespan of the Oman ophiolite, from the Tethyan mid-ocean ridge through obduction to present-day exposure in the mountains of Oman.

In the following sections, we describe the main alteration characteristics of the gabbroic, ultramafic, and rodingitized rocks within (1) the lower crustal gabbroic rocks, defined as the Layered Gabbro Sequence; (2) the CMTZ, consisting of a serpentinized dunite sequence associated with wehrlite (Dunite Sequence) and intervals of dunites intruded by gabbroic rocks in the Dunite with Gabbro Sequence; and (3) serpentinized harzburgites with minor irregularly distributed dunite (without magmatic texture) and gabbroic layers in the Mantle Sequence (Table T3). In addition, characteristic vein generations and mineral infillings are described for the main lithologic sequences. See the Alteration log (supplemental Table ST3) and Vein log (supplemental Table ST4) for continuous downhole observations for Hole CM1A. Abbreviations used in the text and figures are defined in Table T5 in the **Methods** chapter.

During macroscopic core description, the alteration team identified and logged the alteration characteristic for each subunit identified by the igneous group and identified the proportions and mineral assemblages contributing to the background alteration, patch alteration, halos, and deformation-related alteration (Figs. F30–F35; supplemental Table ST3). If distinctly different metamorphic features were prevalent within an igneous subunit, the alteration team recorded the features on additional lines of the spreadsheet for that interval in the logs. Overviews of the overall downhole variations in alteration intensity, alteration mineral assemblages, and vein fillings are shown in Figures F30–F34. Total alteration intensity mainly reflects the background alteration intensity (given in parenthesis in the following discussion) and is highly variable downhole, ranging from <10% in gabbroic rocks in the Layered Gabbro Sequence to 100% in dunitic intervals (Figs. F30, F31). The mean alteration intensity is ~30.4% (20.2%) for the Upper Gabbro Sequence, 94.7% (95%) for the Dunite Sequence, 84.7% (86.5%) for the Dunite with Gabbro Sequence, 90.8% (91.7%) for the overall CMTZ, and 82.1% (87.1%) for the Mantle Sequence. Alteration intensity, however, varies greatly depending on rock type and increases with increasing vein density or deformation, as discussed below.

X-ray diffraction results

Approximately 230 XRD analyses of material sampled from Hole CM1A were performed using a PANalytical CubiX^3 X-ray diffractometer (Table T4). A compilation of the spectra and sample locations within the core is given in supplementary Figure SF1. The main target of these analyses was to identify the vein fillings and their alteration halos (if present). The background composition was rarely analyzed; results of XRD on bulk rock powders collected at the rig site are presented in **Geochemistry: Hole CM1A**.

Downhole variations in the vein mineral assemblages determined by XRD are shown in Figure F34. In the upper 100 m of the core, prehnite was confirmed to be the main vein mineral with or without chlorite, although in the uppermost part of the core, calcite and aragonite veins are also present (Samples 2Z-2, 41 cm; 4Z-2, 5 cm). In addition, veins with epidote group minerals together with chlorite are also relatively abundant in the gabbroic intervals of the Layered Gabbro Sequence. Minor amphibole veins were observed as infillings in rare dark green veins in the gabbroic rocks within the Layered Gabbro Sequence. More complicated mineral assemblages were detected at greater depths and closer to metasomatic alteration fronts related to magmatic intrusions, as well as in the transition zone between the lower crust and the mantle (e.g., Sections 54Z-3, 54Z-4, 55Z-2, 59Z-2, 63Z-3; 136–160 m depth). In these domains, highly altered units are composed mostly of diopside with accompanying vesuvianite, garnet (hydrogrossular and possibly uvarovite) chlorite, and xonotlite ($Ca_6Si_6O_{17}[OH]_2$). These calc-silicate minerals also occur in veins and are characteristic of rodingitization of mafic rocks within with serpentinites (Frost, 1975; Honnorez and Kirst, 1975). In the Mantle Sequence, background alteration in the serpentinized peridotites was confirmed to consist of serpentine ± brucite and coalingite ($Mg_{10}Fe^{3+}{}_2[CO_3][OH]_{24}\cdot 2[H_2O]$). Coalingite is present on rusty reddish brown fourth-generation serpentine vein surfaces (see Table T4) and may be widespread as a weathering product of serpentine. Abundant calcite was detected in veins sampled from the serpentinized harzburgites below Section 170Z-1. Spinel, mostly magnetite, was confirmed to be present together with serpentine in the banded veins and in the mesh textures.

Less common examples of minerals identified by XRD analyses include calcite + pyrite in veins in the Layered Gabbro Sequence, amphibole + serpentine background occurring near the metasomatic alteration fronts, coalingite + calcite as replacements of serpentine and as infillings of fractures, hydrogrossular + serpentine as a replacement after plagioclase in metasomatic intervals, clay minerals (kaolinite) on the fault surface, and possibly zeolite in cataclastic zones.

Layered Gabbro Sequence

Alteration in the Layered Gabbro Sequence

Sections 1Z-1 through 63Z-3; 1–160.23 m

Background alteration intensity in the gabbroic rocks of the Layered Gabbro Sequence varies from nearly fresh (5%) to highly altered (95%) (overall average = ~20%). Slightly altered gabbros with <8% total alteration occur in the upper 104 m of the core (to Section 42Z-1) and make up 7.4% of the total core (Figs. F30, F36; supplemental Table ST3). Intervals with higher alteration intensity are present at 70–80 m (average = 45%), 120–130 m (average = 57%), and 140–150 m (average = 55%) (Fig. F30). Alteration intensity is higher in olivine-rich intervals and increases with degree of veining and deformation. Olivine-rich lithologies, such as wehrlitic to dunitic rocks, are abundant in the highly altered interval at 140–150 m. Deformation-related alteration as the dominant type of alteration (>65% total alteration) is limited to intervals in Section 23Z-3 (51.7 m) and Sections 42Z-3, 42Z-4, and 43Z-4 (106.6–109.8 m). Within the deformation-related alteration interval at 51.7 m (Section 23Z-3), the proportion of alteration halos is also higher than in the overlying and underlying intervals (Fig. **F36**). In addition, the proportion of alteration halos around veins increases from 110 m toward the top of the CMTZ at 160 m (Fig. **F36**). Overall, total alteration intensity is higher in intervals from 110 m downsection to the CMTZ than in the layered gabbro–dominated intervals.

In intervals classified as having slight alteration background, alteration is localized along veins, mainly filled with prehnite and/or chlorite (Figs. **F36**, **F37**). Background alteration is dominated by the occurrence of secondary plagioclase after plagioclase (milky white phases replaced by a fine-grained mineral aggregate), chlorite and amphibole (most likely tremolite/actinolite) replace plagioclase and pyroxene, and serpentine + magnetite replace olivine (Fig. **F38**). The olivine grains commonly have a yellow-green colored phase in the core centers, which is possibly clay minerals or fine-grained brucite (Fig. **F37**). On a thin section scale, clays are locally concentrated in olivine. Mineral zoning is observed along olivine and plagioclase boundaries in highly altered gabbros: tremolite/actinolite-dominant zones occur at the contact with olivine and are in turn bordered by chlorite-rich domains at the contact to plagioclase (Fig. **F38**). Tremolite/actinolite-dominant zoning in cores surrounded by chlorite-rich margins is commonly observed in highly altered gabbros and, thus, are interpreted as olivine pseudomorphs. Clinopyroxene is partly replaced by amphibole + secondary clinopyroxene in highly altered samples (Fig. **F38**).

Alteration patches are generally defined by differences in color compared to the background alteration and make up 0.1% of the alteration in the Layered Gabbro Sequence (Fig. **F35**). The most common colors of the alteration patches are light gray to greenish gray. Alteration patches are generally irregular to rounded in shape and either 3–6 cm or >6 cm in size. Patch alteration intensity ranges 60%–85%. On the whole, alteration patches are very limited and seem to be related to the presence of veins or deformation in the CMTZ sequences of Hole CM1A.

Alteration halos are the second most prevalent alteration feature after background alteration (Fig. **F35**). Halo alteration intensity ranges 5%–100% and makes up 8.1% of the total alteration intensity of the Layered Gabbro Sequence. Alteration halos are mostly associated with veins and are very rarely found at lithologic boundaries (only Section 50Z-3; Fig. **F35**). Secondary minerals present in halos mainly include secondary plagioclase (fine-grained aggregate after primary plagioclase), amphibole, chlorite with minor amounts of prehnite, and likely zeolite/clay minerals.

Deformation-related alteration is present in 1.9% of total alteration intensity. Deformation-related alteration intensity ranges 50%–90%. The high degrees of alteration in the deformed intervals are difficult to consider in isolation from the hydrothermal veins because the veins commonly form a large component of these intervals. Deformation-related alteration ranges from 2–3 cm scale bands to up to 1 m and is generally associated with brecciation and cataclasis. Deformation-related alteration is locally present in Hole CM1A (Fig. **F35**); the highest proportions (80%–100% of an alteration interval) are found at discrete depths at 52 m and 106–110 m (Fig. **F36**). The dominant secondary mineralogy is similar to the other alteration types and is dominated by chlorite + amphibole. Many veins of chlorite, prehnite, and carbonate are associated with deformation-related alteration.

Alteration in the intercalated dunite and clinopyroxene- or plagioclase-bearing dunite intervals is dominated by background alteration, with serpentine and magnetite forming typical serpentine mesh textures after olivine. Serpentine makes up ~90% of the alteration, and magnetite up to 10%, with a relatively homogeneous distribution downhole (Fig. **F33**). Fine-grained magnetite forms along the mesh rims and outlines the former olivine grains.

Veins in the Layered Gabbro Sequence

Veins in gabbroic intervals

Veins in the gabbros in Layered Gabbro Sequence are typically of millimeter width and their distribution and mineralogy vary throughout the sequence. Individual and networks of veins and vein sets were recorded downsection; representative examples of veins in the Layered Gabbro Sequence are shown in Figure **F39**. Four types of crosscutting veins with variable distribution and mineral fillings were recognized, and their characteristics are presented in Table **T5**. The minerals filling veins were identified macroscopically and recorded in the Vein log (supplemental Table **ST4**) and thin section logs (**Supplementary material** > **B_Thin_section_descriptions**). Mineral infillings were confirmed by XRD on selected samples, and the results are summarized in Figure **F34** and Table **T4**. The veins in the Layered Gabbro Sequence formed as many as 4 generations, but the crosscutting relationships between the generations are highly variable, so vein type cannot always be equated with a specific vein generation.

The uppermost type of veins are filled almost exclusively with calcite and are prominently abundant in two intervals of the Layered Gabbro Sequence. They dominate in Sections 2Z-2 through 12Z-4 (1.98–26.14 m) and also occur in Sections 16Z-1 (35.65–35.68 m), 18Z-4 (41.08–41.12 m), and 35Z-1 (83.70–83.73 m) and irregularly occur in Sections 43Z-1 through 56Z-1 (107.43–140.17 m). They are mostly vuggy or massive and contain minor iron oxyhydroxides, which account for their orange and yellowish white color and local halo. Some of carbonate veins are composite. They occur either as single veins or form networks of subparallel veinlets of more or less planar morphology. They also follow the foliation of the host rocks.

Below 26.14 m (Section 12Z-4), prehnite ± chlorite veins are the dominant vein type. They exhibit a wide variety of textures, structures, morphologies, and connectivity relationships as well as variations in width, color, and proportion of prehnite/chlorite. Following criteria outlined in Figure F22 in the **Methods** chapter, prehnite ± chlorite vein textures in the Layered Gabbro Sequence can be classified as massive, vuggy, sheared, overgrowth, patchy, brecciated, and polycrystalline; massive textures are the most common. Most of the veins are surrounded by alteration halos with an average halo width of 4 mm (range = 0.5–50 mm), but they can also be uniform, intravenous, composite, and banded. They occur as vein networks or as single crosscutting or branched veins and show planar, irregular, and curved morphologies. Their average width is 2 mm but varies strongly throughout the upper part of Hole CM1A from <0.5 mm up to 20 mm. With depth, the width of the prehnite-chlorite veins as well as the width of associated alteration halos increases. The alteration halos associated with the prehnite-chlorite veins are also variably developed, irregularly extending outwards into the wall rock. The prehnite-chlorite veins exhibit a wide range of color from milky white, white, gray, and light green to green. The percentage of replacement of the primary minerals by secondary assemblages is highly variable, ranging 30%–100%, most commonly 50% (Fig. F35).

The third type of veins in the Layered Gabbro Sequence are assemblages dominated by clinozoisite/epidote + prehnite with a large variety of subordinate minerals. In the following discussion, we refer to these veins simply as clinozoisite-prehnite veins. These veins become the most common downhole and are associated with extensive alteration halos (Fig. F39). The clinozoisite-prehnite veins first appear in Section 20Z-3 (45.68–46.37 m) and then are present in Section 23Z-2 (51.43–51.67 m) but become abundant from Sections 44Z-1 through 63Z-3 (109.81–159.96 m). They form an extensive vein network close to the boundary between the gabbroic intrusion at the lower boundary of the Layered Gabbro Sequence and the underlying Dunite Sequence. The relative proportions of clinozoisite to prehnite in the veins varies strongly throughout the gabbroic intervals of the core, with the epidote group minerals averaging 27.5% but reaching up to 100% in Section 44Z-1 (supplemental Table ST4). Other notable minerals identified in the clinozoisite-prehnite veins include chlorite, clay minerals (kaolinite), zeolites (possibly phillipsite), and serpentine (lizardite and chrysotile), as well as hydrogarnet replacing feldspars. XRD analyses identified xonotlite and vesuvianite ($Ca_{10}[Mg,Fe]_2Al_4Si_{15}O_{34}[OH,F]_4$), which form patchy veins in the brecciated domains and thicker vein networks (Fig. F38).

Throughout the upper part of the Layered Gabbro Sequence, 0.5 mm amphibole and serpentine veins are present. They are massive or patchy, uniform and locally haloed, single and irregular, and hard to distinguish macroscopically due to their dark green to black color. The amphibole and serpentine veins are commonly subparallel to each other or are branched with vein tip morphologies.

Locally in the lower part of the Layered Gabbro Sequence, late-stage sulfide-rich polycrystalline calcite veins fill fractures and the euhedral carbonate crystals are as large as 3 mm (Fig. F39; Section 57Z-1).

Veins in intercalated ultramafic subunits

Similar to the gabbroic intervals, the veins in the intercalated ultramafic rocks within the Layered Gabbro Sequence form 2 generations (Fig. F39; Table T5). The first generation of veins in the ultramafic intervals is restricted to the olivine-rich domains in the plagioclase-dominated subunits and only occurs in the upper 130 m of Hole CM1A. These veins are linked to background serpentinization and are filled predominantly with serpentine group minerals constituting >95% of the vein filling; sizes of single crystals are <10 µm in diameter (Fig. F40). Magnetite is subordinate in these veins and forms <20 µm sized crystals that are commonly present in the centers or at the margins of the veins, as observed in thin section. Serpentine and magnetite form multiple networks with complex connectivity. Throughout the sequence, the vein network of serpentine + magnetite has a relatively constant average width of 0.5 µm (Fig. F40). The serpentine and magnetite veins exhibit massive textures, uniform structures, and irregular morphologies and are black, with little variation with depth downhole. The consistent lack of alteration halo around the serpentine-magnetite veins makes them distinctive from other veins in the Layered Gabbro Sequence. Locally, they become more prominent in the intercalated ultramafic subunits deeper in the sequence.

The second generation of veins in the intercalated ultramafic subunits occurs as either chlorite only or prehnite-chlorite veins that cut the serpentine-magnetite mesh network and also occur in the underlying Dunite with Gabbro Sequence (Fig. F39). The chlorite-only veins have variable thicknesses ranging 0.5–2 mm (average = 1 mm). The chlorite veins are mostly massive, but thicker veins can be polycrystalline. They are typically branched and most commonly are surrounded by a thin (1 mm wide) green chlorite-rich halo. Some veins have minor calcite (<5%). The prehnite-chlorite veins have a wide range of vein width (<0.5–7 mm) and exhibit planar or branching morphology. These veins are massive and commonly have light greenish white alteration halos with highly irregular width (0.5–5 mm; average = 1 mm) that fades diffusively into the background alteration.

Opaque mineral assemblages in the Layered Gabbro Sequence

Opaque minerals were identified in the Layered Gabbro Sequence in thin sections (Cores 7Z–178Z) with a petrographic microscope in reflected light (Fig. F12). Layered gabbros and intercalated ultramafic subunits contain a wide range of opaque minerals including primary and secondary sulfides and oxides.

Secondary sulfides in the layered gabbro intervals are predominantly pyrite and chalcopyrite, which form grains <100 µm in diameter and are associated with late-stage calcite veins. Large (a few hundred micrometers in diameter) aggregates of Ni-sulfides are particularly abundant in the intervals where serpentinized ultramafics are intercalated with layered gabbro and are bound to the later lithology. Magnetite is present in numerous gabbros, where it forms as a replacement of olivine.

Crust–Mantle Transition

Alteration in the Dunite Sequence

Sections 63Z-4 through 107Z-3

The dominant alteration phases and intensity of alteration change drastically at the top of the CMTZ in Section 63Z-4 (160.23 m) from where dunite becomes the main rock type (99.7%) (Figs. F30–F32). This boundary is marked by a subvertical fault between highly deformed, strongly rodingitized gabbro and completely serpentinized dunite (Fig. F41). Alteration in the Dunite Sequence is relatively constant at >95% total alteration, with the exception of thin chromite-rich layers, where alteration ranges 60%–70% or more rarely reaches up to 90%. Alteration in the serpentinized dunites is dominated by background alteration, with serpentine and magnetite forming typical serpentine mesh textures after olivine. Serpentine makes up ~90% of the alteration and magnetite up to 10%, with relative homogeneous distribution downhole (Fig. F32). The fine-grained magnetite along the mesh rims outlines the former olivine grains, and its abundance throughout the sequence makes the core characteristically black (Fig. F40). Macroscopic logging of the Dunite Sequence also identified carbonate (or hydrocarbonate) in the matrix, which reacts with HCl and leaves a light mark on the cut core surfaces.

The contact between upper crust and the Crust–Mantle Transition (Mohorovicic Discontinuity; Moho) is marked by the presence of a highly deformed, banded rodingitized gabbro in interval 63Z-4, 6–15 cm (Fig. F42). XRD analyses of the banded domains identified diopside + grossular in green bands and chlorite + grossular in dark gray bands at the contact to the serpentinized dunite (Table T4). Vesuvianite and diopside form green bands toward the center of the rodingite, whereas xonotlite fills white, translucent patches that are irregularly distributed within the rodingitized portion of the contact zone.

Alteration in the Dunite with Gabbro Sequence

Sections 107Z-3 through 142Z-4; 249.99–310.99 m

Background alteration is the main alteration type in the Dunite with Gabbro Sequence and commonly amounts for 100% of the total alteration (Fig. F30). Vein halos are only locally present in minor narrow (<1 m) intrusions of gabbro. In general, the background alteration intensity is either very high or complete (90%–100%) throughout the sequence, but deeper than 293 m alteration is slightly less intense (70%–85%). Gabbroic intrusions with variable grain sizes are observed especially in the upper part of the Dunite with Gabbro Sequence, in sections

- 107Z-3,
- 108Z-1,
- 109Z-1 and 2,
- 111Z-3 and 4,
- 119Z-3,

and are characterized by a diversity of alteration intensity, ranging 15%–100%. The typical background alteration texture is pervasive, but locally highly fractured rocks are associated with very high alteration intensities.

The Dunite with Gabbro Sequence is marked by the irregular presence of rodingitized dunite and wehrlite and by diopsidite with serpentine breccia. However, the background alteration is strongly defined by the protolith rock types. Consequently, the most common background alteration is the near complete serpentinization of dunite manifested as serpentine (90%) and magnetite (10%) with rare subordinate secondary plagioclase and some unidentified phases (<5%). The assemblage of serpentine + magnetite dominates for almost 8 m from Sections 107Z-3 through 113Z-3 (250.25–258.03 m). At 258.03–278.06 m, a 2 m thick microgabbroic intrusion (interval 113Z-1, 77.5–97.5 cm, through 113Z-4, 0–39 cm) is strongly altered with the replacement of primary igneous phases by amphiboles (up to 15%), secondary plagioclase (up to 35%), chlorite (up to 40%), and locally, clay minerals, reaching up to 50% in interval 113Z-2, 0–93.5 cm, whereas the proportion of serpentine and magnetite drops to <50% (Figs. F32, F36). Veins of amphibole and plagioclase (both up to 60%) and chlorite (up to 30%) are surrounded by 3 mm wide, green, strongly altered halos. Ca-metasomatism (see Metasomatism and rodingite in intercalated gabbroic subunits) characterized by diopside amounting for 90% of the total secondary mineral assemblage occurs at 270–279 m (119Z-2, 2–97.5 cm, through 123Z-2, 0–45 cm) and 290–293 m (113Z-1, 9.5–24 cm, through 133Z-4, 0–27 cm). However, throughout these intervals the mineralogical proportions are highly variable (supplemental Table ST3). In the lowest part of the Dunite with Gabbro Sequence, amphibole, secondary plagioclase, and chlorite (up to 5%) occur as subordinate phases together with the dominant serpentine + magnetite assemblage (Figs. F32, F34).

Metasomatism and rodingite in intercalated gabbroic subunits

An important feature of the CMTZ in Hole CM1A is the occurrence of interlayered dunitic and gabbroic intervals that have undergone extensive metasomatic alteration producing Ca-rich rodingite mineral assemblages in the gabbroic intrusions. Rodingites are generally considered to be Ca-rich mafic dikes in serpentinized peridotites that commonly have low silica concentrations compared to their unaltered precursor lithologies (e.g., Frost 1975; Honnorez and Kirst, 1975; Frost and Beard, 2007; Python et al., 2011). In Hole CM1A, intervals with rodingite display a wide spectrum of mineralogical assemblages and textures and are commonly found in coarse-grained and pegmatitic gabbroic domains. They are nearly always limited to <1 m thick intrusions in the ultramafic sequences and occur at contacts between variably altered gabbroic and completely serpentinized dunitic units or in patches in altered dunite and harzburgite units. Particularly good examples are found at 250–293 m in Sections 107Z-3, 108Z-1, 109Z-1, and 133Z-1 through 133Z-3 (Fig. F43). The completely altered (100% secondary minerals) domains are primarily composed of white and light green euhedral to subhedral diopside (up to 80%) exhibiting a variable of grain sizes ranging <0.01–5 mm. XRD analyses indicate that diopside ± serpentine replaces clinopyroxene. Chlorite + prehnite replacing plagioclase commonly occurs as part of the background alteration assemblage but also as infillings in veins that crosscut the rodingites and extend into the dunitic wall rock. Some crystals exhibit elongation textures caused by plastic deformation related to the later diopside veins (Sample 107Z-3, 80–85 cm). Locally, relict igneous minerals (clinopyroxene and spinel) can be observed as remnants after the highly intense metasomatic processes. Other common calc-silicate minerals within the rodingitized gabbroic domains include white and gray (translucent) xonotlite, light green and brownish vesuvianite, and whitish garnets (hydrogrossular) commonly together with serpentine, bright green uvarovite, green chlorite, and pinkish to reddish brown titanite (all confirmed by XRD; see Figs. F34, F42–F44; Table T4). These minerals form patches, bands, and veins in the diopsidic background. In the lower part of Hole CM1A, rodingites are commonly crosscut by serpentine vein networks with hydrogarnet crystals overgrown on them.

Calc-silicate veins occur in the rodingites and at contacts between (micro)gabbroic intrusions and serpentinized dunite. They are highly varied in terms of mineralogical assemblage, appearance, and connectivity, which leads to difficulties in determining their relationship with the altered background. Vein-filling minerals in the rodingites include prehnite, chlorite, amphibole, diopside, vesuvianite, xonotlite, and garnets (grossular, hibschite, hydrogrossular, andradite, uvarovite), which form either polycrystalline or monomineralic veins or occur as distinct banding at the contact to the surrounding dunites (Figs. F43, F45; Table T5). Locally, the metasomatic overprint can extend a few millimeters into the dunitic wall rock, primarily evidenced by the occurrence of chlorite.

Veins in ultramafic sequences of the CMTZ

Veins observed in dunite intervals within the CMTZ can be divided into two main types: serpentine veins related to serpentinization reactions and veins related to Ca-metasomatism and rodingitization in intercalated, highly altered gabbroic intrusions. Local amphibole veins occur in the following gabbroic Intervals (supplementary Table ST4):

- 113Z-2, 21–90 cm,
- 113Z-2, 81–83 cm,
- 113Z-4, 11–58 cm,
- 133Z-4, 0–26 cm.

Four vein generations can be distinguished in the serpentinized ultramafic (dunitic, harzburgitic, websteritic) rocks within the CMTZ (Table T5; Fig. F46). The first serpentine vein generation (V1) occurs as randomly oriented networks of submillimeter veins forming mesh and bastite textures (pseudomorphic replacement of olivine and pyroxene) and are ubiquitous in the partly to completely serpentinized rocks. First generation (V1) veins are dark green to black and uniformly distributed throughout the altered dunites. They are characterized by massive texture, composite structure, and highly irregular morphology. The V1 veins mainly consist of serpentine (>95%) and magnetite, although magnetite content is variable (V1 veins in bastite domains (orthopyroxene pseudomorphs) can be magnetite-free. Brucite was identified by XRD (Table T5) in Sections 66Z-2, 67Z-2, 85Z-2, and 93Z-3 and in thin sections of serpentinized dunite (e.g., Samples 102Z-1, 64–69 cm; 125Z-2, 0–5 cm; 138Z-1, 47–52 cm; and 169Z-2, 0–5 cm). In harzburgite and other pyroxene-bearing lithologies, V1 veins also occur in zones with bastite textures, but they can be difficult to recognize in hand specimen because of the thin vein width.

The second generation (V2) of serpentine veins forms networks of dark green to black, massive, composite, irregular, or curved veins. Their width is highly variable, ranging from 0.5 to >30 mm in the most developed branches, and they cut across the serpentine mesh and (where present) bastite textures. These veins contain serpentine and abundant magnetite, which forms in parallel bands in both the centers and toward the margins of the veins. In some instances, these veins can be traced through entire sections and subunits on cut surfaces. These V2 serpentine-magnetite veins are particularly apparent in X-ray computed tomography (XCT) scans (Fig. F47). The margins of serpentine V2 veins can be difficult to recognize macroscopically where they transition into the background alteration in the dunites. However, they commonly exhibit crosscutting relationships with white third-generation (V3) serpentine veins (see below). Formation of the V2 serpentine veins likely began during the formation of mesh (and bastite) texture, but crosscutting relations indicate that their formation continued after formation of the mesh texture was complete. It is conceivable that some V1 serpentine veins grew and coalesced, effectively turning into V2 serpentine veins. This process may have been transitional and involved remobilization of iron in vein minerals (e.g., Beard et al., 2009). Serpentine V2 veins crosscut by discontinuous wavy white veinlets ("Frankenstein" veins) are common in the serpentinized dunite cumulate and harzburgite sections. Parasitic veins that cut across V2 veins are in many cases indistinguishable from (and synchronous with) the third-generation (V3) serpentine veins.

V3 serpentine veins are greenish white to green and chiefly consist of massive or cross-fiber serpentine (likely chrysotile). They are heterogeneous in terms of connectivity and morphology as well as abundance. They are characteristically massive and uniform in width (0.5–2 mm), texture, and structure. However, the V3 serpentine veins can have variable connectivity and be categorized as isolated, single, branched, en echelon, crosscutting, ribbon, anastomosing, or overlapping. Almost all of the V3 serpentine veins are either parallel or subparallel and form a more or less connected network throughout an entire core section (1 m scale). They can also be planar, curved, irregular, or exhibit vein tip morphology. Some V3 serpentine veins form networks of small (<0.1 mm) parallel, discontinuous veinlets. Some serpentine V3 veins contain minor carbonate, probably calcite, in amounts up to 5%. Rare larger (up to 3 mm) V3 veins swell to form relief on cut core surfaces. The swelling nature of serpentine suggests chrysotile as the main vein-filling mineral. These veins can form dense networks that cut or follow earlier textures and vein generations. In some intervals they are subparallel and locally perpendicularly crosscut each other. However, in many sections the connectivity of V3 veins is not well established.

The fourth-generation (V4) serpentine veins are dominated by serpentine slip-fiber veins that also contain up to 10% carbonate (calcite or coalingite as identified with XRD; Fig. F45). The margins of the V4 serpentine veins are commonly slickensides consisting of either chrysotile or lizardite or both (as identified by XRD; Table T5) and are particularly apparent on fracture surfaces where pieces of the core have broken. Accessory clay and iron oxyhydroxides can be present as late phases. The color of these veins ranges from white to bright green and rusty orange-brown. Their width ranges 0.5–50 mm; however, often measurements cannot be clearly made because of their steep dip and extensive fracturing along vein walls. Some serpentine V4 veins are subparallel, either to each other or to the background foliation, and occur at regular spacing of 5–30 cm. A microscopic network of late, fine <0.5 mm thick carbonate (calcite or coalingite) veins is also observed in the serpentinized dunite intervals; these commonly crosscut other vein generals and follow the serpentinized olivine grain boundaries (Fig. F48).

Mantle Sequence

Alteration in the Mantle Sequence

Sections 142Z-4 through 179Z-4; 310.99–404.21 m

The Mantle Sequence is dominated by dunitic and harzburgitic rocks, in which the total alteration (average = 86.5%) is essentially identical to total background alteration intensity (average = 86.2%). Background alteration is pervasive and remains high to complete, although the distribution of alteration is less homogeneous compared to the ultramafic rocks in the Dunite with Gabbro Sequence (Figs. F30, F32). Total alteration generally ranges 70%–100% with no clear relation to depth; cores with total background alteration <70% are limited to <1 m thick intervals at 311.15–372.85 m depth (Sections 143Z-1 and 3, 144Z-1, 145Z-1 and 2, 150Z-4, and 166Z-2).

The main secondary mineral assemblage forming the background alteration in the Mantle Sequence is serpentine (90%–100%) and magnetite (up to 5%), with subordinate amphiboles (commonly tremolitic amphibole), secondary plagioclase, and chlorite (together up to 10%) in plagioclase-impregnated domains. Ca-metasomatized intervals in the dunites are associated with rodingitized mafic intrusions and consist mostly of diopside (~80%) and serpentine (~20%). Chromitite and chromite-rich layers are most commonly <10 cm thick and are generally less altered, consisting primarily of chromite with rare bright green uvarovite (Cr garnet) crystals.

Alteration patches start to appear at depths below 325 m (Section 147Z-3) and continue to be abundant down to 386 m (Section 158Z-2). Patch alteration represents 30%–45% of the total alteration in Sections 148Z-1, 146Z-4, 157Z-2, and 157Z-4 through 158Z-2. The alteration intensity in the alteration patches is mostly complete and the patch shape is either vein-like or highly irregular. The average size of a patch is ~3 cm, but locally patches can be >20 cm. Secondary mineral assemblages in the patches are diverse but primarily include amphiboles, secondary plagioclase, and chlorite in various proportions. Patches composed of calcite and clay minerals are also present, especially closer to the bottom of the profile, and are present in intervals 173Z-4, 0–71.5 cm, and 175Z-3, 0–66 cm. The main type of halo alteration within the ultramafic lithologies in the Mantle Sequence is vein halo, composed of serpentine (~90%), magnetite, and amphibole (both <5%), but in the central part of the sequence (Sections 149Z-1 through 155Z-1), these minerals are locally present up to 10%.

Veins in the Mantle Sequence

Veins in the Mantle Sequence are chiefly represented by 4 generations of serpentine veins and are similar to those previously described for the ultramafic intervals in the Dunite with Gabbro Sequence (Table T5; Figs. F49–F51). They are homogeneous in composition (95% serpentine and up to 5% magnetite and calcite), but toward the bottom of the hole (from Section 174Z-1; 398.18 m), the different generations of serpentine veins tend to be replaced by late-stage calcite and clay minerals (V5), which reach up to 70% of the vein minerals in Sections 178Z-1 through 179Z-3 (see supplemental Table ST4). Rarely, mineralogically different veins are observed. For instance, in Core 147Z (324–325 m), prehnite + chlorite + epidote vein networks are present in gabbroic interlayers that have been variably altered to Ca-silicate minerals. From Sections 151Z-1 through 152Z-4 (335–341 m), chlorite and tremolitic amphibole make up 90%–100% of the vein-filling phases. In addition, networks consisting of these minerals occur in core sections that are highly altered due to Ca-metasomatism related to alteration of (micro)gabbroic intrusions (e.g., intervals 160Z-1, 64–71 cm, and 160Z-2, 5–9 cm). They exhibit a wide variety of connectivity patterns and are commonly polycrystalline and composite, with widths ranging 0.5–10 mm (Fig. F49). Rare serpentine veins overgrown with garnets are also present in these zones. As in the serpentinized sequences occurring shallower in the hole (Fig. F48), late calcite veins that follow the pathways of V3 and V4 serpentine veins are abundant, especially in the lowest part of the core from Section 170Z-1 to the bottom of the hole. They are either massive or sheared, uniform and irregular, and partially replace serpentine.

All thin sections of serpentinized ultramafic rocks contain V1 veins, which make up the typical serpentine mesh texture and are composed of serpentine (probably lizardite) and magnetite. The presence of brucite is inferred in transparent V1 serpentine veins that show orange-brown discoloration and commonly occur in the cores of olivine pseudomorphs that are pervasively serpentinized (Kahl et al., 2015). However, the small grain size of serpentine and brucite makes unambiguous microscopic identification difficult. Brucite was not identified in veins in the harzburgites by XRD. Magnetite forms grains <1 µm to several tens of micrometers, and individual grains may coalesce and form continuous trails of magnetite in the vein center or margins or both. Nickel sulfides and nickel iron sulfides are present in serpentine-magnetite V1 and V2 veins; however, they are more abundant in V2 veins where magnetite forms aggregates that are several hundred micrometers in diameter (Fig. F52).

Opaque mineral assemblages in ultramafic intervals

Reflected light microscopy of the opaque phases revealed that within the ultramafic intervals occurring in the CMTZ and the Mantle Sequence pentlandite and pyrrhotite are the principal sulfides; these occur as inclusions in primary minerals. Chromian spinel is a common minor phase in dunite, wehrlite, and harzburgite. Pentlandite (of likely secondary origin), heazlewoodite, millerite, polydymite, and awaruite occur in serpentinized ultramafic units (Fig. F52). Common assemblages include pentlandite-heazlewoodite-magnetite, pentlandite-awaruite-magnetite, and pyrite-millerite-magnetite. Heazlewoodite and awaruite are only found as inclusions in magnetite from the ultramafic lithologies. In serpentinized dunite and harzburgite, large sulfide grains are less abundant; however, small sulfide grains (<1–3 µm) are ubiquitous in the mesh and bastite textures. The small grain size precludes their identification under reflected light microscopy. Magnetite is also common in serpentine veins, where it forms trails in the center of veins or along vein margins. Chromian spinel in ultramafic rocks is variably altered to ferrichromite. Pyrite and chalcopyrite veins cut magnetite in the mesh texture in completely serpentinized dunite. Iron oxyhydroxides were identified in split cores where they commonly occur together with calcite in late veins.

Discussion

Serpentinization of ultramafic lithologies

Ultramafic lithologies in the CMTZ and Mantle Sequences in Hole CM1A include dunite, harzburgite, wehrlite, and websterite, as well as olivine-rich mafic lithologies such as troctolite. Due to the abundance of olivine, the ultramafic rocks have undergone extensive to complete serpentinization. Serpentinized dunite chiefly consists of serpentine and magnetite in addition to brucite after olivine. The relative proportions of these minerals are variable, though difficult to quantify on the basis of visual estimates and XRD only. Brucite was detected with XRD in serpentinized dunites from the CMTZ (igneous Sequences 2 [Fig. F50A, F50B] and 3) and in dunites from the Mantle Sequence (Sequence 4), but it was not detected in serpentinized ultramafic sections in the Layered Gabbro Sequence (Sequence 1).

Pseudomorphic mesh textures after olivine, bastite after pyroxene, and nonpseudomorphic interlocking and interpenetrating textures (Wicks et al., 1977) are prevalent in the serpentinized intervals of Hole CM1A. Where relict olivine is present (Fig. F50A, F50B), it is surrounded by serpentine and magnetite. If olivine is completely serpentinized, the mesh centers are chiefly composed of serpentine with minor magnetite and accessory minute grains of sulfide minerals. Serpentine and magnetite are abundant in mesh rims where they trace former olivine grains and subgrain boundaries. Brownish discolorations in mesh centers and in coronas around olivine may indicate the presence of brucite (Fig. F50A, F50B); however, due to the fine-grained nature of serpentine-brucite intergrowths it is not possible to verify these without more detailed analysis. In serpentinized plagioclase-bearing wehrlite, olivine is altered to serpentine, chlorite, and magnetite. Orthopyroxene and clinopyroxene are altered to serpentine. Chlorite is present in some but not in all bastite textures. Bastite is most commonly free of magnetite. In some samples, serpentine in bastite texture is altered to talc. Representative examples of these features in partially serpentinized harzburgite are shown in Figure F48C and F48D (Sample 178Z-1, 85–90 cm). Pseudomorphic textures after olivine and pyroxene in the ultramafic rocks from Hole CM1A are indicative of serpentinization under static conditions. Although nonpseudomorphic textures can form during serpentinization under dynamic conditions or after serpentinization is complete, these are rarely present in Hole CM1A.

The metamorphic conditions and tectonic setting of vein formation cannot be concluded with certainty. Vein formation may have taken place in an oceanic setting or during obduction; however, the abundance of magnetite in V1 and V2 veins suggests that vein formation likely took place at temperatures higher than ~200°C (cf. Klein et al., 2014). At lower temperatures, iron is preferentially taken up by brucite, which limits the extent of magnetite formation. The formation of abundant magnetite indicates strongly reducing conditions during serpentinization, which is consistent with the presence of sulfur-poor sulfides and Ni-Fe alloy (awaruite) in some serpentinites where these phases are preserved due to armoring by magnetite, which has prevented their destabilization (cf. Früh-Green et al., 2004; Klein and Bach, 2009). The presence of iron oxyhydroxides, coalingite, and clay in veins is indicative of postserpentinization alteration probably at low temperatures under relatively oxidized conditions.

Ca metasomatic alteration and rodingite formation

A highlight of the Hole CM1A drill core is the occurrence of interlayered dunitic and gabbroic intervals that have undergone extensive metasomatic alteration producing calc-silicate assemblages in the gabbroic intrusions that are typical of rodingites. The formation of rodingites is considered to reflect the transfer of silica (and aluminium) from the mafic domains to the ultramafic domains associated with the hydration of olivine to serpentine group minerals during serpentinization (Frost et al., 2008). In the Hole CM1A drill cores, rodingitization of the gabbroic intrusions and serpentinization of the dunite and harzburgite domains are likely to have occurred simultaneously and are interdependent (Honnorez and Kirst, 1975). Desilicification in the gabbroic domains can provide a source of Si for the formation of talc in the neighboring serpentinites. However, talc is rare or absent in the Hole CM1A drill cores, which suggests limited desilicification in this section of oceanic lithosphere. Ca concentrations can also increase in the gabbroic domains during this process, with the breakdown of plagioclase and loss of Na loss during alteration (Frost et al., 2008). The presence of diopside ± serpentine, garnet, xonotlite, and prehnite suggest upper prehnite-pumpellyite–lower greenschist facies metamorphic conditions. The calc-silicate assemblages in Hole CM1A are similar to mineral assemblages found in rodingites from the Ronda peridotites in the Betic Cordilleras (Southern Spain; Esteban et al., 2003). The mineral assemblages in the Ronda rodingites include xonotlite + hydrogrossular with pectolite (serpentine), prehnite, and albite, in contact to lizardite. Such assemblages point to formation temperatures ranging 300°–350°C (Esteban et al., 2003). The presence of brucite in the dunitic intervals is also consistent with alteration temperatures in this range (Früh-Green et al., 2004).

Structural geology: Hole CM1A

Hole CM1A, drilled across the CMTZ, yielded 404 m of core that records the downhole temperature structural history of this part of the Samail Ophiolite. We present results from core descriptions and thin section observations based on a structural scheme defined and detailed in **Structural geology** in the **Methods** chapter. Hole CM1A is inclined, drilled towards due north at 30° relative to vertical (Fig. **F4** in the **Introduction to Science Theme 1B** chapter), and consequently is approximately perpendicular to the crust/mantle boundary, which locally dips at 30°S (see Fig. **F2** in the **Introduction to Science Theme 1B** chapter). In this report, all recorded dips are reported in the core reference frame (CRF), and so are also approximately true dips relative to the crust/mantle boundary. The key high- and low-temperature structural observations are presented in the summary. **Structural geology: Hole CM2B** in the **Site CM2** chapter correlates observations from both holes and provides an overview of the structural history.

Magmatic structures

Magmatic contacts

The majority of magmatic contacts in the core are those that define magmatic layering. These are typically planar and sharp, modal, and grain size boundaries and are discussed in more detail in **Magmatic layering**. In addition, there are crosscutting intrusive contacts and tectonic contacts in several key places throughout the core.

The most unambiguous intrusive contacts are found at the contacts between layered gabbro and wehrlite-dunite units at 124.3–129 m (Sections 50Z-4 through 52Z-1) and 142–146.8 m (Sections 57Z-2 through 59Z-1). These boundaries vary from irregular and sharp (dipping up to 63° discordant to the magmatic layering) to more gradational and nominally subparallel to the layering. These contacts and the presence of xenoliths of partially resorbed gabbro within the wehrlite-dunite units clearly show that the parent magma intruded the Layered Gabbro Sequence (Fig. **F53A**).

Conversely, the 4 foliated gabbro units within the Dunite with Gabbro Sequence appear to be intrusive into the dunite (Sections 113Z-1 through 133Z; 258–292 m) The uppermost Unit 57 at 258–260 m (Sections 113A-1 through 113Z-4) has a sharp faulted upper contact and an irregular lower intrusive contact (Fig. **F53B**) and small 1 cm sized xenoliths of dunite. The upper and lower contacts of the foliated gabbro Unit 60 at 276.75–278.78 m (Sections 123Z-1 through 124Z-1) are discordant; this gabbro unit also includes xenoliths of dunite (Fig. **F53C**). The deepest gabbro Unit 62 at 290–292 m (Sections 133Z-1 through 133Z-4) has a faulted upper contact and a lower intrusive contact. This unit consists of highly altered, partially rodingitized, fine-grained (1–2 mm diameter) foliated gabbro cut by rodingitized coarser grained (3–5 mm diameter) homogeneous gabbro. One important observation for understanding the genesis of the foliation in the gabbros as a whole is that these relatively small, 1–2 m thick, intrusive gabbros can have moderate mineral foliation (Korenaga and Kelemen, 1997; Jousselin et al., 2012), implying that the foliation can develop in relatively thin intrusive units.

Numerous other smaller (<20 cm), discordant gabbros occur throughout Hole CM1A (Fig. **F53D, F53E**). These grade from approximately parallel-sided veins to bodies with more irregular geometries and are found within both the gabbros (e.g., interval 113Z-3, 40–45 cm) and the ultramafic rocks (e.g., interval 83Z-2, 68–75 cm) (Fig. **F53E**). A suite of small (<20 cm diameter) gray veins and very irregular patches of completely rodingitized gabbros occurs within the Mantle Sequence at 324.6–383.7 m (Sections 147Z-2 through 171Z-1). These are further discussed in **Magmatic veins**.

Magmatic layering

Magmatic layering occurs throughout the Layered Gabbro Sequence with layers ranging in thickness from a few millimeters to a maximum thickness of 3.72 m. The layering is dominantly defined by changes in the modal content of olivine, clinopyroxene, and plagioclase and is most easily seen in the core when olivine is partially or completely serpentinized (Fig. **F54**). Isomodal layers are dominant, with boundaries defined by changes in phase (i.e., a new mineral appears) or ratio (i.e., a clear change in the proportion of minerals) (Fig. **F54A, F54B**). However, layers defined by modal grading, changes in grain size, or a combination of these variables are also present, albeit less common (e.g., Sections 6Z-1, 47.5 cm, and 60Z-1, 47 cm). A well-developed example of modally graded layers is present in interval 59Z-3, 41–74 cm, that exhibits both normal grading from more olivine/pyroxene-rich bottoms to more plagioclase-rich tops, and to a lesser extent, reverse grading from plagioclase-rich bottoms to olivine/pyroxene-rich tops. Boundaries between layers are commonly sharp and planar, but gradational and less regular boundaries do occur. Monoclinal folding of the layering is present at 60.5 and 63.2 m (intervals 26Z-2, 34–65 cm, and 27Z-2, 0–42 cm; Fig. **F55A**). These folds are asymmetric, open folds with axial planes dipping 70° and with a perpendicular spacing between axial planes of ~1.5 m. Discordant contacts between layers are rare (Fig. **F55B, F55C**), possibly indicative of the structures recognized as low-angle cross-bedding by Pallister and Hopson (1981).

The following measurements are summarized in Figure **F56**: thickness of all layers thicker than a few millimeters, variation of layer thickness with depth through the Layered Gabbro Sequence, and layer thickness frequency. Relatively uniform gabbros tend to form the thickest layers and olivine gabbro thinner layers (Fig. F56A). Layer thickness shows a log-normal distribution (Fig. F54B, F54C) with a mean thickness of 21 cm.

The magmatic layering (and foliation) has a mean dip of 11° in the CRF and is therefore overall subparallel to the crust/mantle boundary. However, the dip increases from ~5° at the top of Hole CM1A to ~12° at 60 m, a dip that continues to the bottom of the Layered Gabbro Sequence at 160 m (Fig. F57A). Local mapping in the area of the drill site (Fig. F2 in the **Introduction to Science Theme 1B** chapter) constrains the azimuth of the dip to be to the SSE and records similar steepening of the layering towards the crust/mantle boundary (from ~38°S to >48°S in a geographic reference frame). Weak layering (and the parallel foliation) in the two intrusive gabbros within the Dunite with Gabbro Sequence have slightly steeper dips of 33° and 17°, respectively.

In more detail, the dip of the layering/foliation varies in a complex but commonly systematic way (Fig. F57A). The data reveal cycles of varying dip beginning with a relatively abrupt increase in dip from 0°–5° to >20° over a few meters, followed by gradually decreasing dips back to 0°–5° over 10–15 m. Additionally, some of the abrupt changes in dip correlate with changes in lithology. For example, the decrease in dip at 146.8 m CAD (Chikyu adjusted depth) (Section 59Z-1) to the bottom of the Layered Gabbro Sequence begins at the base of the intrusive wehrlite unit at 146.8 m CAD. These recurring trends within the cycles record gradual fanning of the dip of the layering/foliation. A potential explanation of these trends is the large-scale boudinage or necking of 10–30 m thick layers with contrasting rheology within the mush zone of the magma chamber during plate spreading. These cycles are similar to those that occur in core from Hole GT1A and especially Hole GT2A, except that those cores record a larger wavelength of variation, ~60–100 m (Fig. F87).

Magmatic foliation

The majority of the gabbros within the Layered Gabbro Sequence and the intrusive gabbros within the Gabbro with Dunite Sequence have magmatic foliation. In most cases mineral foliation parallels the layering. However, occasionally mineral foliation is oblique to the layering. It is most commonly planar, although rarely may curve to become parallel to the layering. The mineral foliation ranges from moderate through weak (Fig. F58) to absent. In general, the magmatic foliation is less well developed than in the layered gabbros drilled in Holes GT1A and GT2A. The foliation is most distinct in the cores when defined by elongate, irregular, commonly kinked olivine crystals with aspect ratios up to 10:1, but both pyroxene and plagioclase can also show mineral foliation. Some plagioclase crystals are tabular, typically with aspect ratios of 2:1 and very rarely with aspect ratios up to 4:1 (e.g., interval 14Z-3, 10–15 cm). In these cases, shape-preferred orientation (SPO) of plagioclase defines the foliation. However, most commonly plagioclase is equant with equilibrated grain boundary textures and shows no SPO, although the consistent orientation of albite twin planes indicates plagioclase crystallographic-preferred orientation (CPO). Rarely, some samples have plagioclase that shows deformation twins and undulose extinction indicating minor crystal-plastic deformation at near-solidus temperatures (Fig. F58C). Some clinopyroxene crystals are elongated with aspect ratios of 2:1 and so also can also define foliation.

Dunite layers

A total of 48 separate commonly orthopyroxene-bearing and rarely plagioclase-bearing dunite layers were recognized within the Mantle Sequence (Fig. F59). These layers tend to have parallel planar boundaries but are nearly always completely (100%) serpentinized and are common loci for lower temperature alteration and veining, making recognition sometimes difficult. The dunite layers range in thickness from 1 cm to 16.7 m (mean = 1.24 m) and show an approximately log-normal frequency size distribution (Fig. F60). The thinner layers (<2 m) are concentrated at 311–325 m (Sections 143Z-1 and 147Z-3) and 362–375.6 m (Sections 160Z-4 and 167Z-3). The dunite layers have a mean dip of 21° in the CRF, but dips range 5°–66° (Fig. F61). To first order, they are subparallel to the crust/mantle boundary but are slightly more steeply dipping than the mean dip of the layering within the Layered Gabbro Sequence (21° vs. 12°). Varying dip directions in the same section show that the layers are not necessarily parallel to each other (Fig. F59). Given the 60° plunge of the borehole, a calculated geographic dip of 51.3° for the layers (assuming that these layers dip in the same direction as the regional crust/mantle boundary) is similar to the dip of intrusive gabbros and other features structures within the Dunite with Gabbro Sequence mapped in the field (48°–58°) (Fig. F2 in the **Introduction to Science Theme 1B** chapter).

Magmatic veins

Magmatic veins of different types occur throughout the core, and the orientations of 122 veins were documented (Figs. F57B, F62). Five compositional vein types were identified:

- Anorthosite veins
- Discordant, generally planar gabbro veins
- Irregular, rodingitized gabbro veins and patches
- Chromitite veins
- Diopsidite veins

A total of 43 anorthosite veins (Figs. F57B, F62A) were measured within the Layered Gabbro Sequence. They largely occur as layer-parallel veins or segregations with a mean individual thickness of 1.1 cm. Their total combined perpendicular thickness is 47.25 cm, and thus they comprise 0.3 vol% of the Layered Gabbro Sequence. They have dips ranging 0°–36° (mean = 8°), comparable to the dip of the magmatic layering.

A total of 49 discordant, commonly coarse grained, and mostly undeformed gabbro veins occur throughout the core (Figs. **F57B**; **F62B, F62C**) with 26 of them concentrated in the lower 60 m of the Layered Gabbro Sequence. These veins are moderately altered to highly altered (see **Alteration: Hole CM1A**). Those within the Layered Gabbro Sequence have a mean individual thickness of 4.2 cm and a total thickness of 126.5 cm (comprising 0.79% of the Layered Gabbro Sequence). The dips of the gabbro veins range 0°–82° (mean = 23° throughout the whole core), with dominantly gentle dips (mean = 14°) observed within the Layered Gabbro Sequence.

Gray gabbro veins and patches

Numerous completely rodingitized, centimeter-scale irregular, gray gabbro veins and patches occur in the Mantle Sequence at 324.6–383.7 m (Sections 147Z-2 through 171Z-1; Fig. **F63**). These vary in geometry from (a) steeply dipping veins, (b) aligned, disaggregated, irregular patches, to (c) apparently completely irregular isolated patches. Thirty-one of these features were recorded, including 10 that could be oriented, and those features have dips ranging from subhorizontal to vertical (Fig. **F57B**). Many of these patches show evidence of semibrittle and brittle deformation (Fig. **F63D**; Sample 156Z-4, 26–30 cm) and are a focus for low-temperature deformation within the Mantle Sequence.

A total of 11 hydrothermal diopsidite veins (Fig. **F57B**) (Python et al., 2007) were recognized at 326–355 m (interval 148Z-1, 8 cm, to 157Z-3, 11.5 cm) within the upper part of the Mantle Sequence. Although some of these veins are steeply dipping (66°–81°) and planar, they most commonly occur as dismembered veins or more irregular patches. They appear to crosscut the rodingitized gabbro patches described above and commonly display brittle deformation (Sample 143Z-4, 47–51 cm).

A total of 9 discrete, thin chromitite veins and one larger, 3 cm wide vein (Fig. **F57B**) occur in the Dunite Sequence with a mean perpendicular thickness of 0.5 cm and a total thickness of 5.6 cm (comprising 0.06% of the Dunite Sequence). The orientations of 7 veins were measured and dips range 18°–80° (Fig. **F57B**).

Crystal-plastic/semibrittle deformation

In Hole CM1A, no significant subsolidus crystal-plastic fabrics were observed. However, throughout the hole there are several generally narrow domains with apparent incipient crystal-plastic deformation and/or low-temperature (i.e., subgreenschist to low-greenschist facies conditions) semibrittle deformation. Ubiquitous alteration of the deformed zones hinders recognition of higher temperature deformation; however, inspection of thin sections confirms the semibrittle to brittle nature of this deformation (e.g., Sample 156Z-4, 26–30 cm). Gabbroic veins/bodies within the ultramafic sequences and particularly within the Mantle Sequence seem to localize this semibrittle deformation.

Figure **F64** emphasizes the paucity of higher-temperature deformation. There are only 10 thin zones within the Layered Gabbro and Dunite Sequences that show semibrittle deformation and, with the exception of the strongly foliated cataclasite found at the crust/mantle boundary (Section 63Z-4), only weak to moderately foliated fabric. Coarse-grained gabbros at 36.6 m (intervals 16Z-2, 45–60 cm, through 16Z-3, 0–45 cm) and 150 m (interval 60Z-1, 46–71 cm) (Fig. **F65C**) are from 60 cm and 41 cm thick layers, respectively. These gabbros are altered but only show evidence for incipient crystal-plastic deformation and/or semibrittle deformation. Samples from 72.5 m (interval 30Z-3, 17–20 cm) show semibrittle textures within sheared serpentine-rich olivine gabbros. The sample from 160 m (Section 63Z-4) is a completely altered highly deformed gabbro (see **Deformation at the Layered Gabbro/Dunite Sequence boundary**), and the sample from 199.8 m (87Z-3, 61.5–63.5 cm) is a 2 cm wide deformed gabbro vein.

Evidence for weak semibrittle deformation is present towards the bottom of the Dunite with Gabbro Sequence (~271 m; Fig. **F64**). Here, one gabbro horizon (interval 119Z-3, 32.5 cm, to 120Z-1, 17 cm; 270.4–271.9 m) in particular is disrupted by extensional, brittle, and semibrittle faulting (Fig. **F65D**). Weak deformation is also reflected by alignment of plagioclase-rich melt segregations in the dunite from Sections 138Z-2 through 142Z-3 (301–310 m).

More but still restricted semibrittle to incipient crystal-plastic deformation is recognized from 290 m (Section 133Z-1) in the Dunite with Gabbro Sequence to the bottom of the hole in the Mantle Sequence (Fig. **F64**). This deformation is largely confined to various small gabbroic bodies, including centimeter-thick deformed and altered gabbro veins, millimeter-thick plagioclase segregations, rodingitized gray gabbro veins and patches (see **Magmatic veins**; Fig. **F63**), and very rare 1–3 cm thick shear zones within dunite.

Deformation at the Layered Gabbro/Dunite Sequence boundary

The contact between the base of the Layered Gabbro Sequence and the underlying Dunite Sequence (160.23 m CAD; Section 63Z-4) occurs at the bottom of a 20 m long continuous section of layered gabbros. Immediately below the section containing the contact is a 3 m wide low-temperature fault zone recorded by disrupted and discontinuous core. The contact is a subvertical (in the CRF) fault zone showing evidence for semibrittle deformation of layered gabbro next to less deformed but still sheared dunite (Fig. **F65**). The most intensely deformed region within the gabbro is a 2–3 cm wide zone of foliated cataclasite and low-grade protomylonite adjacent to the dunite. The fault likely slipped under greenschist to subgreenschist conditions but has been completely replaced by chlorite, diopside, vesuvianite, and grossular (see **Alteration: Hole CM1A**). Numerous structural indicators such as the overall relationship of gabbro to the dunite, deflected foliation in the gabbro, sense of shear in a gabbro vein in the dunite, local imbrications in the gabbro foliation, and asymmetry of side wall cutouts at the contact at the gabbro/dunite (Fig. **F65B**) indicate that the gabbro was down-faulted relative to the dunite (displacement top to the left in Fig. **F65A**). The fault zone is likely late with relatively small displacement that cuts the crust/mantle interface at this location.

Crystal-plastic deformation in harzburgites

The relatively high degree of alteration present in the harzburgites from the Mantle Sequence makes recognition of crystal-plastic deformation difficult. Most of the harzburgites exhibit protogranular textures with equant and rounded orthopyroxene (Fig. **F66**). Weak porphyroclastic textures are present in a few samples, but these examples are mostly uncertain in quality owing to the extent of alteration. One of the most convincing examples is illustrated in Figure **F66** (Sample 178Z-1, 80–85 cm) that shows slightly elongate and aligned orthopyroxene crystals defining very weak foliation. Figure **F67** shows the dip of the orthopyroxene porphyroclastic foliation recognized in the least altered part of the Mantle Sequence from 390 m (Section 17Z-3) to the bottom of the hole. The mean dip of the foliation is 60°, but there is a large range of dips, in part reflecting the difficulty of making the measurements. Inspection of thin sections from this part of the core suggests that harzburgites containing foliation (e.g., Sample 166Z-4, 53–56 cm) also exhibit olivine CPO (based on a common extinction angle of grains).

Thin plagioclase segregations (1 mm to a few millimeters thick) occur in parallel arrays within the Mantle Sequence and the lower part of the Dunite with Gabbro Sequence (297–356 m; interval 137Z-2, 28.5 cm, to 157Z-4, 79 cm). These segregations have a mean dip of 19° (Fig. **F67**), similar to the orientation of the dunite layers (21°) in the in the Mantle Sequence (Fig. **F61**).

Brittle deformation

Brittle structures

Brittle deformation structures are ubiquitous throughout Hole CM1A. As detailed below, the style and intensity of brittle deformation varies with depth and correlates well with rock type, with abrupt increases in the fracture density and intensity of brittle deformation in the ultramafic rocks below the Layered Gabbro Sequence. In the Layered Gabbro Sequence, higher temperature amphibole and secondary plagioclase veins represent the highest temperature brittle deformation features. In contrast, crosscutting relationships in the ultramafic sequences of Hole CM1A (i.e., the Dunite, Dunite with Gabbro, and Mantle Sequences) indicate that significant brittle deformation only commenced after development of the serpentinite mesh texture, with the most intense brittle deformation occurring synchronously with the later stages of serpentine veining.

Fault displacement is difficult to assess from observation of core. However, the local continuity of mapped units in the field (Fig. **F2** in the **Introduction to Science Theme 1B** chapter), the limited thickness of fault zones in the core, and correlations between sequences and lithologic units between core from Holes CM1A and CM2B (see **Igneous petrology: Hole CM2B** in the **Site CM2B** chapter) all suggest that the fault zones we observed are relatively minor—and we cautiously conclude that they result in only modest (0.1–10 m) disruption of the spatial relationships between lithologic units. However, an abrupt change in the dip of serpentine veins across the boundary between the Layered Gabbro Sequence and the Dunite Sequence at the top of the top of the Crust–Mantle Transition and the presence of a distinct foliated cataclasite at that boundary provides evidence for some fault displacement, on the order of tens of meters, although the amount of slip remains conjecture.

The orientations, deformation intensity, and downhole distribution of brittle deformation features were recorded in all drilled sections (see **Supplementary material** > **E_Tabulated_VCD_data**; also see Tables **T6**, **T7**, **T8**). The intensity of discrete brittle structures was recorded at the centimeter scale using a scale that ranges from 1 (minor fracturing) to 5 (ultracataclasite); a scale of 6 was reserved for pseudotachylite, which was not observed (see **Structural geology** in the **Methods** chapter). In total, 1752 brittle features were logged. In addition, we recorded a semiquantitative log of fracture density (see **Supplementary material** > **E_Tabulated_VCD_data**). These data are summarized in Figure **F68**, which shows how fracture density, deformation intensity, vein density, and fault zone location vary within Hole CM1A. These data were smoothed by averaging the value of each 10 cm interval in the core with the values in the 10 cm intervals immediately above and below it (repeating the averaging calculation 3 times). In the following sections we present data on the orientations of these features in the CRF.

Alteration veins

The orientations of 1653 alteration veins were measured. All veins >0.5 mm width were measured in the Layered Gabbro Sequence. Owing to the extremely high density of veins in the ultramafic sequences, we used a different approach; a representative orientation was measured for each set of parallel veins in a given vein generation within each core section. Individual veins were defined, located, and described by the alteration team (see **Alteration: Hole CM1A** for a breakdown of each vein generation within ultramafic sequences). Figure **F69** shows an example of crosscutting relationships illustrating the generation of veins in the ultramafic sequences. Where individual veins cross local lithologic changes, vein composition and vein density can change. For example, vein density generally is higher in intrusive gabbro material than in the host serpentinite (Fig. **F70**).

The distribution of vein dips varies between sequences. Vein dips are primarily 80°–90° in the Layered Gabbro Sequence (Fig. **F71**). In contrast, a broader distribution of vein dips is observed in the ultramafic sequences. However, there are distinct horizons within the ultramafic sequences that show a narrower range of dips such as between 225 and 250 m (Fig. **F71**). Overall, the ultramafic sequences display a prominence of steeply dipping veins (60°–80°), although the distribution is much broader than that observed for the Layered Gabbro Sequence.

Downhole plots of vein dips in the Layered Gabbro Sequence, sorted by composition, are shown in Figure **F72**; histograms of orientations for the different vein compositions are shown in Figure **F73**. Similarly, downhole plots of vein dips in the ultramafic sequences, sorted by serpentine vein generation, are illustrated in Figure **F74**, and histograms for the different vein types are shown in Figure **F75**.

The majority of veins within the Layered Gabbro Sequence dip at 80°–90° in the CRF and therefore are oriented approximately perpendicular to the paleocrust/mantle boundary. Consequently, these veins exhibit near-orthogonal crosscutting relationships to the igneous layering in the gabbros. Amphibole veins, generally the highest temperature brittle features observed in the core, only have dips of 60°–90° (Fig. **F71**). Plagioclase and chlorite veins also show a significant number of steep dips, whereas the distribution of prehnite veins is more variable. Serpentine veins are typically high angle in the Layered Gabbro Sequence (Fig. **F71**) partly reflecting the cluster of veins observed in the uppermost 20 m of Hole CM1A (Fig. **F71**). Similarly, the prevalence of low-angle dips of calcite veins dominantly reflects vein orientations in the uppermost 20 m of the hole.

In the ultramafic sequences, the broad distribution of vein dips is generally similar for all 4 serpentine vein generations (Fig. **F74**). This observation suggests that the later stage serpentine veins form by reactivation of preexisting vein sets. Thus, care must be taken when interpreting the evolution of stress state from the vein orientations. One exception is the clear second peak of lower angle dips for V3 veins (Fig. **F74**), producing a bimodal distribution. As shown in Figure **F74**, the second peak arises from including very thin and dominantly subhorizontal chrysotile + carbonate veins (Fig. **F75A–F75C**) into the V3 group (which also includes the white chrysotile veins that form as either ladder cracks or parallel cracks on preexisting V2 veins; Fig. **F69A**). Ambiguity arises because the timing of the thin V3 group with respect to V4 is ambiguous, and some of the white chrysotile veins in the V3 group are not related to previous vein generations (e.g., Fig. **F75D**). Therefore, we caution against correlating the anomalous V3 vein orientation to a specific stress state in the interpretation of structural history.

The abrupt change in the dip of serpentine veins across the boundary between the Layered Gabbro Sequence and the Dunite Sequence (with high-angle dips in the Layered Gabbro Sequence; see Fig. **F71**) and clearly gentler dips in the Dunite Sequence (Fig. **F71**) suggests block rotation during displacement along the fault at the boundary between these units.

Fractures and slickensides

Fractures with and without mineral vein fill are abundant throughout Hole CM1A, and crack/fracture morphology ranges from straight to irregular. Where slickenside planes with clear slickenline lineations were observed, the sense of shear was recorded. Irregular and/or hemispheric-shaped cracks oriented approximately normal to the core (Figs. **F75E**; **F76**) were observed in all lithologic units in Hole CM1A. The shape of these cracks indicates that they grew in a stress field with a gradient symmetric around the hole, suggesting they formed during drilling. These features were noted in the log/brittle spreadsheet, but we do not include them in the analysis of fracture orientations.

Histograms showing the dip of fractures (including both cracks and slickensides) for the Layered Gabbro and ultramafic sequences are shown in Figure **F77**. Fracture dip angles are lower in the Layered Gabbro Sequence than in the ultramafic sequences, which show a significantly greater proportion of 60°–80° dip angles. The prevalence of gentler dips in the Layered Gabbro Sequence may partly reflect difficulty in separating drilling-induced fractures from preexisting fractures.

A total of 141 shear sense indicators on slickensides were recorded (Table T6), with 117 of those having a measurable plunge (Fig. F78). There were slightly more normal sense indicators than reverse sense (48% vs. 41%, respectively), with the remainder being strike-slip. Strike-slip motions were most commonly observed along later stage veins (V3–V4; see Alteration: Hole CM1A). Within the Layered Gabbro Sequence, the shear sense indicators are evenly divided between normal and reverse, although regions of dominantly reverse or normal sense indicators are evident (Fig. F78). In the ultramafic sequences, normal shear sense indicators are more prevalent than reverse shear sense indicators (55.2% vs. 38.8%) (Table T6).

Crosscutting relationships indicate that the majority of the brittle structures formed late in the structural history of the ophiolite. Some later stage V3 and V4 veins display crack-seal/stretching vein morphology (Fig. F79), consistent with a structural history involving reactivation of preexisting veins and multiple precipitation episodes. However, the essentially random distribution of slickenline plunges in the ultramafic sequences (Fig. F78), together with the lack of a clear shear sense, make more detailed interpretations of structural history difficult.

Based on the comparison of dips for the measured slickenside planes to the dips of all veins in the Layered Gabbro Sequence and the ultramafic sequences (Fig. F80), we were alerted to the potential for bias in the data. Specifically, because we can only measure the slickensides on fractures exposed in the drill core, we are concerned that the shear sense data might be biased by the possible prevalence of opening vein fractures with lower angle dips during drilling.

Fault zones

Although the intensity of discrete brittle deformation is slightly greater in the ultramafic sequences compared to the Layer Gabbro Sequence, the fracture density and number of fault zones are significantly higher in the ultramafic sequences (Figs. F68, F81).

Fault zones are observed in all sequences of Hole CM1A (Fig. F81). Three styles of faulting are observed in Hole CM1A: cohesive cataclastic zones, vein/fracture networks, and incohesive cataclastic zones. Figure F81 summarizes the downhole distributions of these different styles of faulting. The depth intervals of the damage zones for each type of fault are listed in Table T9. The width of the damage zones for fault/vein fracture networks in the ultramafic sequences (mean thickness = 2.3 m) is generally larger than those in the Layered Gabbro Sequence (mean thickness = 0.97 m). The Dunite with Gabbro Sequence displays the greatest brittle deformation intensity and the largest number of fault zones. Figure F82 illustrates 2 generations of extension-parallel faulting in a gabbro layer (interval 119Z-2, 33–50 cm) in the fault zones that occur within the Dunite with Gabbro Sequence. The boundary between Dunite with Gabbro Sequence and the Mantle Sequence occurs in a ~50 m wide interval of continuous core, where the degree of brittle deformation is lower than that observed in the Dunite with Gabbro Sequence but greater than that in the Layered Gabbro Sequence.

Cohesive cataclastic zones form within discrete intervals marked by cemented brecciation of a wide range of clast sizes (Figs. F83, F84). Although not prevalent enough to be significant in terms of deformation intensity, these zones commonly exhibit evidence for deformation involving semibrittle flow in chlorite-rich layers and occur at distinct horizons within the core (see Gray gabbro veins and patches). The cohesive cataclastic zones are typically bounded by shear veins. In some cases, vein-related deformation crosscuts cohesive cataclastic zones (Fig. F79). These observations indicate that faults with cohesive cataclasite are the earliest (and highest temperature) style of faulting in Hole CM1A. Cohesive cataclasite is only observed in the ultramafic sequences (Fig. F81).

Vein-related faulting is the culmination of deformation on fault zone networks comprising shear veins and extensional fractures. Many of these fault zones are defined by intervals of rubble comprising phacoids (cobble-sized fragments bounded on all sides by slickensides, some of which preserve mirror-like surfaces). Shear veins are observed where a clear offset is visible on the cut surface of the core (e.g., Fig. F82). Within both the Layered Gabbro Sequence and the ultramafic sequences, vein-related faulting is defined by zones of crosscutting and parallel veins and generally associated with areas of greater wall rock alteration (Figs. F85, F86).

Incohesive cataclasite, defined by significant grain size reduction that in some occurrences produces clay-like gouge, is present in all sequences of Hole CM1A (Fig. F81). Fault zones with incohesive cataclasite overprint preexisting vein-related deformation (Fig. F85) and form within zones with a high intensity of vein-related deformation (Fig. F86). These observations indicate that the incohesive cataclasite forms at lower temperatures by strain localization in preexisting fault zones.

Here we present a semiqualitative method to constrain fault zone thickness and intensity. The Fault Zone Intensity Index (FZII) shown in Figure F81 is a semiquantitative formula that combines the fracture density, deformation intensity, and damage zone thickness for every 10 cm interval of core. The FZII correlates well with the location of fault zones identified during core description and was formulated to provide a basis on which to identify the most significant faults. The FZII was calculated using the formula

$$\mathrm{FZII} = (F/3 + D/5) \times (T/T_{max}), \quad (1)$$

where

F = smoothed fracture density (0–3; see **Structural geology** in the **Methods**),
D = smoothed deformation intensity (0–5),
T = smoothed fault damage zone thickness, and
T_{max} = maximum damage zone thickness encountered in Hole CM1A (28.63 cm).

Comments on the major sequence boundaries

The three boundaries between the four major sequences that form the CMTZ vary in character. The boundary at 160.23 m (interval 63Z-4, 0–35 cm) between the Layered Gabbro Sequence and the Dunite Sequence is a relatively late, high-angle, greenschist facies fault (see **Deformation at the Layered Gabbro/Dunite Sequence boundary**). The boundary between the Dunite Sequence and the Dunite with Gabbro Sequence (249.99 m; Section 107Z-3) is marked by a ~2.5 m long (in the CRF) subvertical anastomosing zone of hydrothermal alteration. In contrast, the boundary between the Dunite with Gabbro Sequence and the Mantle Sequence (310.99 m; interval 142Z-4, 32.5 cm) is marked by the first appearance of harzburgite and is a lithologic contact.

Summary

The cores from Hole CM1A record a complex history of lower crust formation and consequent upper mantle evolution. They also record a subsequent down-temperature history, including the onset of post-ridge-related deformation (and alteration) and later deformation/erosion/weathering. Here we present the key observations from the high- and low-temperature structures present in the core. A more detailed summary is provided in **Structural geology: Hole CM2B** in the **Site CM2** chapter.

Key observations from high-temperature structures

- The gabbros in the Layered Gabbro Sequence show well-defined layering and weak to moderate mineral foliation; however, the strength of the mineral foliation is on average less than that seen in the gabbros of Holes GT1A and GT2A. The layering and foliation are usually parallel and steepen with depth downsequence from ~5° to 12°, consistent with the increasing dip of the foliation towards the paleo-Moho mapped in surface exposures. The mean layer thickness is 21 cm, similar to the mean layer thickness of 24 cm seen in Hole GT1A. The dip of the layering/foliation increases and decreases cyclically at 20 m wavelength, a feature similar to the 50–100 m wavelength cyclicity seen in Holes GT1A and GT2A (Fig. **F87**).
- The base of the Layered Gabbro Sequence and contact with the underling Dunite Sequence or paleo-Moho is marked by a thin (20 cm wide) subvertical semibrittle, now greenschist facies, fault zone.
- Two 5 m thick wehrlite/dunite layers intrude into the bottom of the Layered Gabbro Series and four thin (~2 m thick) gabbro layers intrude into the Dunite with Gabbro Sequence. Based on surface mapping constraints it is likely that the dunites of the Dunite Sequence and the Dunite with Gabbro Sequence are one single dunite sequence that is intruded by local and discontinuous gabbro bodies.
- No significant crystal-plastic deformation is recorded in the core; however, low-temperature semibrittle fault zones are common.
- The mean thickness and dip of dunite layers in the Mantle Sequence is ~1.24 m and 21°, respectively. This dip, and the mean dip of the gabbro layering, suggests that these features are slightly oblique (dipping at ~50° and ~40°, respectively) to the paleo-Moho, which dips ~30°SSE.
- The harzburgite texture varies between apparently annealed and weakly deformed; evidence for crystal-plastic deformation includes the alignment of orthopyroxene and spinel lineations.

Key observations from low-temperature structures

- Deformation features during cooling between magmatic and greenschist-grade conditions are essentially negligible.
- Greenschist-grade veins and associated semibrittle deformation are the highest temperature brittle deformation features observed in Hole CM1A.
- Significant brittle deformation is associated with the development of veins and postdates the formation of mesh-textured serpentinite.
- The similar dips of veins, slickensides, and faults further support the role of vein formation as a key step in the evolution of brittle deformation.
- Structural relationships indicate that brittle deformation is focused at lithologic contacts (e.g., between gabbro and ultramafic rock).
- Veins have a broad distribution of orientations.

Geochemistry: Hole CM1A

Whole-rock chemical compositions were performed on 95 samples collected from Hole CM1A: 40 gabbros, 27 dunites, 19 harzburgites, 2 wehrlites, 2 troctolites, 1 rodingite, and 4 samples from peridotite/gabbro contacts. A total of 55 samples were selected by the shipboard science party as representative of the different lithologies recovered along Hole CM1A. A thin section was taken systematically at the top of each geochemistry sample (see **Thin section descriptions**). A total of 40 samples were collected on site every 10 m during operations; they were powdered at the University of Southampton and analyzed for major and trace element concentrations at the University of Edinburgh (see **Geochemistry** in the **Methods** chapter). A thin section was taken for each on-site sample, and XRD analyses were also performed on each on-site geochemistry sample for bulk rock mineral characterization.

All sample powders were ignited and analyzed for major and trace element concentrations by X-ray fluorescence (XRF) on board *Chikyu*. Additional gas chromatographic separation was undertaken on non-ignited powders to determine their volatile element content (H_2O, CO_2, and inorganic carbon). The analytical procedures and precision and accuracy of the methods are described in **Geochemistry** in the **Methods** chapter. Trace element concentrations of hand-picked mineral concentrates were determined in situ by laser ablation–inductively coupled plasma–mass spectroscopy (LA-ICP-MS; see **Geochemistry** in the **Methods** chapter) on pyroxene from different rock types (gabbros, dunites, wehrlite, and harzburgite). The in situ method was also used on pressed powder pellets for determination of trace element concentrations in selected gabbro and dunite. Whole-rock major, trace, and volatile element contents are reported in Table **T10**. Whole-rock, clinopyroxene, and orthopyroxene LA-ICP-MS trace element compositions are reported in Tables **T11**, **T12**, and **T13**, respectively.

Loss on ignition, CO_2, and H_2O contents

Loss on ignition (LOI) values in Hole CM1A range 0–15.5 wt%. LOI variability broadly correlates with sample lithology and depth: LOI in the Layered Gabbro Sequence (0–160.23 m), which is dominated by gabbroic rocks, ranges 0–12.58 wt%, whereas the Dunite (160.23–249.99 m), Dunite with Gabbro (249.99–310.99 m), and Mantle (310.99–404.21 m) Sequences have LOI ranging 0–15.2 wt% (Figs. **F88**, **F89**). The concentrations of CO_2 and H_2O correlate with the measured LOI values (Fig. **F88B, F88C**). The average concentration of CO_2 throughout Hole CM1A is ~0.2 wt%. Nitrogen was below the detection limit in all Hole CM1A samples.

The gabbros and olivine gabbros show similar H_2O concentrations, ranging 0.48–16.68 wt%. The measured range of H_2O concentration in gabbros and olivine gabbros varies very little with depth, indicating strong hydrothermal alteration throughout. The 2 troctolites have H_2O concentrations of 1.58 and 10.40 wt%. H_2O concentration in dunitic rocks is consistently >6.70 wt%. The highest H_2O concentration was measured in Sample 79Z-2, 11–18 cm (186.11 m; H_2O = 15.20 wt%), reflecting the high degree of serpentinization of this sample, whereas the lowest value was observed in Sample 158Z-1, 59.0–65.0 cm (356.80 m), with H_2O content of 6.70 wt%. One of the two wehrlites analyzed shows significant H_2O content (Sample 92Z-2, 0.0–5.0 cm; 210.15 m; H_2O = 15.60 wt%). The rodingite sample is characterized by lower H_2O content of 1.23 wt%. Samples taken from the Mantle Section show similar H_2O contents to upper dunitic cumulates, ranging 9.83–15.40 wt%. Only 2 samples show higher H_2O concentration (H_2O > 15 wt%), indicating more intense alteration (Table **T10**; Fig. **F88C**).

Hole CM1A samples show contrasting CO_2 concentrations between gabbro and peridotite units. Gabbro and olivine gabbro samples have CO_2 contents ranging 0.01–0.82 wt%, with higher values observed in gabbros. The lower concentrations are typical of the medium-grained olivine gabbros and the fresher parts of the gabbroic section (e.g., Sample 24Z-4, 52–59 cm; 56.07 m; CO_2 = 0.01 wt%, H_2O = 0.66 wt%). Harzburgites recovered from the deepest part of Hole CM1A (Samples 175Z-4, 1–8 cm, and 179Z-1, 1–8 cm; 394.3 and 401.2 m, respectively) display higher CO_2 (1.15–1.11 wt%) and H_2O (12.55 and 13.13 wt%) concentrations, consistent with the observed degree of alteration. Dunites have CO_2 contents ranging 0.03–0.37 wt%, whereas rodingite CO_2 concentration is 0.42 wt%. The concentration of inorganic carbon (IC) ranges 0.01–0.31 wt%. Inorganic carbon concentration increases with depth; the highest value measured was from a sample from the deepest core drilled at this hole (175Z-4, 1–8 cm; ~394.3 m) (Table **T10**; Fig. **F88A**).

Whole-rock major and minor elements

Hole CM1A samples display a wide range of major element compositions, principally reflecting the different rock types that were sampled in the borehole (Table **T10**; Figs. **F89–F92**). This is especially true for the change from the Layered Gabbro Sequence (lowermost Sample 63Z-1, 0–5 cm; 158.25 m) to the Dunite Sequence, which marks the top of the CMTZ. This boundary is characterized by a sharp and significant increase in Mg# (100 × Mg/[Mg + Fe]$_{atomic}$) and Cr and Ni concentrations and associated decreases in CaO, Al_2O_3, and TiO_2 contents.

To describe the changes in whole-rock chemistry in Hole CM1A, 5 main rock types were defined and analyzed: olivine gabbro, gabbro, wehrlite, dunite, and harzburgite. Moreover, 1 rodingite (Sample 133Z-3, 18–24 cm; 291.97 m) was analyzed as Ca-metasomatized gabbro, and other rocks are a distinctive feature of the lower parts of Hole CM1A (Table **T10**; Fig. **F3**).

Olivine gabbros, gabbros, and rare troctolites from the Hole CM1A Layered Gabbro Sequence display similar chemical compositions to gabbros and olivine gabbros from Holes GT1A, GT2A, and GT3A. Mg# = 71–85, CaO = 1.5–19 wt%, Al_2O_3 = 2–27 wt%, TiO_2 = 0.08–0.5 wt%, Cr = 87–2079 ppm, and Ni = 63–1355 ppm. The compositions of olivine gabbros and gabbros in the Layered Gabbro Sequence overlap. Olivine gabbros display Mg# = 71–85, CaO = 4–19 wt%, Al_2O_3 = 2–27 wt%, and TiO_2 = 0.08–0.47 wt%. Gabbros have Mg# = 74–81, CaO = 5.5–18 wt%, Al_2O_3 = 4.5–24.5 wt%, and TiO_2 = 0.10–0.45 wt%. The rodingite Sample 133Z-3, 18.0–24.0 cm (297.5 m), has Mg# = 88, CaO = 28 wt%, and Al_2O_3 = 4 wt%. This sample has the highest TiO_2 content (0.62 wt%) and lowest Cr and Ni contents, 47 and 172 ppm, respectively, of all Hole CM1A samples.

Excluding the few dunites that occur in the Layered Gabbro Sequence, dunite and harzburgites show similar chemical compositions in Hole CM1A, characterized by higher Mg# (83–92), Cr (131–3672 ppm), and Ni (304–2786 ppm) and lower CaO (< 2.0 wt%), Al_2O_3 (< 0.99 wt%), and TiO_2 (< 0.04 wt%) contents compared to the upper gabbroic sequence. The 2 wehrlitic rocks, one from near the base of the Layered Gabbro Sequence and the other from the middle of the Dunite Sequence (55Z-1, 26–32 cm, and 92Z-2, 0–5 cm, respectively) have concentrations of Cr = 1158 ppm and 1826 ppm, and Ni = 1048 ppm and 2628 ppm, respectively. Dunite constitutes a major component of Hole CM1A. Dunites were sampled in all sequences of the hole. Dunites from the Layered Gabbro Sequence have distinctly low Mg# (~83) compared to the other sequences. This tendency is also observed in some dunites from the Dunite with Gabbro Sequence at ~260–280 m, although Mg# is slightly higher (Mg# = 86.5–88.0). Apart from this interval, dunites from the CMTZ and Mantle Sequence have high Mg# of 87–92 (Figs. F90, F91).

Harzburgites constitute about the half of the mantle sequence, alternating with dunites at the top of the sequence then becoming the dominant rock type downhole (Figs. F89, F90). They have Mg# of 88.2–92.2 and CaO, Al_2O_3, and TiO_2 contents of 0.15–2.0 wt%, 0.23–0.98 wt%, and 0.01–0.03 wt%, respectively (Fig. F91). In the Mantle Sequence, TiO_2 decreases from 0.03 to 0.01 wt% from top to bottom, whereas Al_2O_3 concentrations display no trend. The relationship between CaO content in harzburgites and depth is different from the other major elements; the successive increasing and decreasing trends show a well-defined zigzag pattern (i.e., increasing from 0.91 to 1.98 wt% between 311 and 340 m, decreasing to 0.47 wt% at ~360 m, increasing again to 1.17 wt% at ~380 m, and finally decreasing to 0.74 wt% at ~404 m). Intervals with the highest CaO contents are characterized by high abundance of carbonate veins (Figs. F90, F91).

Hole CM1A dunite and harzburgites show similar major and minor chemical compositions to other Oman ophiolite samples from published studies (Fig. F92). The dunites plot above the mantle fractionation array in the MgO/SiO_2 vs. Al_2O_3/SiO_2 diagram, whereas the harzburgites plot below the mantle fractionation array. The FeO vs. MgO content in dunites and harzburgites from Hole CM1A plot within the fields of pure/slightly impregnated dunites and highly impregnated dunites/harzburgites of the Samail ophiolite, respectively. Layered Gabbro Sequence dunites contain lower MgO compared to dunites from other sequences, making the former similar to mantle harzburgite but with higher FeO content. Lower CaO and Al_2O_3 also distinguish the dunites from the harzburgites. The higher CaO contents present in harzburgites is strongly correlated to the presence of carbonate minerals in veins.

Whole-rock trace elements

Gabbros from Hole CM1A display a large range of variation in Ni, Co, and Cr, with concentrations ranging 63–1187 ppm, 4–132 ppm, and 87–4116 ppm, respectively (Table T10; Fig. F91). Yb_{CN} varies 1.9–4.9. Rare earth element (REE) patterns are nearly parallel between the 3 analyzed samples, with minor variation of chondrite-normalized La_{CN}/Sm_{CN} (0.25–0.30), La_{CN}/Yb_N (0.19–0.28), and Gd_{CN}/Yb_{CN} (1.1–1.4) ratios and a well-defined positive Eu anomaly (Eu/Eu* = 1.3–1.6). Multielement patterns show significant depletion in high-field-strength elements (HFSE) relative to REE (Nb_{PMN}/La_{PMN} = 0.04–0.20; Zr_{PMN}/Sm_{PMN} = 0.23–0.35; ratios normalized to primitive mantle).

The 2 olivine gabbros analyzed by LA-ICP-MS (18Z-1, 26–33 cm, and 41Z-2, 0–6 cm; 38.57 and 109.89 m, respectively) (Fig. F93) display contrasting REE patterns. The slope of their heavy REE (HREE) pattern is very similar (Gd_{CN}/Yb_{CN} = 1.2–1.3). However, the more enriched second sample shows stronger depletion in light REE (LREE) relative to medium REE (MREE) (La_{CN}/Sm_{CN} = 0.20), as well as a less significant positive Eu anomaly (Eu/Eu* = 1.5) relative to the first, more primitive, sample (La_{CN}/Sm_{CN} = 0.47; Eu/Eu* = 2.6). The multielement patterns of the 2 samples show the same depletion in HFSE relative to REE than gabbros (Nb_{PMN}/La_{PMN} = 0.04–0.10; Zr_{PMN}/Sm_{PMN} = 0.21–0.35), especially in the most enriched olivine gabbro.

Dunites have low REE contents with a ΣREE < 170 ppb; Yb_{CN} = 0.14–0.25. Two dunites are characterized by a W-shape REE pattern (Samples 58Z-2, 1–6 cm, and 75Z-3, 66–73 cm; 143.93 and 178.58 m, respectively), showing depletion in MREE relative to HREE

(Gd_{CN}/Yb_{CN} = 0.12–0.20) and LREE (La_{CN}/Sm_{CN} = 1.4–3.6) and a variable positive Eu anomaly (Eu/Eu* = 1.8–4.6). The third dunite Sample 51Z-1, 31–39 cm (129.157 m), is characterized by continuous depletion from HREE to LREE (La_{CN}/Yb_{CN} = 0.07) and a strong positive Eu anomaly (Eu/Eu* = 4.0). Dunite multielement patterns display moderate to strong positive anomalies in U (U_{PMN}/La_{PMN} = 3.3–6.6), Pb (Pb_{PMN}/Ce_{PMN} = 7.3–34.8), Sr (Sr_{PMN}/Nd_{PMN} = 3.9–12.6), and Ti (Ti_{PMN}/Gd_{PMN} = 2.0–6.3).

Pyroxene minor and trace elements

Clinopyroxene

Clinopyroxene concentration in gabbros is highly variable, with Ti and Yb_{CN} contents ranging 1251–5510 ppm and 2.8–8.6, respectively (Table **T12**; Fig. **F94**). All the REE patterns show a nearly flat HREE segment (Gd_{CN}/Yb_{CN} = 0.87–1.3), strong depletion in LREE (La_{CN}/Sm_{CN} = 0,02–0,12; La_{CN}/Yb_{CN} = 0.01–0.11), and no or slightly positive Eu anomaly (Eu/Eu* = 0.96–1.3). Multielement patterns are characterized by depletion in HFSE relative to REE (one value for Nb_{PMN}/La_{PMN} = 0.07, Zr_{PMN}/Sm_{PMN} = 0.08–0.51), and by a negative Pb anomaly (Pb_{PMN}/Ce_{PMN} = 0.15–0.36).

Clinopyroxenes in olivine gabbros have Ti and Yb_{CN} contents ranging 1444–3827 ppm and 3.4–9.7, respectively (Table **T12**; Fig. **F94**). REE patterns show a slightly variable HREE segment, from quite flat to slightly enriched in MREE (Gd_{CN}/Yb_{CN} = 1.0–1.5), and depletion of LREE relative to MREE (La_{CN}/Sm_{CN} = 0.06–0.15; La_{CN}/Yb_{CN} = 0.07–0.16). Clinopyroxenes in olivine gabbros display only slight negative to positive Eu anomalies (Eu/Eu* = 0.85–1.2), independently from the shape of the surrounding LREE and HREE segments. Only one clinopyroxene (Sample 133Z-1, 76–83 cm; 292.04 m) presents an anomalous signature with low Ti (496 ppm) and Yb_{CN} (1.7). It is also characterized by a REE pattern continuously depleted from HREE to LREE, with La_{CN}/Yb_{CN} = 0.29 (La_{CN}/Sm_{CN} = 0.53; Gd_{CN}/Yb_{CN} = 0.61), and presenting a slight negative Eu anomaly (Eu/Eu* = 0.92). Multielement patterns show negative anomalies in HFSE (Zr_{PMN}/Hf_{PMN} = 0.17–0.61) and Pb (Pb_{PMN}/Ce_{PMN} = 0.03–1.1), similar to gabbros, as well as a strong depletion in large-ion lithophile elements (LILE) Th and U relative to REE (e.g., Th_{PMN}/La_{PMN} = 0.13–0.47). The anomalous clinopyroxene shows moderate HFSE depletion relative to MREE (Zr_{PMN}/Sm_{PMN} = 0.56) and a positive Pb anomaly (Pb_{PMN}/Ce_{PMN} = 3.1).

Clinopyroxene in one wehrlite (Sample 55Z-1, 26–32 cm; 137.49 m) contains Ti and Yb_{CN} ranging 2947–3699 ppm and 5.7–7.8, respectively. REE patterns are similar to those of gabbros with a flat HREE segment (Gd_{CN}/Yb_{CN} = 1.1–1.2) and progressive depletion toward LREE (La_{CN}/Sm_{CN} = 0.07–0.11; La_{CN}/Yb_{CN} = 0.06–0.10). The positive Eu anomaly is slight in wehrlite clinopyroxenes with Eu/Eu* < 1.2. Multielement patterns are characterized by the same strong negative anomalies in HFSE as observed for (olivine) gabbros, with Zr_{PMN}/Sm_{PMN} = 0.13–0.20.

Two clinopyroxenes from a dunite sample (158Z-1, 59.0–65 cm; 356.80 m) contain lower Ti and Yb_{CN} than (olivine) gabbros and the wehrlite, with values ~385 ppm and 1.1–1.2, respectively. REE patterns are slightly depleted from HREE to MREE (Gd_{CN}/Yb_{CN} = 0.67–0.84) then to LREE with a similar slope to the HREE segment (La_{CN}/Sm_{CN} = 0.31–0.55; La_{CN}/Yb_{CN} = 0.27–0.50). The flatter of the two clinopyroxene patterns exhibits a positive Eu anomaly in REE pattern (Eu/Eu* = 1.5), as well as negative anomalies in HFSE (Nb_{PMN}/La_{PMN} = 0.56; Zr_{PMN}/Sm_{PMN} = 0.57), Pb (Pb_{PMN}/Ce_{PMN} = 0.60), and Sr (Sr_{PMN}/Nd_{PMN} = 0.53).

Orthopyroxene

Orthopyroxenes in dunites from Hole CM1A contain Ti and Mn contents ranging 11.5–64.6 ppm (Table **T13**; Fig. **F94**). They are also characterized by very low trace element contents (e.g., Yb_{CN} = 0.10–0.52), with strong depletion from HREE to MREE with Dy_{CN}/Yb_{CN} ranging 0.16–0.33; LREE were not determined by LA-ICP-MS, as concentrations were below the detection limit (see **Geochemistry** in the **Methods** chapter). Multielement patterns show high concentrations of LILE, Th, and U relative to REE and a positive anomaly in Ti (Ti_{PMN}/Gd_{CN} = 9.1–15.7 in 2 samples).

Orthopyroxenes in harzburgites are richer in Ti (69.3–116.7 ppm), Mn (960–2045 ppm), and Yb_{CN} (0.33–0.68) than in dunites; 1 sample (143Z-1, 3–10 cm; 311.25 m) contains orthopyroxenes with particularly high values (Ti = 309–342 ppm; Mn = 1015–1319 ppm; Yb_{CN} = 1.3–1.9) (Table **T13**; Fig. **F94**). In all samples orthopyroxene is depleted from HREE to MREE with Dy_{CN}/Yb_{CN} = 0.03–0.37. Multielement patterns show high values in Pb (Pb_{PMN} = 0.3–2.7) and Sr (Sr_{PMN} = 0.01–0.48), as well as LILE (e.g., Rb_{PMN} = 0.03–0.23), Th, and U that result in U-shaped extended patterns. Orthopyroxenes in the most enriched sample also show a positive Ti anomaly (Ti_{PMN}/Gd_{PMN} = 3.3–4.8).

Paleomagnetism: Hole CM1A

The paleomagnetic and rock magnetic analyses conducted aboard *Chikyu* during ChikyuOman Phase 2 (2018) were limited to discrete sample measurements and comprised, in the following order (a) measurement of anisotropy of magnetic susceptibility (AMS), which also includes measurement of the bulk magnetic susceptibility, (b) magnetic remanence measurements prior to and following stepwise alternating field (AF) demagnetization, and (c) thermal demagnetization (THD) on selected samples. Although some of the samples were also used for physical properties measurements, all paleomagnetic analyses were conducted beforehand and the data sets are thus not affected. Overall, we employed similar measurement routines to those used during Phase 1. Treatment increments applied during thermal and alternating field demagnetization were adjusted to the coercivity and blocking temperature distributions of individual samples and thus differed from sample to sample.

Figure F95 summarizes the magnetic properties (remanence, susceptibility, and magnetic shape anisotropy) measured downhole in Hole CM1A. Systematic differences can be seen between the rocks of the Layered Gabbro Sequence (1.50–160.23 m), the strongly serpentinized dunites and other ultramafic rocks from the CMTZ (160.23–310.99 m), and the rocks of the Mantle Sequence (310.99–404.21 m). The resolution of finer scale variation in the rock magnetic parameters with depth are difficult to resolve without additional archive-half measurements.

Remanent magnetization

The natural remanent magnetization (NRM) intensities of discrete samples taken from the Layered Gabbro Sequence (Sections 1Z-1 through 63Z-4; 1.50–160.23 m) range from 0.001 A/m to 15.9 A/m. Peak values were measured on samples from few isolated dunitic layers. During AF demagnetization, the gabbros demagnetize over a wide coercivity range of ~20–70 mT and yield median destructive fields (MDF) of 15–25 mT. With few exceptions, most samples yield single-component remanences with only small magnetic overprints, suggesting that drilling overprints did not have a major effect on magnetic remanence. However, we noted that upon demagnetization to alternating fields of 60 mT or more, the remanence directions of some samples trend away from the origin, indicative of acquisition of a small artificial remanence. During thermal demagnetization, samples retain almost their entire remanence up to an applied temperature of 550°C. Although some samples show a sharp decrease in remanence intensity at 600°–630°C, a peak temperature of 650°C was not sufficient to demagnetize others (Fig. F96). Bulk susceptibility measurements accompanying these analyses showed some variation in the susceptibility of individual samples upon heating to temperatures >500°C (Table T14), which did not appear to cause a deflection of the remanence vector.

Serpentinized dunites sampled from the CMTZ (Dunite and Dunite with Gabbro Sequences) (~250–310 m; Sections 107Z-3 through 142Z-4) yield significantly stronger remanence intensities that range 3.9–36.1 A/m. NRM intensities of these samples rapidly decay during AF demagnetization, with MDF ranging 5–10 mT. Vector component diagrams show that most samples yield a small viscous overprint, which was usually removed at applied fields of 8 mT or less, after which the remanences decay univectorially to the origin. In many cases these overprints are directed along-core (Fig. F97), indicative that they may have been acquired during the drilling process. Thermal demagnetization usually occurs over a wide range of blocking temperatures of 200°–590°C. Remanence was measured on only 5 samples from the Mantle Sequence. Their intensities range 0.5–4.9 A/m and thus fall in between those of the Layered Gabbro Sequence and CMTZ, and samples from this zone yield MDFs and blocking temperature ranges that resemble more closely those of the Layered Gabbro Sequence.

Preliminary shipboard interpretation of the remanence and demagnetization data sets was conducted using PuffinPlot (Lurcock and Wilson, 2012). Due to the absence of systematic low-temperature/low-coercivity overprints, we calculated characteristic remanence directions (ChRM) for each sample from the best-fit high-temperature/high-field component by principal component analysis (PCA). In few cases where the high-temperature/high-field components trend away from the origin, we interpreted this to be caused by acquisition of an unwanted artificial remanence and thus calculated the ChRM directions anchored to the origin. A summary of the preliminary shipboard interpretation is given in Table T15, and the distribution of inclination readings with depth illustrated in Figure F95.

The inclinations calculated on samples taken from cores from the Layered Gabbro Sequence (1.50–160.23 m) are consistently shallow and positive (Figs. F95, F98). Within the CMTZ and Mantle Sequence, we exclusively measured pervasively serpentinized dunites with few wehrlites and harzburgites. In contrast to the overlying layered gabbros, these rocks mostly yield remanence directions that are of shallow negative inclination, with few intervals in between in which positive inclinations were recorded. The differences in direction are unsurprising considering the remanence directions of the dunitic rocks most likely reflect recording of secondary magnetite formed during the serpentinization process. Given that Hole CM1A was cored roughly perpendicular to the local CMTZ, no tilt or other structural correction need to be applied to the data set. We calculate our best fit direction separately for the Layered Gabbro Sequence (Sequence I) and serpentinized rock types of the CMTZ using Arason and Levi (2010) maximum likelihood method for inclination data. Our best estimate for the mean inclination of the Layered Gabbro Sequence is inclination = 11.0°, $\alpha95$ = 2.52°, N = 42. Our best mean for samples from the ultramafic rocks of the CMTZ and

Mantle Sequence that yield positive inclinations is inclination = 14.3°, α95 = 6.13°, N = 15, and the best mean for those that carry ChRM directions of negative inclination is inclination = –13.4°, α95 = 5.5°, N = 22.

In its simplest interpretation this result may indicate that the gabbroic sequences and some sections from the CMTZ acquired remanence in normal polarity, whereas the serpentinization process occurred in a reversed polarity field. Within the uncertainties, these paleomagnetic inclinations are also consistent with the paleomagnetic directions measured on surface outcrops (see, for example, Feinberg et al., 1999) and the paleomagnetic data sets measured on lower and mid-crustal rocks (Holes GT1A and GT2B) during ChikyuOman2017 (Leg 1).

Magnetic susceptibility

Bulk magnetic susceptibility

The mean magnetic susceptibility values for discrete specimens measured on olivine gabbro units range from 4,296 to 22,097 × 10^{-6} SI. Serpentinized dunites sampled below 160 m yield much stronger susceptibilities in the range of 96,657.2 × 10^{-6} to 253,888 × 10^{-6} SI, which is consistent with the higher NRM intensities observed and most likely due to the higher magnetite content formed during the serpentinization process. Magnetic susceptibility measured on rocks of the Mantle Sequence ranges from 4,072.0 to 19,073.8 × 10^{-6} SI (Fig. **F95**).

Anisotropy of magnetic susceptibility

Anisotropy of magnetic susceptibility (AMS) determinations were performed on all discrete samples that were collected for paleomagnetic and physical properties investigations prior to conducting any other analyses. Both the corrected degree of magnetic anisotropy P' and the shape of magnetic fabric differs throughout the hole (Fig. **F99**). The layered gabbros sampled from 1.50–160 m yield P' values that range 1.04–1.52 (average = 1.14). The magnetic fabric shape ranges from prolate (T = –0.86) to oblate (T = 0.91). The K_{min} axis are oriented along-core and thus oriented roughly perpendicular to the magmatic foliation observed (see **Structural geology: Hole CM1A**). Serpentinized dunites sampled within the CMTZ (160–310 m) yield on average a higher degree of anisotropy (1.07 ≤ P' ≤ 1.45). With only 8 of 61 samples having value T < 0, they are clearly dominated by oblate fabrics. F-ratios range 1.049–1.42 (Fig. **F100**). However, whereas no clear relation in the distribution of K_{min} inclinations is apparent, K_{max} appears to be clustered along the core-axes. Interpretation of these observations in relation to magmatic fabric requires further postcruise analysis.

Physical properties: Hole CM1A

Physical properties of gabbroic and ultramafic rocks from Hole CM1A were characterized through a series of measurements on whole-round sections, section halves, section-half pieces, and discrete samples (see **Physical properties** in the **Methods** chapter). All whole-round sections were run through the X-ray computed tomography (XCT) scanner and measured for P-wave velocity (V_P), gamma ray attenuation (GRA) density, magnetic susceptibility (MS), noncontact electrical resistivity (NCR), and natural gamma ray radiation (NGR) data with the Whole-Round Multisensor Core Logger (MSCL-W). We also measured point magnetic susceptibility (MSP) and reflectance spectroscopy and colorimetry (RSC) with the Split-Half Multisensor Core Logger (MSCL-C), and line scan color image with the Imaging Multisensor Core Logger (MSCL-I) on the split surface of archive halves. Thermal conductivity was measured on section-half pieces. Compressional wave (P-wave) velocity, electrical resistivity (IMP), and density and porosity (MAD) were measured on discrete minicube samples (20 mm × 20 mm × 20 mm). MAD measurements were also conducted on some irregular-shaped discrete samples. The rock names reported in data tables correspond to the primary lithologies described in **Igneous petrology: Hole CM1A** (Fig. **F3**; Table **T2**).

Whole-round and section half measurements

A total of 559 whole-round and archive-half sections from Hole CM1A were measured. The downhole data plot is shown in Figure **F101** and data are summarized in Table **T16** and supplemental Tables **ST6** and **ST7**.

X-ray computed tomography

XCT was continuously logged for all 559 whole-round core sections recovered from Hole CM1A. The XCT number of minerals is essentially a function of the density and chemical composition of the sample. Hence, XCT numbers in the core sections result from a combination of their mineral composition and pore structure in a voxel (0.625 mm × 0.175 mm × 0.175 mm). Figure **F102** shows examples of XCT images from Sections 27Z-4, 63Z-4, 147Z-4, and 157Z-2. An XCT image of the archive-half split surface, with XCT number represented on a color scale, was generated for every section (see **Supplementary material** > **G_XCT_data**. The average and the mode of XCT numbers for every scan slice (0.625 mm thick) were also computed and plotted downhole (Fig. **F101G**). The average XCT number is more susceptible to the effects of open cracks in the core section than the mode XCT number (e.g., Fig. **F102A**). This is because the XCT number of the air is significantly lower than that of minerals (XCT number of air is approximately –1000; see **Physical properties** in the **Methods** chapter). However, the mode XCT number can overlook the presence of minor but dense minerals (e.g., Cr-spinel), so both values are important to consider.

Intact gabbro, olivine gabbro, dunite, and harzburgite have average XCT numbers of ~3330, ~3390, ~2810, and ~2960, respectively. Cr-spinel ([Fe, Mg] Cr_2O_4)-rich layers yield high CT values of >4000. CT values lower than gabbroic rocks for dunite and harzburgite reflect the high degree of serpentinization of peridotites and/or the porous nature of serpentinite intervals in Hole CM1A. The CT values of rodingitized gabbro and diopsidite are as high as that of gabbro, ~3500. There are clear steps of the CT number mode at depths of 160 m and 250 m (Fig. **F101**). These CT steps correspond to the boundaries between the Layered Gabbro Sequence (I) and the Dunite Sequence that marks the top of the CMTZ and the Dunite and the Dunite with Gabbro Sequences determined by the core description teams (see Fig. **F102B**). Because XCT number of a core sections depends on mineral composition and porosity in core sections, the trends of the average and the mode of XCT number in the downhole plot clearly follow that of GRA density (Fig. **F101**). Figure **F103** shows the correlations between XCT number and GRA density of 5 major lithologies (gabbro, olivine gabbro, dunite, harzburgite, and wehrlite) and all lithology from Hole CM1A. Most rock types in the figure show a positive relation between XCT number and GRA density, although the dunite data form an irregular cloud clustered around the XCT number of ~2922 and the GRA density of ~2.57 g/cm^3, which is similar to the density of the serpentine polymorph lizardite (~2.58 g/cm^3; Mellini and Zanazzi, 1987). These correlations can be controlled by several factors such as modal abundances of low-density minerals (e.g., serpentine), high atomic number elements in minerals (e.g., calcium in diopside, iron in magnetite, and chromium in Cr-spinel), porosity, and pore structure. Overall, the variations in the XCT number downhole reflect the lithologic variations observed in Hole CM1A.

Colorimetry

RSC data were obtained for 559 sections of archive halves from Sections 1Z to 179Z. The specular component included (SCI) setting was used in measurement on Hole CM1A cores, and this setting provides data that are closer to the actual color than that of the specular component excluded setting (SCE; see **Physical properties** in the **Methods** chapter). Color data acquired from reflectance spectroscopy and high-resolution images can provide insights into the variability of different lithologic units recovered from Hole CM1A. Lightness (L*) and chromaticity (a* and b*) variables were generated from the reflected light collected through the spectrophotometer every 2 cm. High L* value indicates lighter colors, with 0 representing black and 100 for white. Directions toward more +a* denote a shift toward red from green, whereas +b* depicts a shift toward yellow from blue. High-resolution (100 pixels/cm) half section images produced by the MSCL-I provides an alternative source of 2-D color data.

A downhole plot of color parameters is shown in Figure **F104**. Reflectance and chromaticity parameters a*, b*, and L* range –13.6–5.5 (σ = 0.6), –17.6–5.5 (σ = 1.7), and 2.5–90.3 (σ = 12.1), respectively. Overall sections tend to show negative a* and b* values, meaning that the colors of cores tend toward mostly greenish and bluish tints. At the boundary between the Layered Gabbro and Dunite Sequences, there are stepwise changes in L* and a* values; 50–27 for L* and –1–0 for a*, respectively. This means that dunite layers are more reddish (brownish) and darker than gabbro layers. There is no significant difference in the color data between the dunite layers in Sequences II, III, and IV and the harzburgite in Sequence IV. However, rodingitized gabbro and diopsidite in the Dunite with Gabbro (III) and Mantle (IV) Sequences show higher L* (~60) and lower a* (about –1) values.

Whole-round compressional wave velocity

Whole-round *P*-wave velocity was measured using the MSCL-W with a 230 kHz *P*-wave transmitter and a receiver for 559 sections at a spacing of 4 cm. Whole-round *P*-wave velocity measurements show large variations because the quality of the measurement is strongly dependent on the condition of the core surface in contact with the transmitter. The average of *P*-wave velocity in each whole-round section measured by MSCL-W is slightly lower than the measurements made on discrete samples (see **Discrete sample measurements**), perhaps due to the dry condition of the core sections during scanning. Cores from the Layered Gabbro Sequence (I) yield higher velocities than the deeper sequence that mostly comprises ultramafic rocks. Averages and maximum values of *P*-wave velocity in each sequence are 5869 m/s and 8996 m/s for Sequence I, 3948 m/s and 8266 m/s for Sequence II, 3436 m/s and 7176 m/s for Sequence III, and 3218 m/s and 6783 m/s for the Mantle Sequence (IV), respectively. The whole-round V_P data are summarized in the downhole plot in Figure **F101B**, together with the discrete sample measurements. These data broadly match each other and follow changes in rock type, and the extent of hydrothermal alteration and weathering in the Hole CM1A cores.

Gamma ray attenuation density

GRA density measurements were conducted for 559 sections at a spacing of 4 cm (Fig. F101A). GRA of intact gabbro and intact ultramafic rocks are 2.9–3.2 g/cm^3 and 2.4–2.7 g/cm^3, respectively. These low densities for the ultramafic rocks in the CMTZ and Mantle Sequences (II, III, IV) suggests that olivine (density ~ 3.3 g/cm^3) in these rocks is nearly 100% serpentinized (density of lizardite serpentine ~ 2.58 g/cm^3; Mellini and Zanazzi, 1987) and the presence of discernible porosity in the intact cores throughout Hole CM1A. The paleo-Moho layer Gabbro/Dunite Sequence boundary is well defined by a sharp (within 20 cm) decrease in GRA from 3.1 to 2.5 g/cm^3. GRA of rodingitized gabbro and other Ca-metasomatized features in the ultramafic rocks are in the range 2.9–3.3 g/cm^3, similar to the densities of the layered olivine gabbros.

Electrical resistivity

NCR data generally indicate that the cores from Hole CM1A are resistive, especially the olivine gabbros of the Layered Gabbro Sequence (I) (Fig. F101E). Most readings in this sequence are greater than or equal to the maximum measurable value (85 Ω·m). In contrast, the rocks of the Dunite Sequence (II) are less resistive, ~5 Ω·m. These low-resistivity intervals are probably due to the high abundance of conductive phases such as magnetite in the strongly to completely serpentinized dunites. The electrical resistivity of the ultramafic rocks is uniformly low in the Dunite Sequence but increases with depth throughout the Dunite with Gabbro Sequence (III; ~250–311 m) and is significantly higher in the Mantle Sequence (IV; average = ~28 Ω·m), albeit still lower than the Layered Gabbro Sequence. This could indicate that the degree of serpentinization and secondary magnetite formation as a by-product of the serpentinization of olivine is different in the different rock types.

Natural gamma ray radiation

NGR on the Hole CM1A is generally low (<1 cps on average; Fig. F101E). In the Layered Gabbro Sequence (I), layers of dunite, especially plagioclase-bearing wehrlite and orthopyroxene-bearing dunite (e.g., Section 58Z-4), display significantly higher counts (>10 cps) than other gabbroic layers in the sequence. Some ultramafic layers in Sequences II, III, and IV also display relatively high NGR. Most of these layers correspond to plagioclase-bearing dunite and harzburgite; thus, NGR in the ultramafic layers might indicate minor potassium in plagioclase or K and U added by hydrothermal alteration. We note that most of the rodingitic gabbro layer does not show significantly higher NGR compared to the ultramafic layer.

Whole-round and half-round magnetic susceptibility

MS was measured on both the MSCL-W with an 80 mm loop sensor and the MSCL-C with a contact sensor MSP probe. Whole-round MS values are shown in the downhole plots (Fig. F101). MS of gabbroic rocks is of the order of 100 × 10^{-5} SI, whereas the ultramafic rocks in all sequences are higher than the upper measurement limit of the MSCL-W with an 80 mm loop sensor (>7000 × 10^{-5} SI for HQ core). High MS in ultramafic layer is probably due to the presence of the magnetite in the layer.

Discrete sample measurements

All data of discrete sample measurements on minicubes are summarized in Tables T17 and T18. Downhole plots are shown in Figure F105.

P-wave velocity

P-wave velocity was measured in Hole CM1A on 152 cube samples along the three principal directions *x*, *y*, and *z* in the CRF (see Table T17; Fig. F105A). *P*-wave velocity is 5.81 ± 0.85 km/s on average (range = 4.32–7.18 km/s). The gabbro samples exhibit higher velocities, with a maximum velocity of 7.18 km/s and minimum of 5.61 km/s (average = 6.71 ± 0.38 km/s). In contrast, dunite samples have significantly lower velocities (down to 4.40 km/s; average= 5.1 ± 0.39 km/s). Harzburgite also has relatively low velocity (down to 5.05 km/s; average = 5.53 ± 0.33 km/s). Rodingitized rocks have relatively high velocities (up to 6.96 km/s; average = 6.45 ± 0.44 km/s). As such, in the Layered Gabbro Sequence (I) the highest *P*-wave velocities are measured (up to 7.18 km/s; average = 6.69 ± 0.43 km/s), whereas the Dunite Sequence at the top of the CMTZ yields the lowest *P*-wave velocity (average = 4.93 ± 0.23 km/s).

Density and porosity

Bulk density, grain density, and porosity were calculated from measurements on 162 cubes (20 mm × 20 mm × 20 mm) and 10 irregularly shaped or broken cube samples stolen from the working-half sections from Hole CM1A, ~1 sample per core and reflecting lithologic and alteration variation (Table T17; Fig. F105A, F105B). Average bulk and grain densities of cube samples from Hole CM1A are 2.76 ± 0.20 and 2.79 ± 0.19 g/cm^3, respectively. In Hole CM1A, the cube samples were mainly taken from relatively homogeneous intervals with few or no visible cracks or veins. Non-cube irregular-shape samples from highly altered or deformed intervals were measured only for density and porosity (Table T18). The highly altered or deformed samples have high porosities (up to 8.35%) and lower bulk densities (down to 2.55 g/cm^3) and grain densities (2.64 g/cm^3). Gabbro and olivine gabbro have higher bulk (average = 2.98 ±

0.09 and 2.96 ± 0.09 g/cm³, respectively) and grain (average = 3.01 ± 0.09 and 2.96 ± 0.09 g/cm³, respectively) densities than dunite (average bulk density = 2.60 ± 0.06 g/cm³, grain density = 2.64 ± 0.05 g/cm³), harzburgite (average bulk density = 2.63 ± 0.07 g/cm³, grain density = 2.66 ± 0.06 g/cm³), and wehrlite (average bulk density = 2.92 ± 0.18, grain density = 2.94 ± 0.16 g/cm³). Rodingitized rocks have the highest densities (average bulk density = 3.12 ± 0.14 g/cm³, grain density = 3.15 ± 0.16 g/cm³) of all the rock types measured in the Hole CM1A.

In the Layered Gabbro Sequence (I), the discrete samples have higher bulk and grain densities (average = 2.95 ± 0.09 and 2.96 ± 0.09 g/cm³, respectively) than the altered ultramafic rocks in the Dunite and Mantle Sequences (Table **T18**). The density of the dunites in the Dunite Sequence (II) at the top of the CMTZ directly below the paleo-Moho is the lowest (average bulk density = 2.57 ± 0.03 g/cm³, grain density = 2.62 ± 0.03 g/cm³) measured but is similar to the harzburgites and dunites of the lowermost Mantle Sequence (IV, bulk density = 2.61 ± 0.09 g/cm³, grain density = 2.64 ± 0.09 g/cm³). In the intervening Dunite with Gabbro Sequence (III) there are variety of rock types and consequently a wide range of densities. As mentioned above, rodingitized rocks in Sequences III and IV have high densities.

The porosity of discrete cube samples ranges 0.03%–9.61% (mean = 1.65%). Porosity is highest in dunite (average = 2.54% ± 1.54%) and lowest in the olivine gabbros (average = 0.80% ± 1.11%). Consequently, Sequence II, predominantly dunite, has relatively high porosity (average = 3.13% ± 1.35%), whereas the Layered Gabbro Sequence (I) has low porosity (average = 0.48% ± 0.91%).

The relationships between densities, *P*-wave velocity, and porosity are shown in Figures **F107** and **F108**. Data from OmanDP Holes GT1A, GT2A, and BT1B are also shown in the diagrams for comparison. Densities and *P*-wave velocity show positive trends, although gabbroic and ultramafic rock types are clustered into separate domains with little overlap (Fig. **F107**). Consequently, there is a negative relationship between *P*-wave velocity and porosity, although gabbroic and wehrlitic rocks show a different trend compared to the ultramafic rocks, best illustrated in log porosity space (Fig. **F108B**). Such trends are also seen in similar rock types (e.g., gabbros vs. ultramafics) from OmanDP Holes GT1A, GT2A, and BT1B; Figs. **F107**, **F108**). *P*-wave velocity is a function of both bulk and grain densities (Fig. **F109A, F109B**). *P*-wave velocity has linear correlation with bulk density that is also seen in those data from other OmanDP holes (GT1A, GT2A, and BT1B; Fig. **F109A**), whereas the relationship between *P*-wave velocity and grain density is less well defined, and the ultramafic rocks display a large range of V_P (~5.7–4.4 km/s) with little change in grain density (~2.58–2.63 g/cm³), hinting that changes in porosity occur together with changes in mineral modes (Fig. **F107B**). The downhole plot of *P*-wave velocity with color scale of bulk and grain densities and porosity reveals certain differences between the sequences and also lithologies (Fig. **F110**).

Electrical resistivity

Electrical resistivity was measured in 149 cube samples from Hole CM1A (Table **T18**; Fig. **F105E**). Resistivities range <1.0–29,500 Ω·m. The electrical resistivity of the ultramafic rocks (dunite, harzburgite, and wehrlite averages 251.8, 337.5, and 519 Ω·m, respectively) are 1–2 orders of magnitude lower than the gabbros (average = 8,104.6 Ω·m). Electrical resistivity in the Dunite Sequence (II) is constantly low compared to other sequences. It gradually increases with depth, ignoring the gabbroic samples, but electrical resistivity decreases in the lower 20 m of the hole. There are subtle relationships between the electrical resistivity and porosity (Fig. **F105D, F105E**).

The downhole plot of the electrical resistivity also clearly shows the differences between sequences and lithologies (Fig. **F111**). Resistivity varies widely and the serpentinized ultramafic rocks show a correlation with *P*-wave velocity, as do grain density and porosity (Fig. **F112**). The more resistive, higher density gabbroic rocks display less well defined relationships, offset to high V_P, and steeper gradients (Fig. **F112**).

Thermal conductivity

A total of 120 thermal conductively measurements were made on core pieces from the working halves of the Hole CM1A cores (Table **T19**; Fig. **F106**). Thermal conductivity ranges 1.97–6.13 W/m·K, and the standard deviation of the average of 6 measurements for each piece (only 2 measurements on interval 158Z-2, 50–59 cm) ranges 0.00–0.34 W/m·K. Olivine gabbro has the lowest thermal conductivity (1.96 W/m·K), whereas rodingitized wehrlite has the highest value (6.13 W/m·K). Thermal conductivities of rodingitized rocks are higher than those of all other lithologies, ranging 3.75–6.13 W/m·K. The mean thermal conductivity of gabbro samples (gabbro, olivine gabbro, and olivine-bearing gabbro) in the Layered Gabbro Sequence is 2.63 ± 0.48 W/m·K. This value is similar to measurements of gabbroic rocks from Hole GT1A (2.58 ± 0.33 W/m·K). Thermal conductivities in the Dunite Sequence are relatively uniform and high (3.12 ± 0.25 W/m·K). In contrast, because of the myriad rock types in the Dunite with Gabbro Sequence (III) there is greater variation in thermal conductivities (2.54–6.13 W/m·K). The thermal conductivities of plagioclase-bearing dunite in the lower part of the Dunite with Gabbro Sequence are low (2.53–2.69 W/m·K) and much less than the dunites from Sequence II. In the Mantle Sequence (IV) harzburgite and orthopyroxene-bearing dunite have similarly low thermal conductivities (2.44–2.50 W/m·K). These values are comparable with that of harzburgite from Hole 1274A, ODP Leg 209, Mid-Atlantic Ridge 15°20′N FZ (Kelemen et al., 2004).

Downhole measurements/ hydrogeological testing: Hole CM1A

Downhole logging and hydrogeological testing operations and acquisition parameters for each borehole are available in Tables **T54** and **T56** in **Downhole logging and hydrogeological testing** in the **Methods** chapter. Raw and processed data from all downhole logs are available in the **Supplementary material** > **L_Wireline logging** and in the ICDP Oman Drilling Project online data repository (**http://oman.icdp-online.org**).

Core scratch test: Hole CM1A

The core scratch test campaign performed by EPSLOG at the JAMSTEC facility in Yokosuka, Japan, between 4 and 13 July 2018 was made on selected core samples taken from the Holes CM1A and CM2B focusing on the transition from the lower crust to mantle rocks totaling 44.6 m in length. Cores from Hole CM1A are divided into two sections: 134.93–159.90 m was of good quality so that most of the cores in that interval could be tested, and 159.90–175.89 m was highly fractured so that only few sparse samples were tested.

The tests were performed by Luc Perneder (EPSLOG) (Perneder, 2018) and supervised by Saneatsu Saito (ODS-JAMSTEC). First, sample intervals were selected. Then samples were tightened on the machine bench and an initial groove at least 1.5 mm deep was created on the whole length of the core while measuring the strength. The rock powers from the groove preparation process were vacuumed and panoramic pictures were taken. Ultrasonic (*P*-wave and *S*-wave) velocity tests were run at two resolutions (4 cm as standard and 2 cm when samples were small or highly fractured). After releasing the samples, rock powers were collected in the sample bags and delivered to the geochemistry team.

The cores were about 3 inches in diameter and slabbed in half, labeled as working and archive. A major constrained requirement from project scientists was to limit the scratch groove depth to 5 mm. This objective was met with the exception of few sections where the groove was 6 mm deep. The cumulative length of these sections with groove depth >5 mm is <1 m.

Three independent sets of data were acquired: (i) the strength log, (ii) the log of ultrasonic velocities V_P and V_S, and (iii) the groove panoramic pictures. The testing campaign was successful in the sense that the scratch and ultrasonic data could be measured on all selected samples while causing little damage to the cores and keeping the groove depth <5 mm, with the exception of very few sections.

During this test campaign, we collected a continuous profile of strength (unconfined compressive [UCS]-equivalent) at centimeter resolution (Figs. **F113A**, **F114A**), ultrasonic *P*-wave and *S*-wave velocity measurements along the core axial direction at a resolution of 4 cm (Figs. **F113B**, **F114B**), and high-definition photographs of the core under visible light taken before the scratch test, focusing on the clean fresh rock surface at the bottom of the scratch groove.

From the petrological identification, the Layered Gabbro Sequence showed strong strength and ultrasonic velocities in the upper section (Fig. **F113**). Sharp changes in the lower section indicate the change to serpentinized dunite (Fig. **F114**).

Imaging spectroscopy: Hole CM1A

All sections of Hole CM1A were imaged onboard the *Chikyu* during Leg 3. The ~400 m of Hole CM1A were imaged in 7.5 12-h shifts over 4 days. A total of 561 sets of images (visible-near infrared [VNIR] and short-wave infrared [SWIR]) were acquired of core sections. A select number of images from the SWIR were processed to reflectance to check data quality. The remainder of the images, including all from the VNIR sensor, will be processed at Caltech, and mineral maps of each core section will be generated.

An example of preliminary mapping is shown in Figure **F115**. Here, interval 23Z-3, 4–41 cm, contains a cataclasite within an extensively altered gabbro. The spectrally dominant phase is prehnite, and some zones dominated by chlorite or thomsonite also occur. Some remnant chlorite and epidote is still present in the zone dominated by thomsonite. There are also small patches of epidote and other minerals present that are not shown for simplicity. At least two episodes of alteration can be discerned from the textures and crosscutting minerals.

Operations: Hole CM1B

Rotary Hole CM1B is located 10 m from cored Hole CM1A (see Figs. **F2**, **F4** in the **Introduction to Science Theme 1B** chapter). Detailed petrological observations were made on core from Hole CM1A during summer 2018 onboard *Chikyu*. Here we summarize the on-site lithology log of Hole CM1B drill cuttings. The log is available in Table **T20**.

All times are reported as local time in Oman (UTC + 4 h).

Drilling summary

- Spud-in: 19 Dec 2017, 14:40 h
- Surface casing (SW) installed: 26 Feb 2018
- Surface casing type/diameter: MS surface casing, 9-5/8 inches
- Surface casing depth: 0.3–10.60 mbgl (m below ground level)
- Hole diameter: 8 inches at 10.60–137.10 mbgl; 6-1/8 inches at 137.10–237.00 mbgl
- Total depth of borehole: 237.00 mbgl
- Completion type: open hole
- Discharge by air lift: NA
- Static water level: 7.40 mbgl (12 Jan 2018)

Geology summary

- Layered gabbro and dunite

Technical issues

During drilling of Hole CM1B, we experienced multiple technical issues with regard to borehole stability. Because of continuous collapse of the hole at 133–137 mbgl, this unstable section was cemented. Further hole stability issues occurred at 186–199 mbgl. This section was also cemented and redrilled. Subsequently, drilling with the 6-1/8 inch tricone bit resumed, but additional bit blockage occurred at 220 and 227 mbgl. Repeated flushing and cleaning of hole was not successful, and further drilling was canceled at a total depth of 237 mbgl because of hole stability.

Operations summary

- 17–18 Dec 2017: mobilize drill rig, drilling accessories, equipment, and material to site.
- 19 Dec 2017: site set up, assemble 14-3/4 inch bit; spud.
- 20 Dec 2017: unstable alluvium, hole size increased to 25 inches to 0.90 mbgl; install 23 inch open steel drum and cement annulus.
- 21 Dec 2017: drill with 12-1/4 inch tricone bit to 10.60 mbgl. Failed 9-5/8 inch conductor casing run in hole (RIH). Pull casing out of hole (POOH).
- 22 Dec 2017: ream hole with 14-3/4 inch bit assembly 4.40–10.60 mbgl. Flush hole, complete POOH, and RIH 9-5/8 inch casing. Cement grout the 14-3/4 and 9-5/8 inch casing annulus.
- 23 Dec 2017: drill 10.60–15.5 mbgl using 8 inch hammer bit assembly. First seepage at 13–14 mbgl (electrical conductivity [EC] = 1503 pS/cm, pH = 8.72, T = 27.7°C). Technical issue with pulldown remote at drill rig. Mechanical maintenance required.
- 24 Dec 2017: wait for rig technician to arrive.
- 25 Dec 2017: pulldown remote fixed; drill with 8 inch hammer drill assembly 15.5–30.0 mbgl.
- 26–27 Dec 2017: drill 8 inch hole 30.0–137.1 mbgl. Water strikes at 30.7 mbgl (1.22 L/s, EC = 1207 pS/cm, pH = 8.71, T = 28.8°C) and 79 mbgl (1.22 L/s, EC = 1382 pS/cm, pH = 8.26, T = 31.8°C). Partial POOH and flush at 137.1 mblg; bit blockage 133–135 mbgl.
- 28–31 Dec 2017: unsuccessfully tried to clear hole by flushing 130–137.1 mbgl using 6-1/8 and 8 inch drill bit assemblies.
- 1–5 Jan 2018: clear borehole using polymer mud circulation and proceed with cementing unstable zone from the bottom of the hole.
- 6 Jan 2018: cement total depth of 129 mbgl. Drill 129–137.10 mbgl through cemented section using 6-1/8 inch tricone bit assembly. Continue drilling 137.10–143.8 mbgl with 6-1/8 inch tricone bit.
- 7–10 Jan 2018: drill 143.8–233 mbgl with 6-1/8 inch tricone bit. Collect and describe drill cuttings every meter. Collect subsamples for subsequent analysis.
- 11 Jan 2018: air pressure control regulator on drill rig failed. Wait for replacement from Muscat.
- 12 Jan 2018: fix/test rig air pressure regulator. Drill bit blockage at 196 mbgl; backfill =3.5 m. Wash/flush blockage 195–233 mbgl. Continue drilling with 6-1/8 inch drill bit assembly to 237 mbgl.
- 13 Jan 2018: bit assembly failed; broken NRV valve. Request new 6-1/8 inch tricone bit from Muscat office.
- 14 Jan 2018: assemble new 6-1/8 inch tricone bit. Observe bit blockage at 143 mbgl. Wash/clear blockage.
- 15–16 Jan 2018: wash/clear hole to 202 mbgl.
- 17–18 Jan 2018: cement unstable section 187–202 mbgl.
- 19 Jan 2018: drill with 6-1/8 inch tricone bit assembly through cemented zone (187–202 mbgl) to 227 mbgl. Observe drill bit blockage at 227 mbgl. Partial POOH.
- 20 Jan 2018: wash/flush hole 205–227 mbgl. Observe drill bit blockage at 212 and 227 mbgl. Decide to cancel borehole at total depth of 237 mbgl due to continuous collapse of the hole. Complete POOH.
- 21–22 Jan 2018: mobilize drill rig, drilling accessories, materials, and equipment to Site CM2A to conduct clearing/wiper run in Hole CM2A for Schlumberger Oil Service geophysical borehole logging.
- 27 Jan 2018: static water level at 7.40 mbgl (casing shoe at 10.60 mbgl). Fill borehole up to ground level for Schlumberger Oil Services geophysical borehole logging. Loading/mobilization of drilling equipment and materials to Site BA1.

Petrology from drill cuttings: Hole CM1B

As in Hole CM1A, the upper 141 m of Hole CM1B is dominated by gabbroic rocks. The cuttings log indicates minor interlayered wehrlite in the intervals at 91–92, 98–99, and 134–137 m (Fig. **F116**). It is not apparent whether these are true wehrlites. The term wehrlite has traditionally been used, over decades of mapping Oman lower crustal lithologies, mainly for rocks with 10%–30% plagioclase (which should be called “olivine melanogabbros” or just “gabbros”), rather than for true wehrlites (which are rare).

Dunite layers observed in core from Hole CM1A shallower than 140 m depth were not detected at these depths in the cuttings from Hole CM1B. At 143, 144, and 146 m, cuttings from Hole CM1B were described as “fault rocks.” Other than these three 1-m-long intervals, at 142–237 m, dunite and minor serpentinite were logged.

Hydrothermal alteration/veins: Hole CM1B

“Serpentinites” were logged in cuttings at 169, 184, 195, 196, and 215 m. Given that the dunites at Site CM1 are all more than 60% serpentinized, it is not clear what is meant by “serpentinite” in the log, but it may reflect more pale green-colored serpentinized dunite fragments rather than black altered dunite cuttings. No veins were recorded in the cuttings log.

Geochemistry: Hole CM1B

XRF analyses of cuttings, at 10 m intervals, were made at Sultan Qaboos University (SQU). These data are imprecise and inaccurate, and some values are entirely incorrect, whereas other values may perhaps have been attributed to the wrong element. Table **T3** in the **Introduction to Science Theme 3** chapter compares SQU analyses of 3 standards (2 peridotites and 1 Mg-rich basalt) with community accepted values and illustrates working curves based on these data for elements with a systematic difference between SQU and community values that can be used to correct the SQU analyses.

Table **T4** in the **Introduction to Science Theme 3** chapter presents SQU analyses of drill cuttings from Hole CM1B, together with approximate CIPW norms for these data. Four options are presented: (1) SQU quantitative analyses without correction, (2) corrected quantitative analyses, (3) SQU semiquantitative analyses without correction, and (4) corrected semiquantitative analyses. Corrected analyses used the working curves from Table **T3** in the **Introduction to Science Theme 3** chapter. In general, these data add little to our understanding of the lithologies in Hole CM1B.

Downhole measurements: Hole CM1B

Wireline logs were recorded by the University of Montpellier group using a slimline logging system and by Schlumberger Oil Services using oil-field type logging tools in January and March 2018 (Tables **T56** and **T57** in the **Methods** chapter). Because of partial blocking and collapse of the borehole at ~130 m below surface, logs from the upper gabbro section of the borehole only are available. The dual laterolog resistivity log shows values >1000 Z·m typical of gabbro, compared to very low values (<100 Z·m) of dunite. The spectral gamma log indicates very low K, U, and Th concentrations, with mostly K-rich alteration zones and a few Th-rich horizons at 115 and 118 m. Fluid electrical conductivity varies between 2759 µS/cm at 10 mbgl to 4865 µS/cm at 129 mbgl, whereas pH and redox potential change from 11.1 to 11.48 and 116 to –300 mV, respectively (**Supplementary material** > **L_Wireline logging**).

References

Arason, P., and Levi, S., 2010. Maximum likelihood solution for inclination-only data in paleomagnetism. Geophysical Journal International, 182:753–771.

Barrat, J.A., Zanda, B., Moynier, F., Bollinger, C., Liorzou, C., and Bayon, G., 2012. Geochemistry of CI chondrites: Major and trace elements, and Cu and Zn isotopes. Geochimica et Cosmochimica Acta, 83:79-92. https://doi.org/10.1016/j.gca.2011.12.011

Beard, J.S., Frost, B.R., Fryer, P., McCaig, A., Searle, R., Ildefonse, B., Zinin, P., and Sharma, S.K., 2009. Onset and progression of serpentinization and magnetite formation in Olivine-rich troctolite from IODP Hole U1309D. J. Petrol. 50:387–403.

Clark, R.N., and Roush, T.L., 1984. Reflectance Spectroscopy: Quantitative Analysis Techniques for Remote Sensing Applications. Journal of Geophysical Research, 89(B7):6329-6340. https://doi.org/10.1029/JB089iB07p06329

Donaldson, C.H., 1982. Origin of some of the Rhum harrisite by segregation of intercumulus liquid. Mineral. Mag., 45(337):201–209. https://doi.org/10.1180/minmag.1982.045.337.23

Elthon, D., 1991. Experimental phase petrology of mid-ocean ridge basalts. In Floyd, P.A. (Ed.), Oceanic basalts: New York (Blackie), 94–115.

Esteban, J.J., Cuevas, J., Tubía, J.M., and Yusta, I., 2003. Xonotlite in rodingite assemblages from the Ronda peridotites, Betic Cordilleras, Southern Spain. Can. Mineral., 41:161–170.

Feig, S., Koepke, J., and Snow, J., 2006. Effect of water on tholeiitic basalt phase equilibria: An experimental study under oxidizing conditions. Contributions to Mineralogy and Petrology, 152:611-638.

Feinberg, H., Horen, H., Michard, A., Saddiqi, O., 1999. Obduction-related remagnetization at the base of an ophiolite: Paleomagnetism of the Samail nappe lower sequence and of its continental substratum, southeast

Oman Mountains. Journal of Geophysical Research, 104(B8):17703–17714.

Frost, B.R, and Beard, J.S., 2007. On silica activity and serpentinization. J. Petrol., 48(7):1351–1368. https://doi.org/10.1093/petrology/egm021

Frost, B.R., Beard, J.S., McCaig, A., and Condliffe, E., 2008. The formation of microrodingites from IODP Hole U1309D: Key to understanding the process of serpentinization. J. Petrol., 49:1579–1588.

Frost, R., 1975. Contact metamorphism of serpentinite, chloritic blackwall and rodingite at Paddy- Go-Easy Pass, central Cascades, Washington. J. Petrol., 16(2):272–313. https://doi.org/10.1093/petrology/16.2.237

Früh-Green, G.L., Connolly, J.A.D., Plas, A., Kelley, D.S., and Grobéty, B., 2004. Serpentinization of oceanic peridotites: Implications for geochemical cycles and biological activity. In Wilcock, W.S.D., Delong, E.D., Kelley, D.S., Baross, J.A., and Cary, S.C. (Eds.), The Subseafloor Biosphere at Mid-Ocean Ridges. Washington DC (American Geophysical Union), 119–136.

Gaetani, G.A., Grove, T.L., and Bryan, W.B., 1993. The influence of water on the petrogenesis of subduction-related igneous rocks. Nature, 365:332-334.

Gerbert-Gaillard, L., 2002. Caractérisation Géochimique des Péridotites de l'ophiolite d'Oman: Processus Magmatiques aux Limites Lithosphére/Asthénosphére. PhD Thesis (Universite´ Montpellier II-Sciences et Techniques du Languedoc).

Godard, M., Jousselin, D., and Bodinier, J.L., 2000. Relationships between geochemistry and structure beneath a paleospreading center: a study of the mantle section in the Oman ophiolite. Earth and Planetary Science Letters, 180(1-2):133-148. https://doi.org/10.1016/S0012-821X(00)00149-7

Hanghøj, K., Kelemen, P.B., Hassler, D., and Godard, M., 2010. Composition and genesis of depleted mantle peridotites from the Wadi Tayin Massif, Oman Ophiolite; major and trace element geochemistry, and Os isotope and PGE systematics. Journal of Petrology, 51(1-2):201-227. https://doi.org/10.1093/petrology/egp077

Honnorez, J., and Kirst, P., 1975. Petrology of rodingites from the equatorial Mid-Atlantic fracture zones and their geotectonic significance. Contrib. Mineral. Petrol., 49:233–257.

Jagoutz, E., Palme, H., Baddenhausen, H., Blum, K., Cendales, M., Dreibus, G., Spettel, B., Lorenz, V., and Wanke, H., 1979. The abundances of major, minor and trace elements in the earth's mantle as derived from primitive ultramafic nodules. Proc. Lunar Planet. Sci. Conf. 10th, 2031–2050.

Jousselin, D., Morales, L.F.G., Nicolle, M., Stephant, A., 2012. Gabbro layering induced by simple shear in the Oman ophiolite Moho transition zone. Earth Planet. Sci. Lett., 331:55–66. https://doi.org/10.1016/j.epsl.2012.02.022

Kahl, W.A., Jöns, N., Bach, W., Klein, F., and Alt, J.C., 2015. Ultramafic clasts from the South Chamorro serpentine mud volcano reveal a polyphase serpentinization history of the Mariana forearc mantle. Lithos, 227:99–147.

Kelemen, P.B., Kikawa, E., Miller, D.J., et al., 2004. Proc. ODP, Init. Repts., 209: College Station, TX (Ocean Drilling Program). https://doi.org/10.2973/odp.proc.ir.209.2004

Khedr, M.Z., Arai, S., Python, M., Tamura, A., 2014. Chemical variations of abyssal peridotites in the central Oman ophiolite: evidence of oceanic mantle heterogeneity. Gondwana Research, 25(3):1242-1262. https://doi.org/10.1016/j.gr.2013.05.010

Klein, F., and Bach, W., 2009. Fe-Ni-Co-O-S phase relations in peridotite-seawater interactions. J. Petrol., 50:37–59.

Klein, F., Bach, W., Humphris, S.E., Kahl, W.-A., Jons, N., Moskowitz, B., and Berquo, T.S., 2014. Magnetite in seafloor serpentinite—Some like it hot. Geology, 42:135–138.

Koepke, J., France, L., Müller, T., Faure, F., Goetze, N., Dziony, W., and Ildefonse, B., 2011. Gabbros from IODP Site 1256 (Equatorial Pacific): Insight into axial magma chamber processes at fast-spreading ocean ridges. Geochemistry Geophysics Geosystems, 12. https://doi.org/10.1029/2011GC003655

Kokaly, R.F., Clark, R.N., Swayze, G.A., Livo, K.E., Hoefen, T.M., Pearson, N.C., Wise, R.A., Benzel, W.M., Lowers, H.A., Driscoll, R.L., and Klein, A.J., 2017. USGS Spectral Library Version 7. U.S. Geological Survey Data Series, 1035:61. https://doi.org/10.3133/ds1035

Korenaga, J., and Kelemen, P.B., 1997. Origin of gabbro sills in the Moho transition zone of the Oman ophiolite: implications for magma transport in the oceanic lower crust. J. Geophys. Res., 102:27729–27749. https://doi.org/10.1029/97JB02604

Lurcock, P.C., and Wilson, G.S., 2012. PuffinPlot: A versatile, user-friendly program for paleomagnetic analysis. Geochemistry, Geophysics, Geosystems, 13(Q06Z45).

MacLeod, C.J., Lissenberg, C.J., and Bibby, L.E., 2013. "Moist MORB" axial magmatism in the Oman ophiolite: The evidence against a mid-ocean ridge origin. Geology, 41:459-462.

Mellini, M., and Zanazzi, P.F., 1987. Crystal structures of lizardite-1T and lizardite-2H1 from Coli, Italy. American Mineralogist, 72:943-948.

Monnier, C., Girardeau, J., Le Mée, L., and Polvé, M., 2006. Along-ridge petrological segmentation of the mantle in the Oman ophiolite. Geochemistry, Geophysics, Geosystems, 7(11). https://doi.org/10.1029/2006GC001320

Mueller, T., Koepke, J., Garbe-Schonberg, C.D., Dietrich, M., Bauer, U., and Wolff, P.B., 2017. Anatomy of a frozen axial melt lens from a fast-spreading paleoridge (Wadi Gideah, Oman ophiolite). Lithos, 272:31-45.

Nicolle, M., Jousselin, D., Reisberg, L., Bosch D., and Stephant A., 2016. Major and trace element and Sr and Nd isotopic results from mantle diapirs in the Oman ophiolite: implications for offaxis magmatic processes. Earth Planet. Sci. Lett., 437:138–149.

O'Driscoll, B., Donaldson, C.H., Troll, V.R., Jerram, D.A., and Emeleus, C.H., 2007. An origin for harrisitic and granular olivine in the Rum Layered Suite, NW Scotland: a crystal size distribution study. J. Petrol., 48(2):253–270. https://doi.org/10.1093/petrology/egl059

Pallister, J.S., and Hopson, C.A., 1981. Samail ophiolite plutonic suite: field relations, phase variation, cryptic variation and layering, and a model of a spreading ridge magma chamber. J. Geophys. Res.: Solid Earth, 86(B4):2593–2644. https://doi.org/10.1029/JB086iB04p02593

Perneder, L., 2018. Scratch test report strength and ultrasonic logging JAMSTEC-P004W. EPSLOG S.A.

Python, M., Ceuleneer, G., Ishida, Y., Barrat, J.A., and Arai, S., 2007. Oman diopsidites: A new lithology diagnostic of very high temperature hydrothermal circulation in mantle peridotite below oceanic spreading centres. Earth and Planetary Science Letters, 255:289–305. https://doi.org/10.1016/j.epsl.2006.12.030

Python, M., Yoshikawa, M., Shibata, T., and Arai, S., 2011. Diopsidites and rodingites: Serpentinisation and Ca-metasomatism in the Oman Ophiolite Mantle. In Srivastava, R.K. (Ed.), Dyke Swarms: Keys for Geodynamic Interpretation: 401. https://doi.org/10.1007/978-3-642-12496-9_23

Rospabé, M., Benoit, M., Ceuleneer, G., Hodel, F., and Kaczmarek, M.-A., 2018. Extreme geochemical variability through the dunitic transition zone of the Oman ophiolite: Implications for melt/fluid-rock reactions at Moho level beneath oceanic spreading centers. Geochimica et Cosmochimica Acta, 134:1-23.

Sun, S.-s., and McDonough, W.F., 1989. Chemical and isotopic systematics of oceanic basalts: implications for mantle composition and processes. Geological Society, London, Special Publication 42:313-345. https://doi.org/10.1144/GSL.SP.1989.042.01.19

Takazawa, E., Okayasu, T., and Satoh, K., 2003. Geochemistry and origin of the basal lherzolites from the northern Oman ophiolite (northern Fizh block). Geochemistry, Geophys. Geosystems, 4.

Wicks, F.J., Whittaker, E.J.W., and Zussman, J., 1977. An idealized model for serpentine textures after olivine. Can. Mineral., 15:446–458.

Figure F1. Photograph showing the CM1 drill site during coring operations at Hole CM1A, looking southeast from the hillside. Hole CM1B borehole was drilled a few weeks later, ~10 m south of Hole CM1A.

Figure F2. Pie charts showing (**A**) unit and subunit count (**B**) and cumulative unit thickness, Hole CM1A.

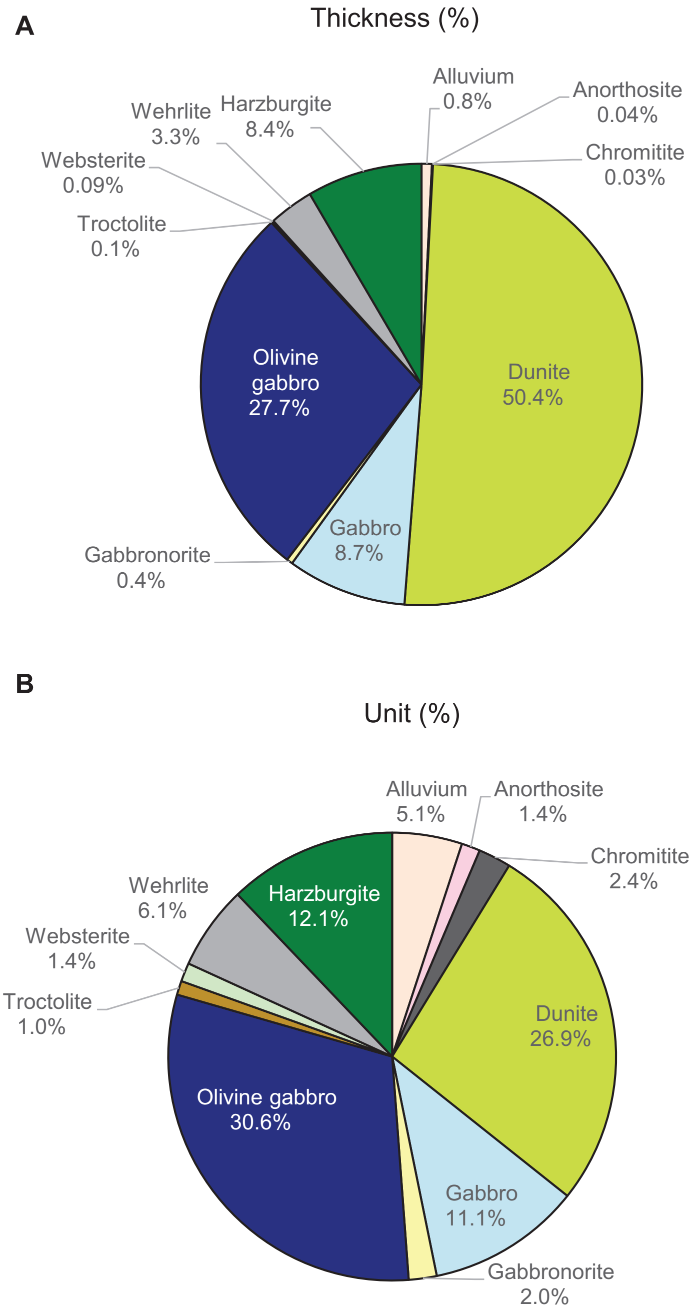

Figure F3. Lithostratigraphic column, sequences, and depth logs for mode (olivine, spinel, plagioclase, clinopyroxene, orthopyroxene), grain size (GS), and layer thickness (LT), Hole CM1A.

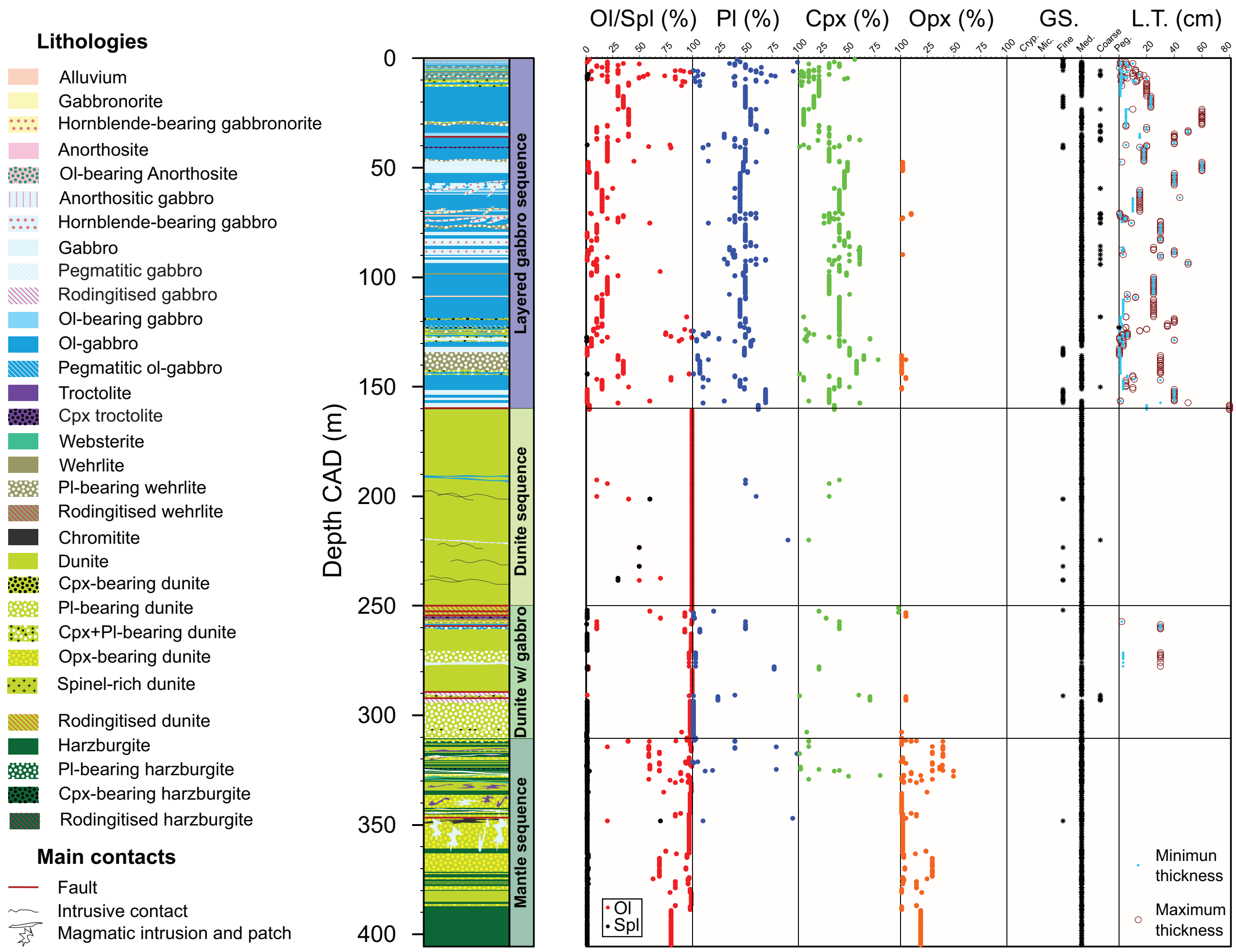

Figure F4. Lithostratigraphic column and pie charts showing the unit and subunit count and the corresponding cumulative thickness for the 4 lithologic sequences defined in Hole CM1A: (**A**) Layered Gabbro Sequence, (**B**) Dunite Sequence, (**C**) Dunite with Gabbro Sequence, (**D**) Mantle Sequence.

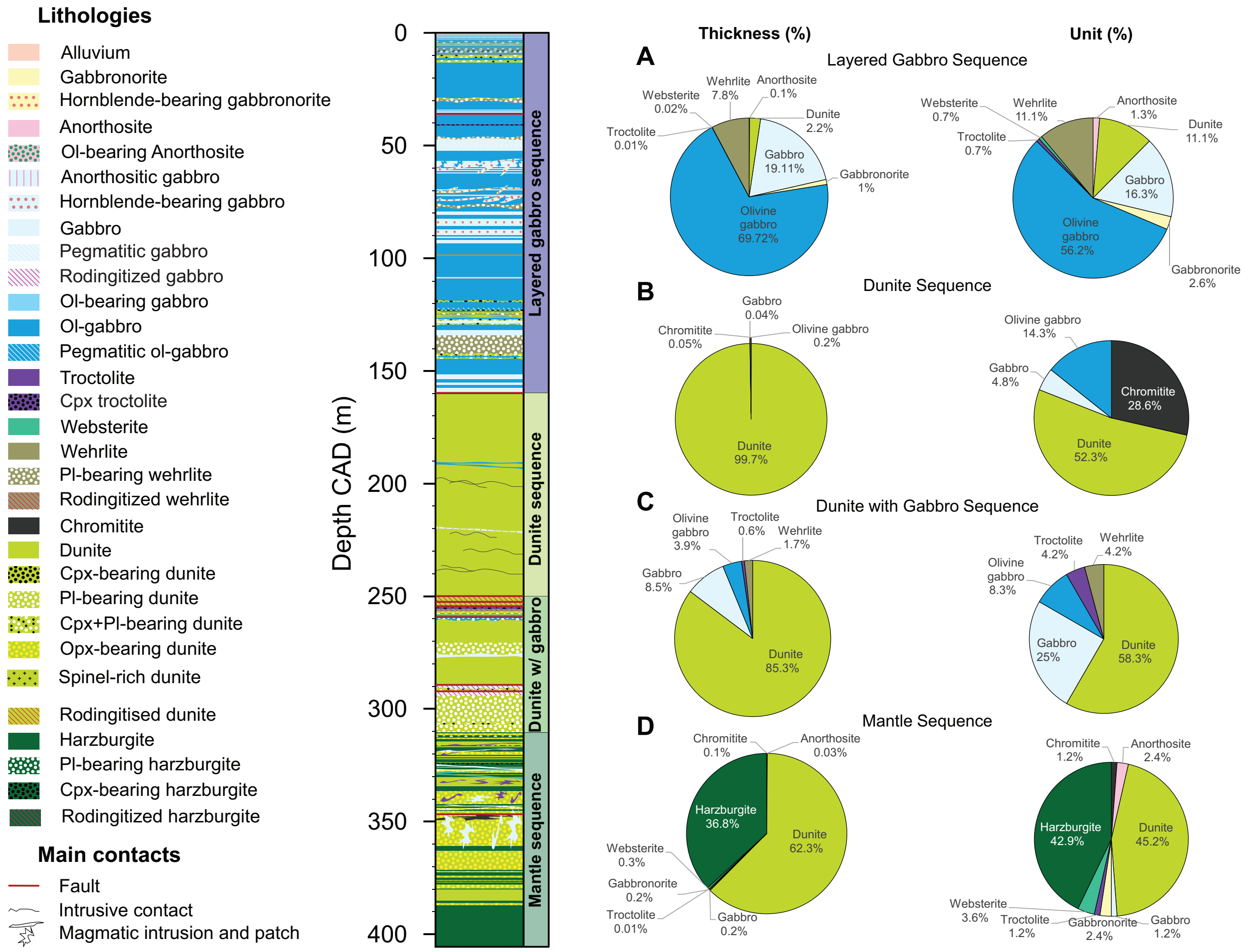

Figure F5. Typical dunites, Hole CM1A. **A.** Dunite in the Layered Gabbro Sequence now totally altered to serpentinite, displaying cumulate texture with a regular network of equant olivine grains with equigranular grain size distribution. Cr-spinel forms small interstitial grains on grain boundaries. **B.** Dunite in the Dunite Sequence with a thin chromitite band.

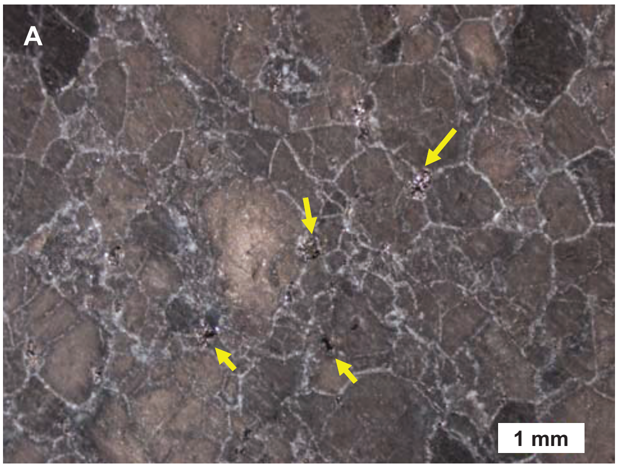

CM1A_128Z-1, 51-68 cm

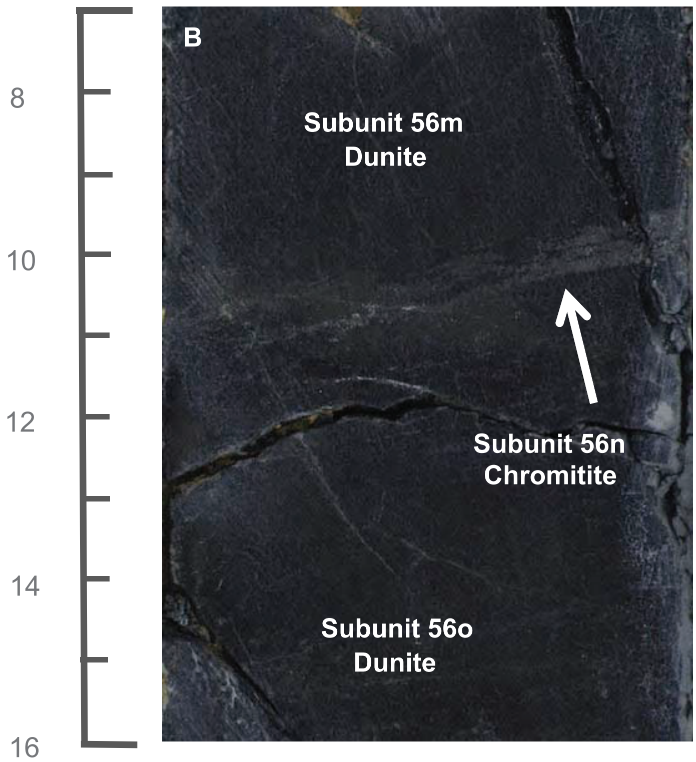

CM1A_96Z-3, 07-16 cm

Figure F6. Typical olivine gabbro and gabbro, Hole CM1A. **A.** Layered gabbro/olivine gabbro. **B.** Layered olivine gabbro. **C.** Weakly layered olivine gabbro with ~5 cm thick olivine-rich layer and >10 cm thick olivine-poor gabbro layers. **D.** Varitextured olivine gabbro with skeletal olivine. **E.** Isotropic gabbro with weak foliation but no modal layering. **F.** Non-layered gabbroic patch in wehrlite.

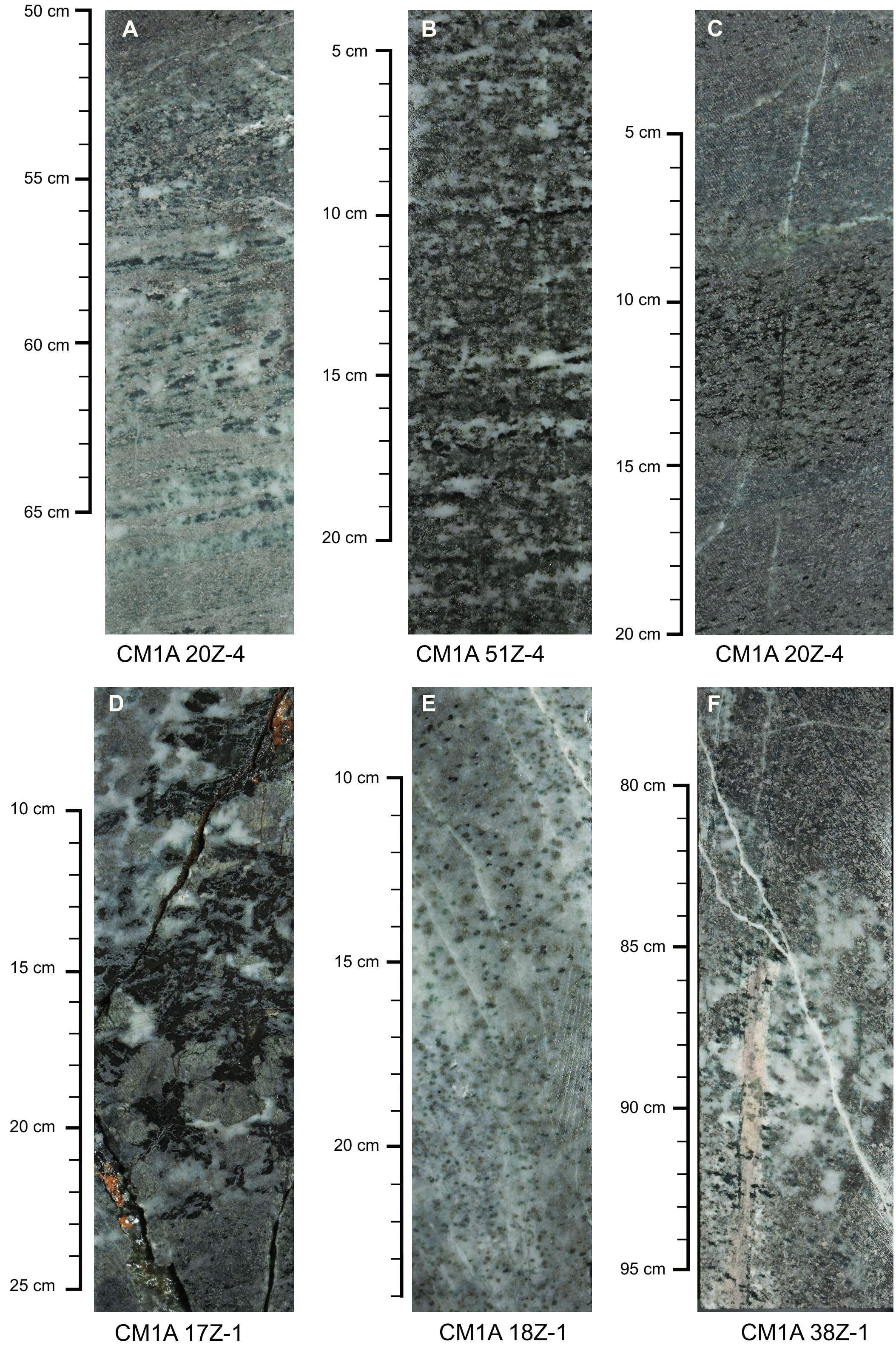

Figure F7. Typical harzburgite with porphyroclastic texture from the Mantle Sequence, Hole CM1A. **A.** Deformed orthopyroxene porphyroclasts as large as 6 mm in a darker olivine matrix can be easily observed by naked eye. **B.** Porphyroclastic texture defined by millimeter-sized orthopyroxene clasts crosscut by a set of white low-temperature alteration veins.

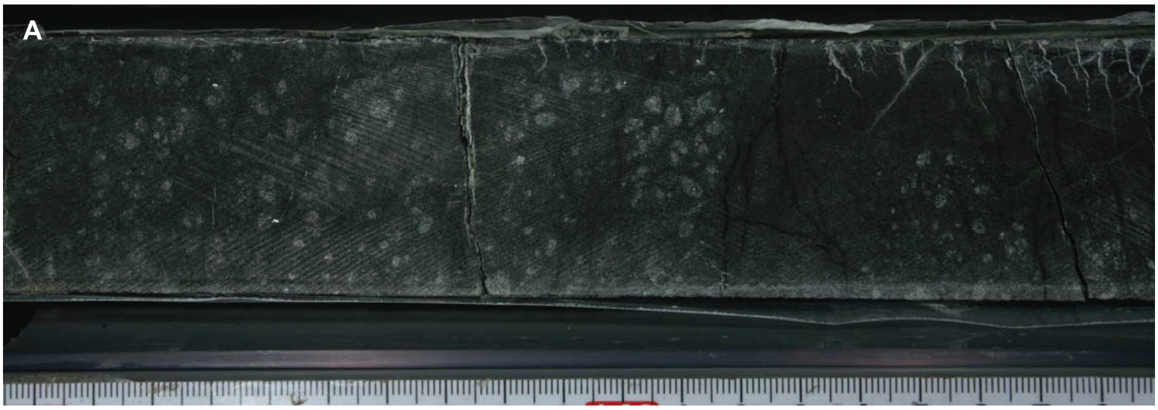

CM1A_163Z-3, 18-23 cm

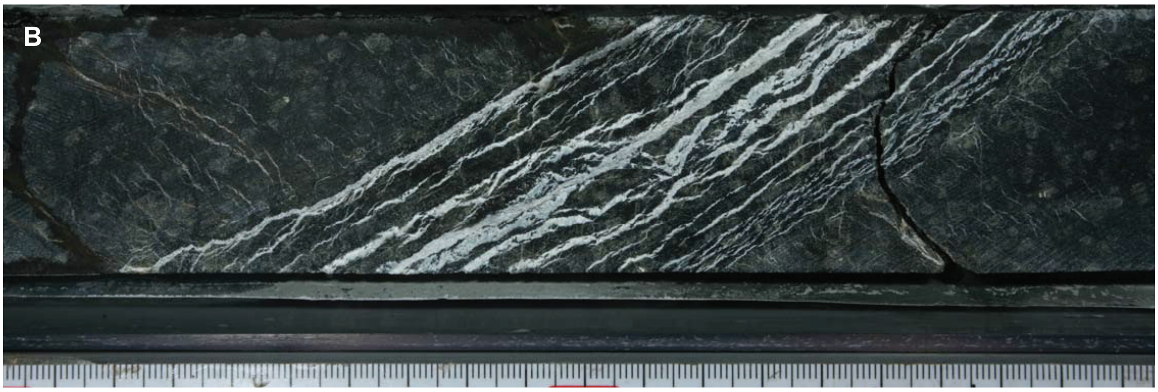

CM1A_177Z-3, 25-46 cm

Figure F8. Typical wehrlite, Hole CM1A, (plagioclase-bearing).

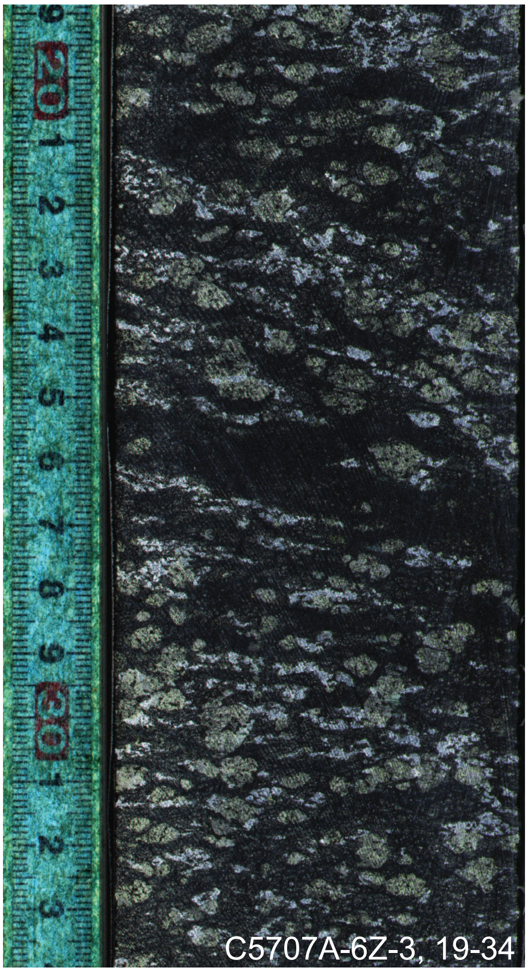

Figure F9. Typical examples of gabbronorite, Hole CM1A.

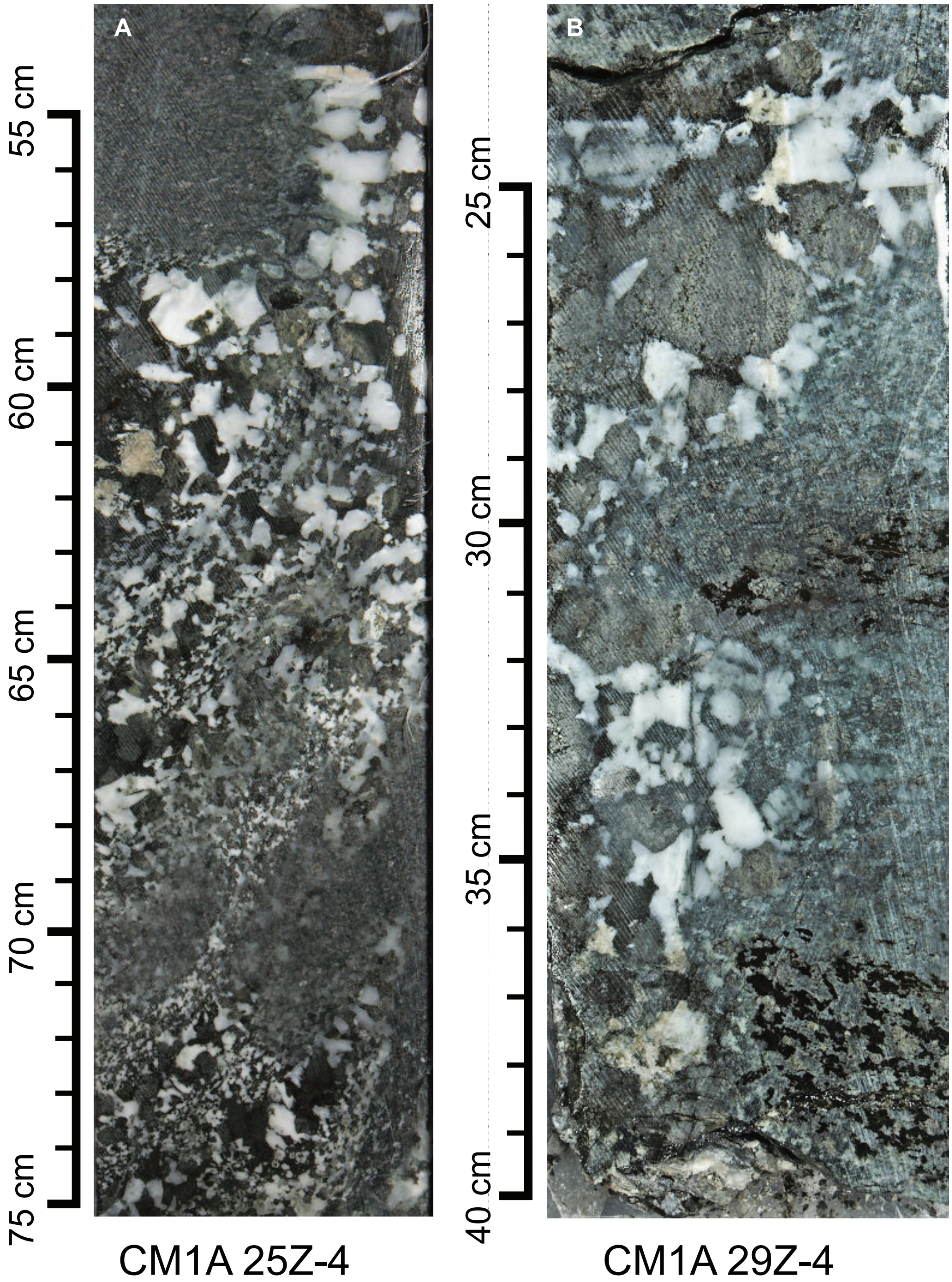

Figure F10. Typical clinopyroxene-bearing troctolite (69–70 cm), Hole CM1A.

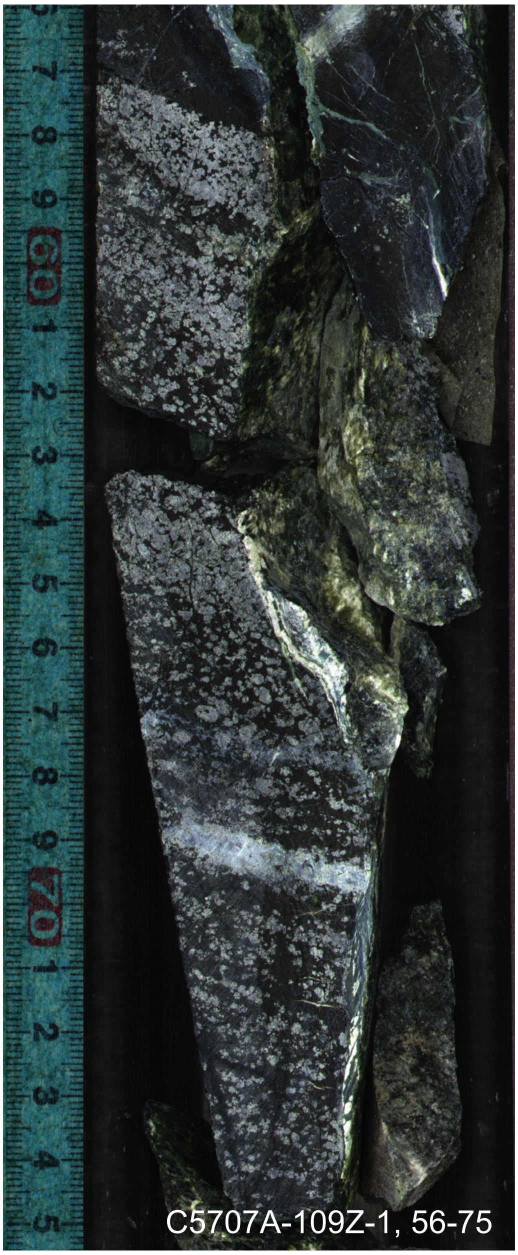

Figure F11. Typical example of websterite forming a 3 cm thick layer (20–23 cm) in plagioclase-bearing wehrlite, Hole CM1A.

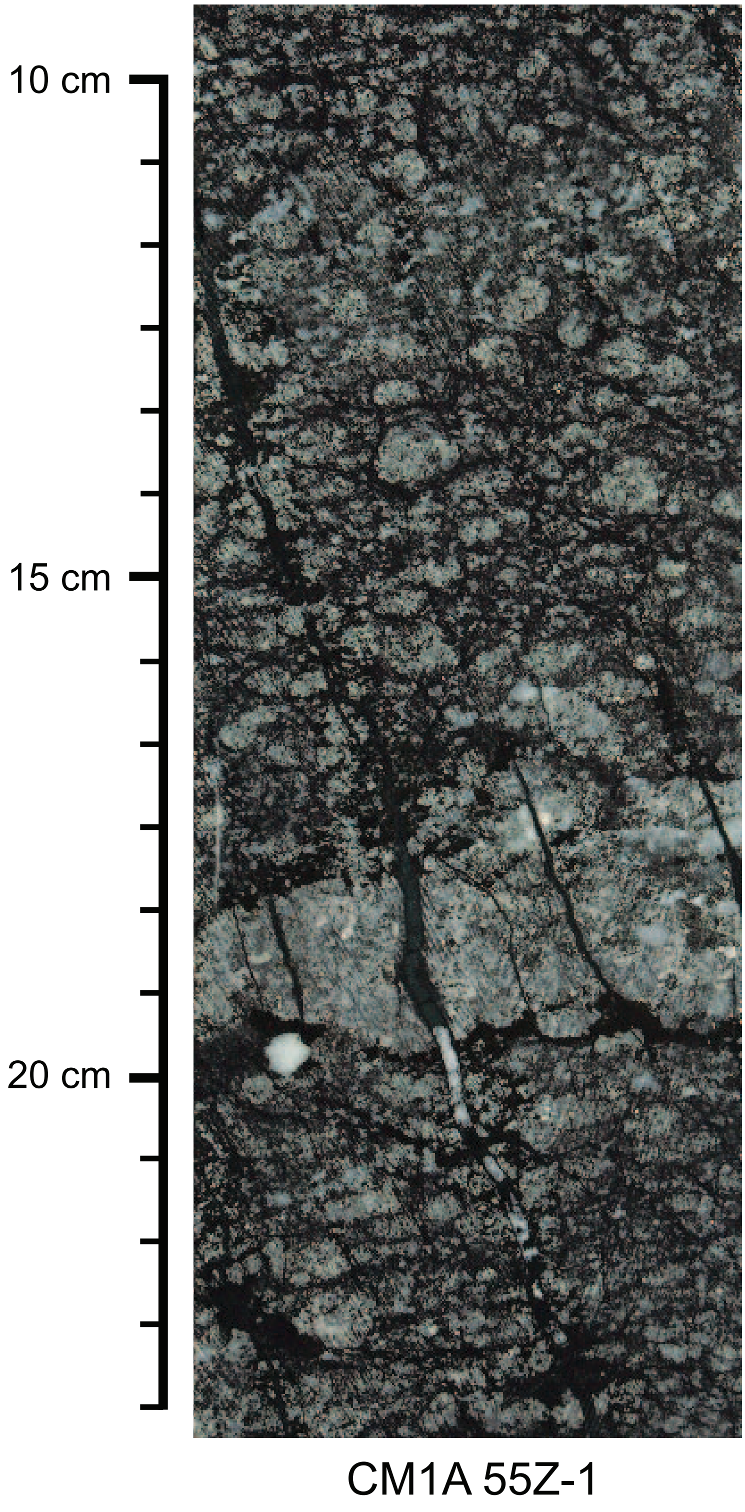

Figure F12. Typical (olivine-bearing) anorthosite bounded by olivine gabbro above and clinopyroxene-bearing dunite below (70–72 cm), Hole CM1A.

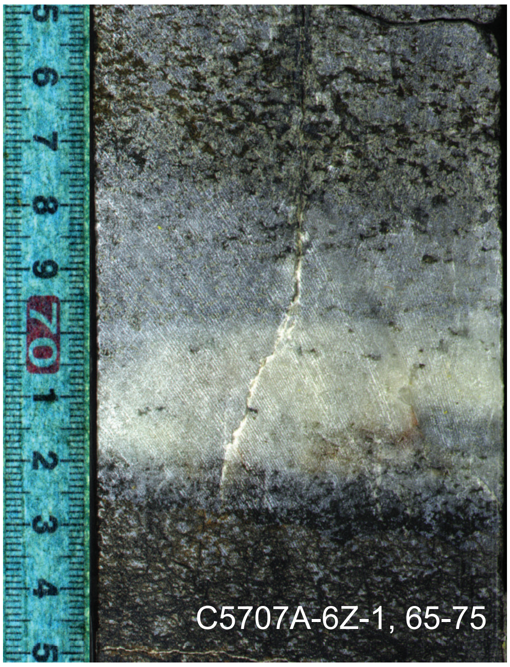

Figure F13. Selected layering features observed in Hole CM1A. **A.** Strong layering. **B.** Weak layering. **C.** Layered series from the Layered Gabbro Sequence. **D.** Layered series from the Dunite with Gabbro Sequence.

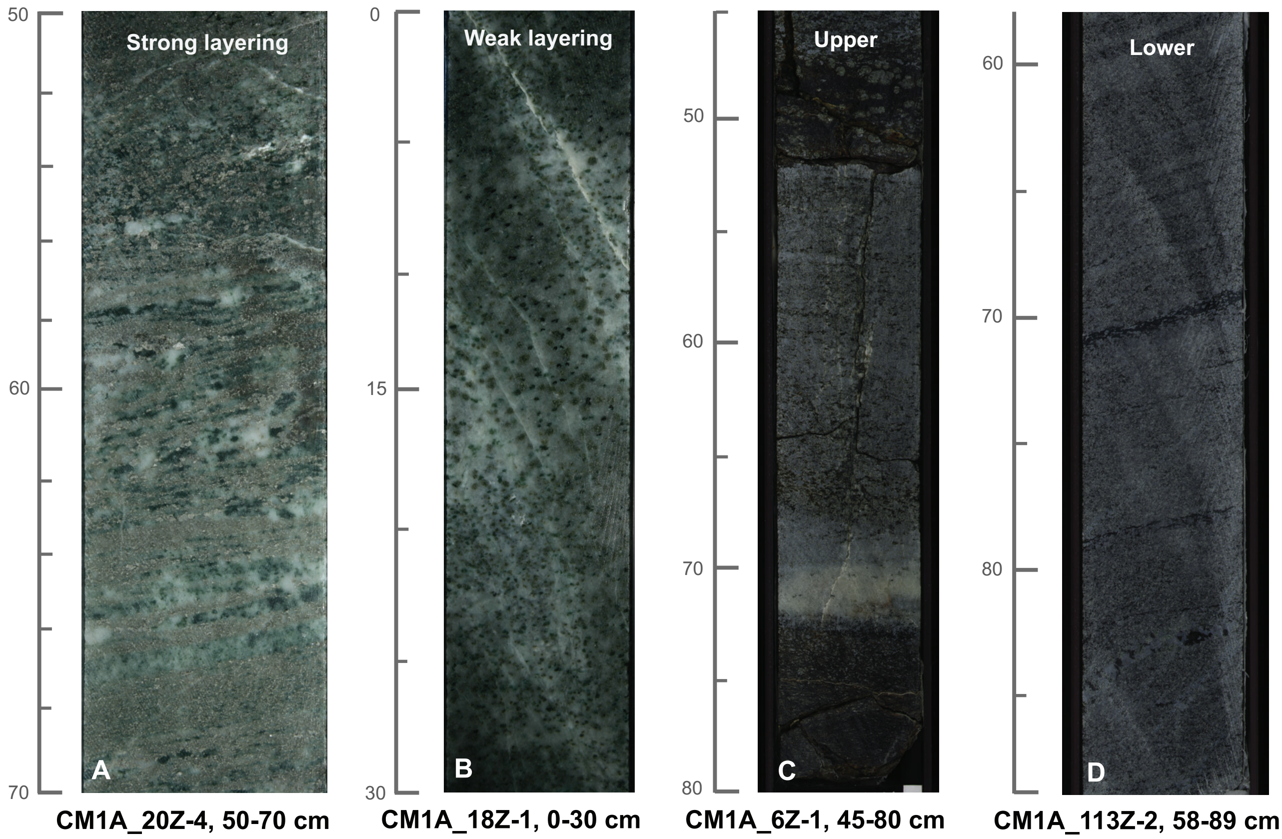

Figure F14. Selected contacts observed in Hole CM1A. **A.** Contact between olivine gabbro and plagioclase-bearing wehrlite. **B.** Contact between olivine gabbro and plagioclase-bearing dunite. **C.** Contact between gabbro and pegmatitic gabbro. **D.** Contact between dunite and olivine gabbro. **E.** Contact between two types of olivine gabbro. **F.** Contact between dunite and (mylonitic) gabbro.

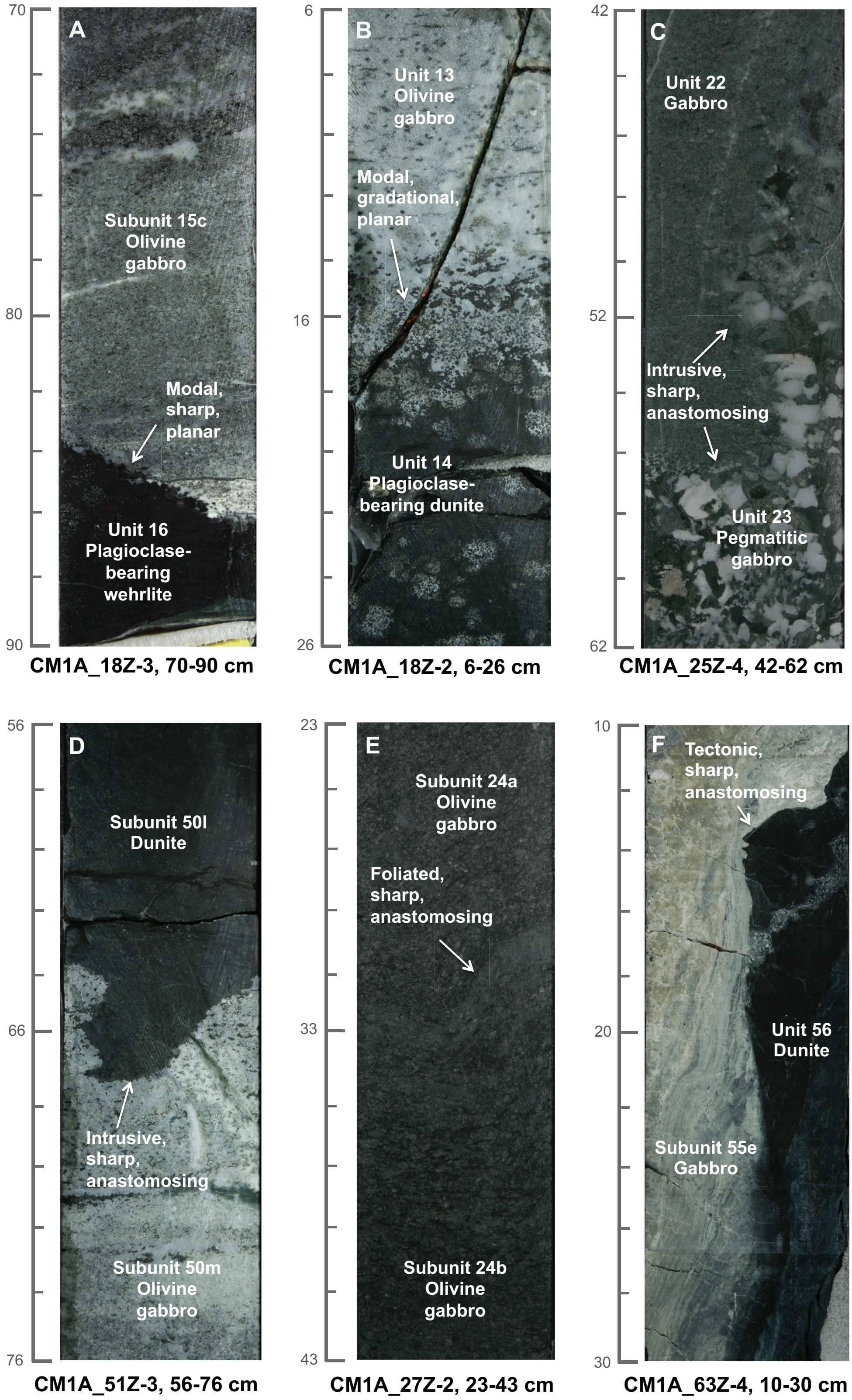

Figure F15. Contacts between the Dunite with Gabbro and Mantle Sequences. **A, C.** Typical dunite of the Dunite with Gabbro Sequence now totally altered to serpentinite with cumulate texture: regular network of equant olivine grains with equigranular grain size distribution and interstitial Cr-spinel (black, shiny grains). **B, D.** First dunite with typical mantle texture occurs ~17 cm downsection: dunite with relics of orthopyroxene porphyroclasts (yellow arrows), indicating the first appearance of true mantle rocks in Hole CM1A.

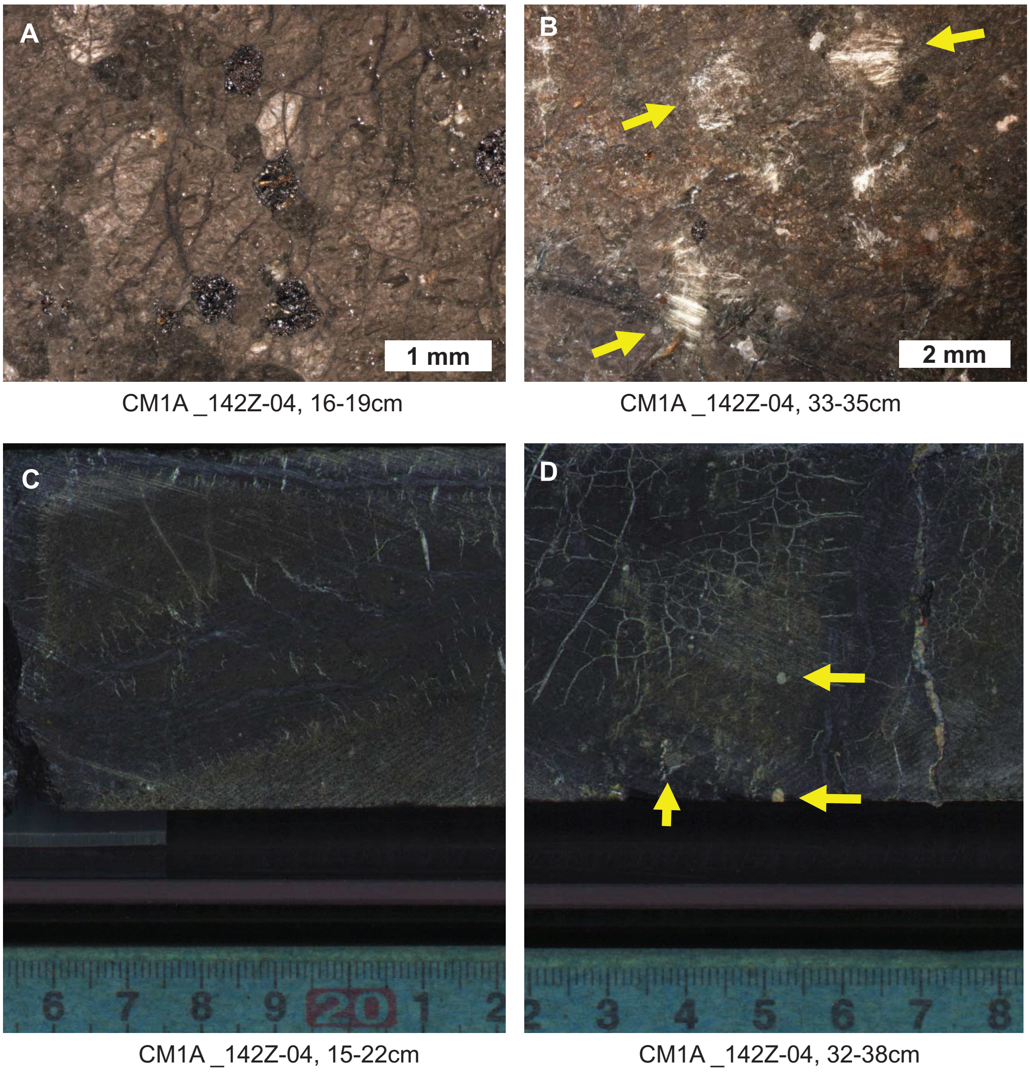

Figure F16. Typical dunite, Hole CM1A. (**A**) Whole thin section scan in plane polarized light (PPL). Red box indicates the position photomicrographs in (**B**) PPL and (**C**) cross-polarized light (XPL). Ol = olivine, Spl = spinel (mineral abbreviations are given in Table T5 in the **Methods** chapter).

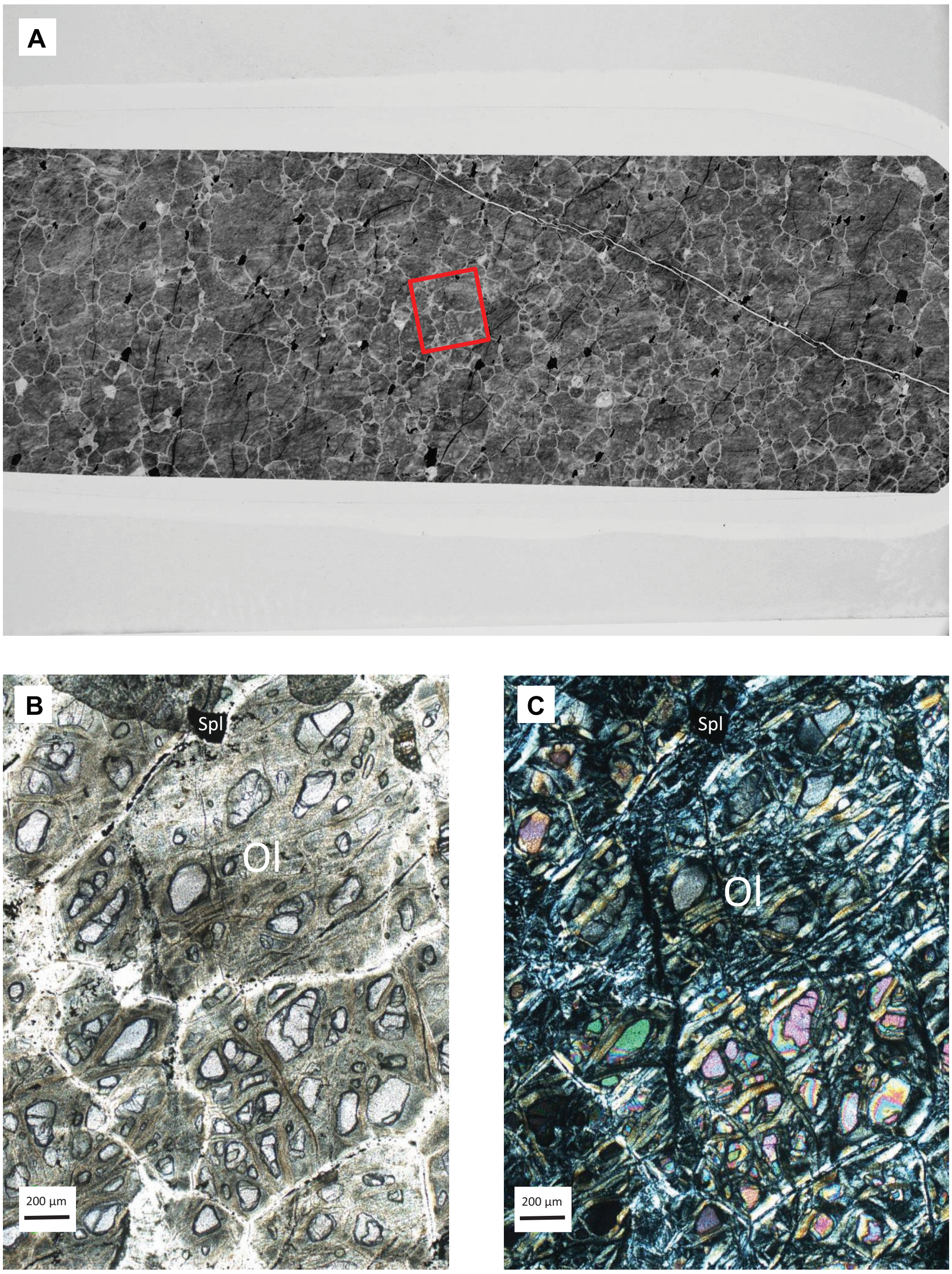

CM1A_142Z1_84-88 cm

Figure F17. Typical olivine gabbro, Hole CM1A. Cpx = clinopyroxene, Pl = plagioclase, Ol = olivine. (**A**) Whole thin section scan (PPL); (**B**) PPL, (**C**) XPL.

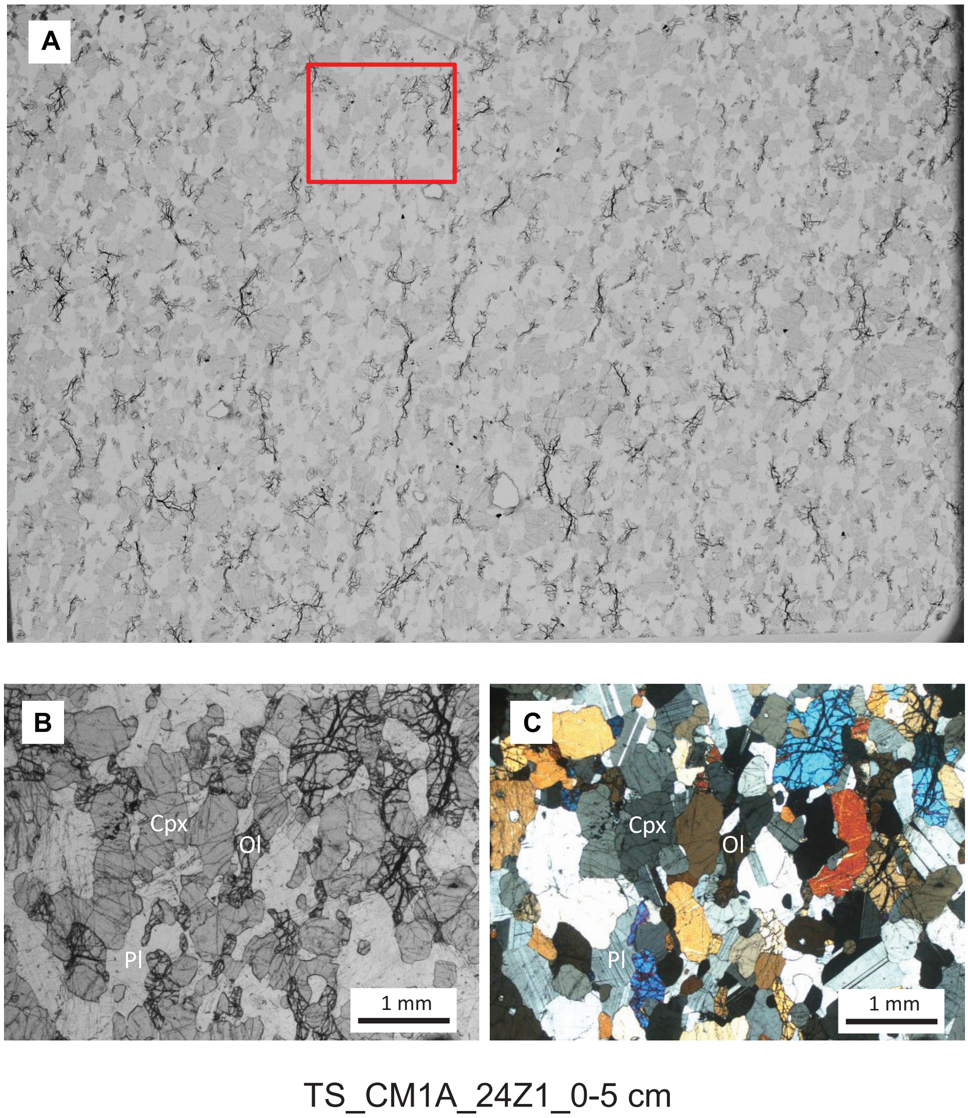

Figure F18. Typical gabbro, Hole CM1A. Cpx = clinopyroxene, Pl = plagioclase. (**A**) Whole thin section scan (PPL); (**B**) PPL, (**C**) XPL.

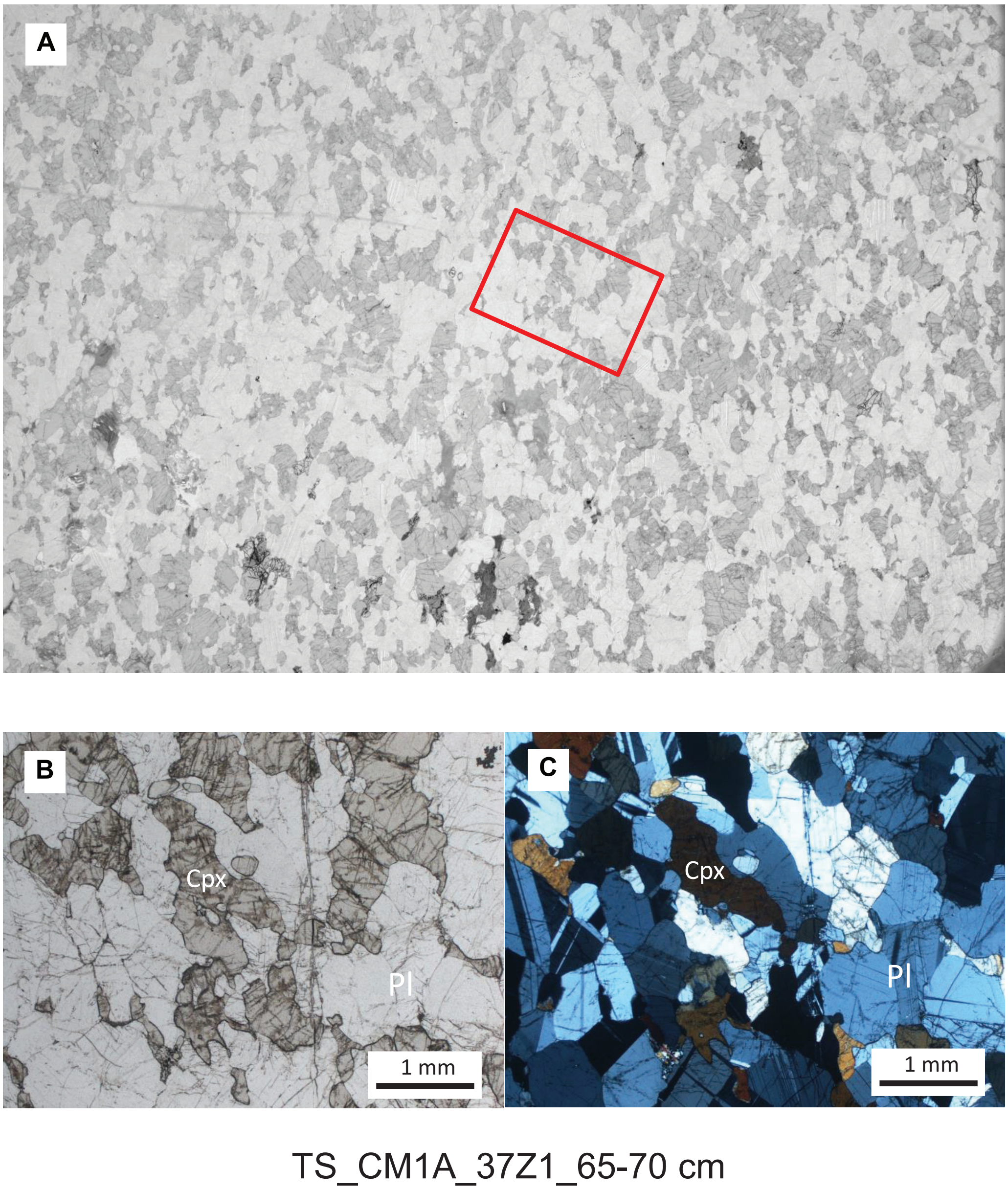

Figure F19. Typical harzburgite, Hole CM1A. Opx = orthopyroxene. **A.** Whole thin section scan (PPL). **B, C.** Plastically deformed orthopyroxene surrounded by neoblasts (arrows) (B: PPL, C: XPL).

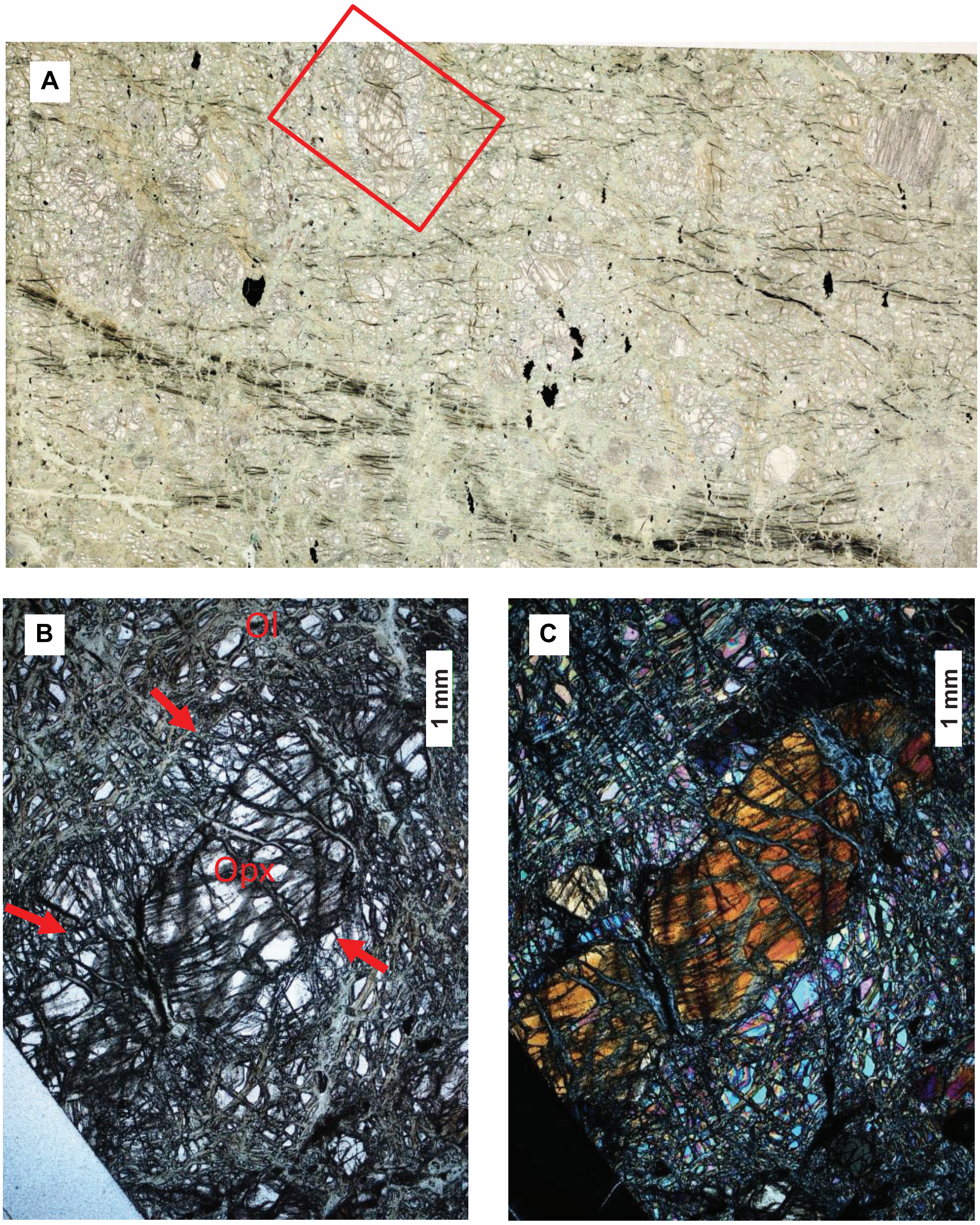

TS_CM1A_145_2_0_5

Figure F20. Typical wehrlite, Hole CM1A. Ol = olivine, Cpx = clinopyroxene. (**A**) Whole thin section scan (PPL); (**B**) PPL, (**C**) XPL.

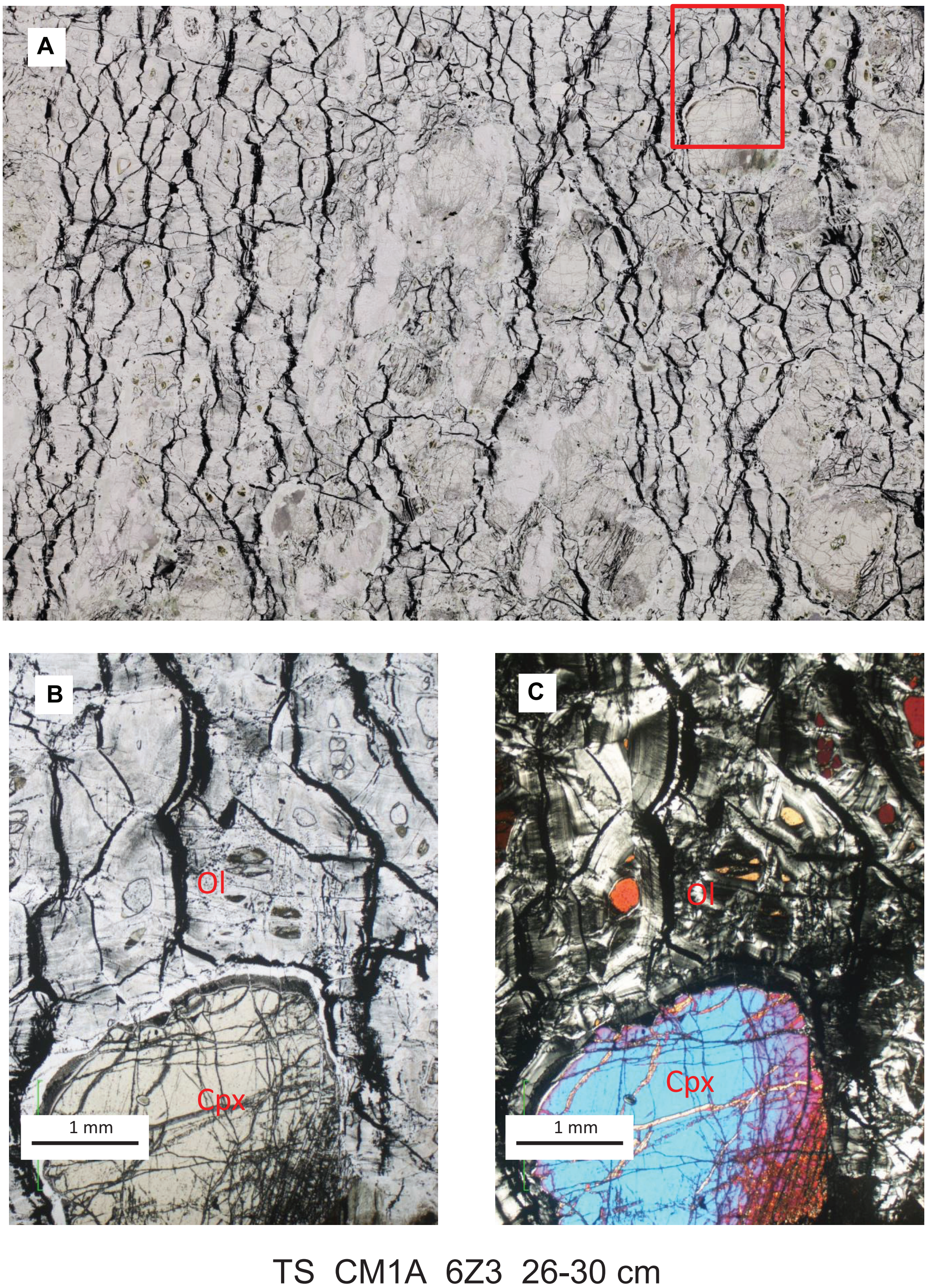

Figure F21. Typical troctolite, Hole CM1A. Ol = olivine, Pl = plagioclase. (**A**) Whole thin section scan (PPL); (**B**) PPL, (**C**) XPL.

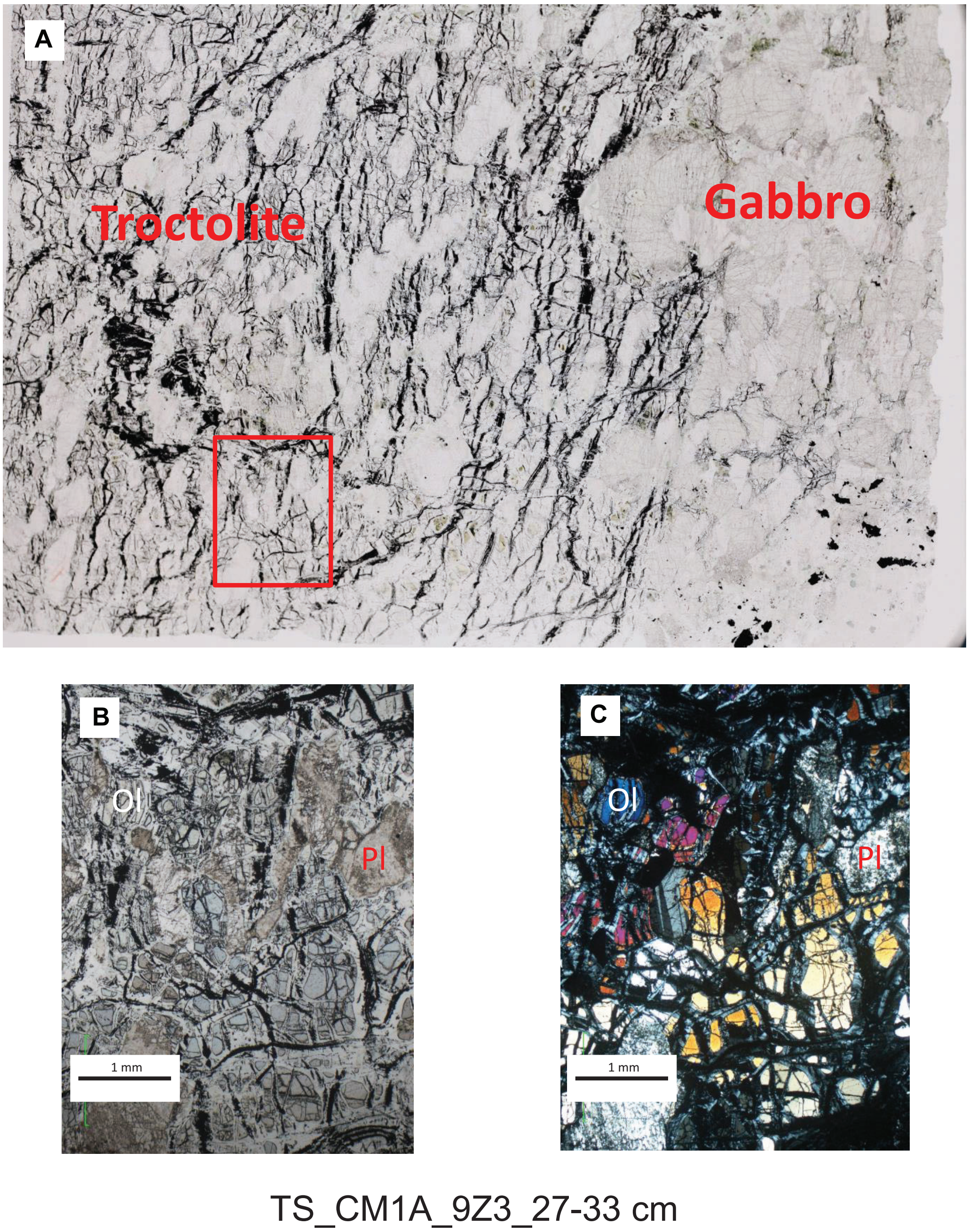

Figure F22. Typical anorthosite, Hole CM1A. Pl = plagioclase. (**A**) Whole thin section scan (PPL); (**B**) PPL, (**C**) XPL.

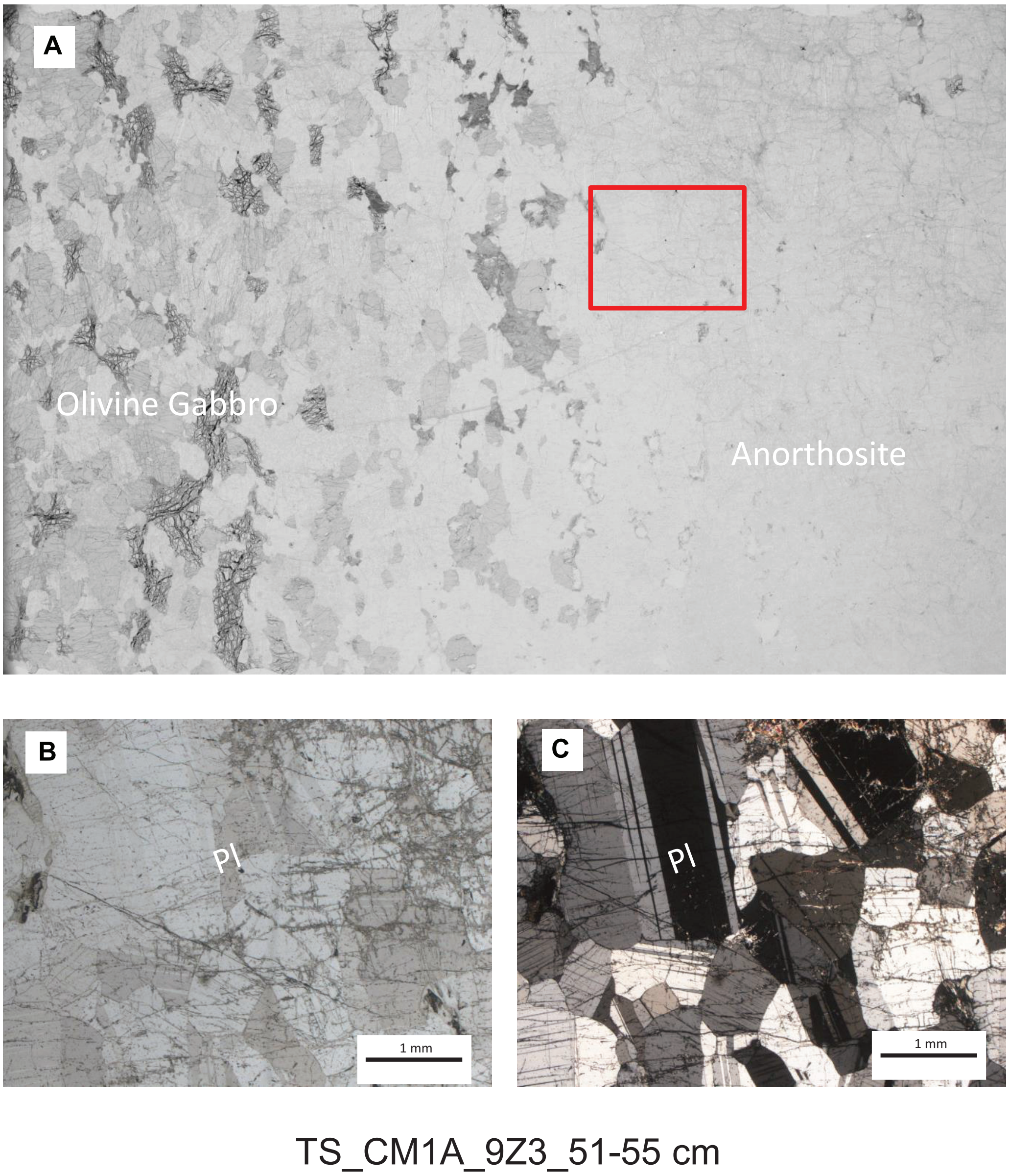

Figure F23. Dunite intruding gabbro, Hole CM1A. pl = plagioclase, ol = olivine, cpx = clinopyroxene. **A.** Core image showing intrusion relationship. **B.** Whole thin section scan (PPL). **C.** Incorporation of anhedral, interstitial olivine into the gabbro (PPL).

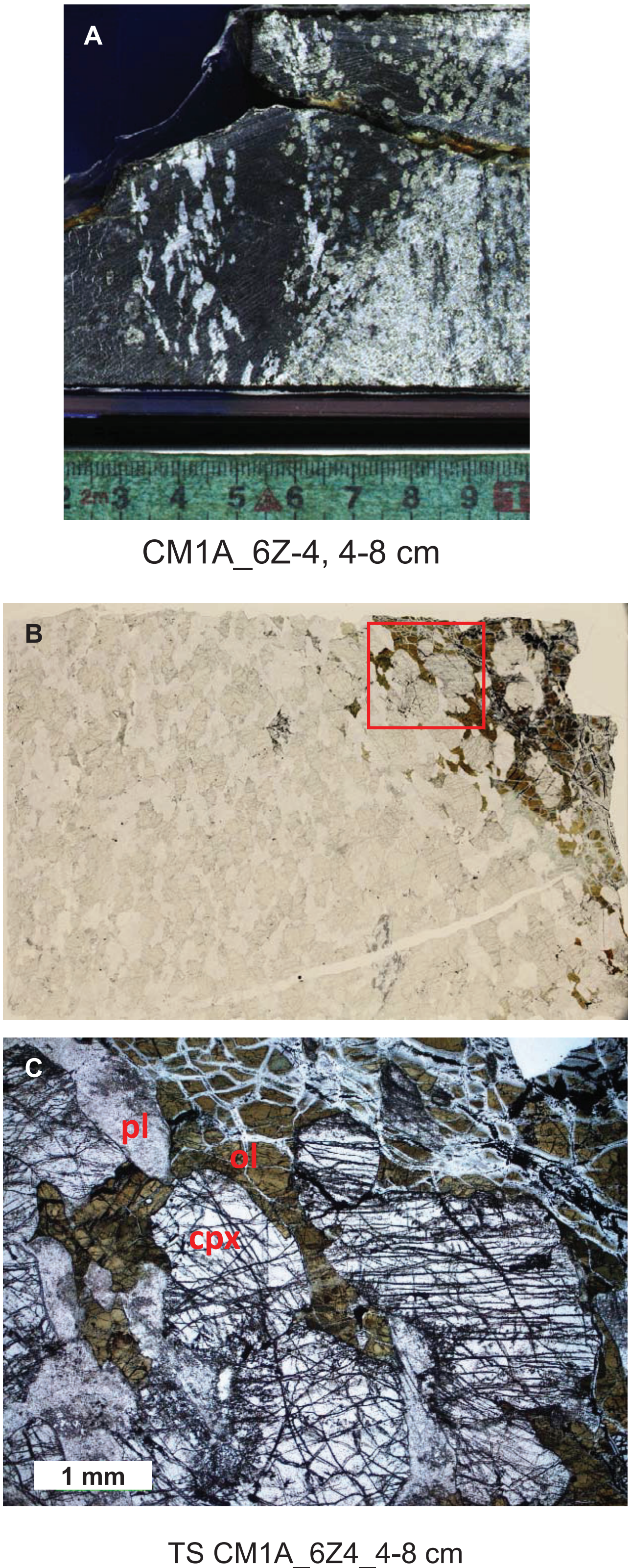

Figure F24. Olivine gabbro showing skeletal olivines implying fast crystal growth, Hole CM1A. ol = olivine, pl = plagioclase, cpx = clinopyroxene. **A.** Core image. **B, C.** Whole thin section scan (B: PPL, C: XPL). **D, E.** Anhedral skeletal feature of the olivine, now totally altered to serpentine (D: PPL, E: XPL).

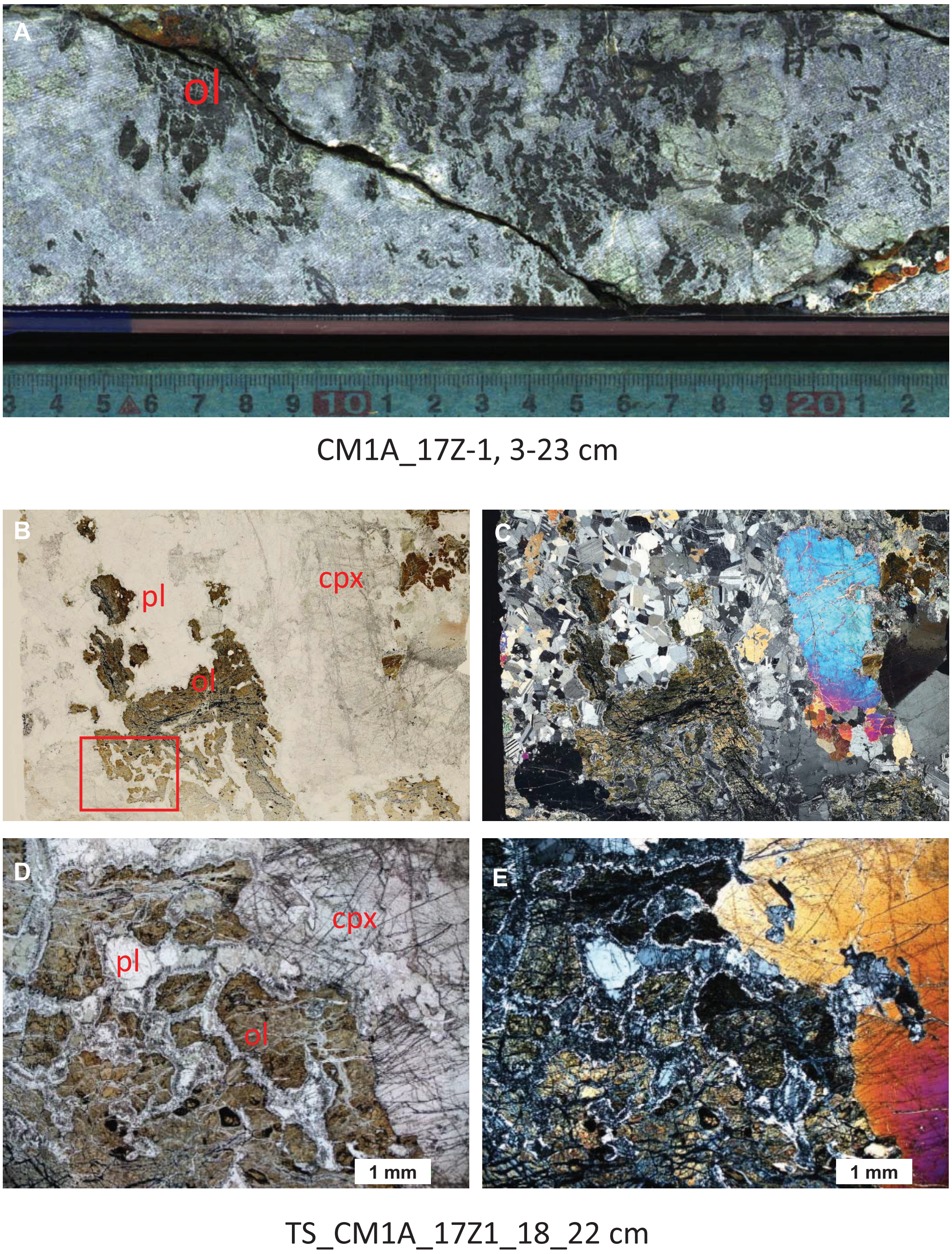

Figure F25. Dunite with poikilitic clusters of plagioclase and clinopyroxene, Hole CM1A. **A.** Core image. (**B**) Whole thin section scan with marked troctolitic and wehrlitic clusters (PPL).

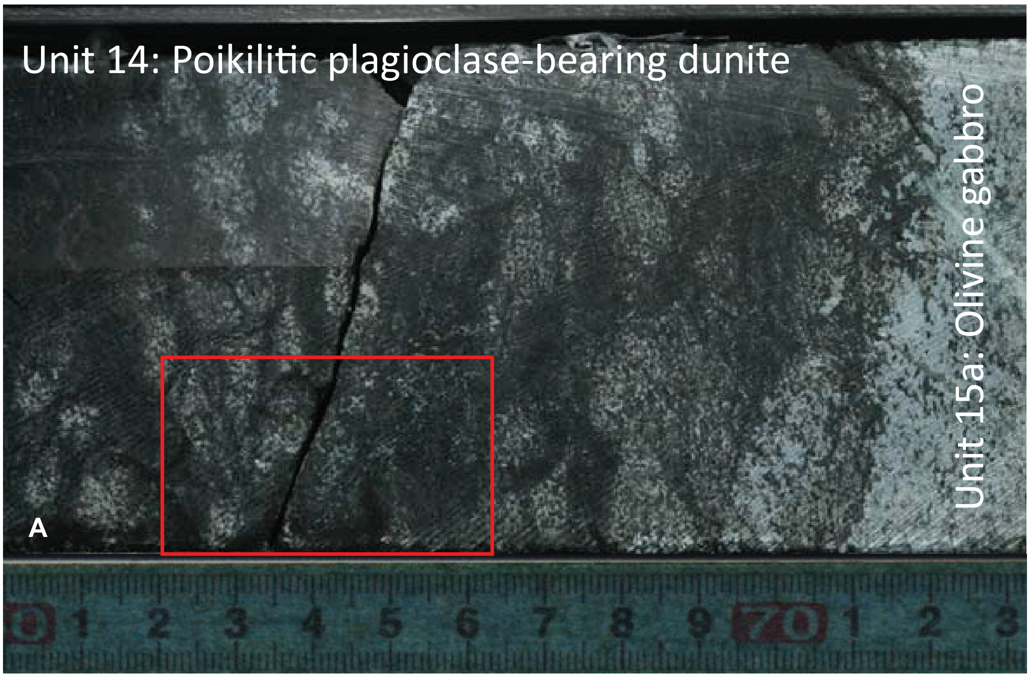

CM1A_18Z-2, 60_73 cm: dunite with poikilitic clusters of plagioclase or cpx

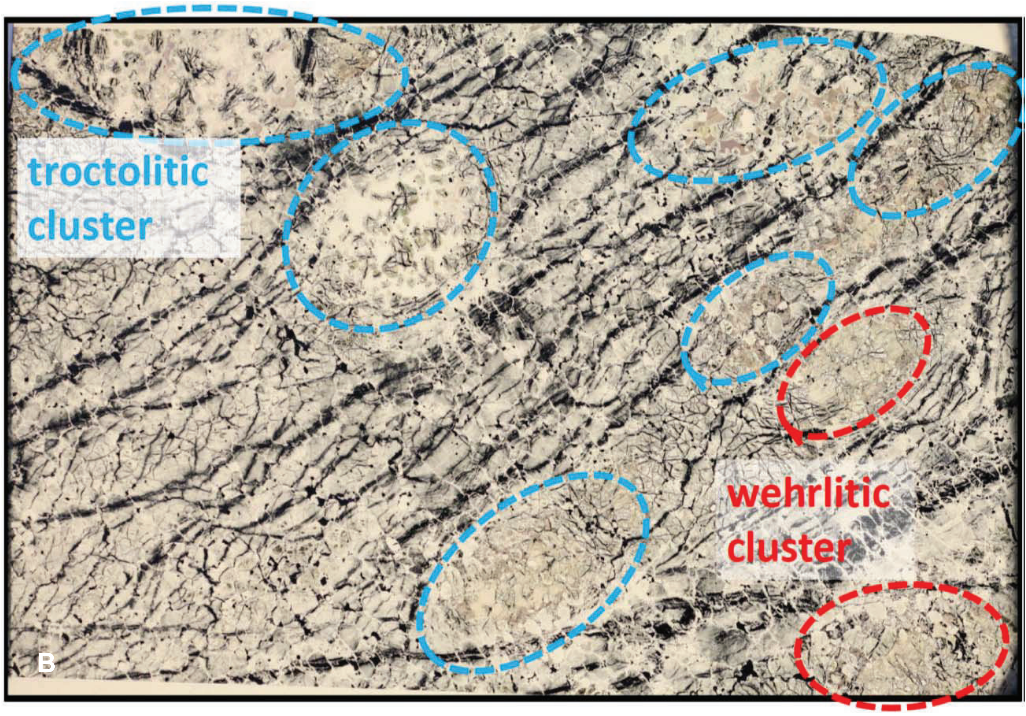

TS_CM1A_18Z2_62-67 cm: dunite with troctolitic and wehrlitic clusters

Figure F26. Dunite with troctolitic clusters (poikilitic plagioclase [pl] enclosing olivine [ol]) and wehrlitic clusters (poikilitic clinopyroxene [cpx] enclosing olivine), Hole CM1A. An overview is presented in Figure F25. **A, B.** Troctolitic cluster (A: PPL, B: XPL). **C, D.** Wehrlitic cluster (C: PPL, D: XPL). **E, F.** Dunitic matrix composed only of olivine (E: PPL, F: XPL).

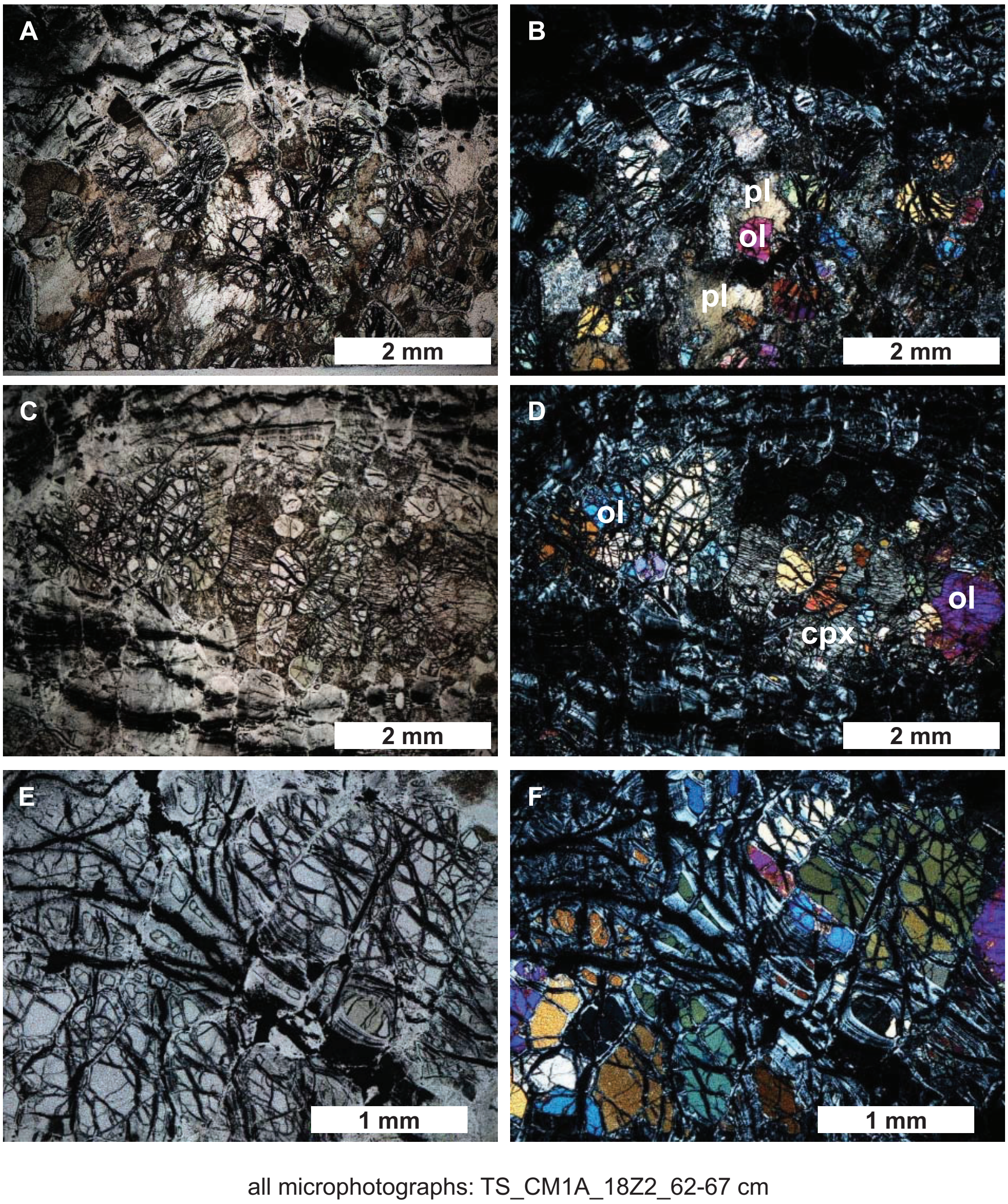

Figure F27. Phase diagram for primitive MORB as a function of water content in the melt illustrating the suppression of plagioclase crystallization with increasing water content (from Feig et al., 2006), Hole CM1A. Variable water contents may explain the early co-crystallization of plagioclase and clinopyroxene in a dunitic mush. Red arrow = plagioclase saturation curve, which is strongly deflected to lower temperature with increasing water content.

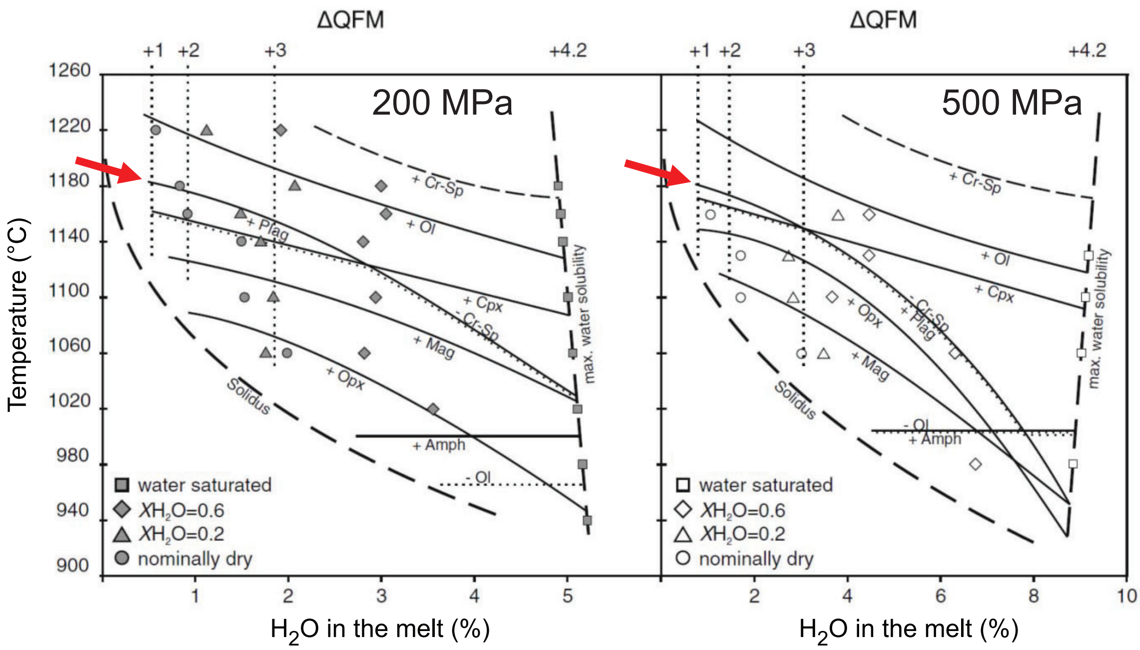

Figure F28. Gabbros bearing brown amphibole, Hole CM1A. **A, C.** PPL. **B, D.** XPL.

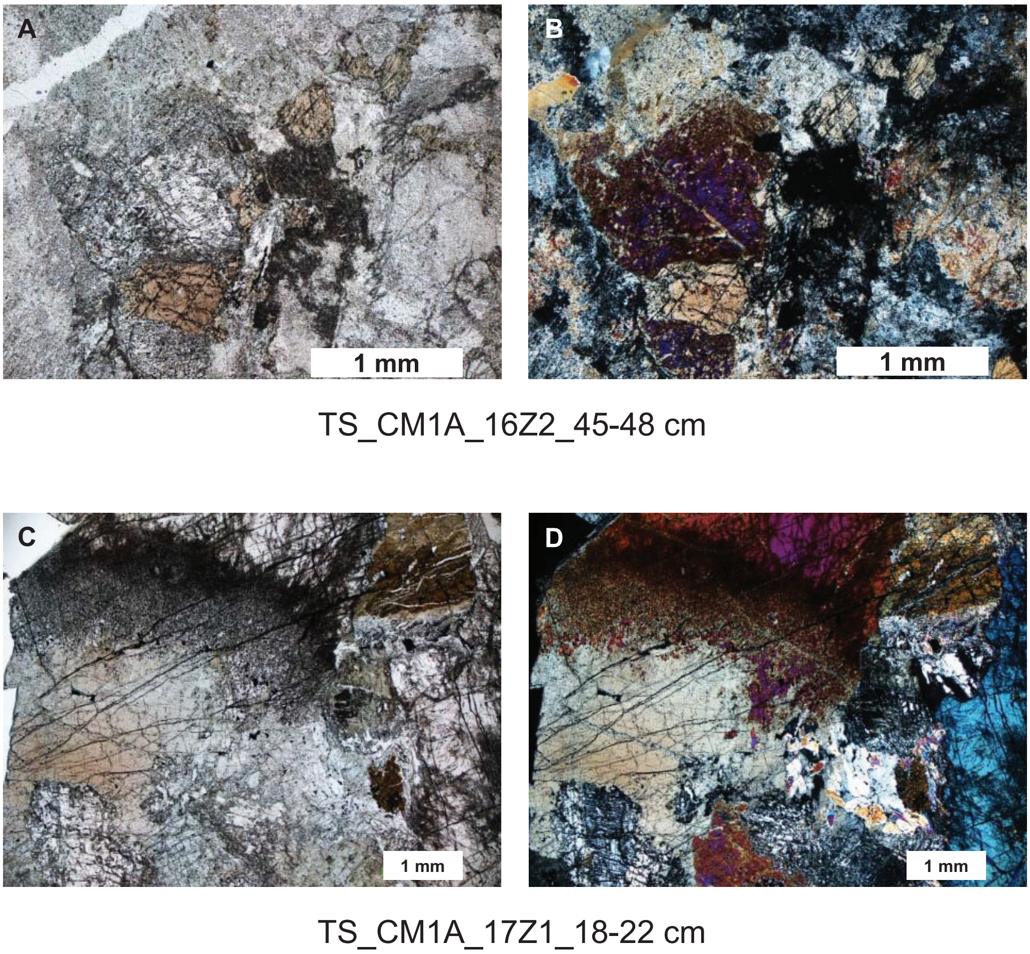

Figure F29. Relict textures of 12 massive dunites from the Layered Gabbro (1 sample), Dunite (5), Dunite with Gabbro (3), and Mantle (3) Sequences, Hole CM1A. Red arrows = relics of olivine in 2 samples; yellow arrows = tiny spinels as inclusions in olivine and on the boundaries between the (former) olivine crystals in 1 representative sample. See text for details.

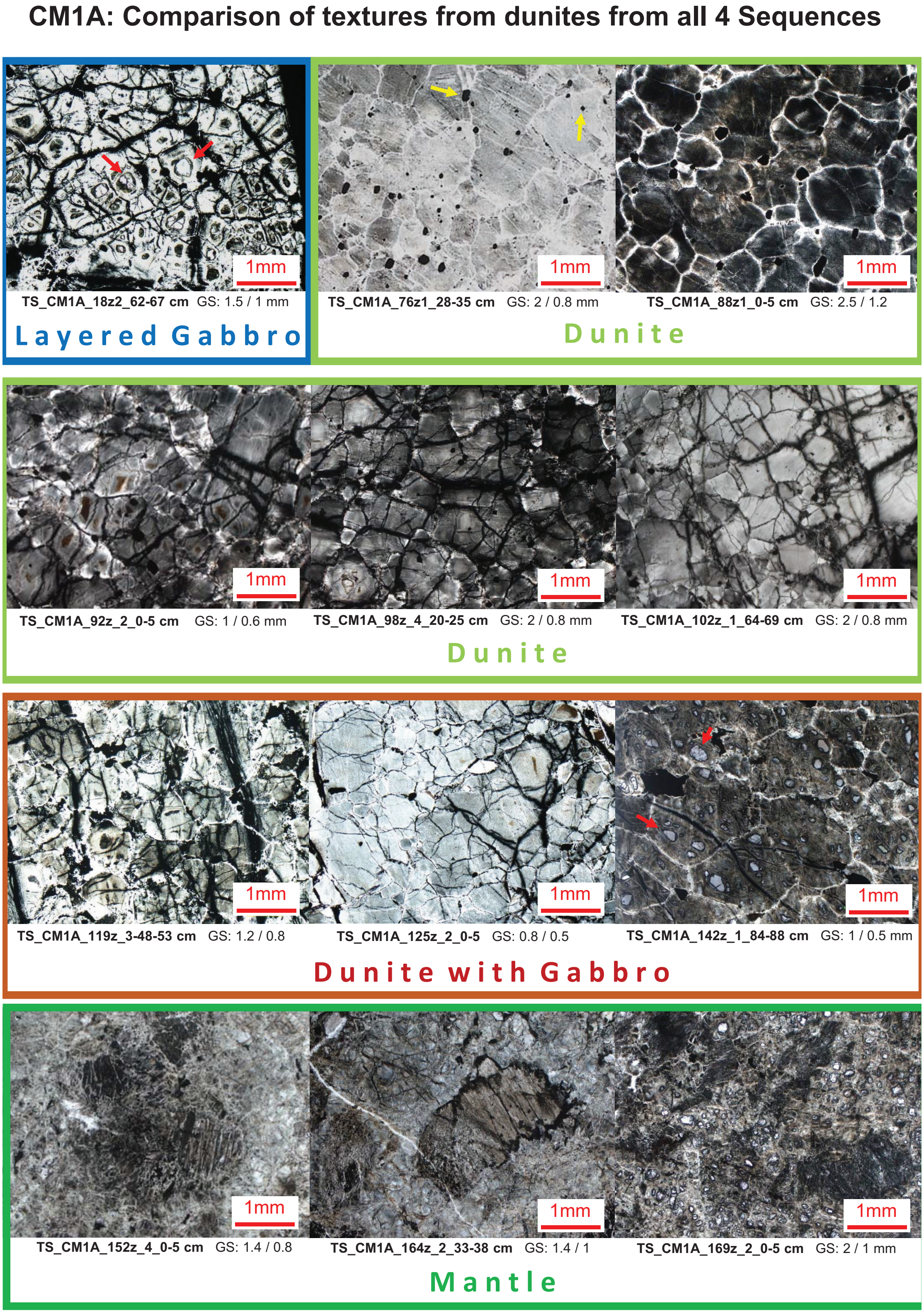

Figure F30. Downhole plots of (**A**) lithology, (**B**) total alteration intensity in the main lithologic groups, and (**C**) 10 m running average for background and total alteration intensity, Hole CM1A. Gabbro = gabbro, gabbronorite, and anorthosite, independent of minor phases or grain size. Olivine Gabbro = olivine gabbro, olivine-bearing gabbro, and troctolite. Rodingitized = gabbro, wehrlite, and dunite that show Ca-metasomatic alteration. Ultramafic = wehrlite, dunite, and harzburgite including varying minor phases. Other = chromitite and websterite.

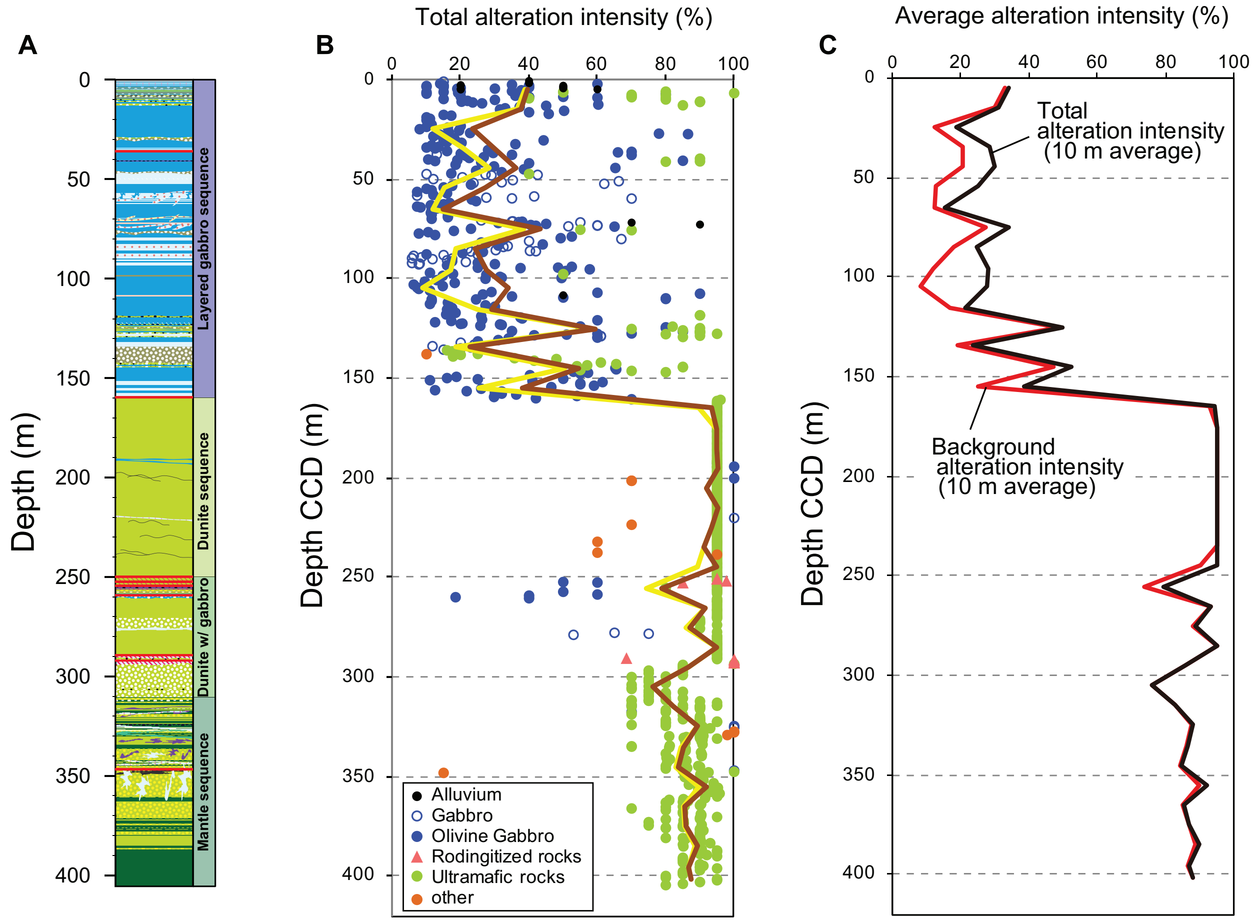

Figure F31. Histograms showing total alteration intensity and variations in background alteration intensity in the main lithologic sequences, Hole CM1A. Main lithologic groups as defined in Figure F2.

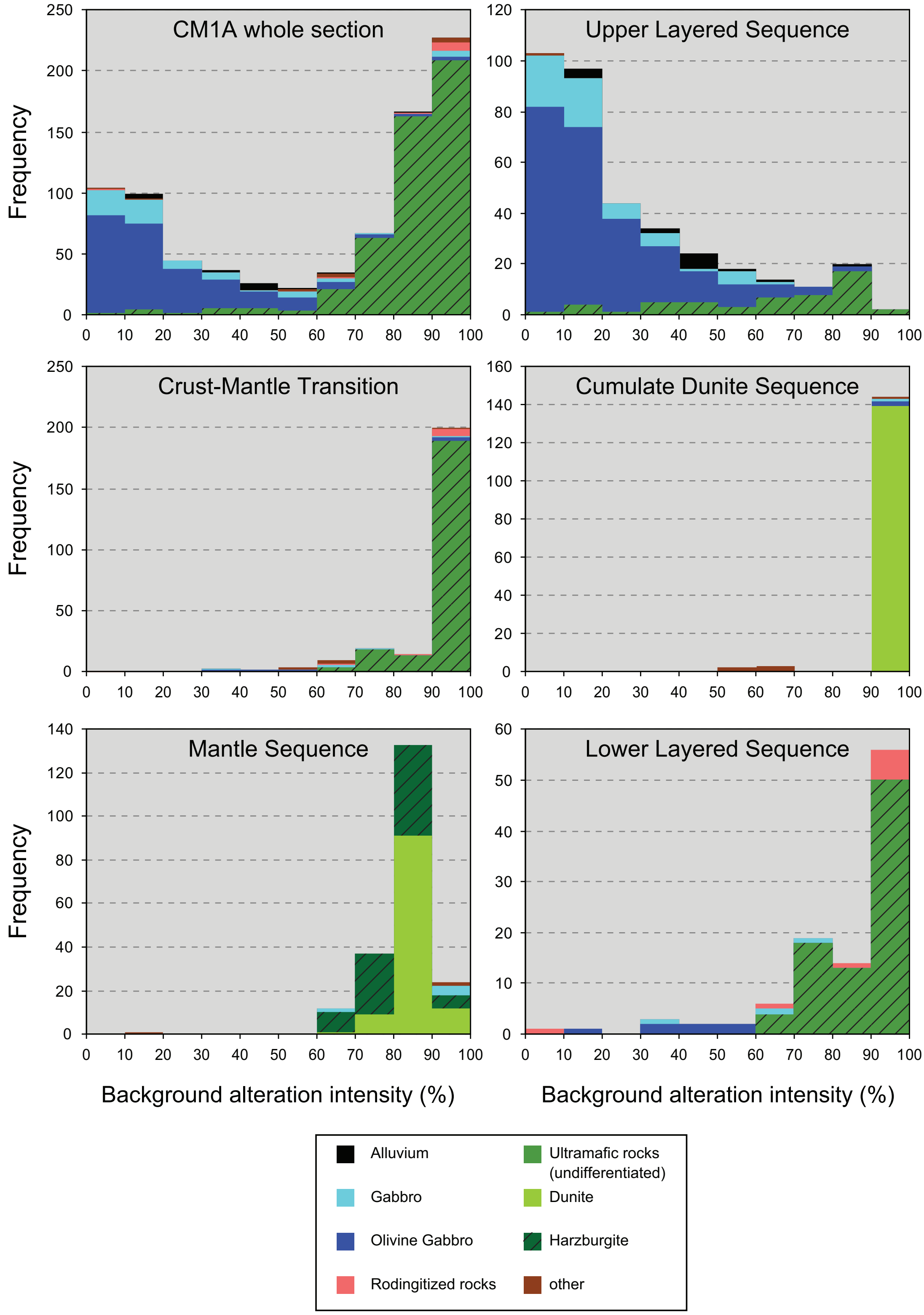

Figure F32. Distribution of secondary minerals in background alteration determined by visual core description and calibrated against thin section observations, Hole CM1A. Fine-grained mineral assemblages as replacement of plagioclase were unidentifiable and are plotted as "altered plagioclase."

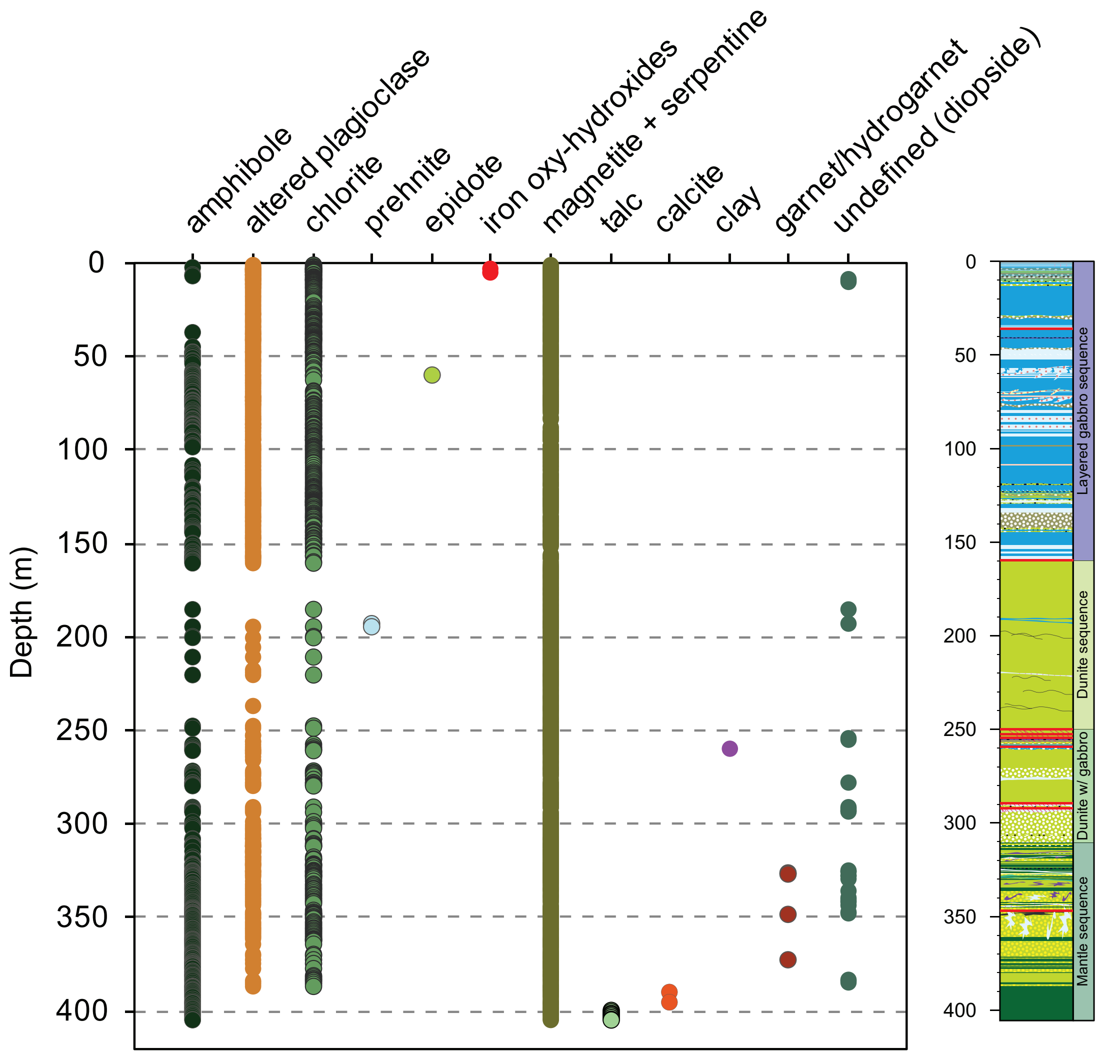

Figure F33. Downhole variation in estimated proportion of vein-filling minerals determined by macroscopic logging, Hole CM1A. Downhole variation in vein density is shown in Figure F68.

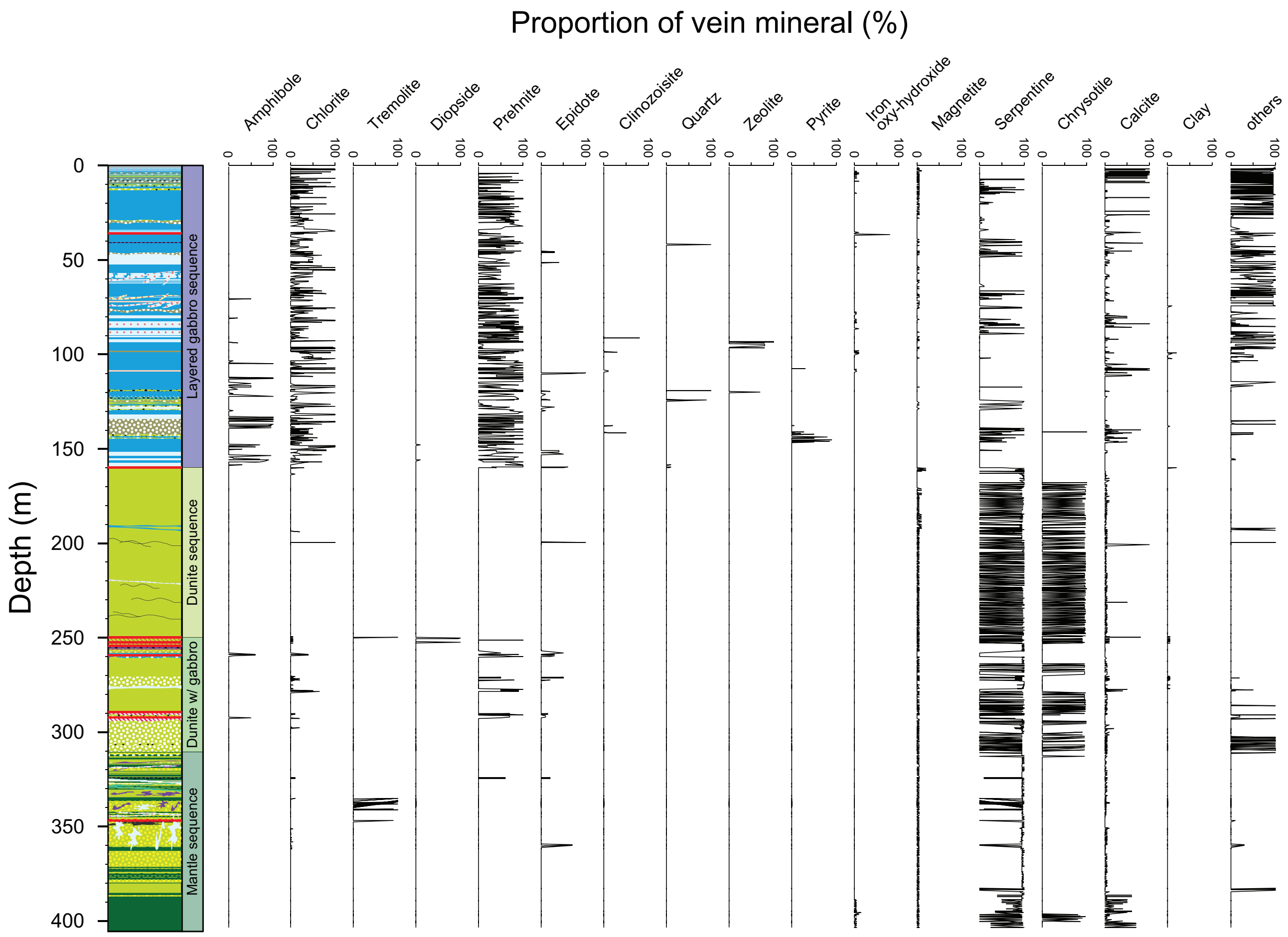

Figure F34. Downhole variations of vein minerals identified by XRD of selected veins and halos (solid circles) and from background or patch alteration domains (open circles), Hole CM1A. Abbreviations as in Table T5 in the **Methods** chapter.

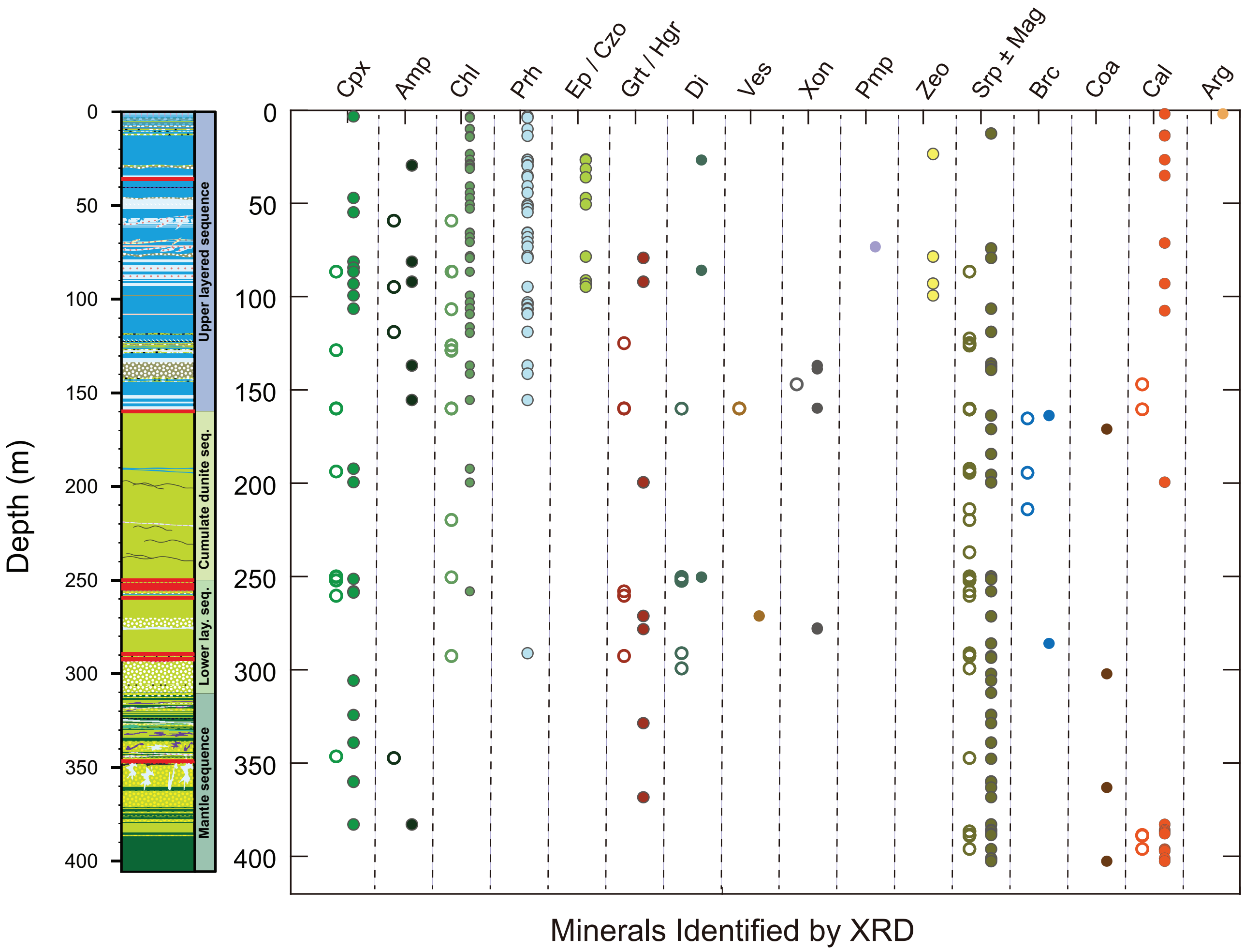

Figure F35. Representative examples of characteristic alteration features showing complexity of alteration in the Hole CM1A drill cores. **A.** Alteration associated with halos along a white prehnite vein. **B.** Alteration halos associated with a lithologic contact between gabbro and clinopyroxene-bearing dunite. **C.** Alteration occurring in patches. **D.** Alteration associated with deformed intervals.

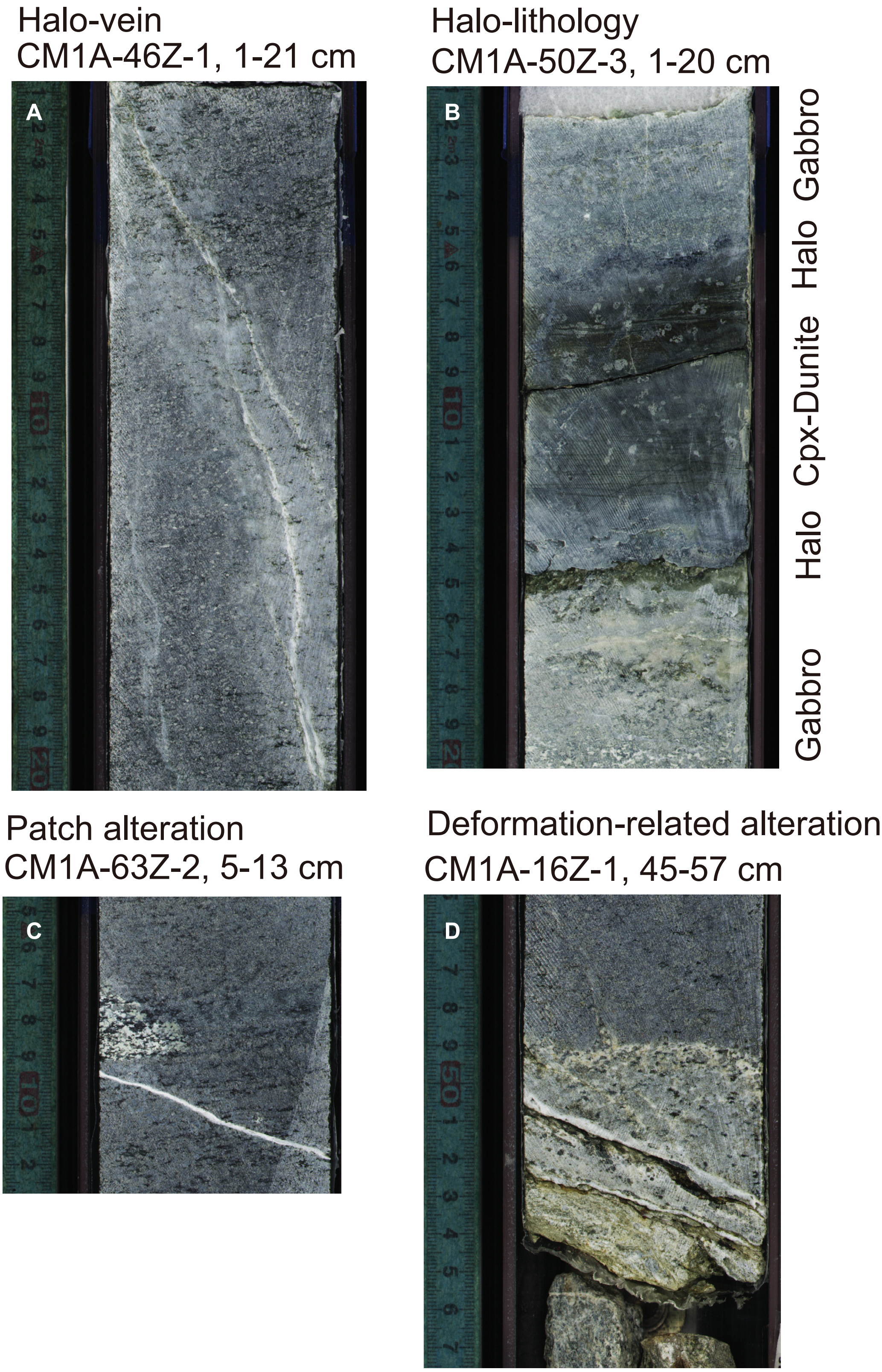

Figure F36. Downhole variations in the proportion of the four alteration types in Hole CM1A (main lithologic groups as defined in Figure F2).

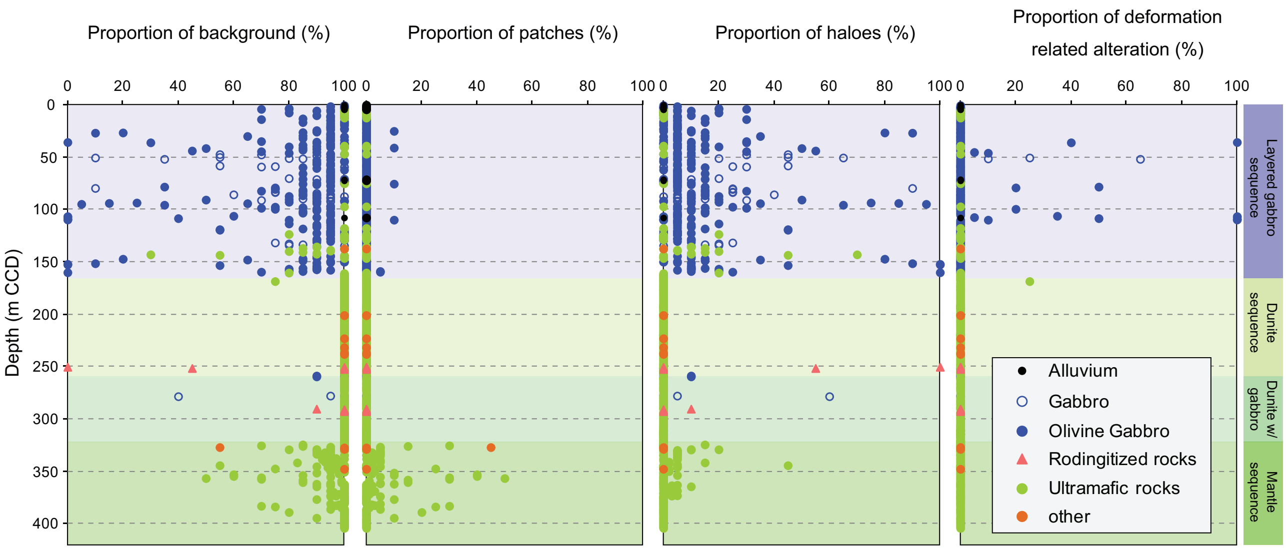

Figure F37. Representative images of full thin sections showing background alteration of gabbros in the Upper Layered Sequence, Hole CM1A. **A, B.** Layered olivine gabbro and gabbro. Olivine (Ol) is partly serpentinized, whereas clinopyroxene (Cpx) and plagioclase (Pl) are less altered. Note olivine in the upper half of olivine-rich gabbro is replaced by yellow-green phases, most likely clay. **C, D.** Slightly altered gabbro with halo of stronger alteration along sub-millimeter vein.

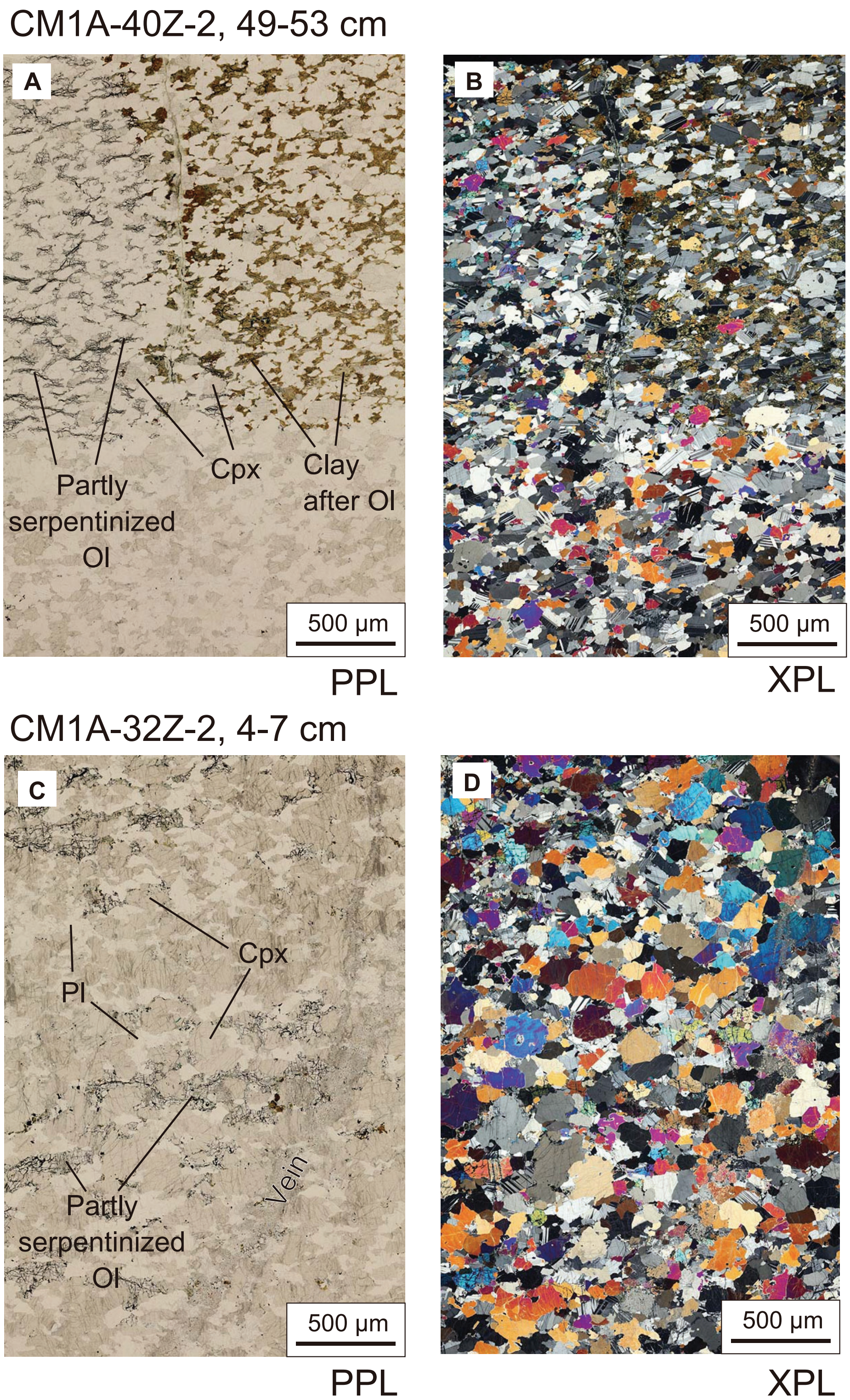

Figure F38. Representative photomicrographs showing background alteration of gabbros in the Upper Layered Sequence, Hole CM1A. **A, B.** "Secondary plagioclase" partly replacing plagioclase (Pl). Note that fine-grained phases replacing plagioclase are not clearly distinguishable. Ol = olivine, Cpx = clinopyroxene. **C, D.** Mineral zoning of tremolite (Tr) (or actinolite) at olivine side and chlorite (Chl) at plagioclase side. **E, F.** Clinopyroxene is partly replaced by tremolite (or actinolite). Mag = magnetite.

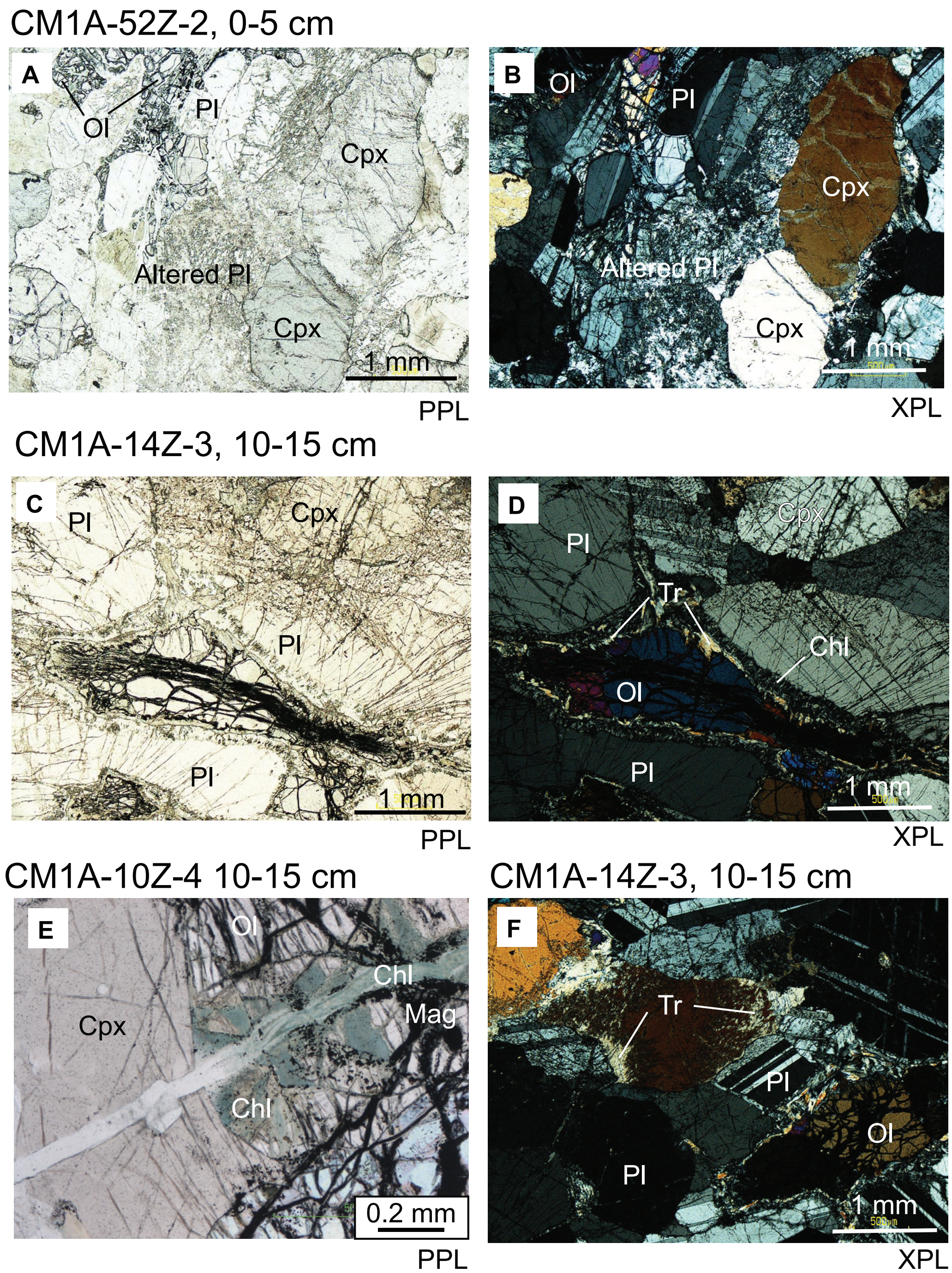

Figure F39. Examples of characteristic veins observed in gabbro of the Upper Layered Sequence, Hole CM1A. **A.** Prehnite (prh)-chlorite (Chl) vein. **B.** Serpentine (Srp) vein network. **C.** Veins with diffusive halo and no clear vein infilling. **D.** Clinozoisite (Czo) vein. **E.** Prehnite-epidote (Ep) vein. **F.** Amphibole (Amp) + chlorite vein. **G.** Calcite (Cal) + aragonite (Arg) vein.

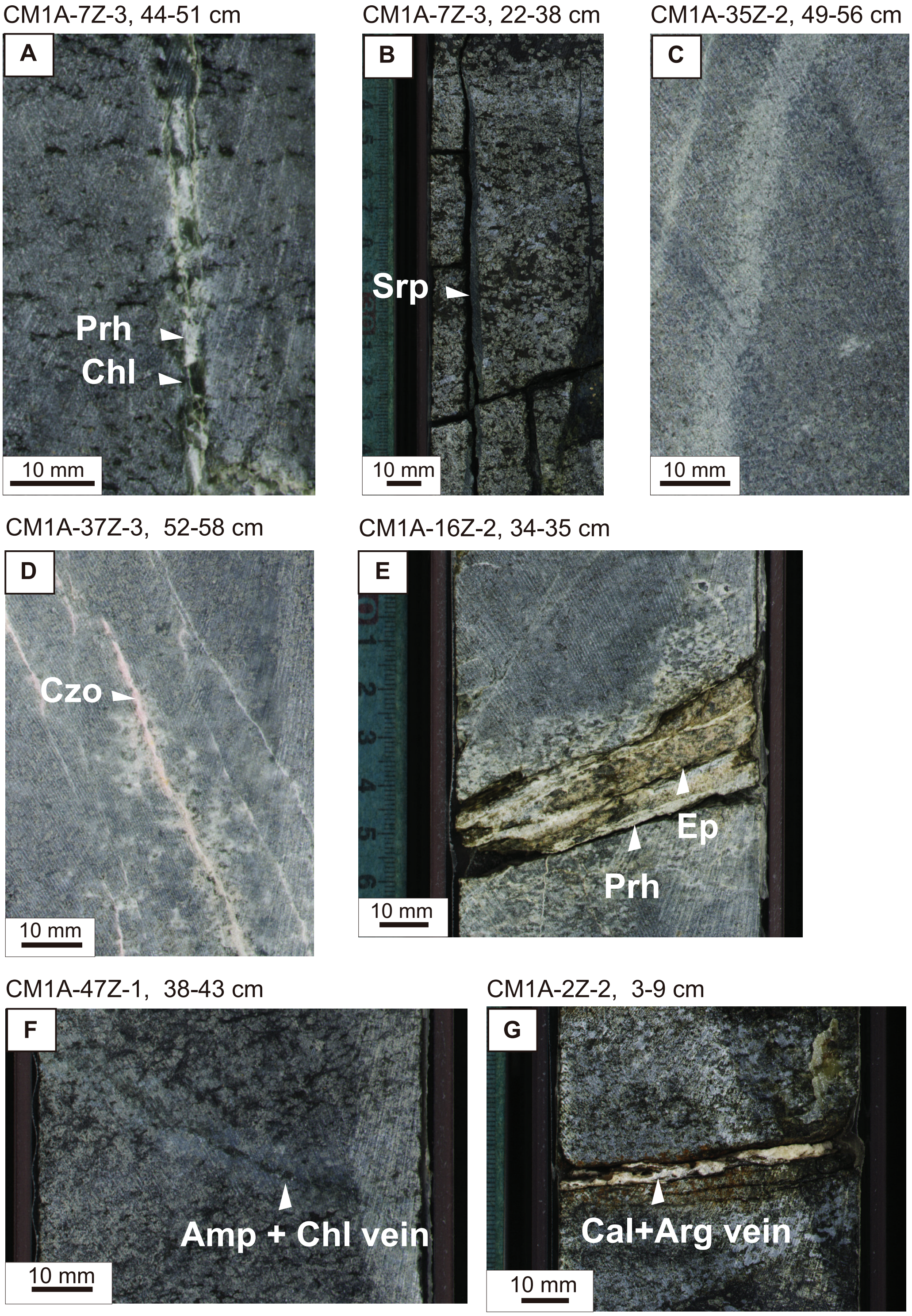

Figure F40. A–E. Typical serpentinization alteration minerals and textures in dunitic intervals, Hole CM1A. Dunite is intercalated with gabbro in the Layered Gabbro Sequence. Ol = olivine, Brc = brucite, Srp = serpentine, Mag = magnetite.

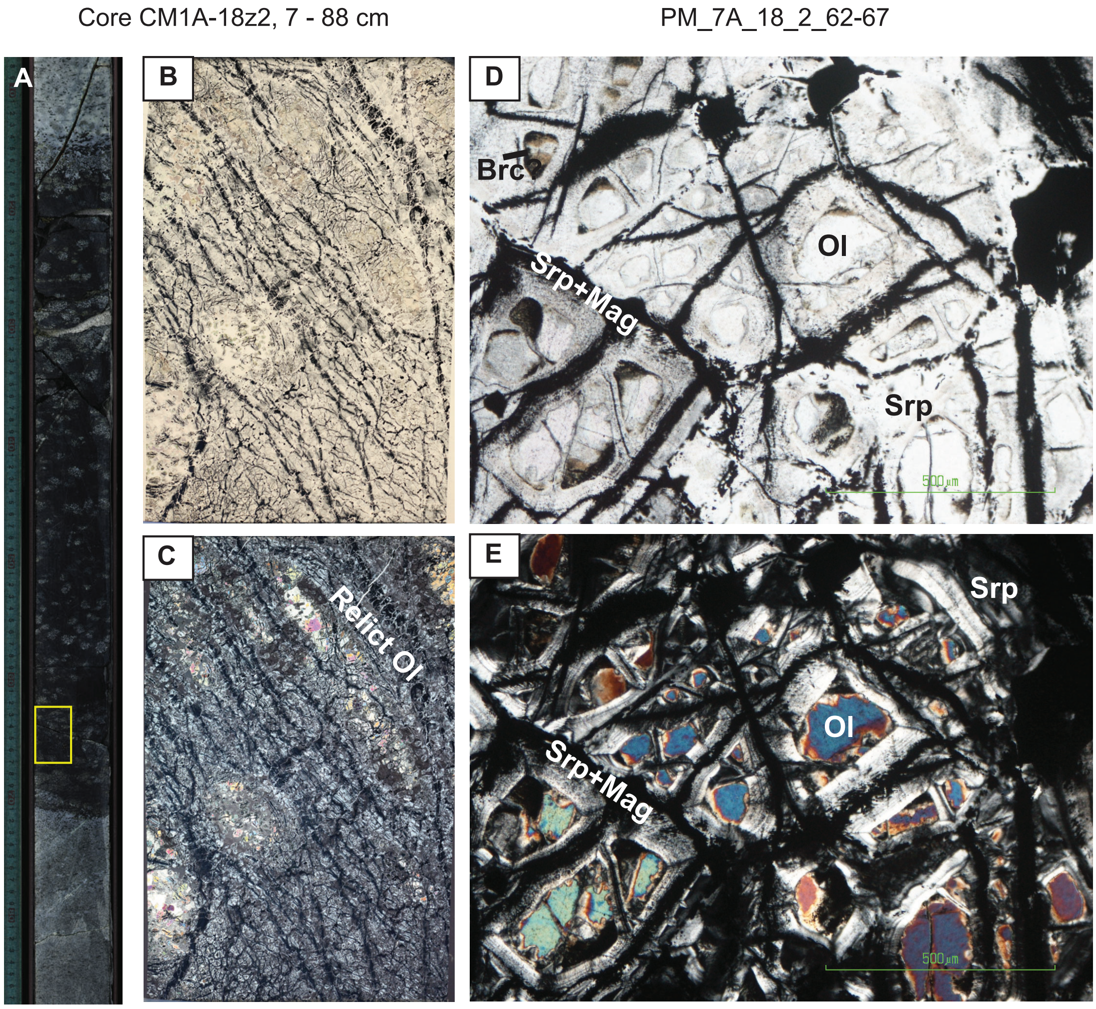

Figure F41. A, B. Serpentine (Srp) veins with sulfides veins in the Upper Layered Sequence, Hole CM1A. **C.** Pyrite (Py) and chalcopyrite (Ccp) mineralization in serpentinized dunite and contact with altered gabbro.

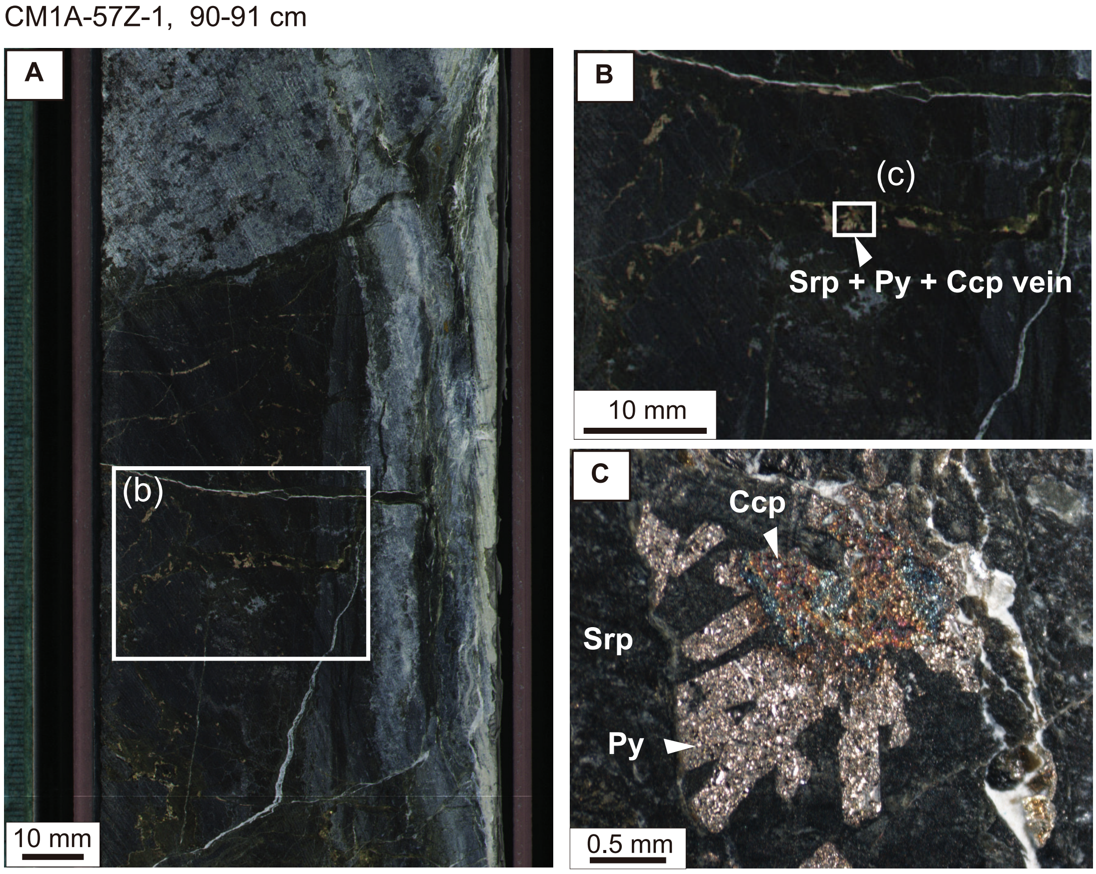

Figure F42. Association of rodingitized gabbro and completely serpentinized dunite at the Crust–Mantle Transition, showing minerals determined by XRD, Hole CM1A. **A, B.** Xonotlite (Xon) veins in banded Ca-metasomatic zone composed of clinopyroxene (diopside [Di]), vesuvianite (Ves), and garnet (Grt) (hydrogrossular), typical of alteration in gabbro in contact with dunite. **C.** Alteration phases in rodingitized gabbros in contact with serpentinized dunite at the top of the Crust–Mantle Transition. Chl = chlorite, Grs = grossular. **D.** Banded and deformed rodingite contact to serpentinized dunite.

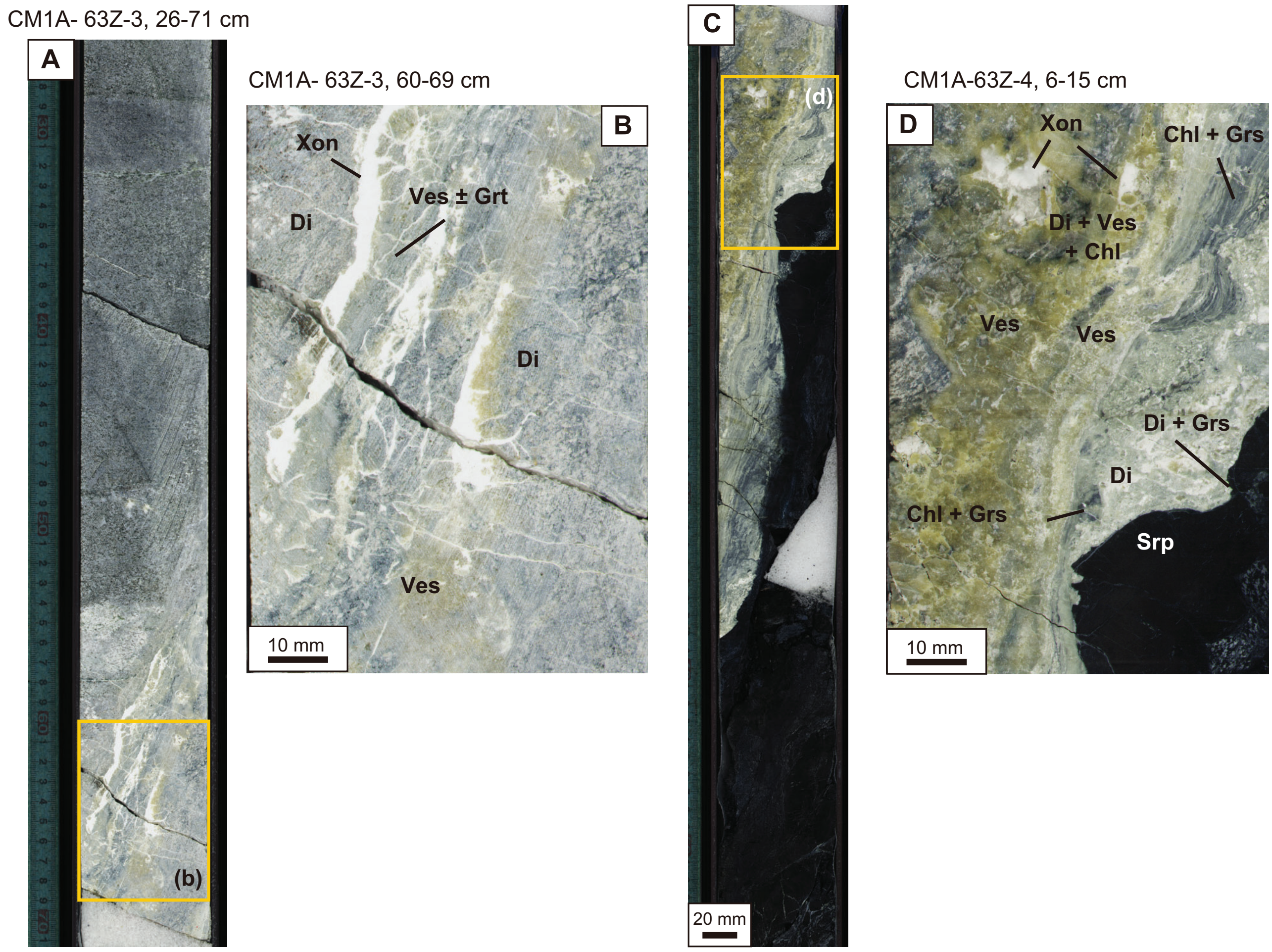

Figure F43. Ca-metasomatism at contacts between gabbros and completely serpentinized dunite in Dunite with Gabbro Sequence; minerals determined by XRD, Hole CM1A. **A.** Deformed serpentine (Srp) bands at contact between a 1 cm thick rodingitized gabbroic vein to serpentinized dunite. **B.** Diopside (Di)-rich, coarse-grained gabbroic domain. **C, D.** Coarse-grained to pegmatitic rodingitized gabbro in dunite with distinct domains of prehnite (Prh) + plagioclase (Pl) (anorthositic), serpentine + titanite (Ttn), and ilmenite (Ilm). Ti-rich minerals in this interval suggest an oxide gabbroic composition of the protolith. Hgr = hydrogrossular.

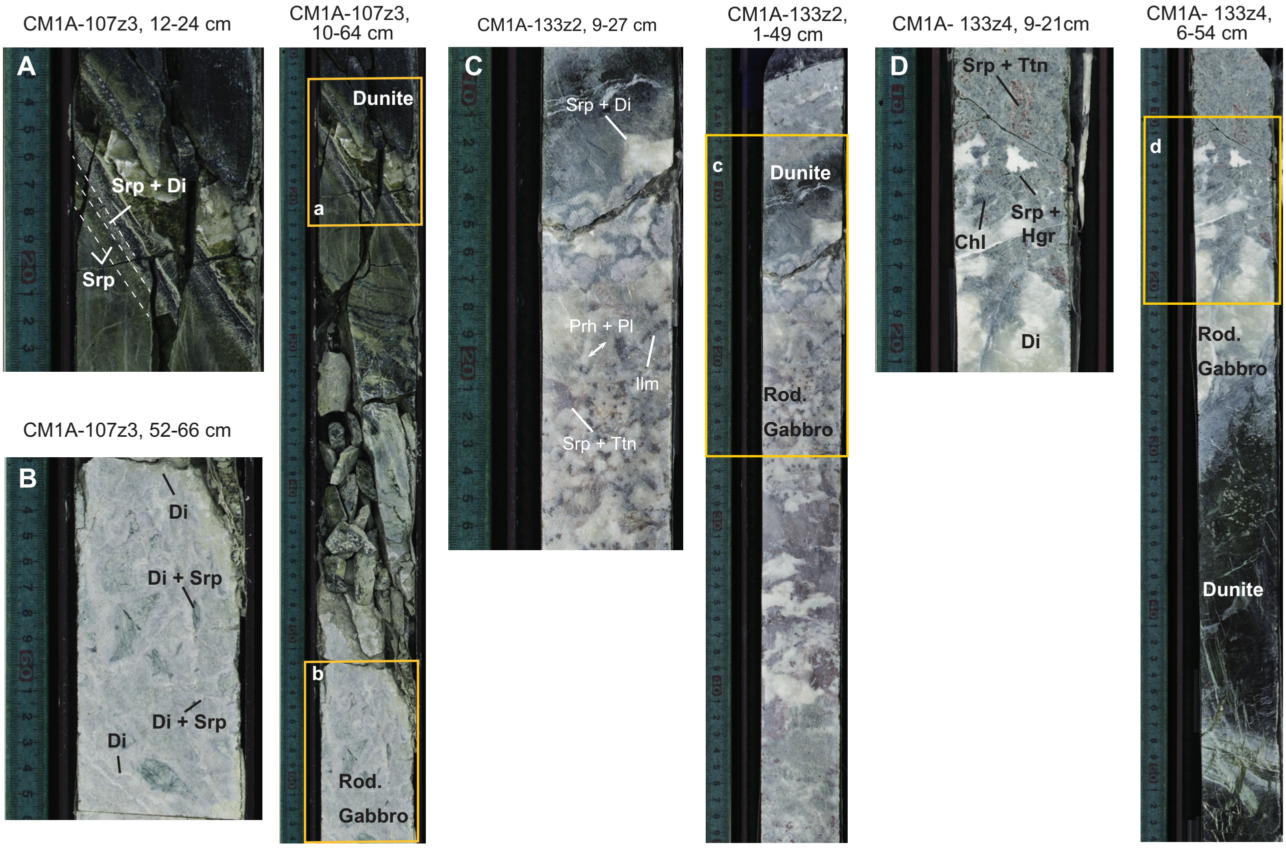

Figure F44. **A–C.** Diopside vein (Di) in diopsidite (B: XPL, C: XPL), Hole CM1A.

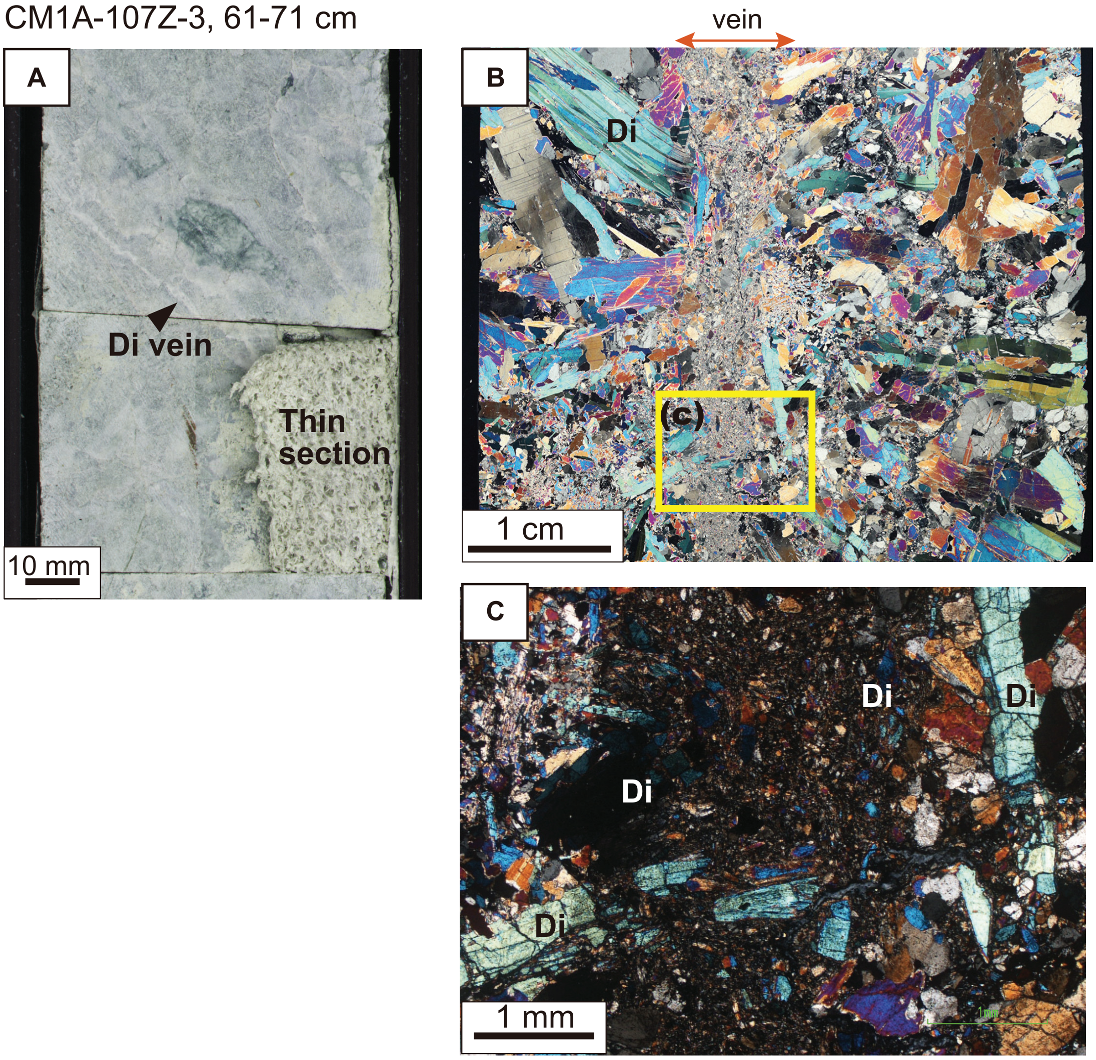

Figure F45. XRD patterns of xonotlite and coalingite, Hole CM1A.

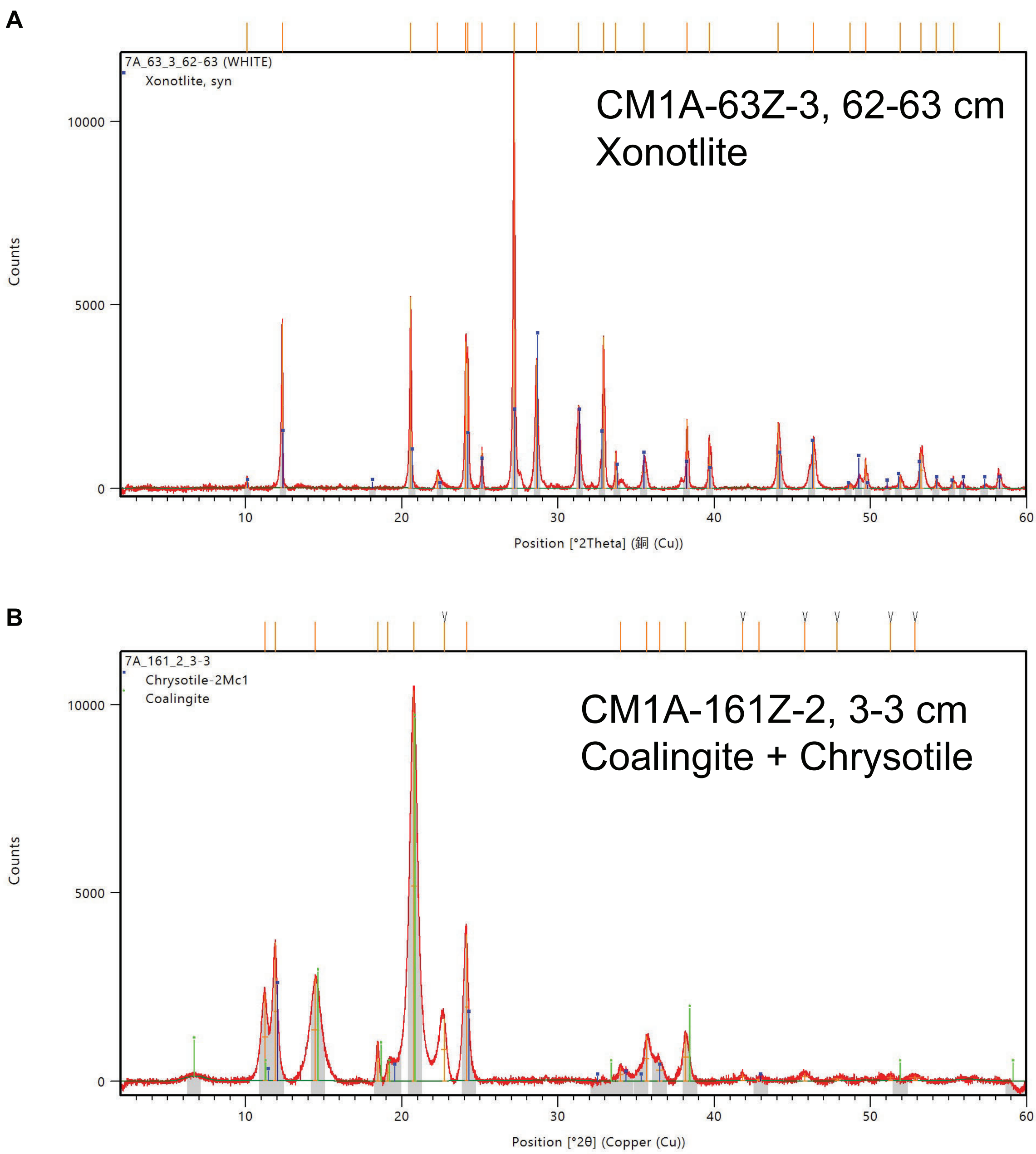

Figure F46. Generations of serpentine veins in dunite (Dunite Sequence), Hole CM1A. **A.** V1: banded serpentine + magnetite vein network as a mesh texture; V2: banded serpentine + magnetite vein cuts the mesh texture; V3: serpentine vein cuts the V1 and V2 vein networks. **B.** Serpentine (Srp) + garnet (Grt) + calcite (Cal) vein in serpentinized dunite.

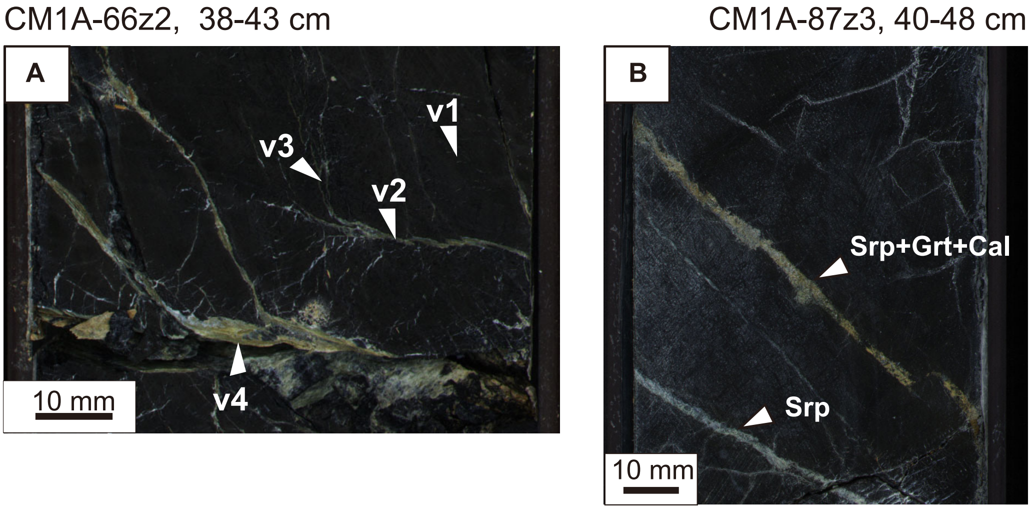

Figure F47. Representative X-ray CT images of serpentinized dunite that highlight abundance of V2 serpentine + magnetite veins and associated alteration halos, Hole CM1A. V2 serpentine + magnetite veins with high magnetite contents show high CT numbers.

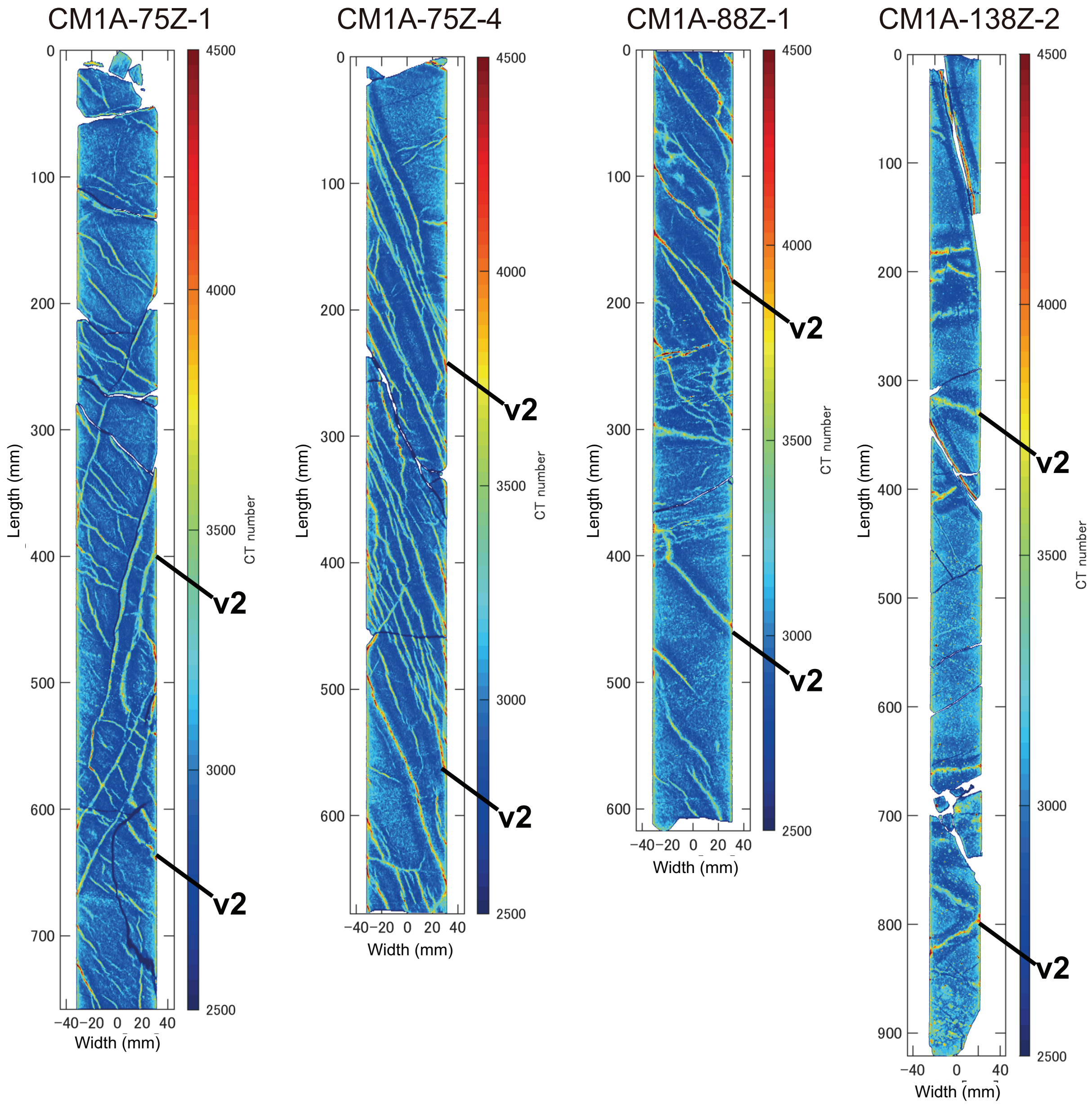

Figure F48. Late-stage calcite vein network in Dunite Sequence within the CMTZ, Hole CM1A. **A–C.** Later calcite vein network in dunite. Calcite veins cut V2 serpentine (Srp) + magnetite (Mag) veins and branch to form network (102X-1, 64–69 cm) (A: PPL, B: XPL, C: RL). **D.** Late-stage calcite (Cal) vein network crosscutting earlier veins and outlining precursor olivine grain boundaries that are now fully altered (80Z-1, 7–12 cm). Bru = brucite.

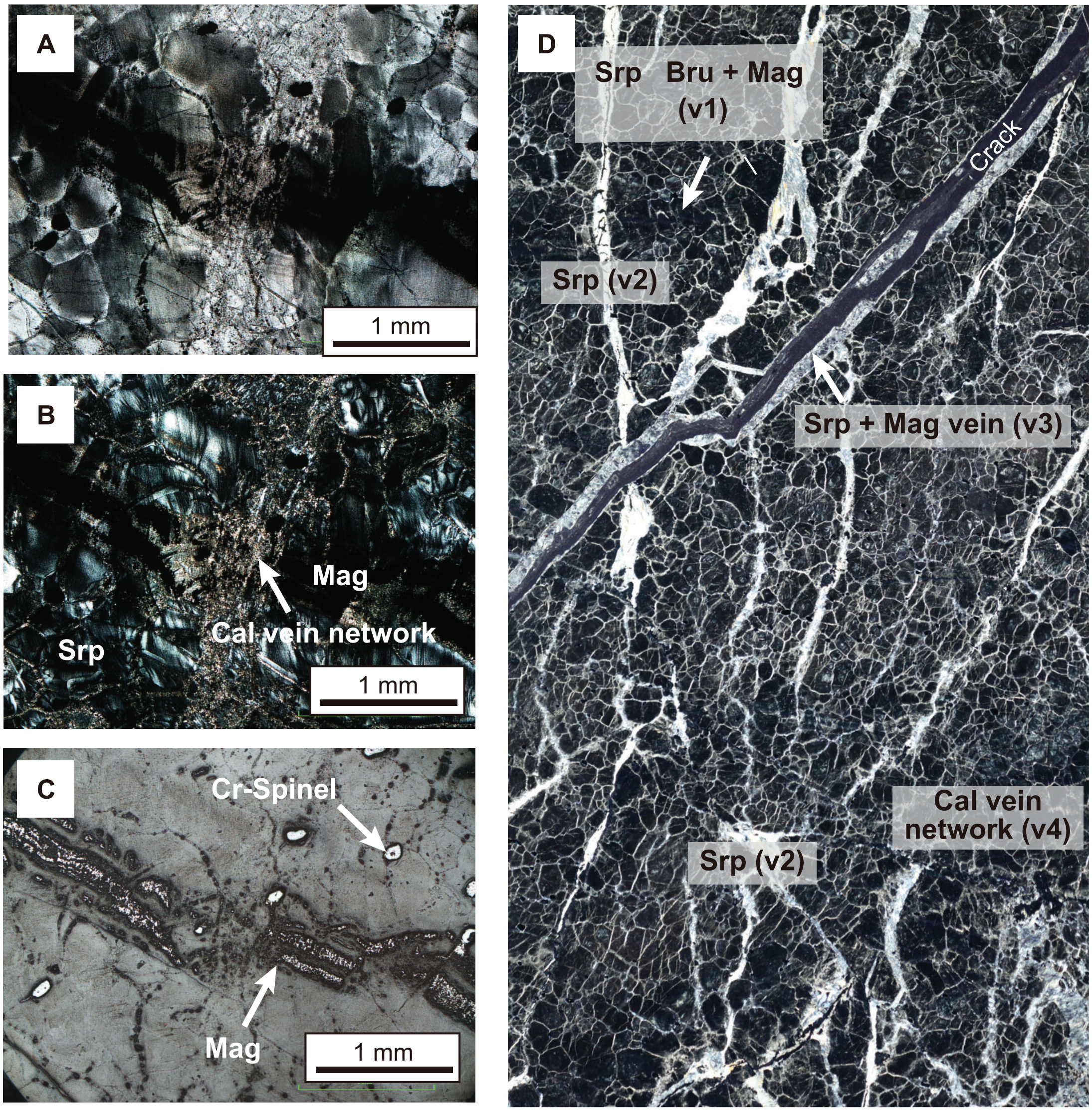

Figure F49. Veins in the mantle sequence, Hole CM1A. **A.** Zebra-like chrysotile (Ctl) V3 vein network in harzburgite cut by V4 vein (serpentine + calcite [Srp + Cal]). **B.** V3 chrysotile veins follow V2 serpentine + magnetite (Mag) veins.

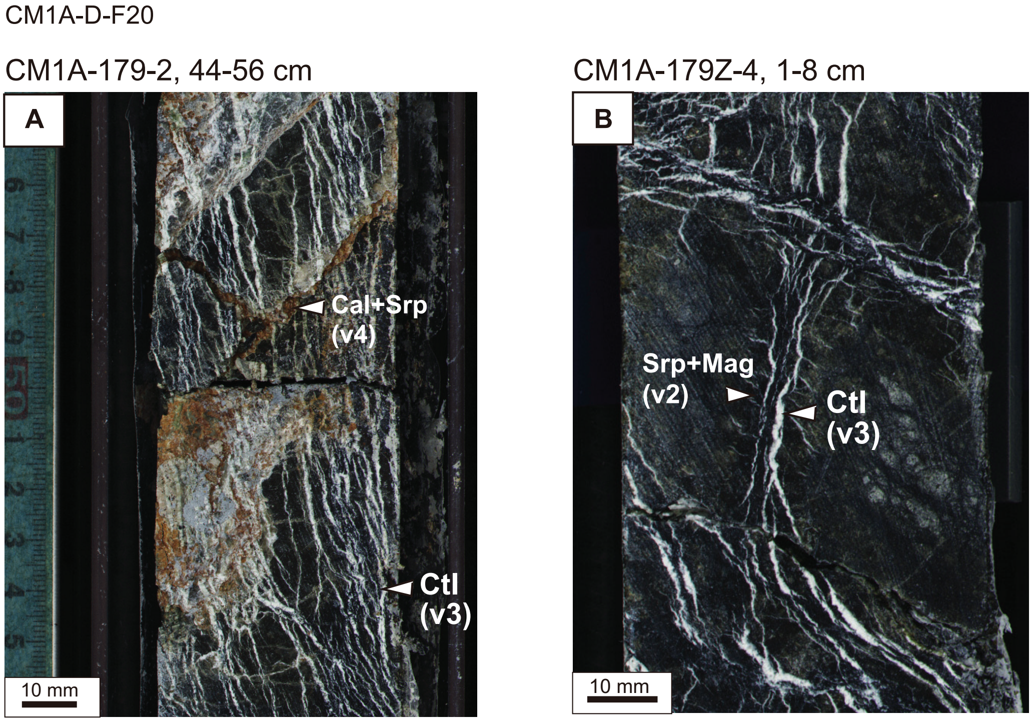

Figure F50. Veins and related alteration, Hole CM1A. **A, B.** "Mesh" texture (V1) in dunite. Srp = serpentine, Brc = brucite, Ol = olivine. **C, D.** Mesh texture after olivine and bastite (locally rimmed with talc [Tlc] in C). Mag = magnetite, Opx = orthopyroxene.

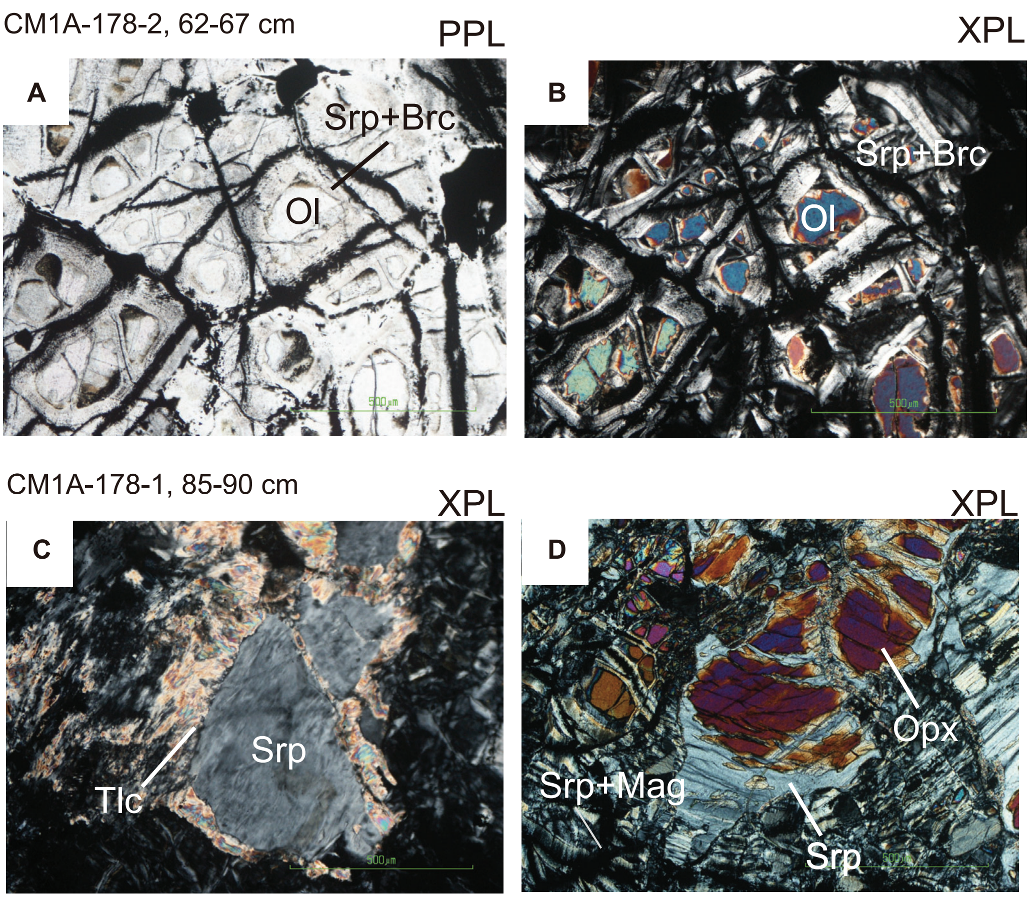

Figure F51. A–C. Vein generations and crosscutting relationships in harzburgite, Hole CM1A. V1: mesh texture (serpentine + magnetite), V2: serpentine + magnetite, V3: serpentine.

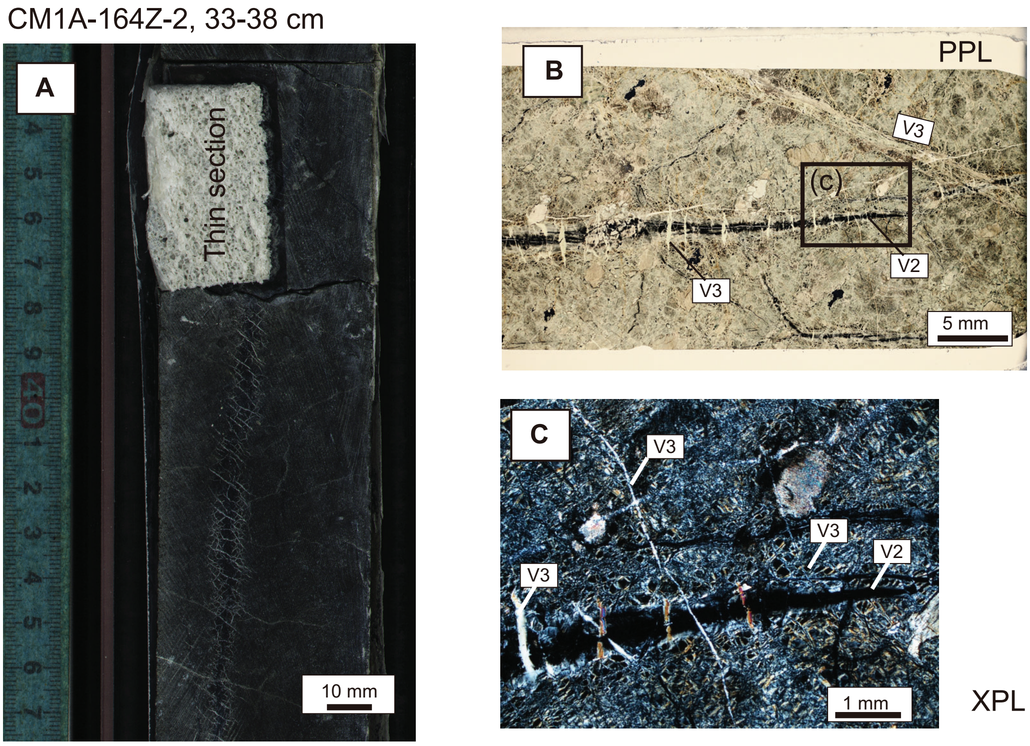

Figure F52. Sulfides and oxides in serpentinized dunite in crust (18Z-2, 62–69 cm), Hole CM1A. **A.** Pentlandite (Pn) and polydymite surrounded by magnetite (Mag). Py = pyrite, Srp = serpentine. **B.** Heazlewoodite surrounded by magnetite and pentlandite in serpentine, Hole CM1A. Ol = olivine. **C.** Magnetite in V2 vein in serpentinites. Spl = spinel.

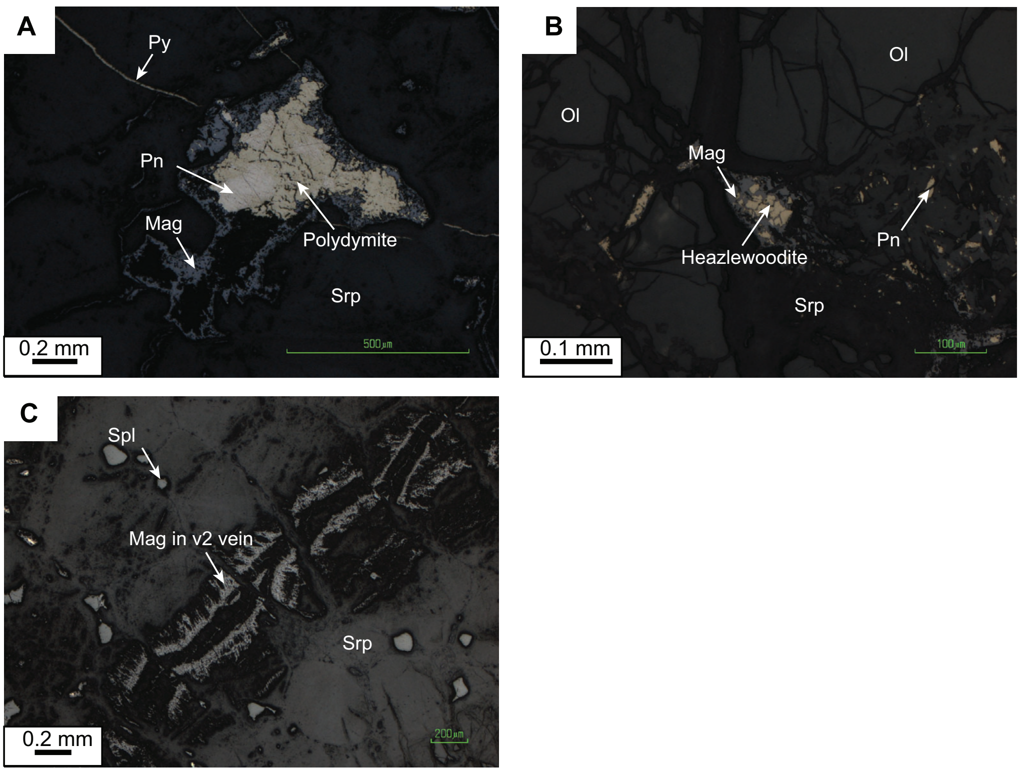

Figure F53. Core photographs of intrusive crosscutting relationships between gabbro and dunite, Hole CM1A. **A.** Wehrlite/dunite intrusion into gabbro. **B.** Olivine gabbro intrusion into dunite. **C.** Dunite xenolith within gabbroic intrusion and intrusive margin. **D.** Discordant gabbro intrusion within foliated gabbro. **E.** Gabbro intruding dunite.

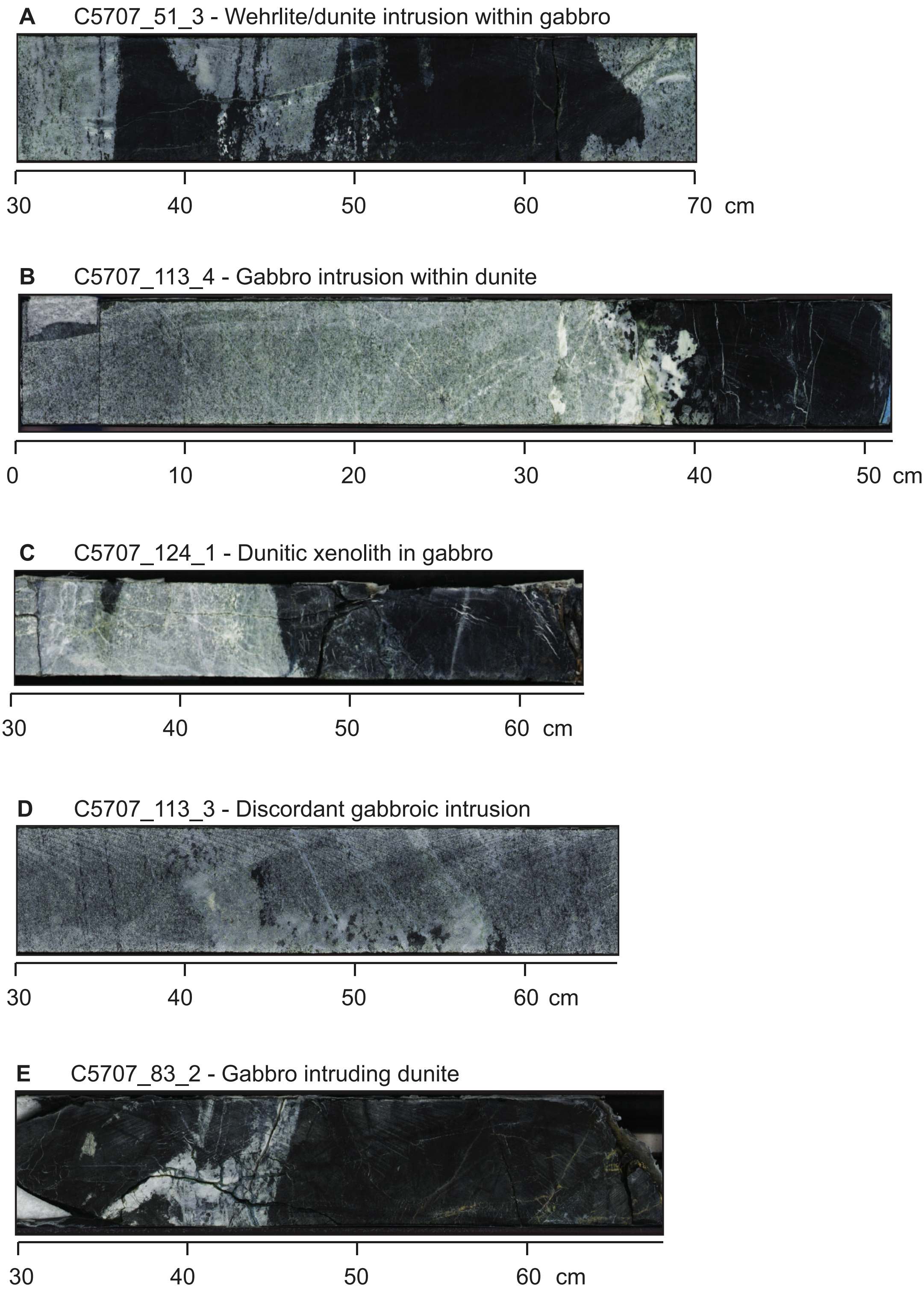

Figure F54. Core and thin section photographs of compositional/modal layering in the gabbroic sequence, Hole CM1A. Red boxes give location(s) of thin section photographs. **A.** Ratio contact between olivine gabbro and olivine-rich gabbro. **B.** Phase contact between olivine gabbro and gabbro.

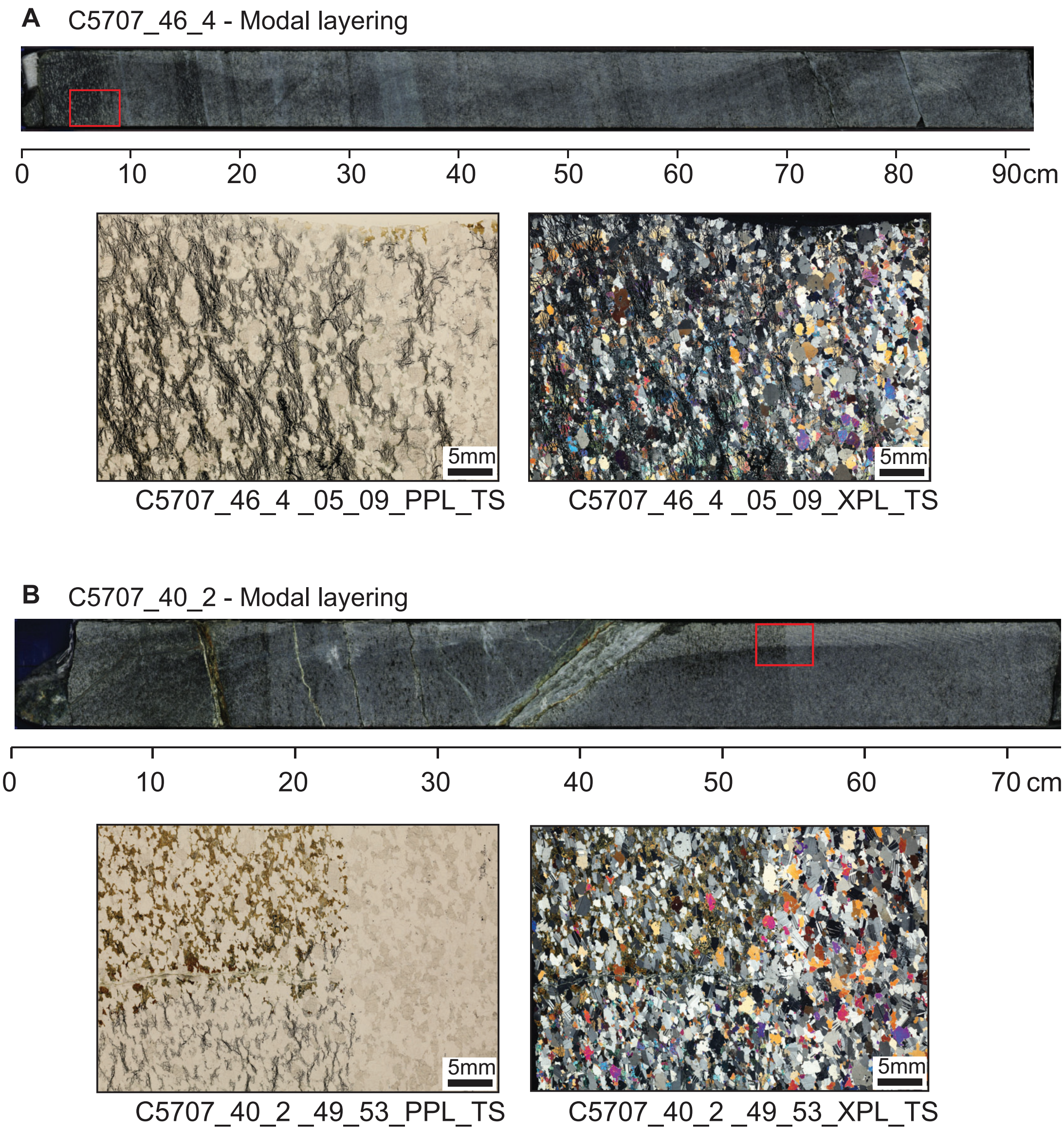

Figure F55. Core and thin section photographs of complexities in the magmatic layering and foliation, Hole CM1A. **A.** Monoclinal folding of layering/foliation. Dashed red lines outline folding. Red arrow gives TS orientation relative to core. **B.** Discordant layering and foliation. Dashed red lines highlight orientation of the foliation. **C.** Discordant layering. Dashed red lines highlight orientation of the foliation.

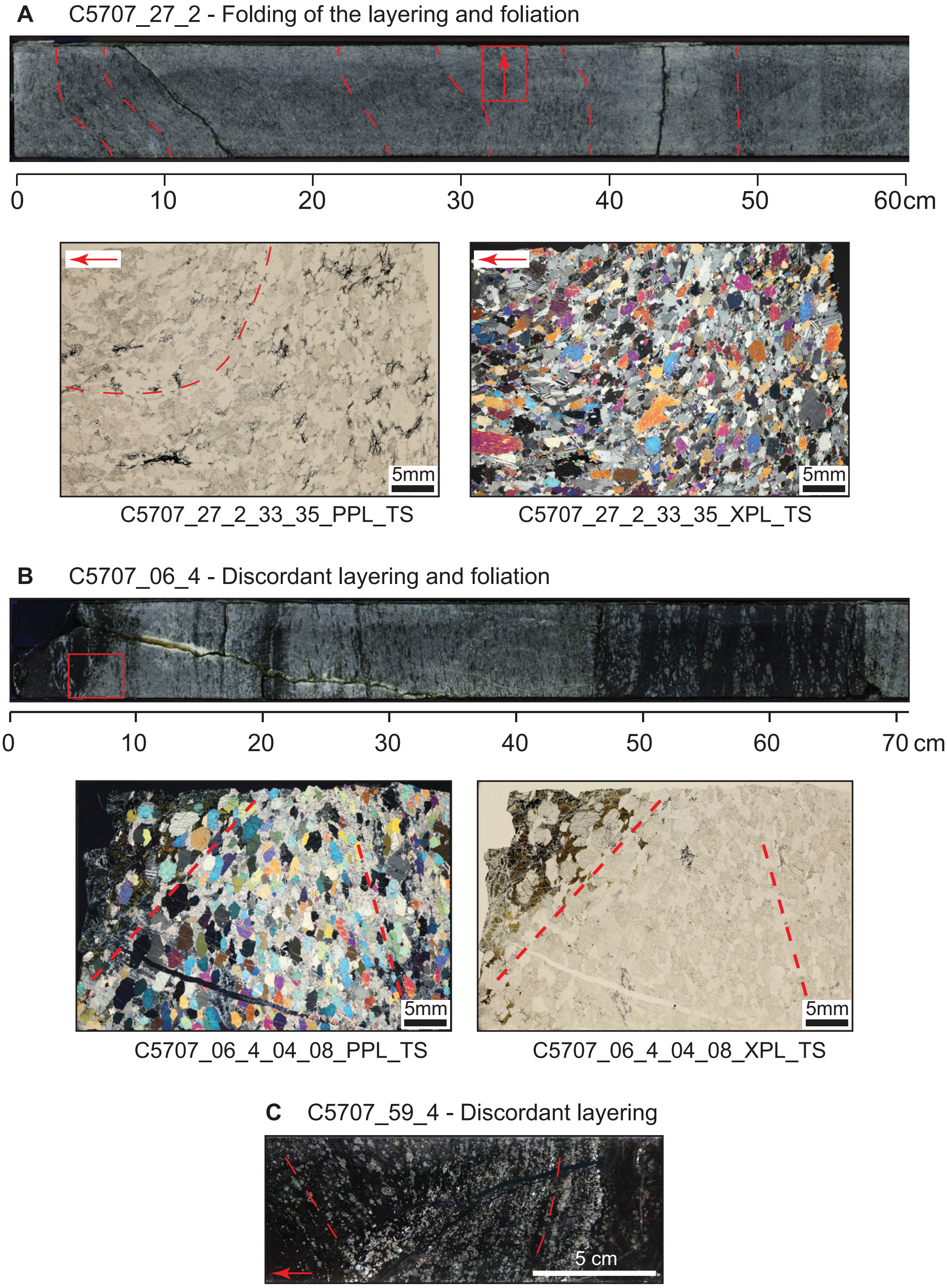

Figure F56. Downhole diagrams of layer thickness within the gabbroic sequence by (**A**) depth, (**B**) frequency by intervals of 5 cm, and (**C**) Ln (layer thickness) frequency by intervals of 0.5, Hole CM1A.

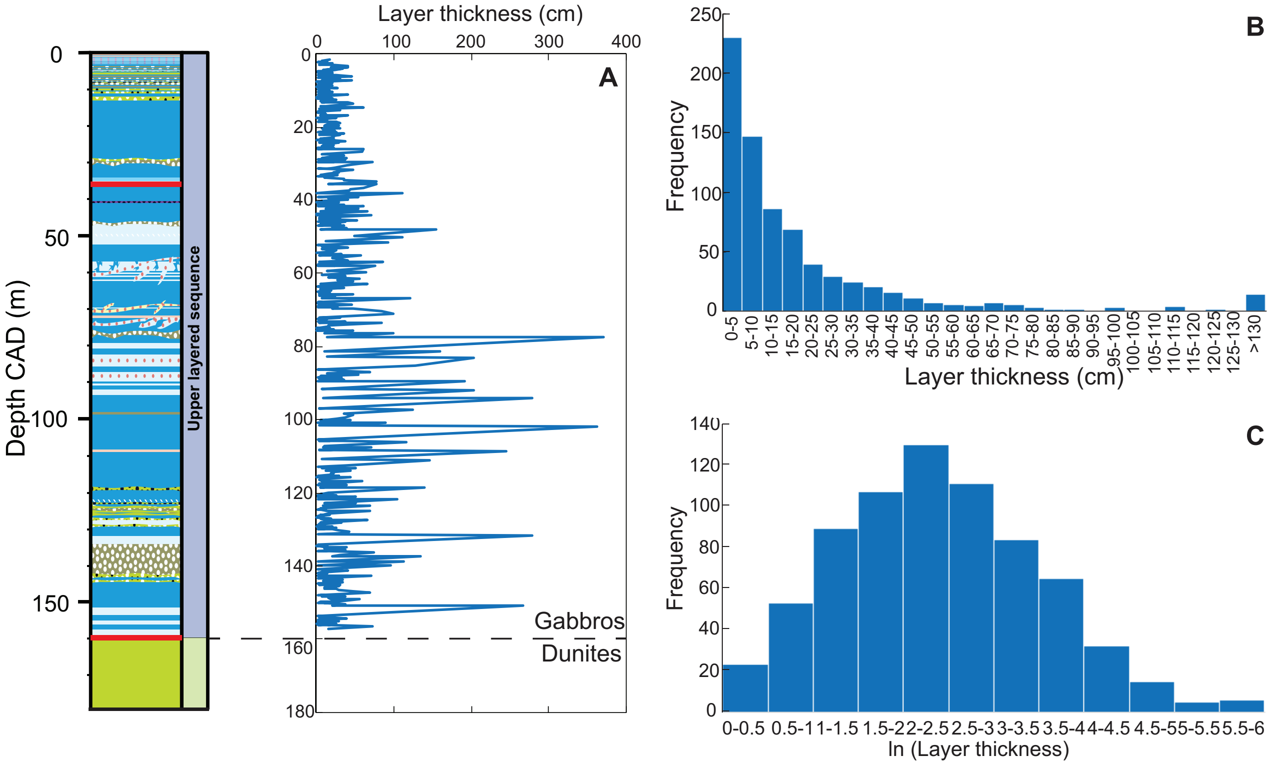

Figure F57. Downhole plot of the dip of (**A**) magmatic layering/foliation and (**B**) magmatic veins with depth, Hole CM1A.

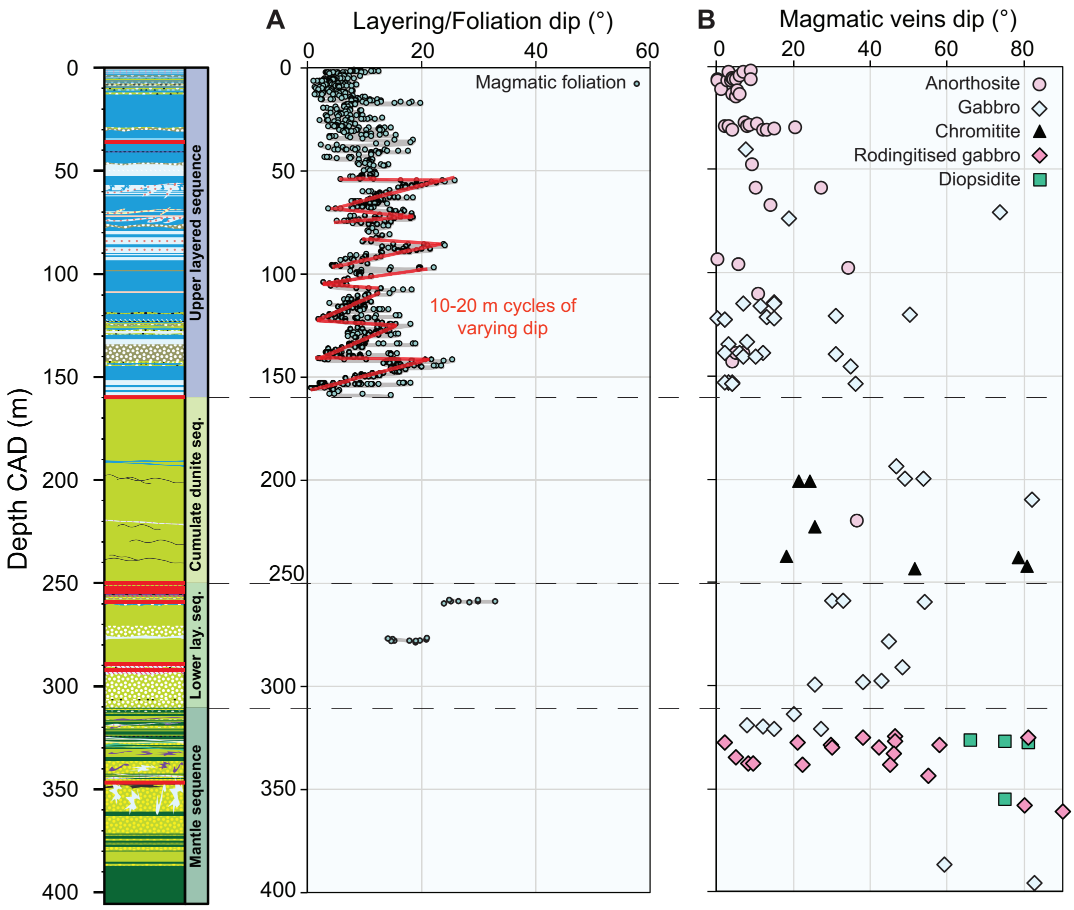

Figure F58. Magmatic foliation within the gabbroic sequence, Hole CM1A. **A.** Weak foliation defined by slight elongation of plagioclase crystals. **B.** Moderate foliation defined by more pronounced elongation of plagioclase and olivine crystals. **C.** Moderate foliation defined by elongation of plagioclase and olivine. The plagioclase shows some above solidus crystal-plastic deformation as evidenced by undulose extinction and deformation twins.

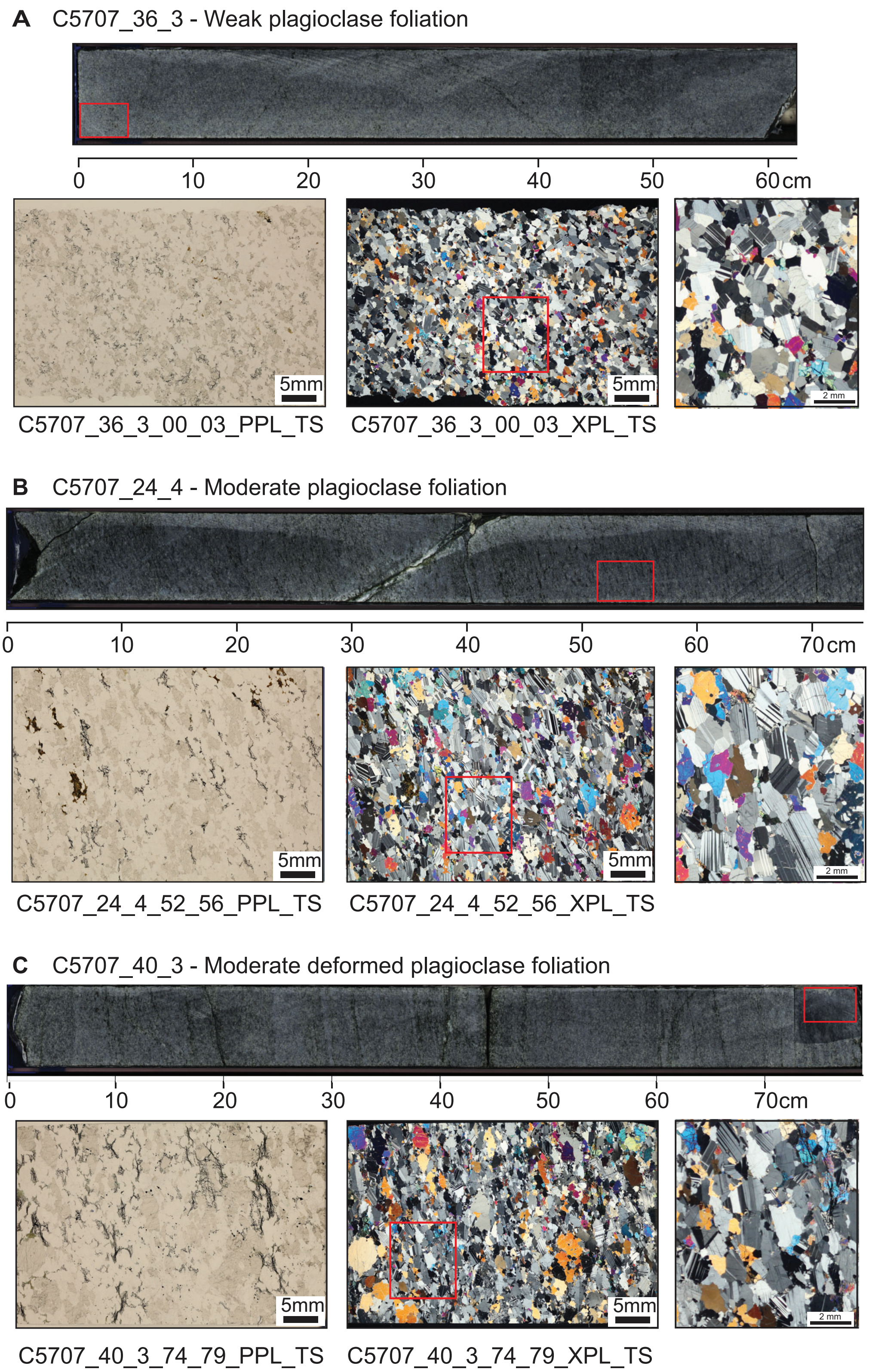

Figure F59. Decimeter-scale layering between harzburgite and dunite illustrating thickness variation and differing dip directions, Hole CM1A. Red dashed lines highlight layer boundaries; white arrow gives the up direction.

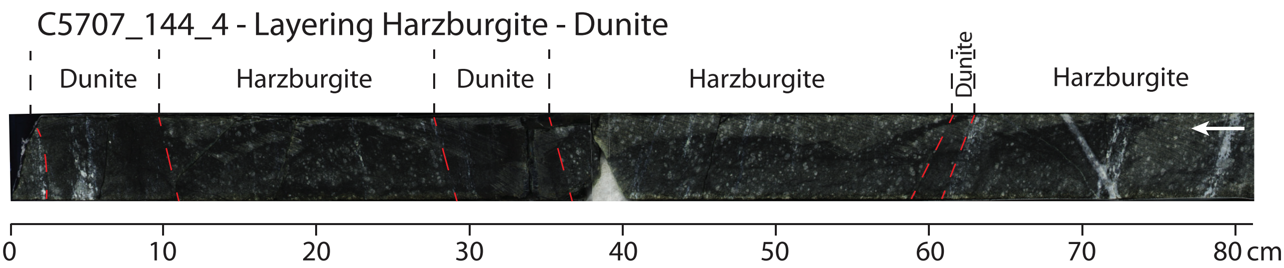

Figure F60. Frequency diagrams of (**A**) layer thickness and (**B**) ln (layer thickness) of the dunitic intervals, Hole CM1A.

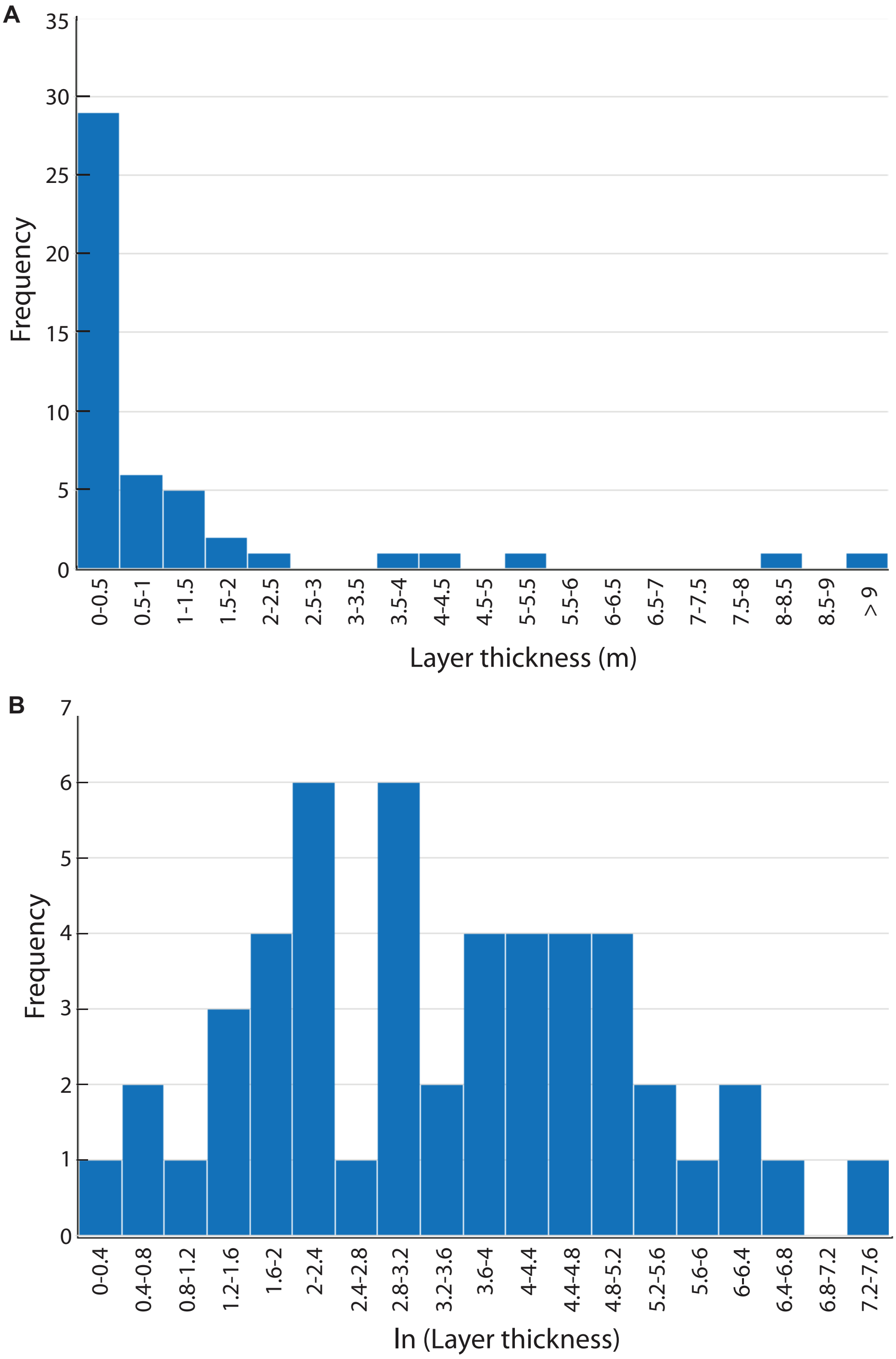

Figure F61. Downhole diagram of the dunite (**A**) layer thickness and (**B**) contact dip angle, Hole CM1A.

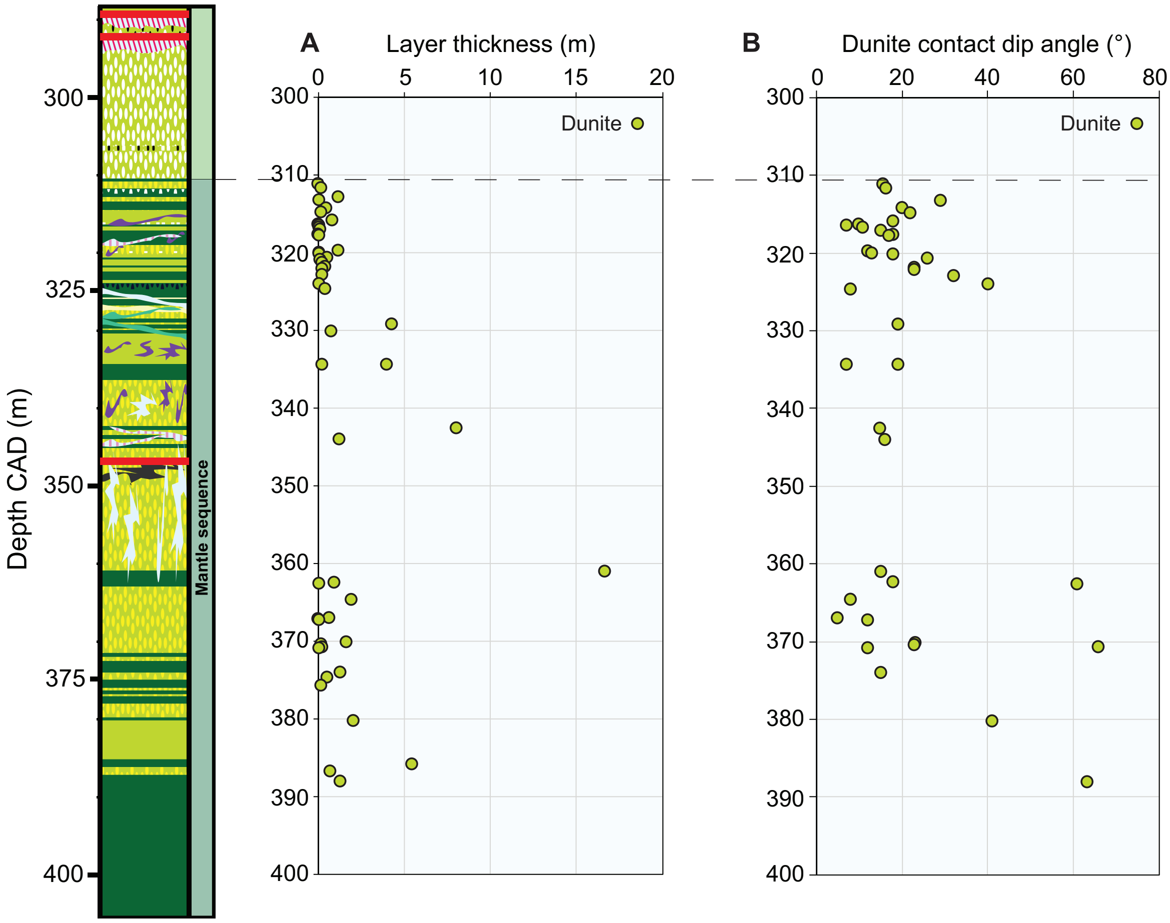

Figure F62. Magmatic veins in the gabbro (outlined by dashed red lines), Hole CM1A. **A.** Concordant to slightly discordant anorthosite veins. **B.** Discordant decimeter-size pegmatitic gabbroic vein. **C.** Discordant centimeter-size gabbroic veins.

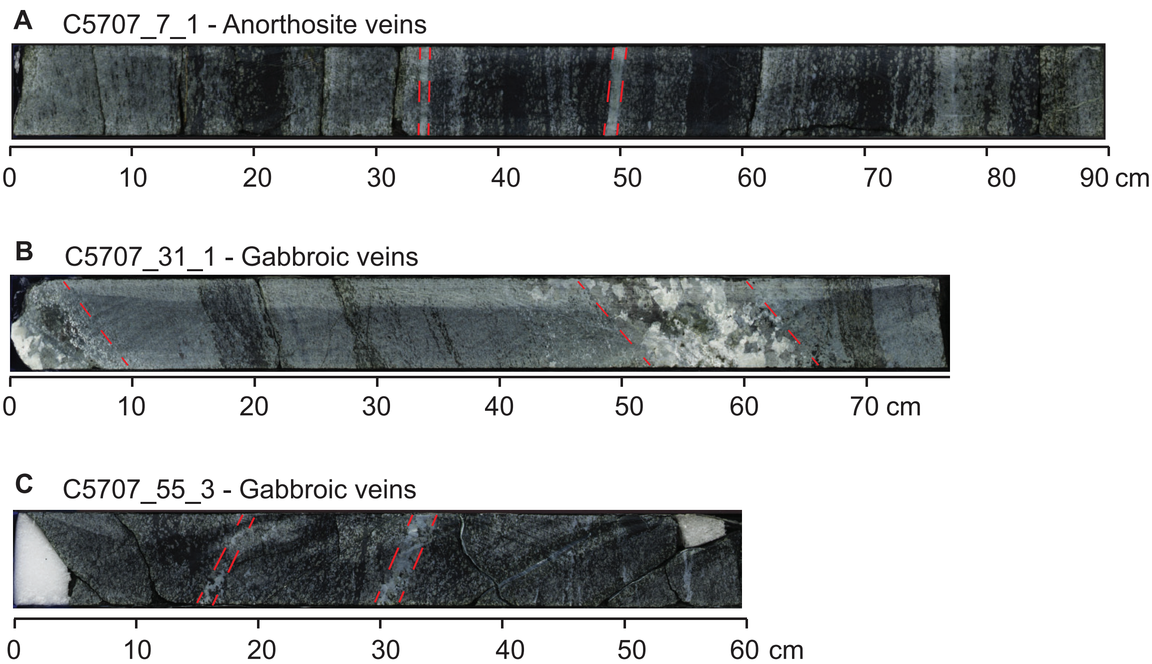

Figure F63. Rodingitized gabbro intrusions in the Mantle Sequence, Hole CM1A. **A.** Relatively planar gabbroic veins. **B.** Irregular gabbroic and diopsidite bodies, and chromititic intrusion. **C.** Irregular gabbroic bodies. **D.** Deformed irregular gabbroic bodies.

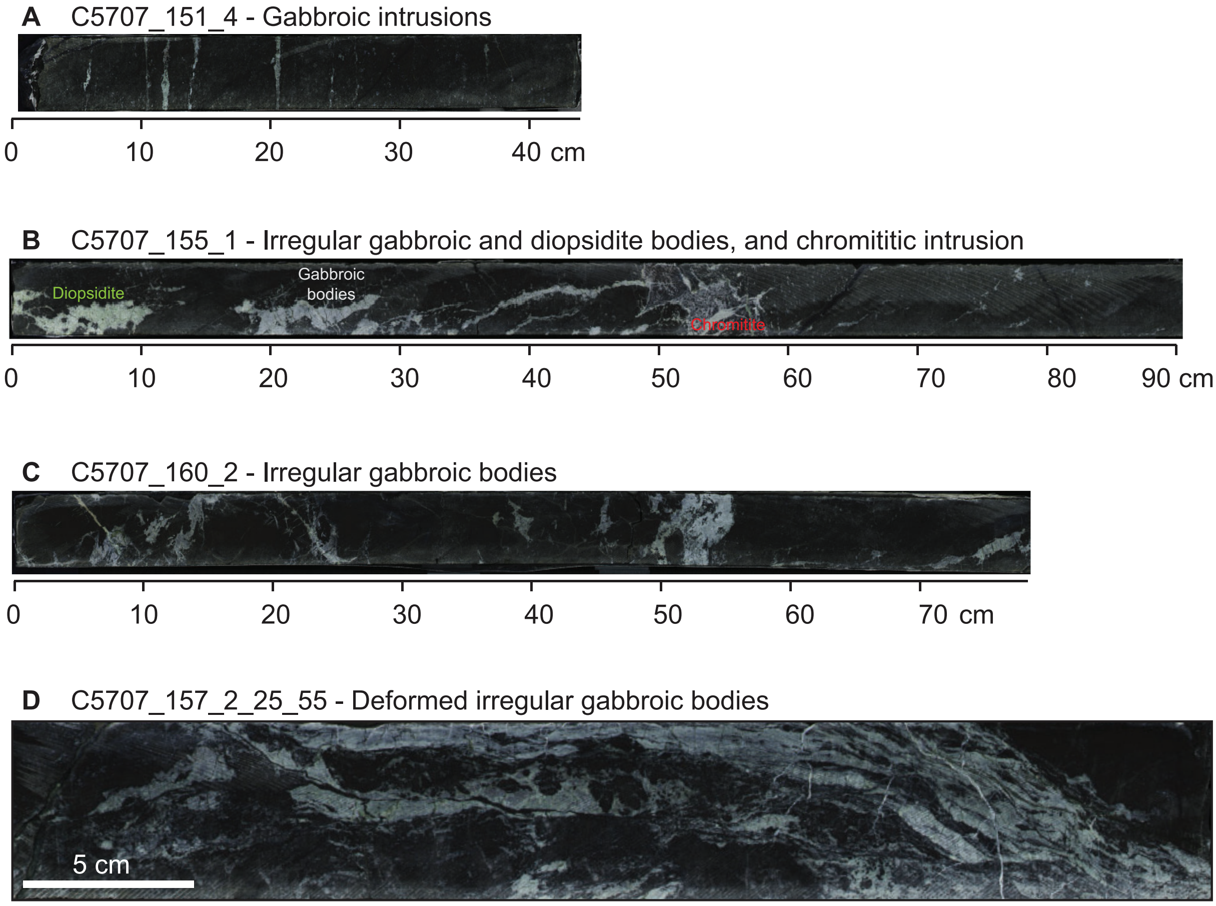

Figure F64. Downhole diagram of semibrittle/crystal-plastic fabric intensity, Hole CM1A. **A.** Gabbros, dunites, small intrusions, and veins. **B.** Harzburgites. 0 = undeformed; 1 = weakly foliated; 2 = moderately foliated; 3 = protomylonite; 4 = mylonite; 5 = ultramylonite; 6 = pseudotachylite.

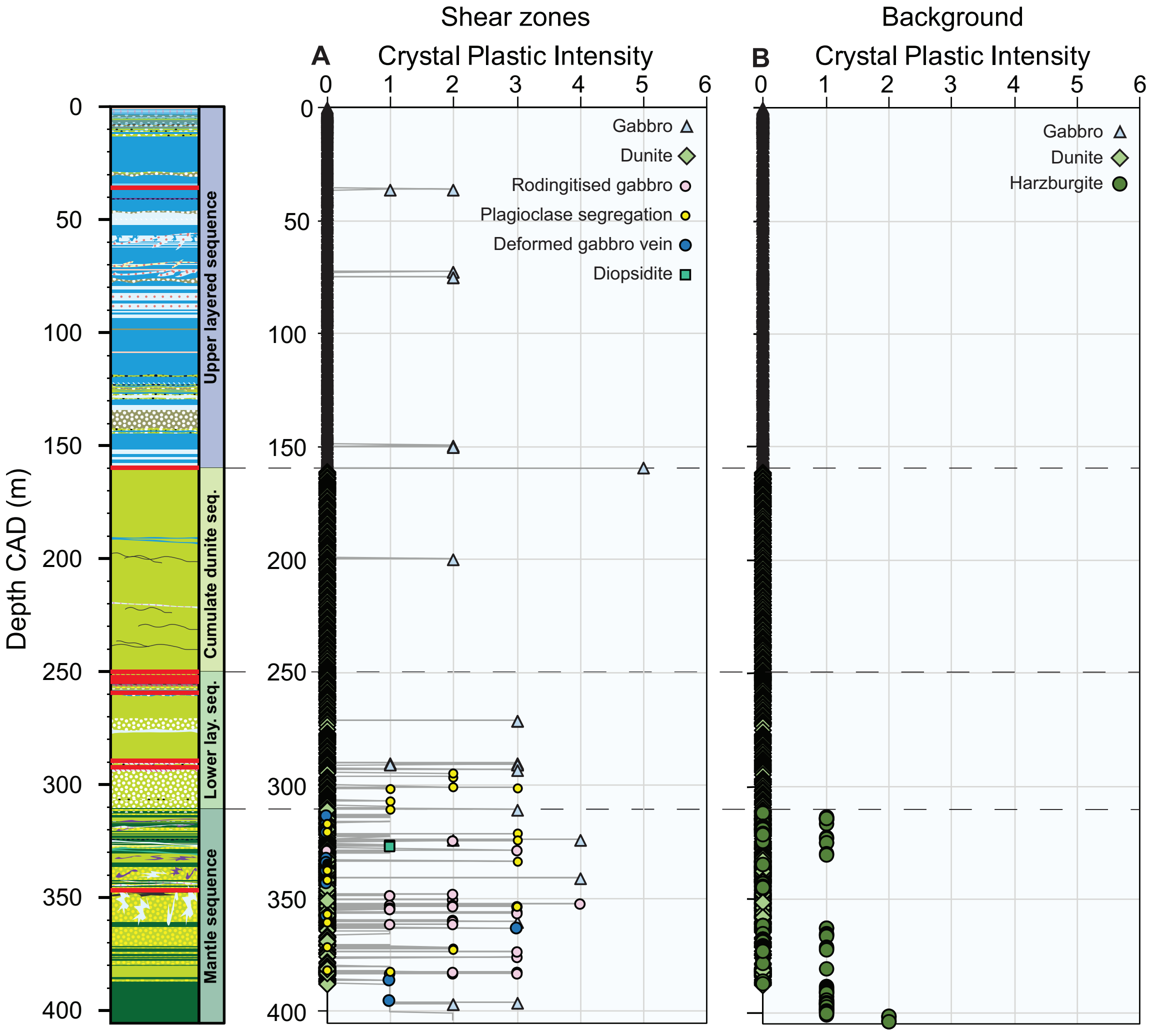

Figure F65. Semibrittle/crystal-plastic fabrics, Hole CM1A. Red arrows indicate up. **A, B.** Interval 63Z-4, 0–35 cm. (A) Contact between the Layered Gabbro Sequence and Dunite Sequence. Blue = shearing within the dunite parallel to faulting; red = reverse imbricate faulting within the foliated cataclastic gabbro; yellow = rotated, relict magmatic foliation in altered layered gabbros. (B) Contact of the foliated cataclasite and dunite. Dark band in center of thin section is the foliated cataclasite. Asymmetric sidewall cutouts visible on the right-hand side of the dark layer. **C.** Coarse-grained olivine gabbro showing incipient crystal-plastic foliation. **D.** Two 1 cm wide semibrittle foliated cataclasites sandwiching an extensionally faulted gabbro layer (119Z-3, 24–40 cm).

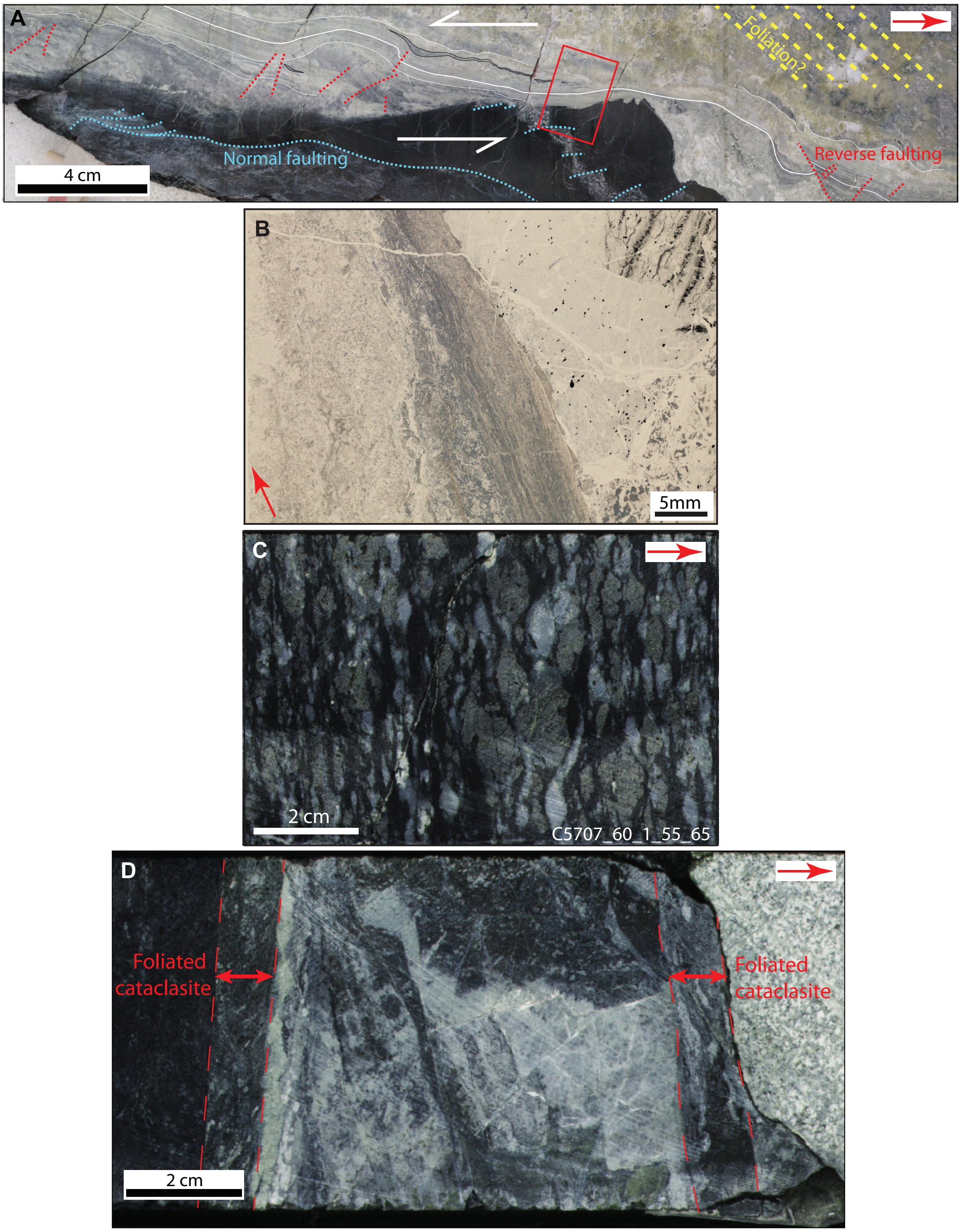

Figure F66. Crystal-plastic fabric in harzburgite, Hole CM1A. Red dashed lines give the orientation of the fabric as defined by oriented, elongate orthopyroxene.

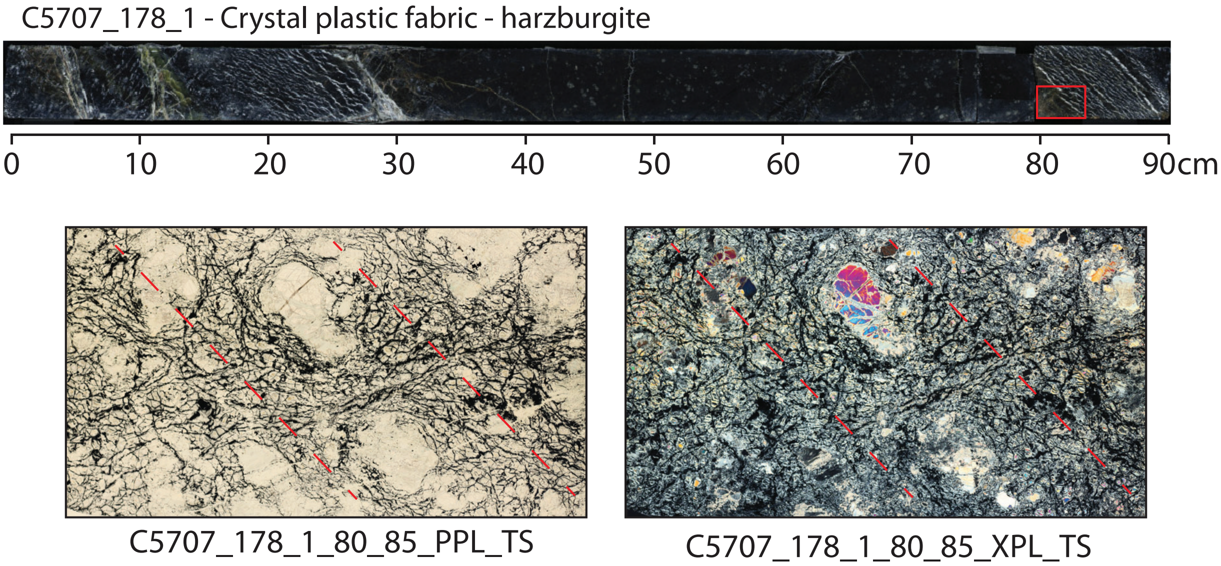

Figure F67. Dip of porphyroclastic harzburgite fabric in the Mantle Sequence and plagioclase segregations in the Mantle Sequence and lower part of the Dunite with Gabbro Sequence, Hole CM1A.

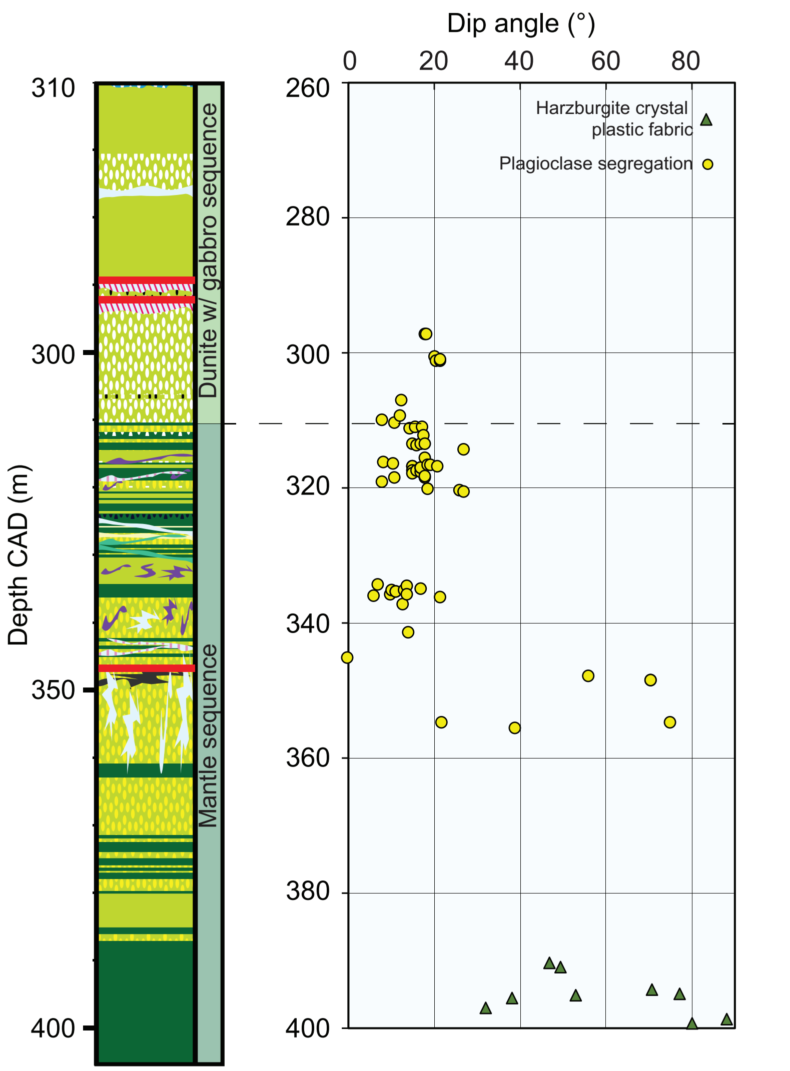

Figure F68. Downhole plot of fracture density, deformation intensity, vein density, and depth of different types of fault zone, Hole CM1A. Yellow dashed line marks the location of the boundary between the Layered Gabbro Sequence and the ultramafic sequences.

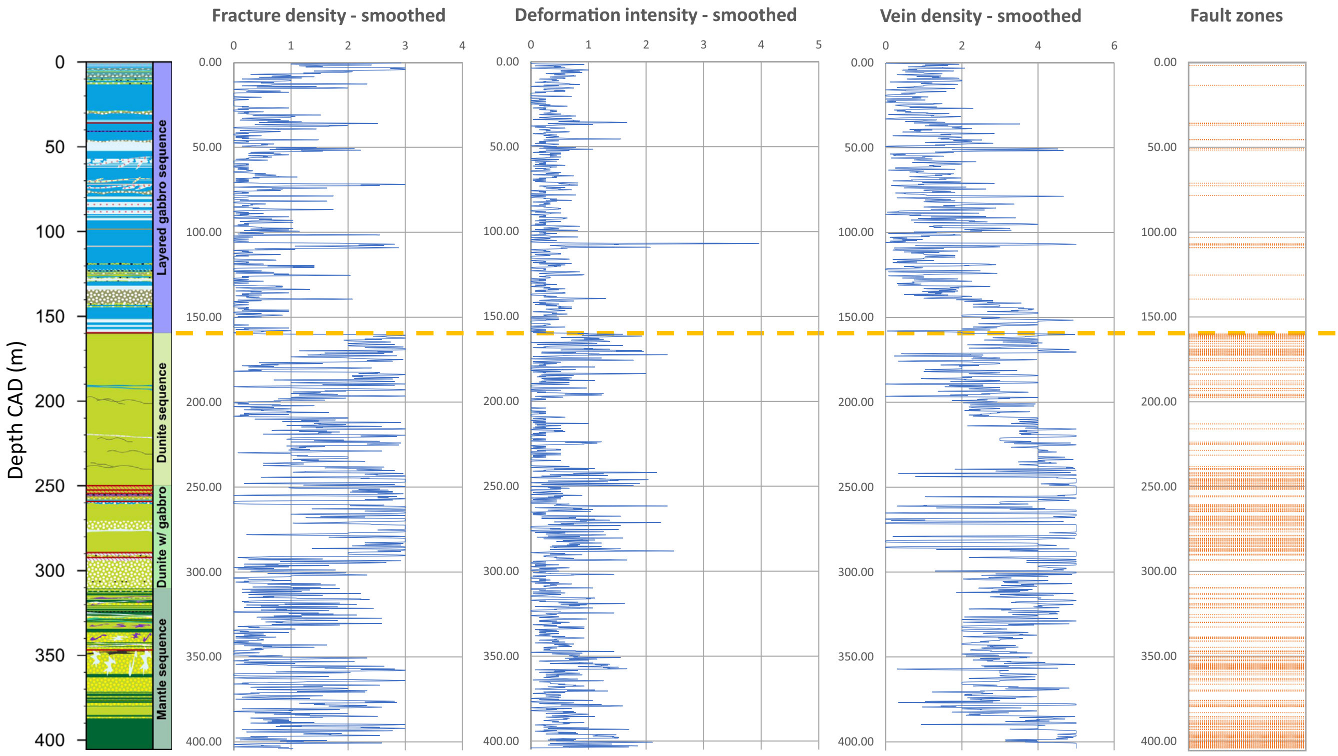

Figure F69. Example of the crosscutting relationships in the ultramafic sequence, Hole CM1A. V2: black serpentine-magnetite veins; V3: 0.1 mm wide chrysotile-carbonate veins and 1 mm wide chrysotile veins; V4: 1–4 mm wide green serpentine formed in the center of the wider V2 serpentine vein. V3 generation veins are observed as extensional and shear veins, with the former primarily perpendicular to V2 and the latter parallel to V2. V3 veins that are parallel to V2 are observed reactivating preexisting V2 orientations. V4 is fractured in this example and is observed with a shear fracture (slickenside) and extensional fracture morphology. V4 is observed within preexisting V2 and V3 veins, suggesting reactivation of preexisting features.

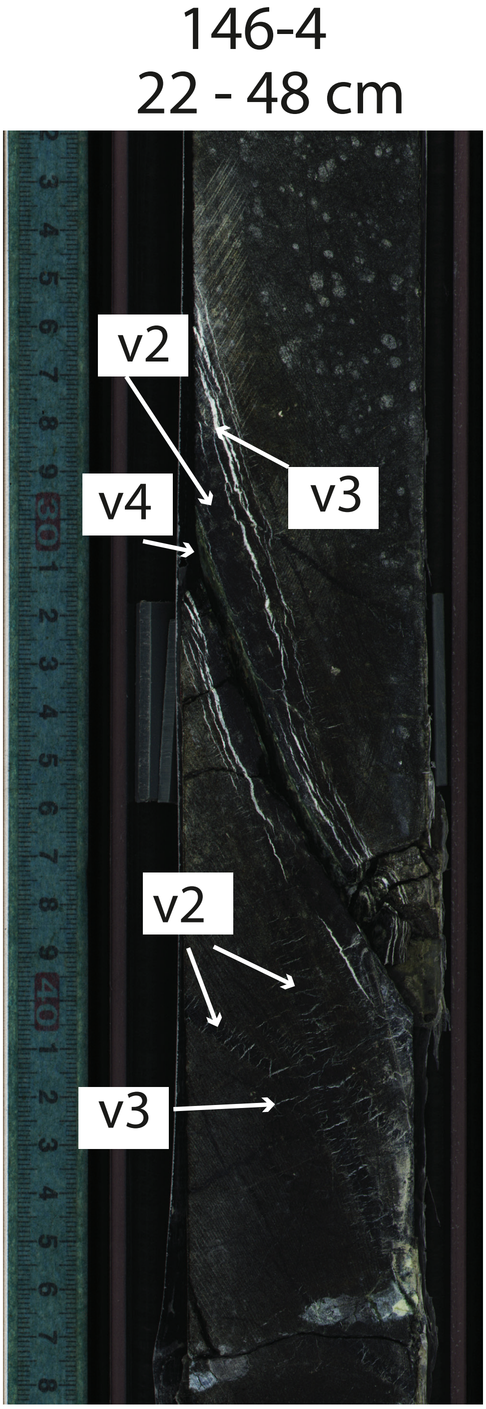

Figure F70. V3 extension veins crosscutting normal to altered gabbro vein orientation, Hole CM1A. Composition of V3 veins contrast based on lithology, with chrysotile-carbonate compositions in the dunite and chlorite-serpentine in the gabbro. Conical drilling-induced fracture is also present.

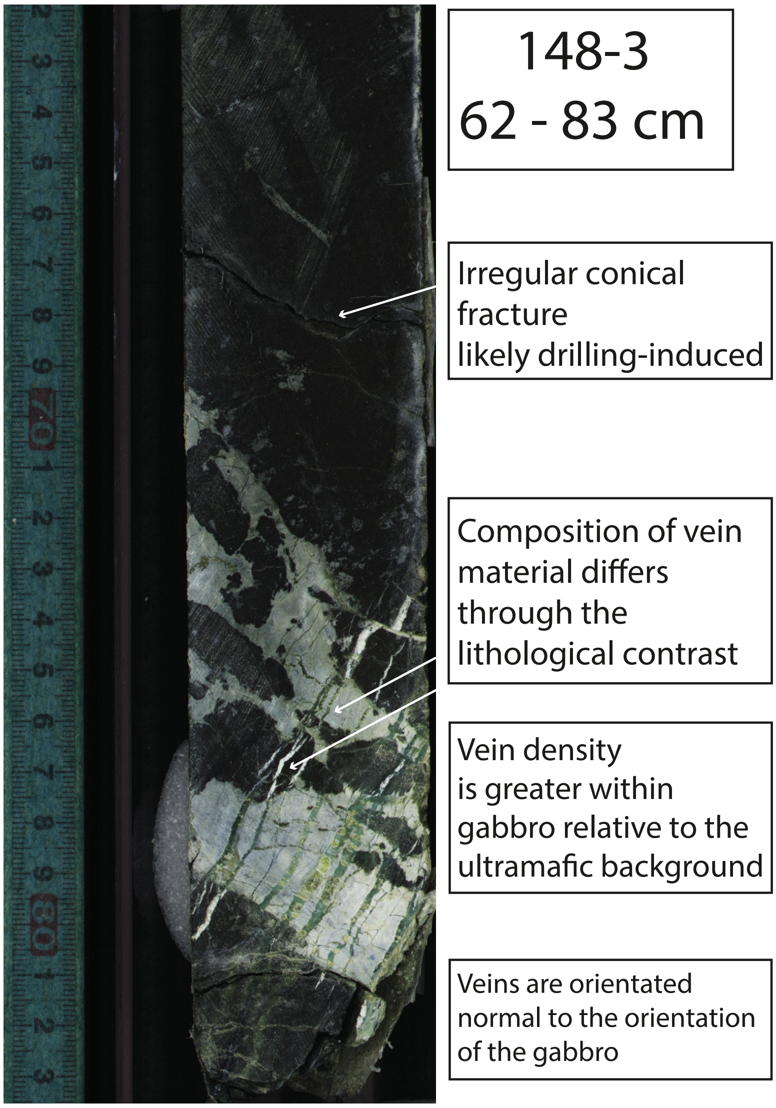

Figure F71. Vein dip angle plot and frequency diagrams of vein dip for the Layered Gabbro Sequence, Dunite Sequence, three ultramafic sequences, and for the combined data set, Hole CM1A. Yellow dotted line on frequency diagrams gives the distribution of dips expected for randomly oriented fractures. Yellow dashed line marks the location of the boundary between the Layered Gabbro Sequence and the ultramafic sequences.

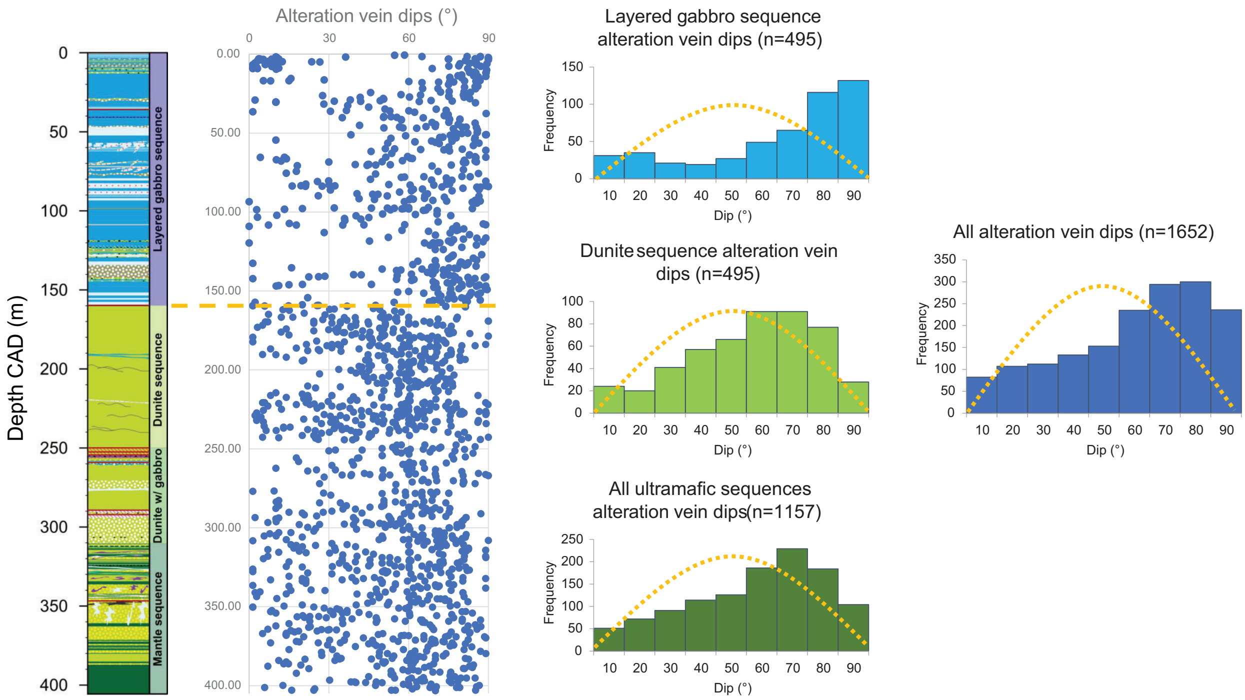

Figure F72. Alteration vein dip angle in the Layered Gabbro Sequence by vein mineralogy/composition, Hole CM1A.

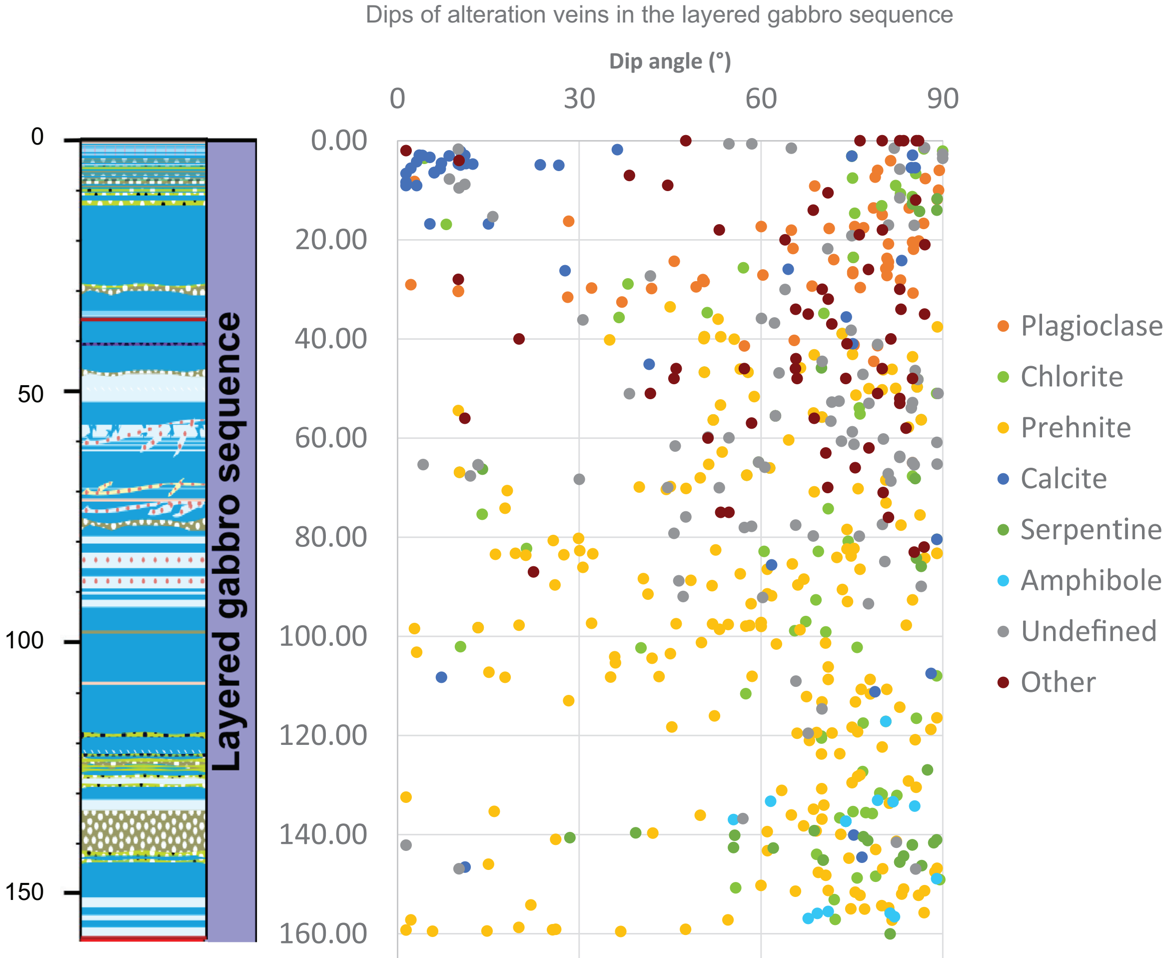

Figure F73. Frequency diagrams of vein dip angle for different vein mineralogy/composition in the Layered Gabbro Sequence, Hole CM1A.

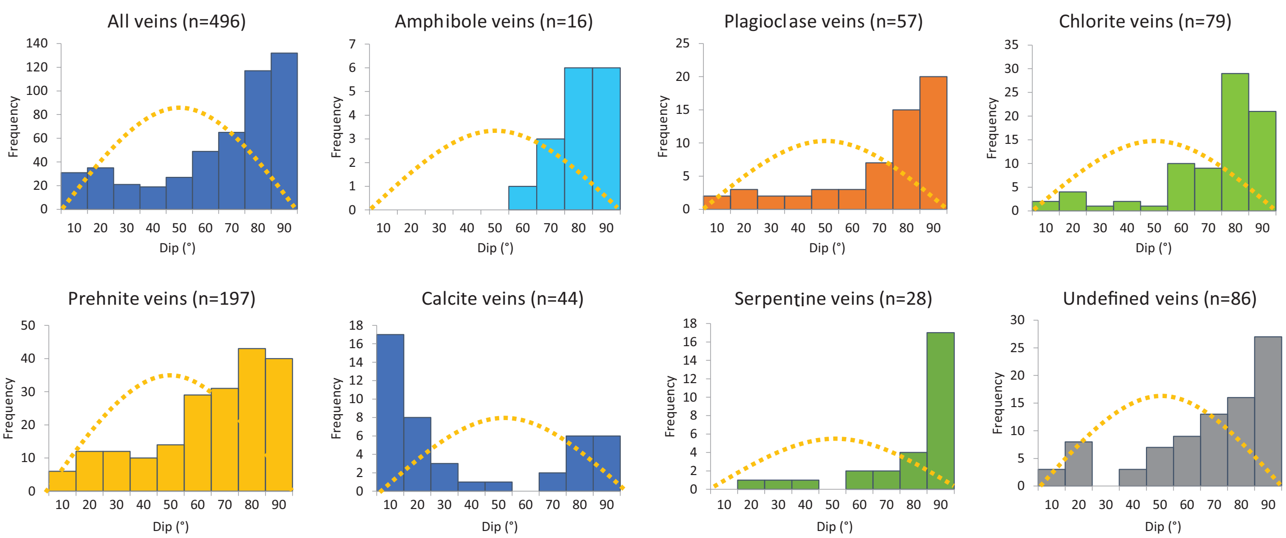

Figure F74. Vein dip angle in the 3 ultramafic sequences, Hole CM1A. The dip angles for each of the 4 serpentine vein generations (V1, V2, V3 and V4) are shown.

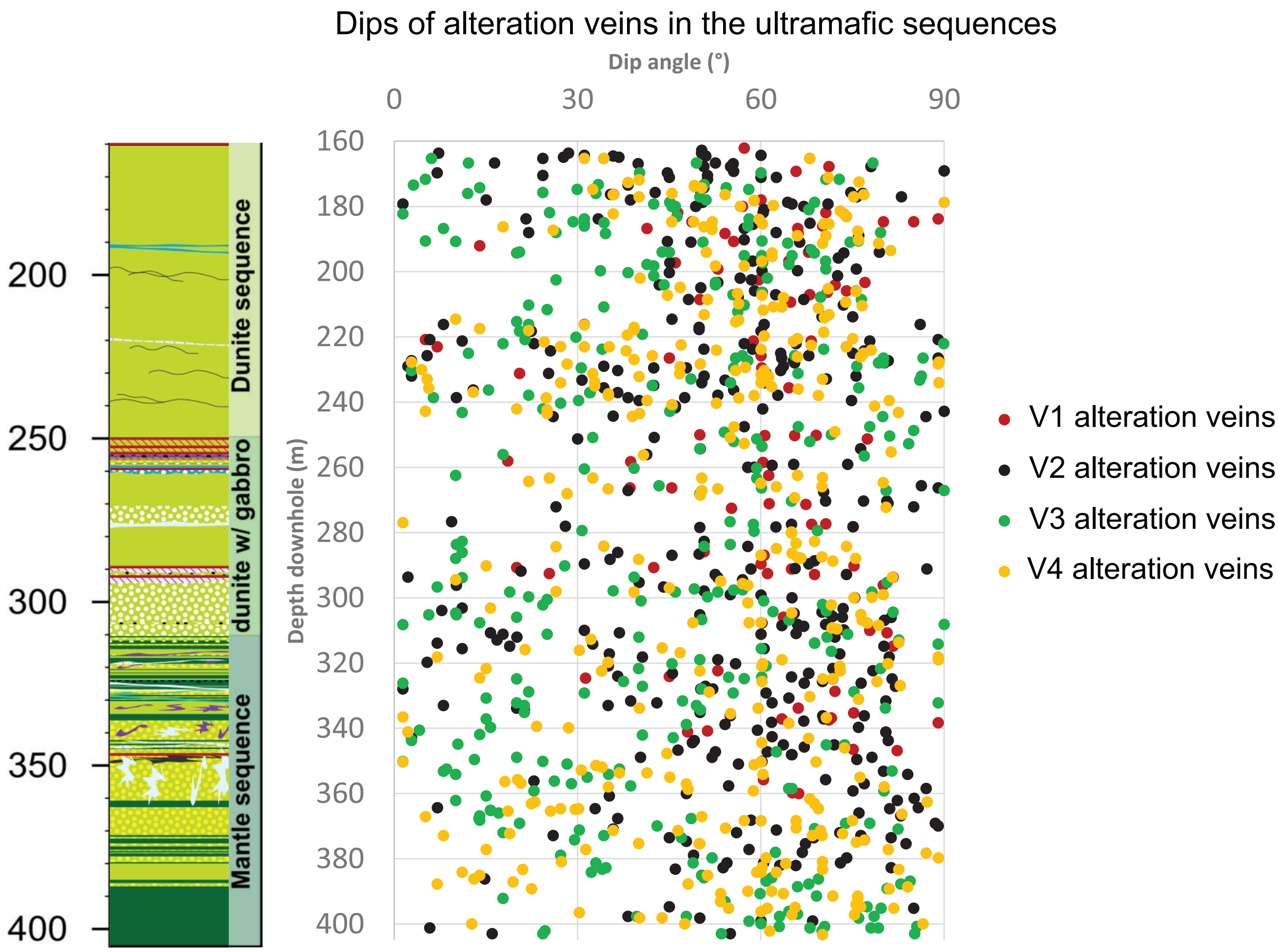

Figure F75. Frequency diagrams of the vein dip angles in the 3 ultramafic sequences for each of the 4 serpentine vein generations (V1, V2, V3, V4), Hole CM1A.

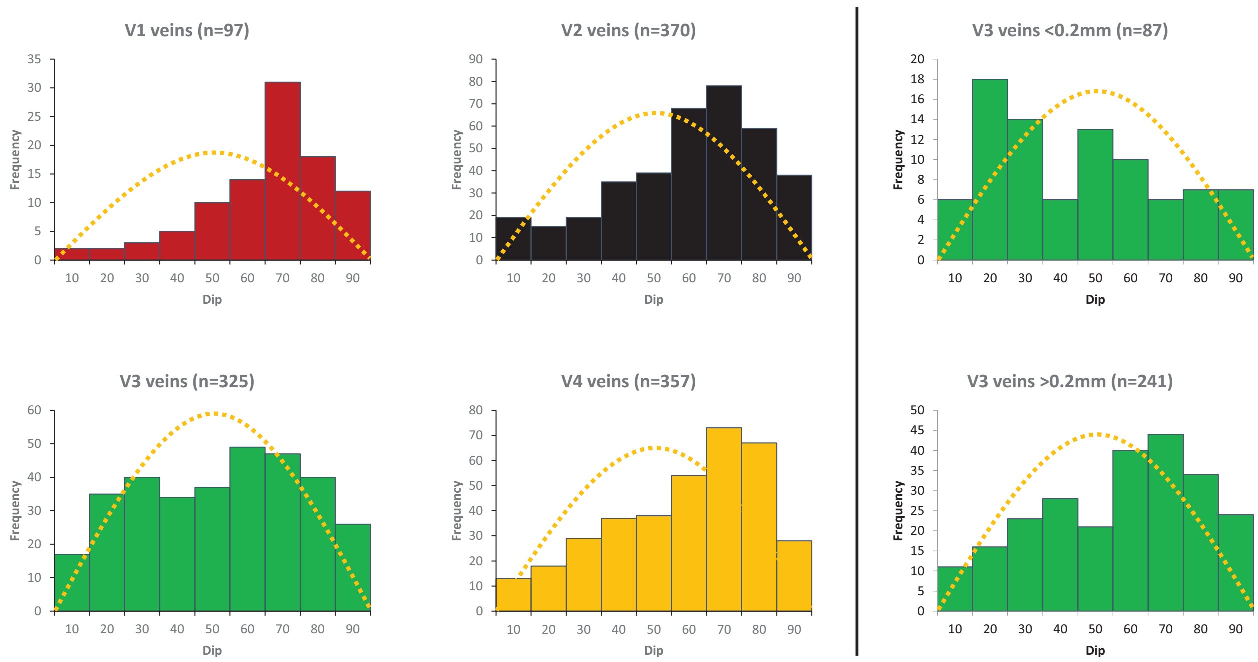

Figure F76. Five examples of fractures, Hole CM1A. **A–D.** Typical straight fracture morphology that crosscuts irregular conical, probably drilled-induced fractures. Some irregular fractures have precipitated V3 vein material composed of chryostile-carbonate with a width of ~ 0.1 mm. **E.** Irregular conical drilling-induced fractures in gabbro.

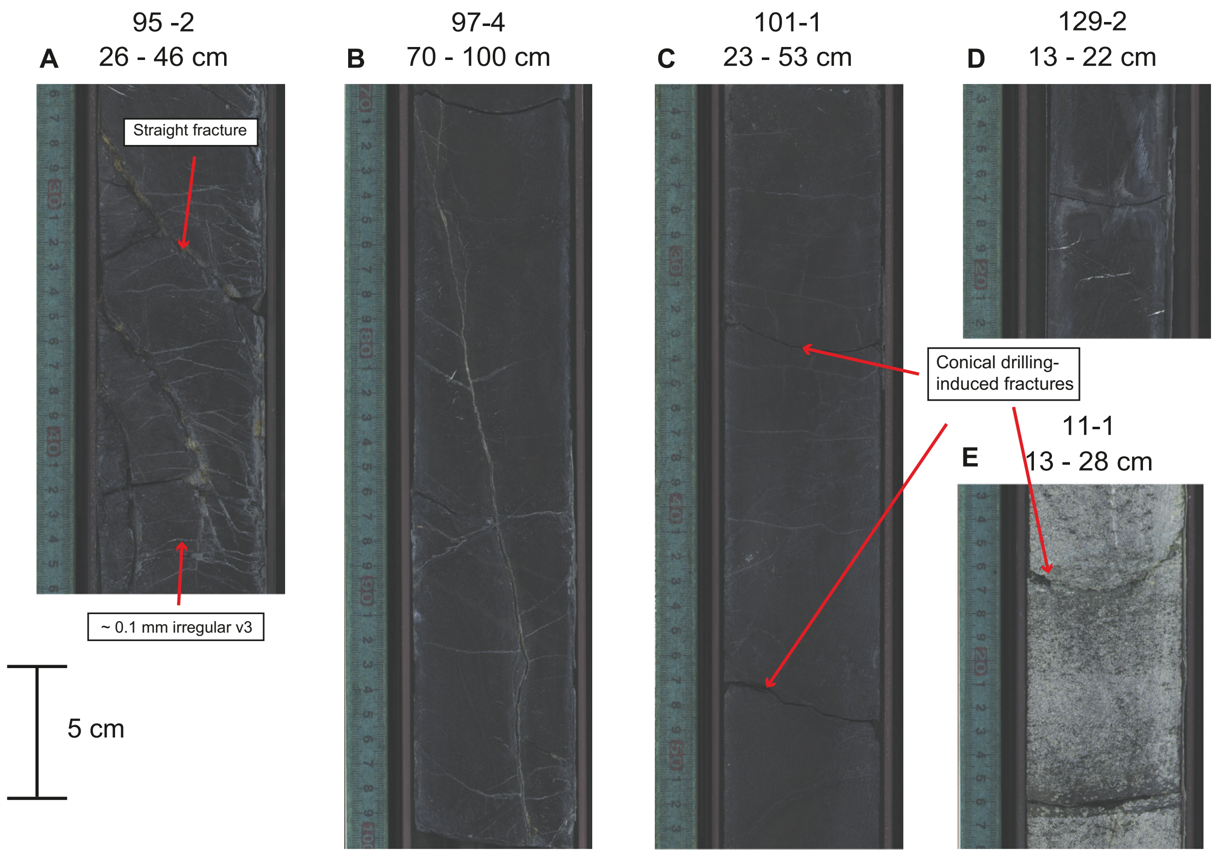

Figure F77. Downhole plot of fracture dip angles, Hole CM1A, with frequency diagrams of fracture dip angles for the Layered Gabbro Sequence, ultramafic sequences, and for the combined dataset. Yellow dotted line on frequency diagrams gives the distribution of dips expected for randomly oriented fractures. Yellow dashed line marks the location of the boundary between the Layered Gabbro Sequence and the ultramafic sequences.

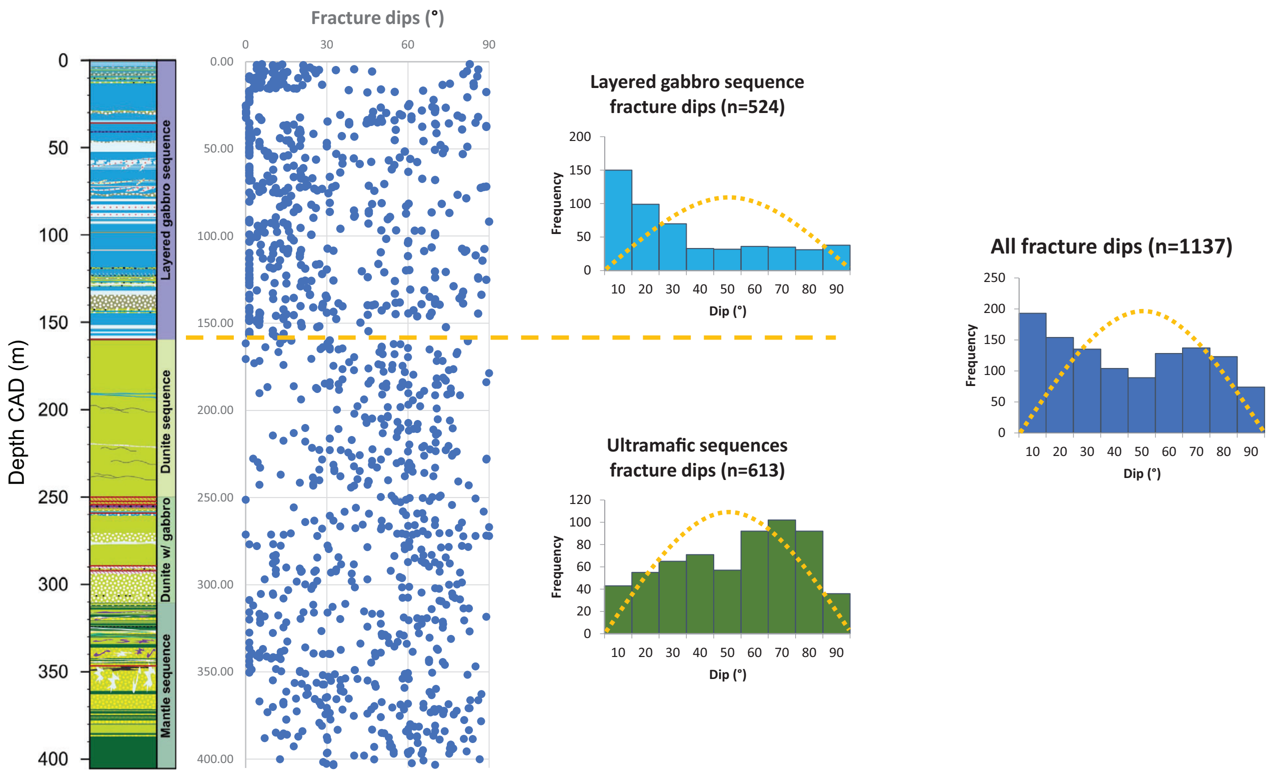

Figure F78. Downhole plot of slickenline plunge and sense of shear, Hole CM1A (see Table T6). Yellow dashed line marks the location of the boundary between the Layered Gabbro Sequence and the ultramafic sequences. Frequency diagrams of slickenline plunge for the Layered Gabbro Sequence, the three ultramafic sequences and for the combined data set. Yellow dotted line on frequency diagrams gives the distribution of dips expected for randomly oriented fractures.

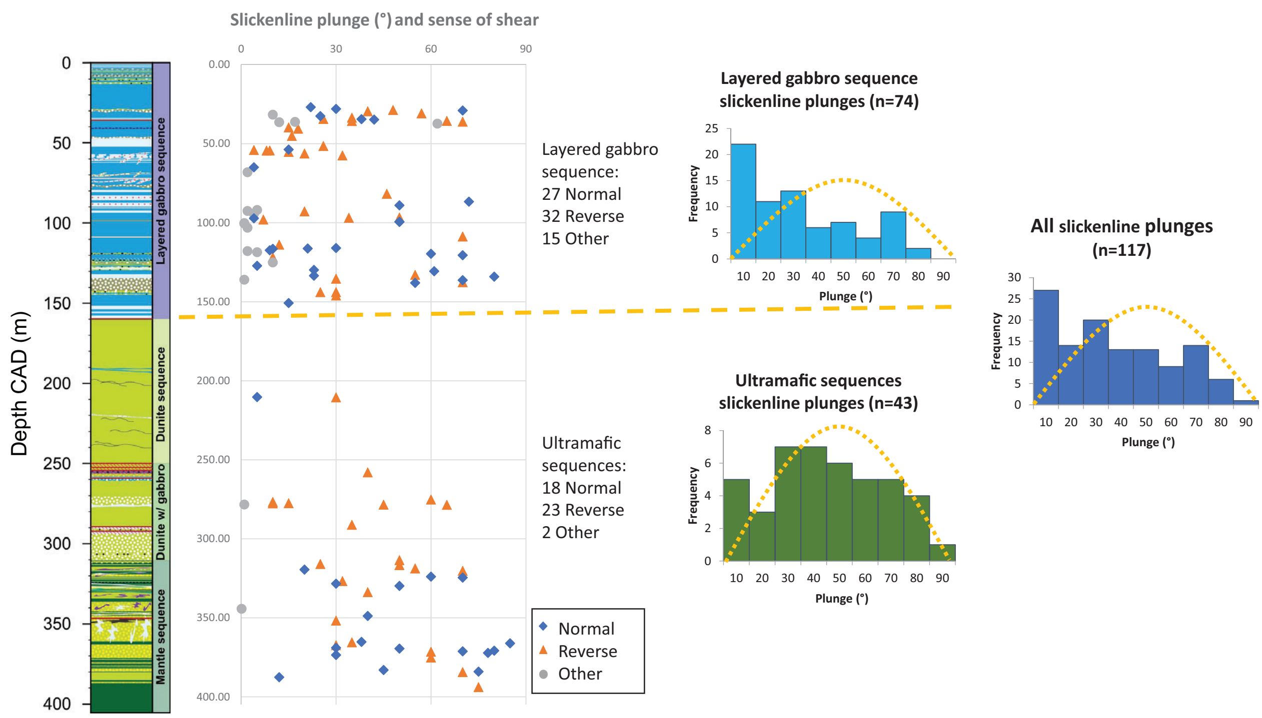

Figure F79. Deformed diopsidite vein adjacent to serpentinized dunite, with cohesive cataclasite forming in fine-grained matrix (gray), Hole CM1A. Serpentine veins crosscutting the cohesive cataclasite display crack-seal/stretching vein morphology suggesting successive crack-seal events and precipitation episodes of a preexisting feature.

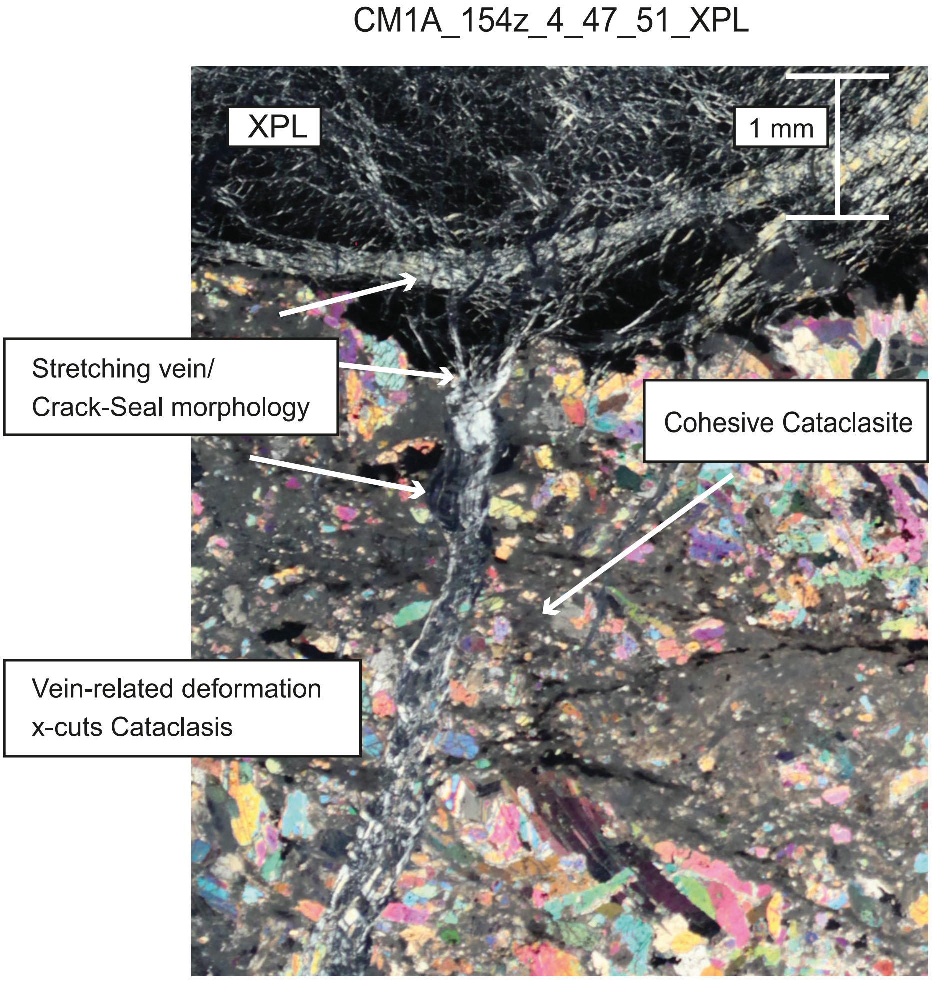

Figure F80. Dip angle frequency plots of planes hosting measured slickenlines and alteration veins from the Layered Gabbro Sequence, the ultramafic sequences, and the combined dataset, Hole CM1A. Yellow dotted line on frequency diagrams gives the distribution of dips expected for randomly oriented fractures.

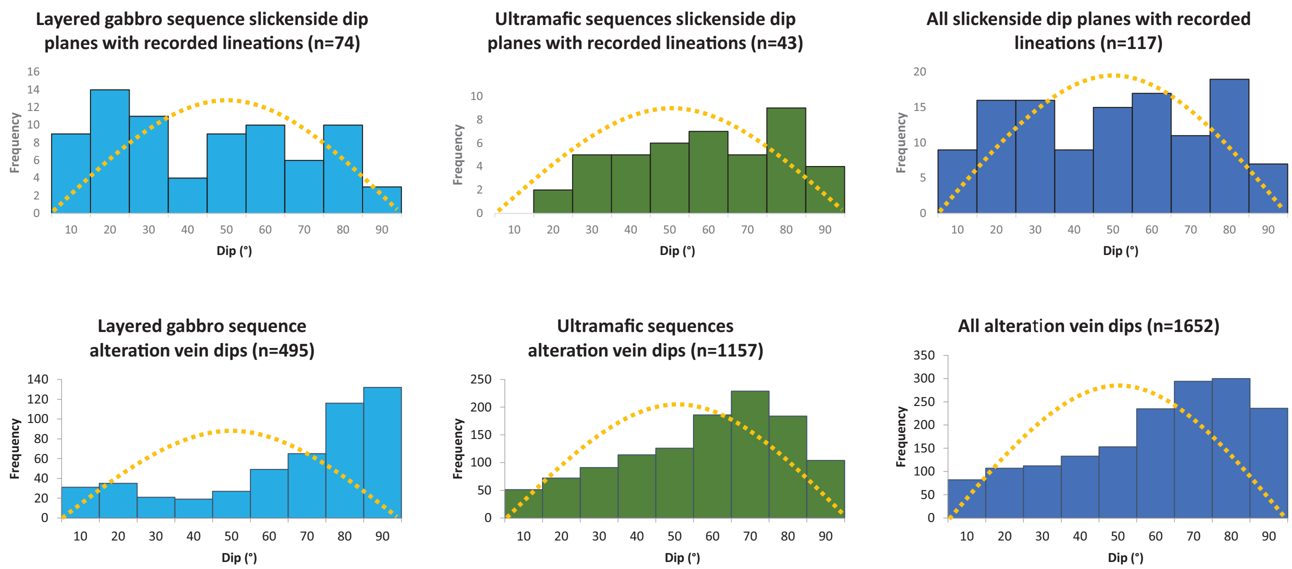

Figure F81. Downhole distribution of various fault types as interpreted from the core, Hole CM1A. **A.** Black = discontinuities between sections of core. **B.** Location of fault zones measured in the core (see Figure **F68**). **C–F.** Interpreted depths and thicknesses of various fault zone types: (C) orange = cohesive cataclasite; (D) blue = fault/vein fracture network; (E) green = incohesive cataclasite; (F) yellow = surface-related deformation. **G.** Red = location of fault zones plotted against the relative brittle intensity of deformation associated with each fault zone.

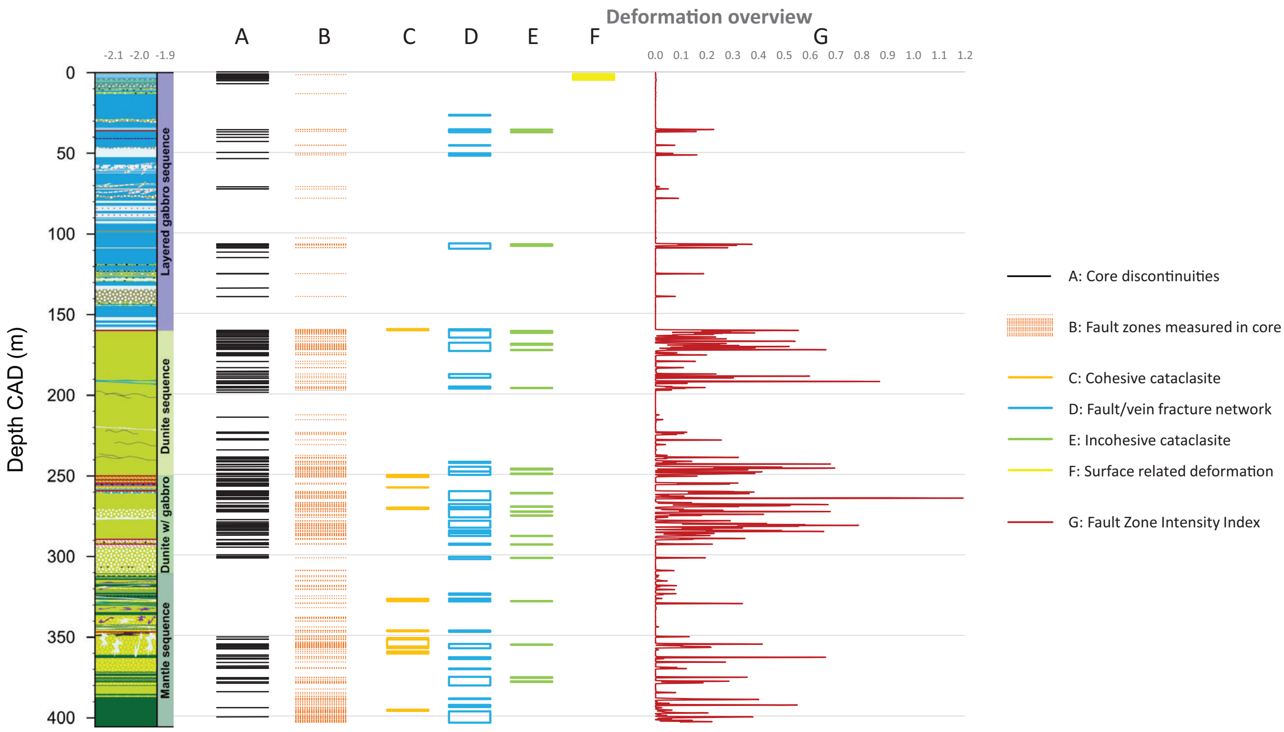

Figure F82. **A.** Vein surface showing subvertical slickenlines on a V4 slickenside plane, Hole CM1A. **B, C.** Two generations of extensional faulting of gabbro layer in dunite, layer-parallel extension.

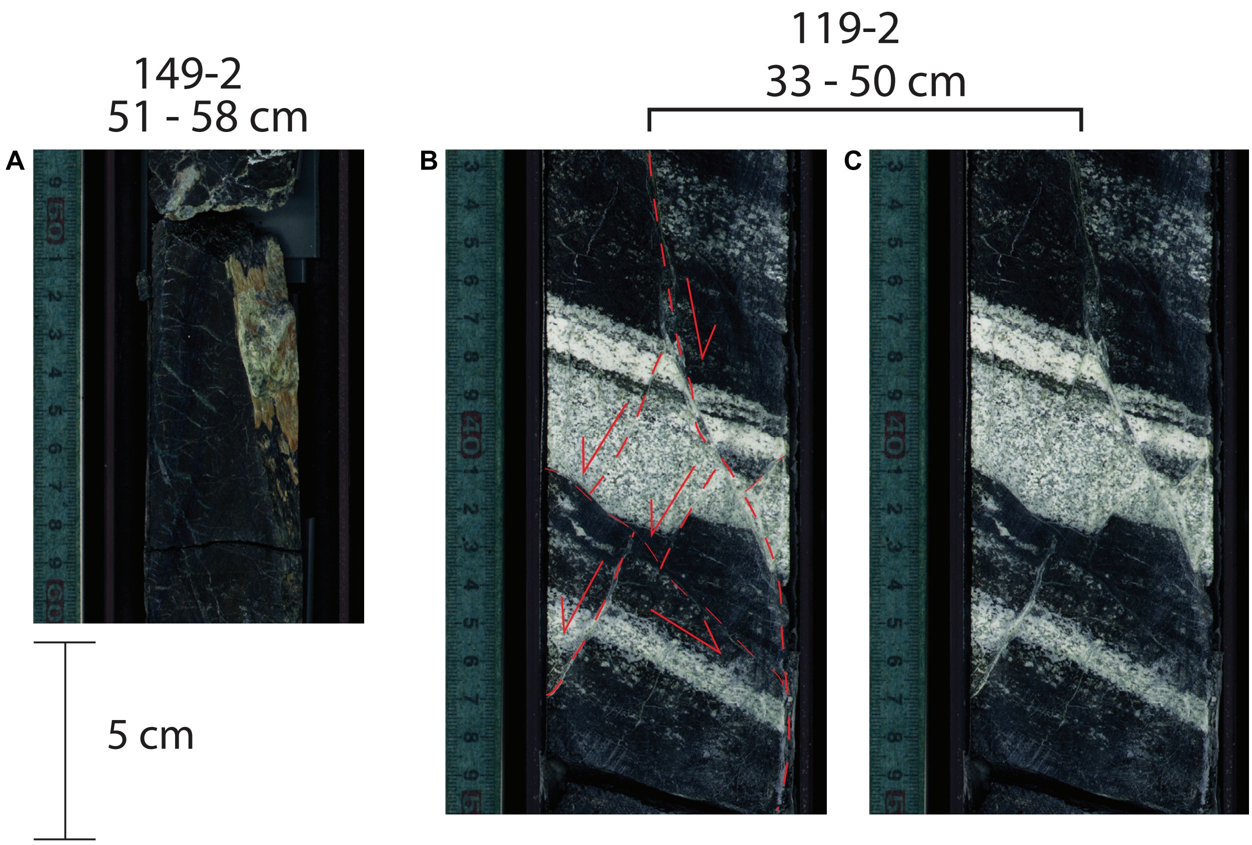

Figure F83. A, B. 10 cm wide zone of brecciation of thin gabbro layer in the Dunite with Gabbro Sequence, shown on (A) cut face of the archive half and (B) reverse side of the working half, Hole CM1A. The zone is bounded by two 1 cm wide foliated cataclasite layers. **C, D.** Example of a δ-porphyroclast sense of shear indicator within the brecciated layer (119Z-3, 23 cm).

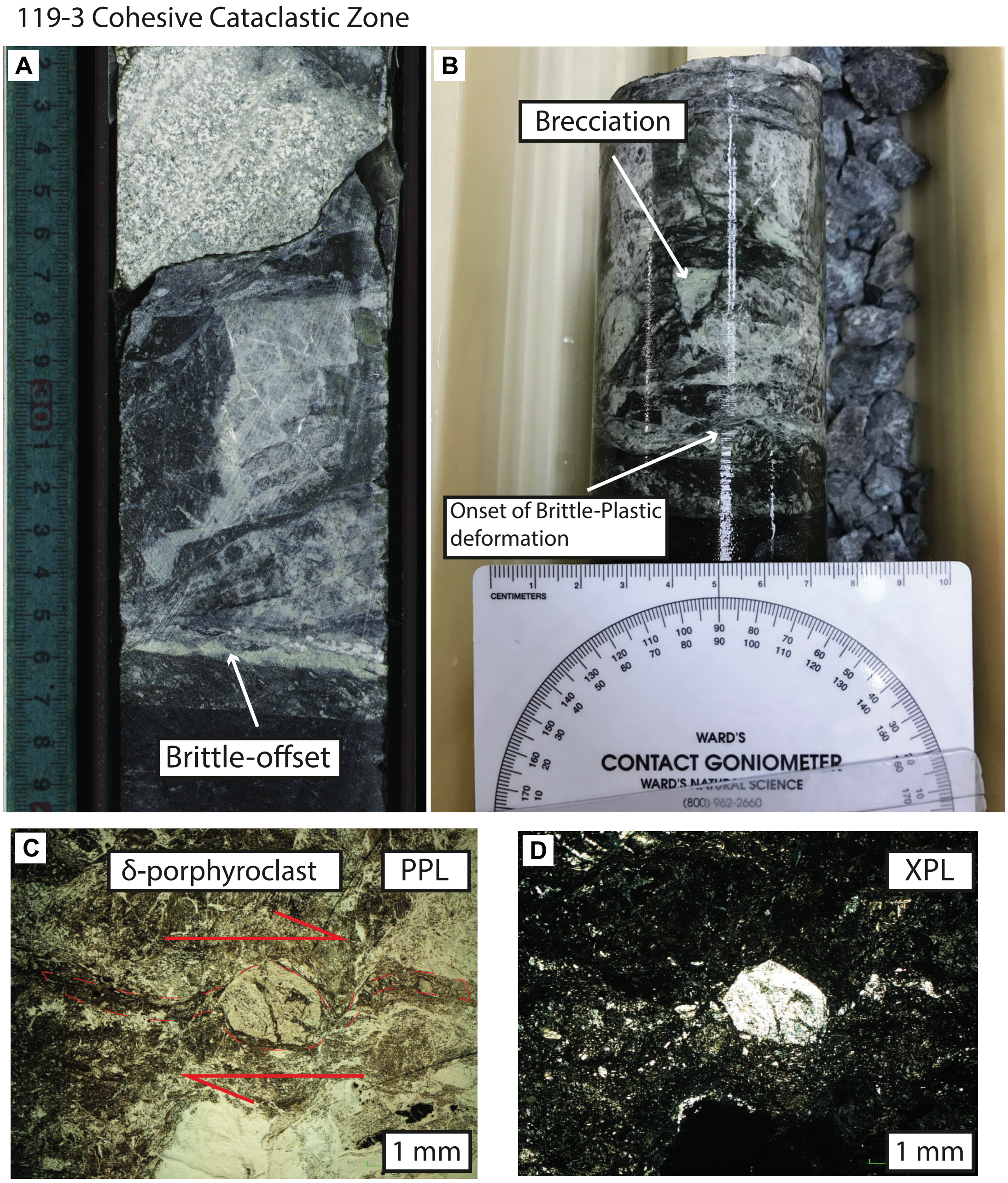

Figure F84. Semibrittle deformed altered gabbro; gray areas in photomicrograph highlight clear cohesive cataclasis, Hole CM1A. (See **Gray gabbro veins and patches**.)

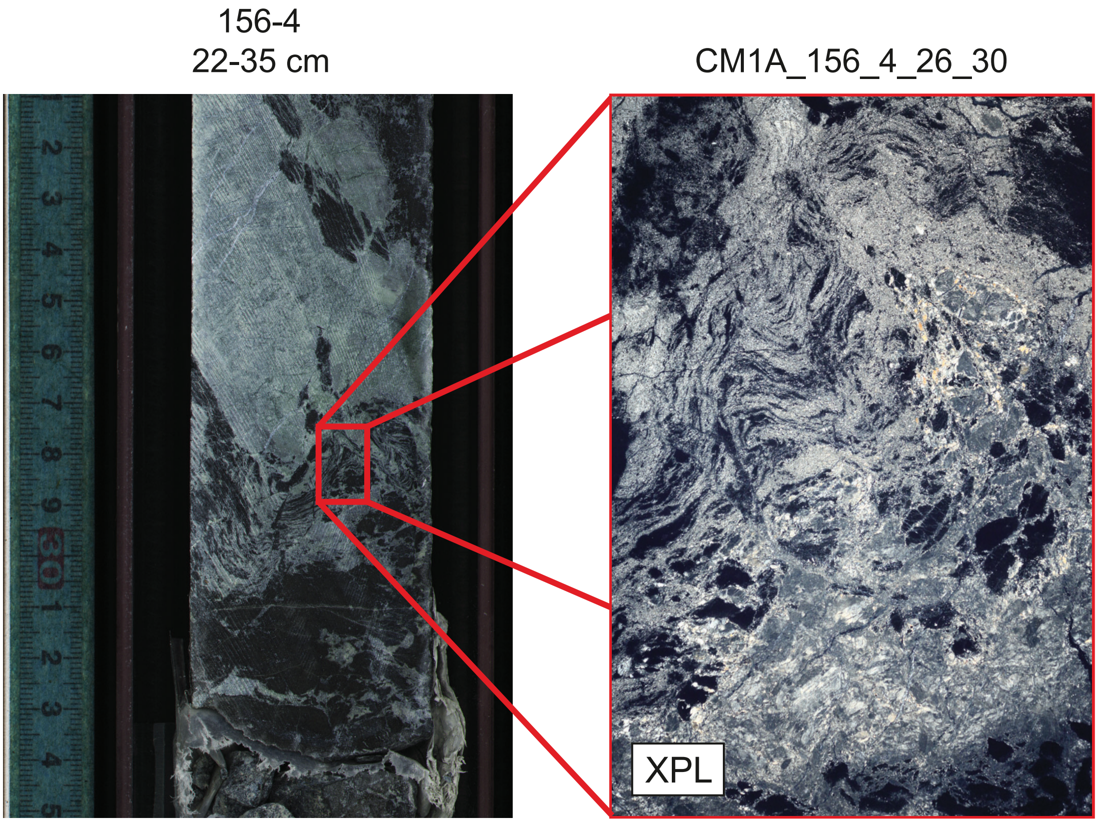

Figure F85. A–D. Examples of (A, B) vein-related brittle deformation and (C, D) incohesive cataclasis in the Layered Gabbro Sequence illustrating that these 2 styles of deformation can occur in close proximity, Hole CM1A.

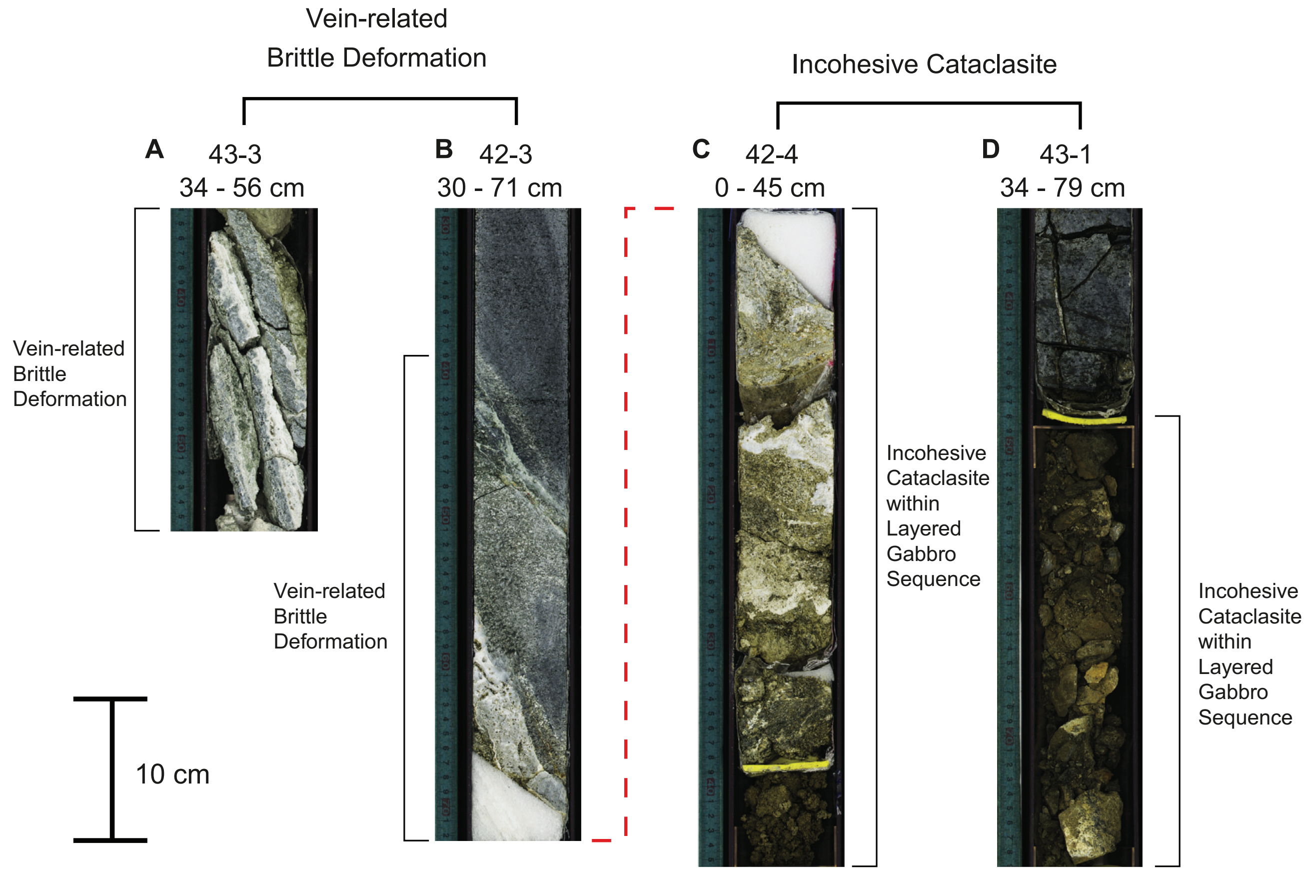

Figure F86. Example of vein-related brittle deformation and incohesive cataclasis in the ultramafic sequences, Hole CM1A. **A.** Vein-related deformation forming a fault-fracture network of chrysotile-carbonate veins. **B.** Incohesive cataclastic zone at 51–78 cm; vein-related deformation above at 19–50 cm. **C.** Incohesive cataclastic zone in dunite.

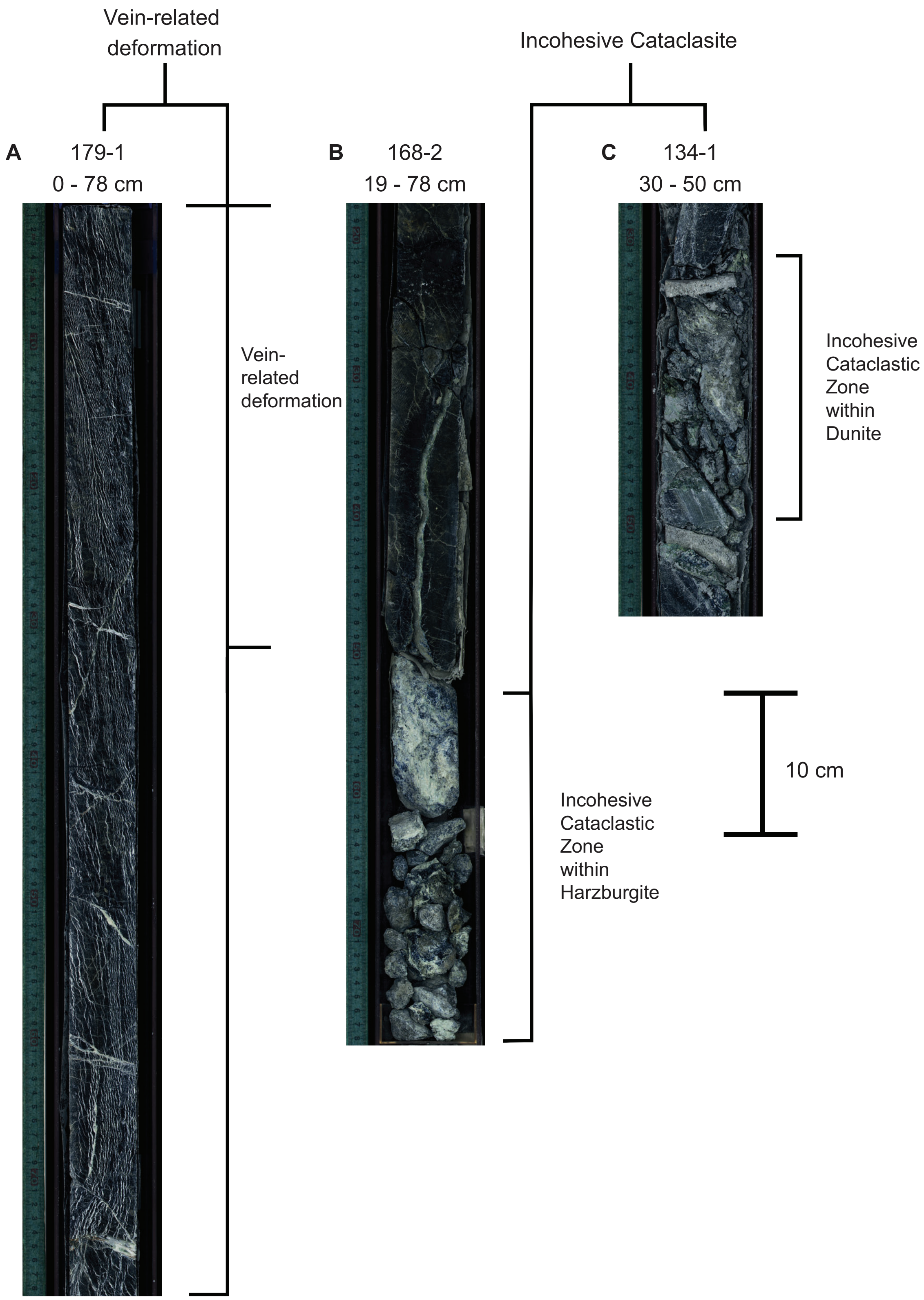

Figure F87. Comparison of the dip of the mineral foliation/layering of gabbro from Holes GT1A, GT2A, and CM1A, illustrating the presence of cycles of increasing dip followed by decreasing dip. The approximate wavelength of the cycles given by the red numbers.

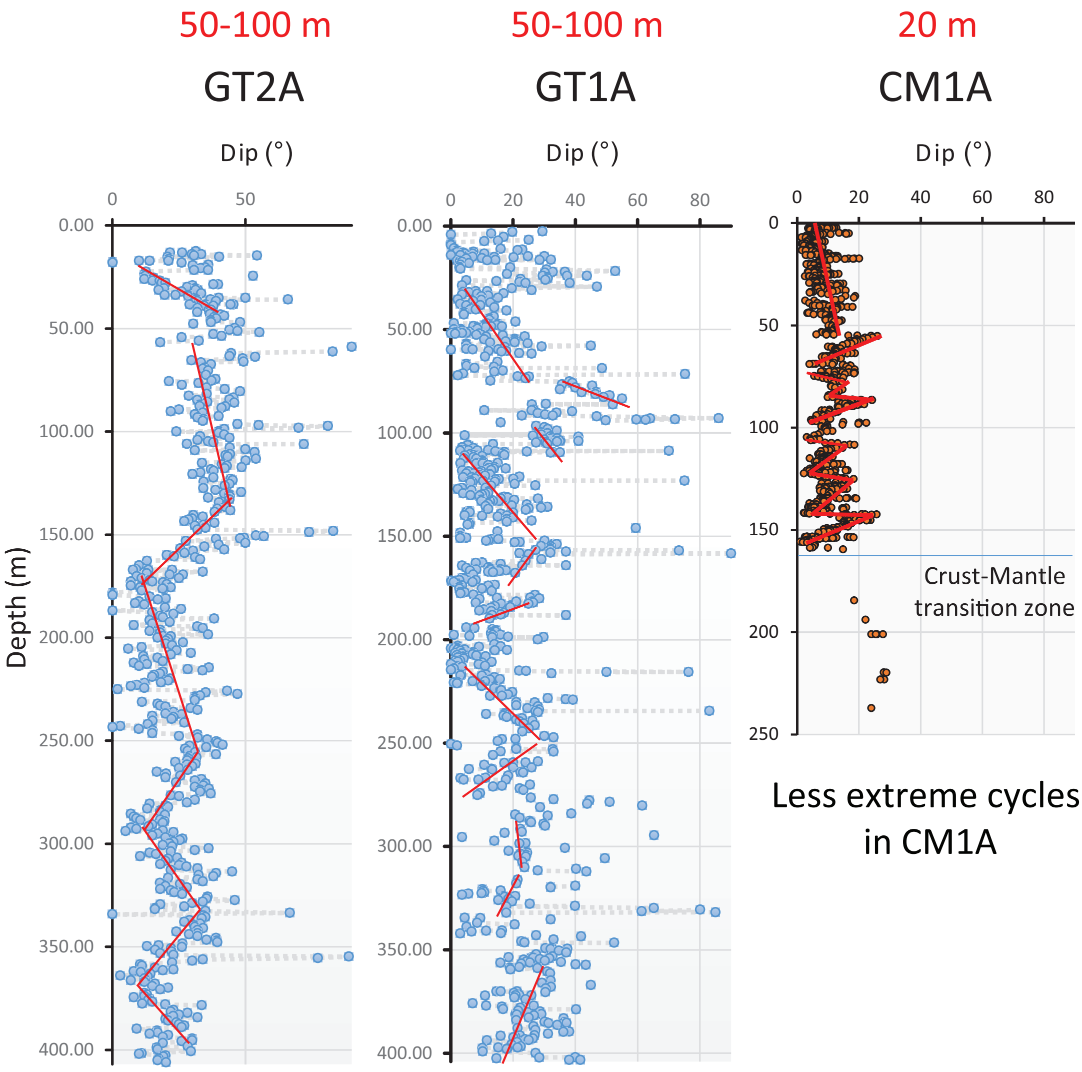

Figure F88. (A) Inorganic carbon (IC), (B) CO_2, and (C) H_2O contents vs. LOI, Hole CM1A.

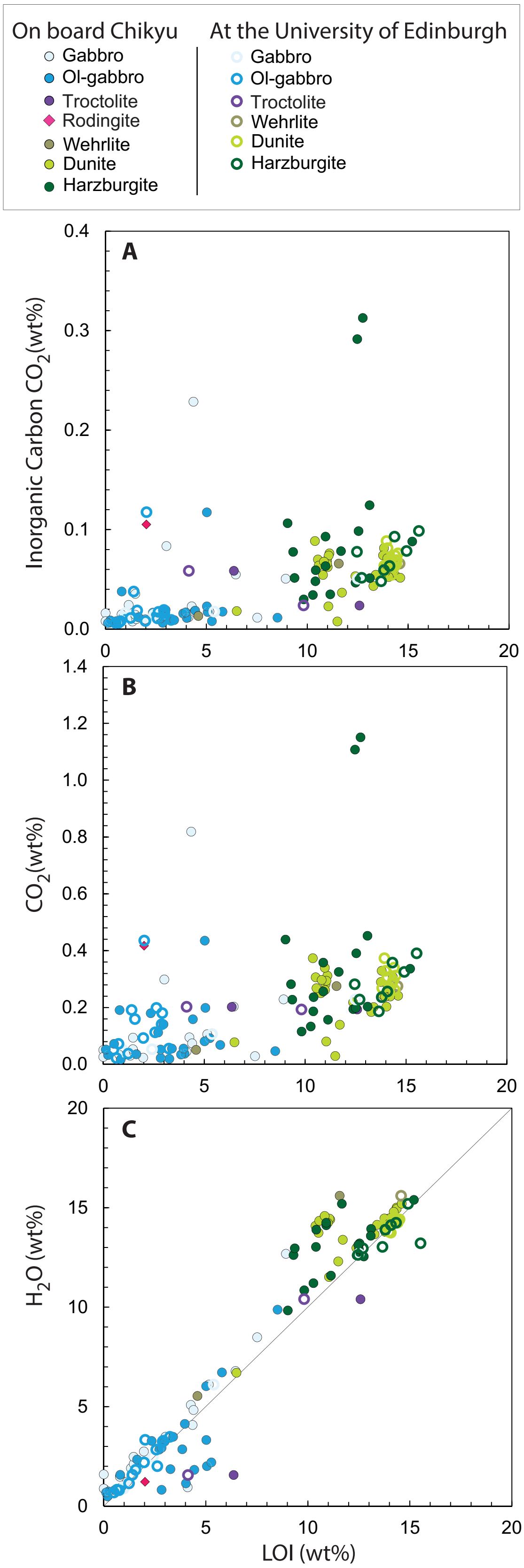

Figure F89. Downhole plots of lithology, LOI, Mg# (cationic Mg/(Mg + Fe); calculated assuming all Fe as FeO), SiO_2, TiO_2, Al_2O_3, FeO, MgO, MnO, CaO, Na_2O, K_2O, P_2O_5, Cr, and Ni in whole-rock samples, Hole CM1A.

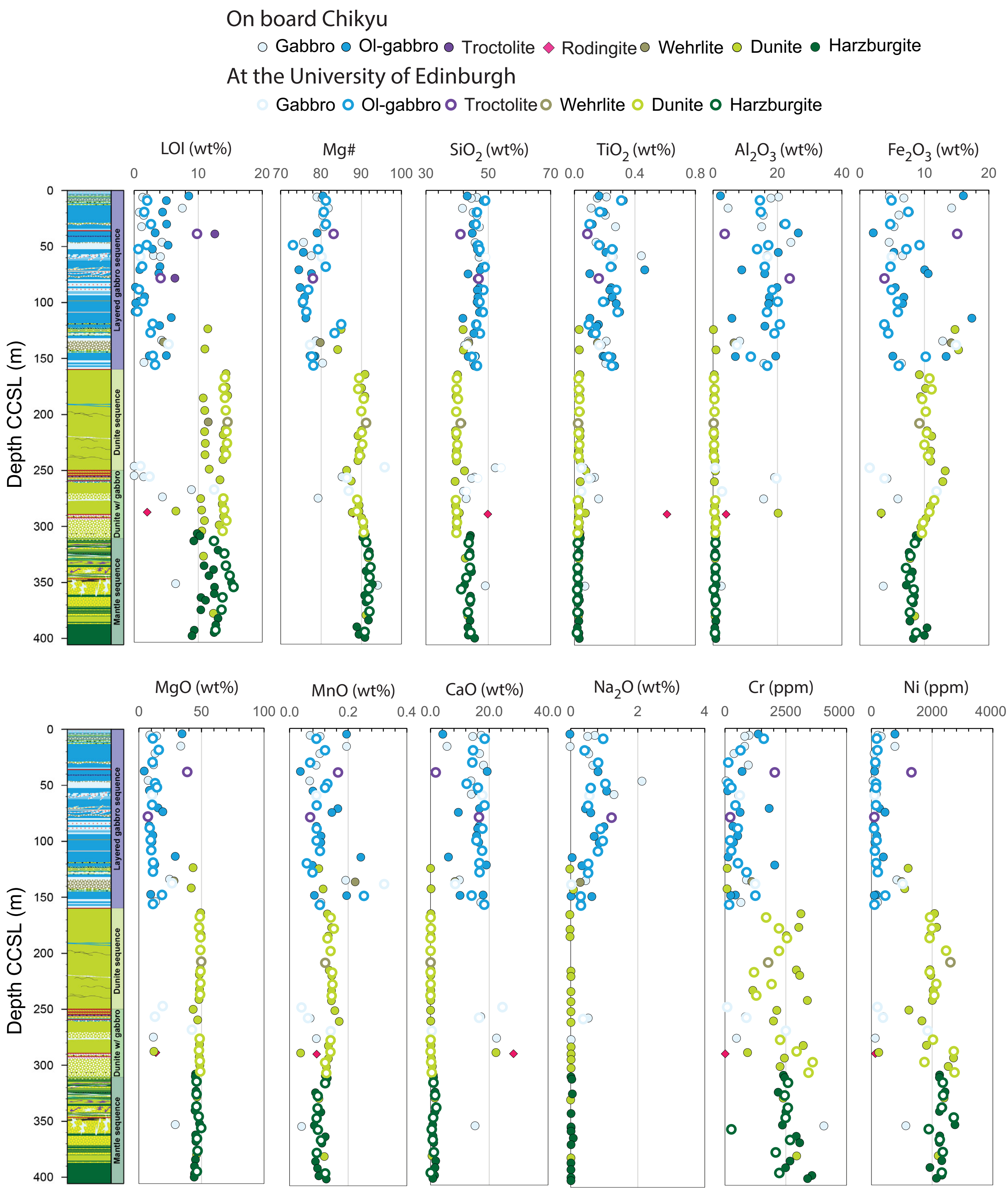

Figure F90. Downhole plots of lithology, LOI, Mg# (cationic Mg/(Mg + Fe); calculated assuming all Fe as FeO), SiO_2, TiO_2, Al_2O_3, FeO, MgO, MnO, CaO, Na_2O, K_2O, P_2O_5, Cr, and Ni in dunite and harzburgite samples recovered from CMTZ and Mantle Sequence, Hole CM1A.

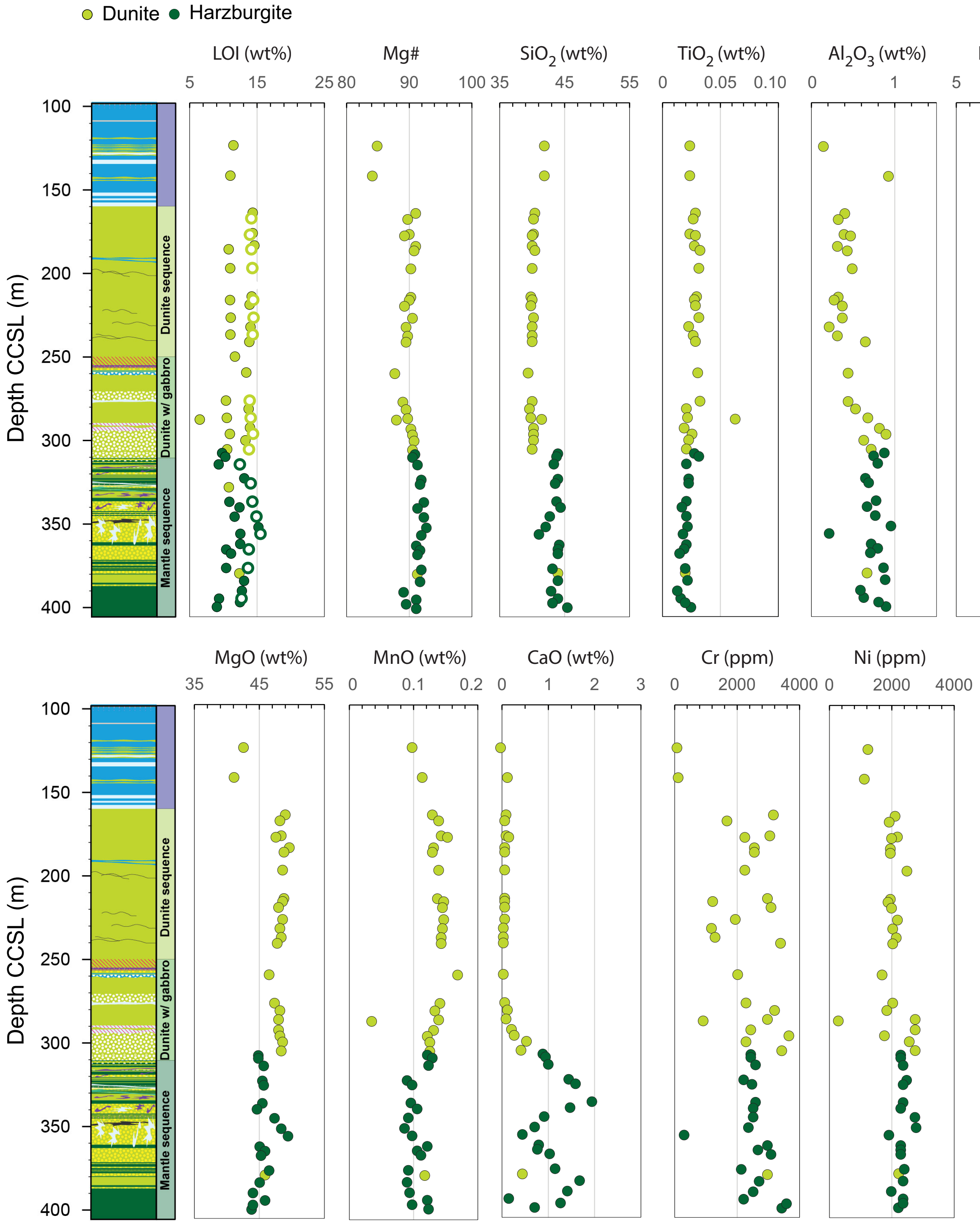

Figure F91. Whole-rock major and minor compositions, Hole CM1A: Mg# (cationic Mg/(Mg + Fe) calculated assuming all Fe as FeO) vs. SiO_2, TiO_2, Al_2O_3, FeO, MgO, MnO, CaO, Na_2O, K_2O, P_2O_5, Cr, and Ni.

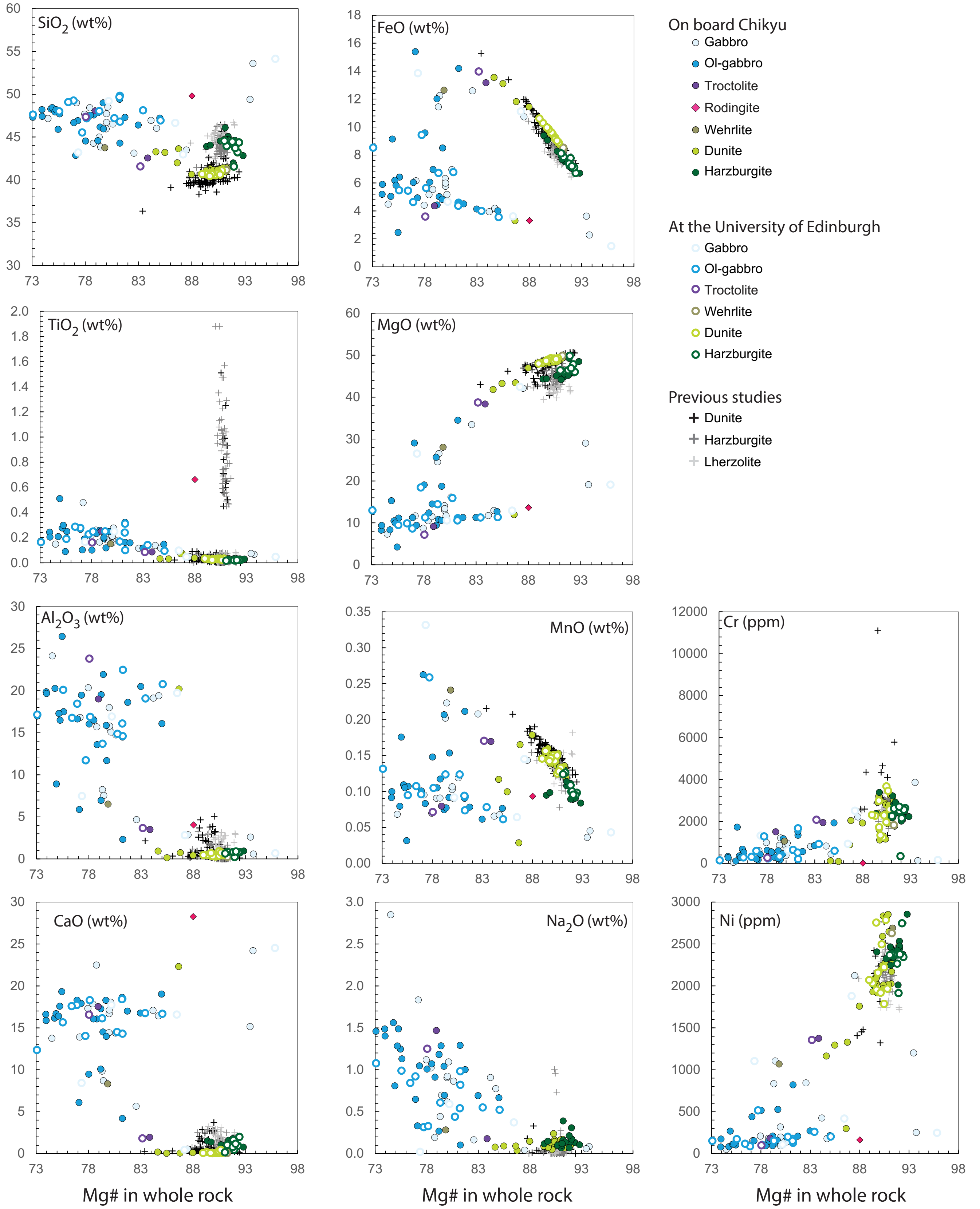

Figure F92. Whole-rock major compositions, Hole CM1A, compared to other dunites (+) and harzburgites/lherzolites (+) from the Oman ophiolite (Godard et al., 2000; Gerbert-Gaillard, 2002; Takazawa et al., 2003; Monnier et al., 2006; Hanghøj et al., 2010; Khedr et al., 2014; Nicolle et al., 2016; Rospabé et al., 2018). (**A**) MgO/SiO_2 vs. Al_2O_3/SiO_2, (**B**) total iron as FeO vs. MgO, and (**C**) Al_2O_3 vs. CaO. Compositions are recalculated on a volatile-free basis. Gray bar = silicate Earth differentiation trend (or "terrestrial array") (Jagoutz et al., 1979). Dashed gray lines = constant Mg# and Al_2O_3/CaO ratios, respectively.

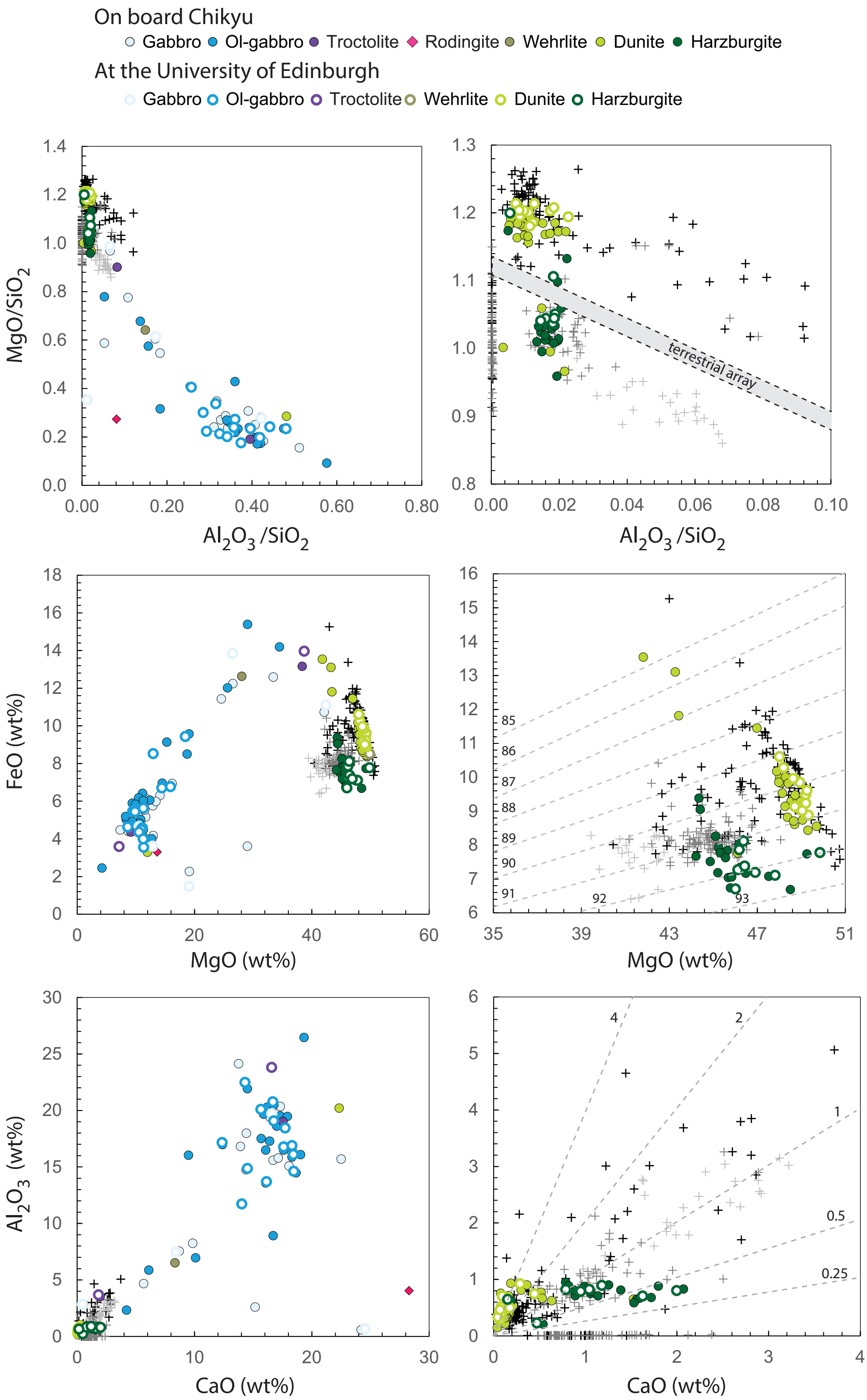

Figure F93. (**A**) Chondrite-normalized REE and (**B**) primitive mantle-normalized multielements patterns of gabbro, olivine gabbro, and dunite, Hole CM1A. Normalizing chondrite and PM values are from Barrat et al. (2012) and Sun and McDonough (1989), respectively.

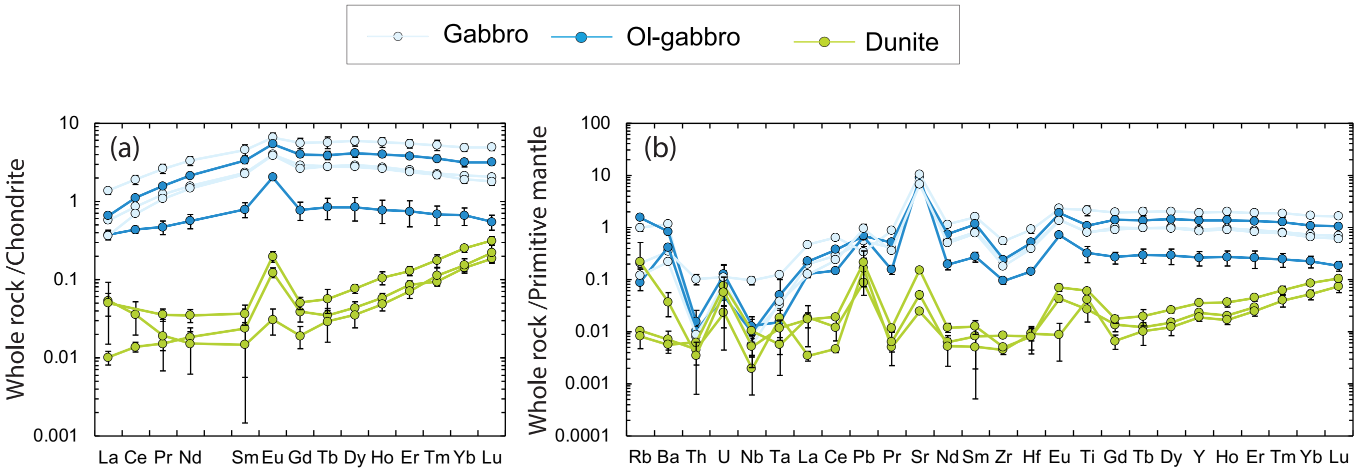

Figure F94. (**A**) Chondrite-normalized REE and (**B**) primitive mantle-normalized multielements patterns of orthopyroxene and clinopyroxene, Hole CM1A. Normalizing chondrite and PM values are from Barrat et al. (2012) and Sun and McDonough (1989), respectively.

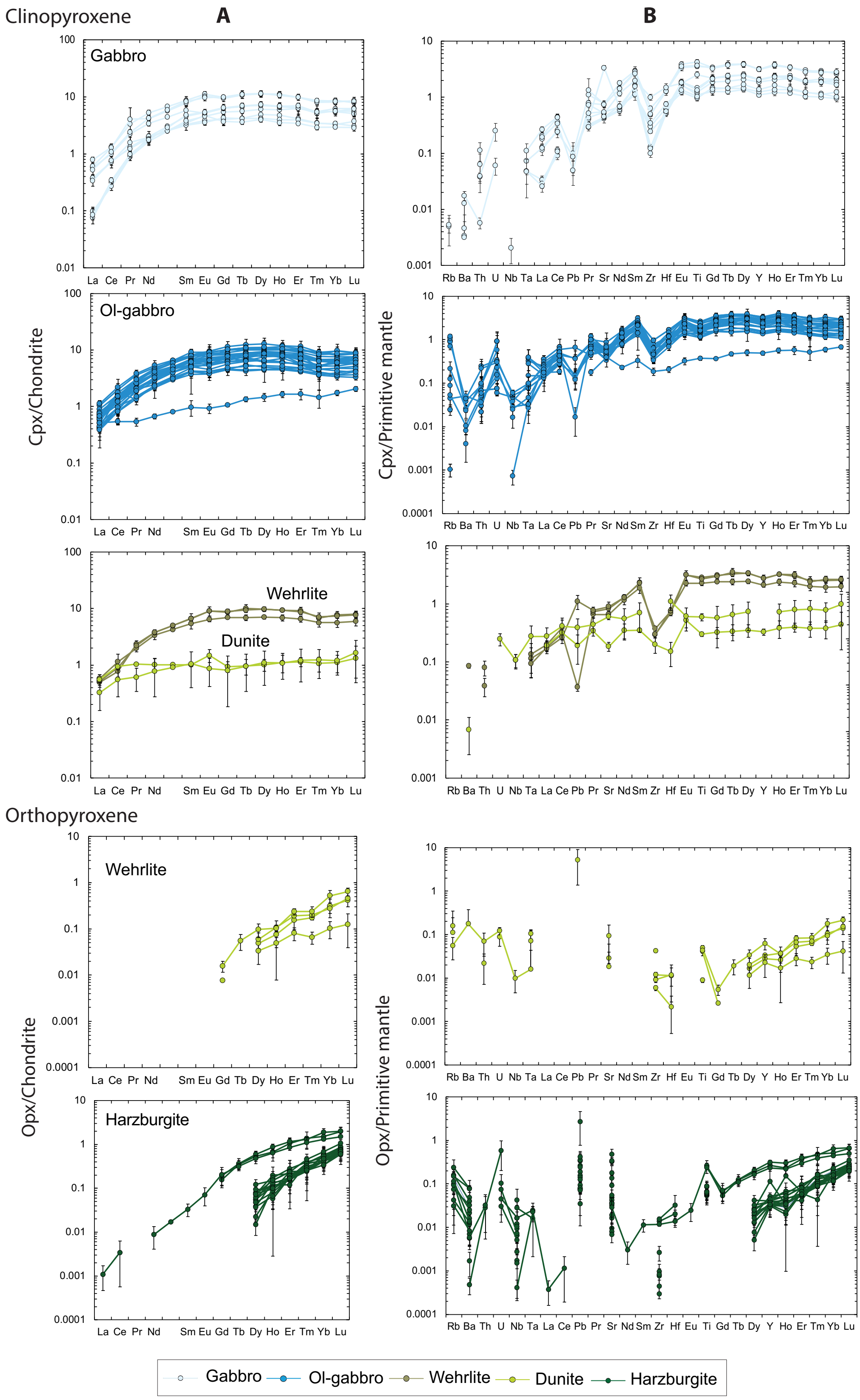

Figure F95. Bulk magnetic susceptibility, NRM intensity, and ChRM inclination, Hole CM1A.

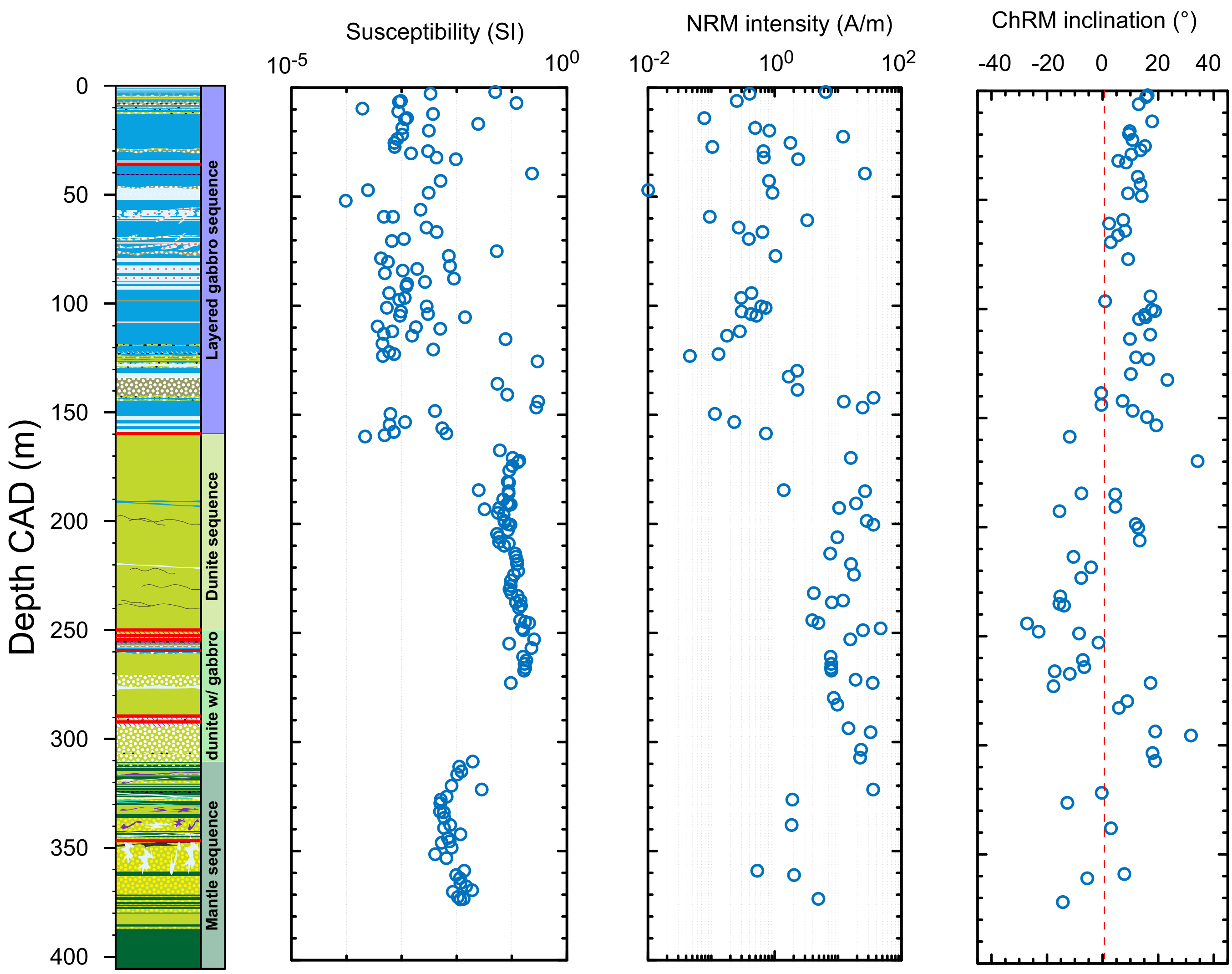

Figure F96. Representative orthogonal vector projections displaying behavior of magnetic remanence directions during progressive (**A, B**) alternating and (**C, D**) thermal demagnetization experiments conducted on discrete samples from the Layered Gabbro Sequence, Hole CM1A.

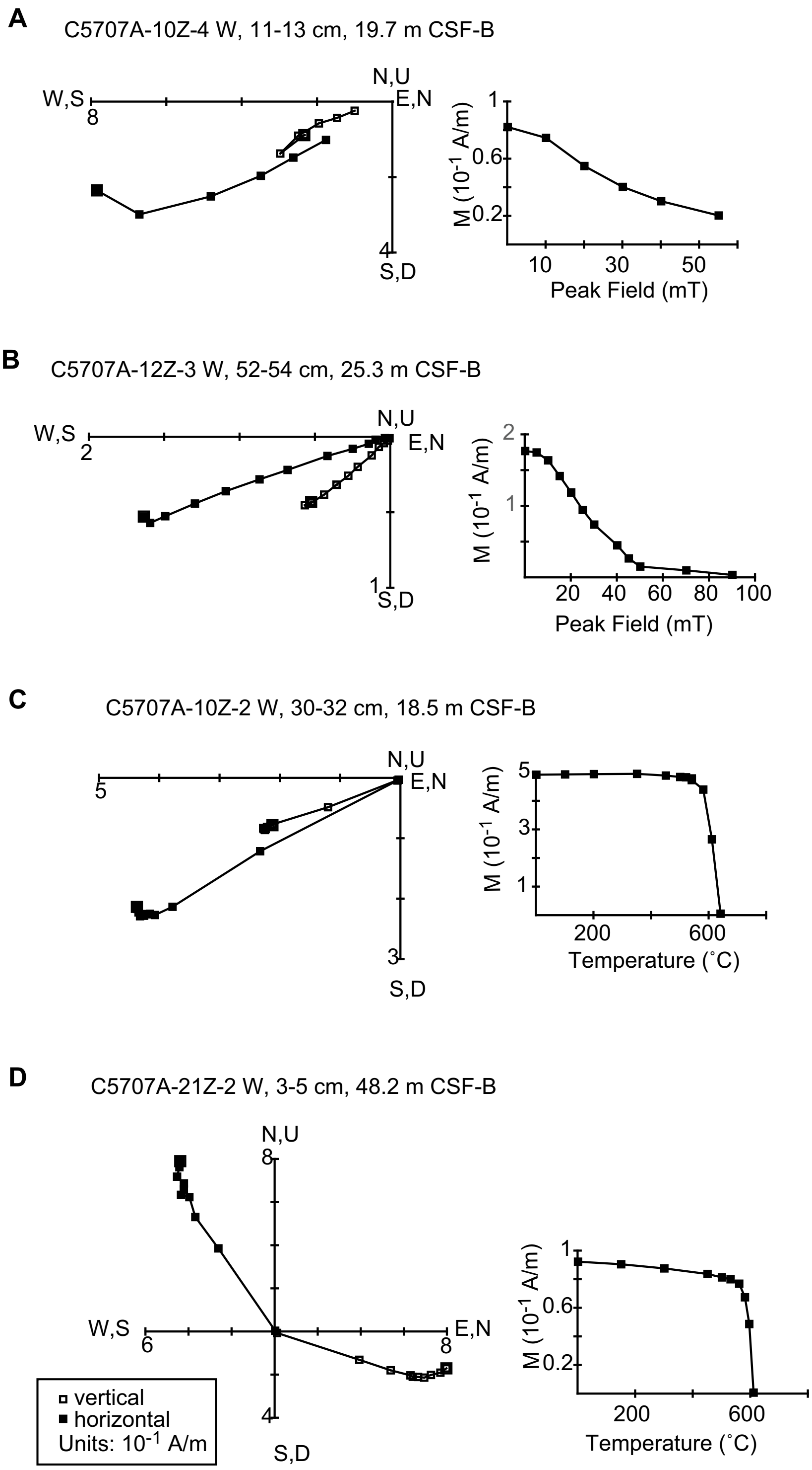

Figure F97. Representative orthogonal vector projections displaying behavior of magnetic remanence directions during progressive (**A, B**) alternating field and (**C, D**) thermal demagnetization experiments conducted on discrete samples from the Crust-Mantle Transition, Hole CM1A.

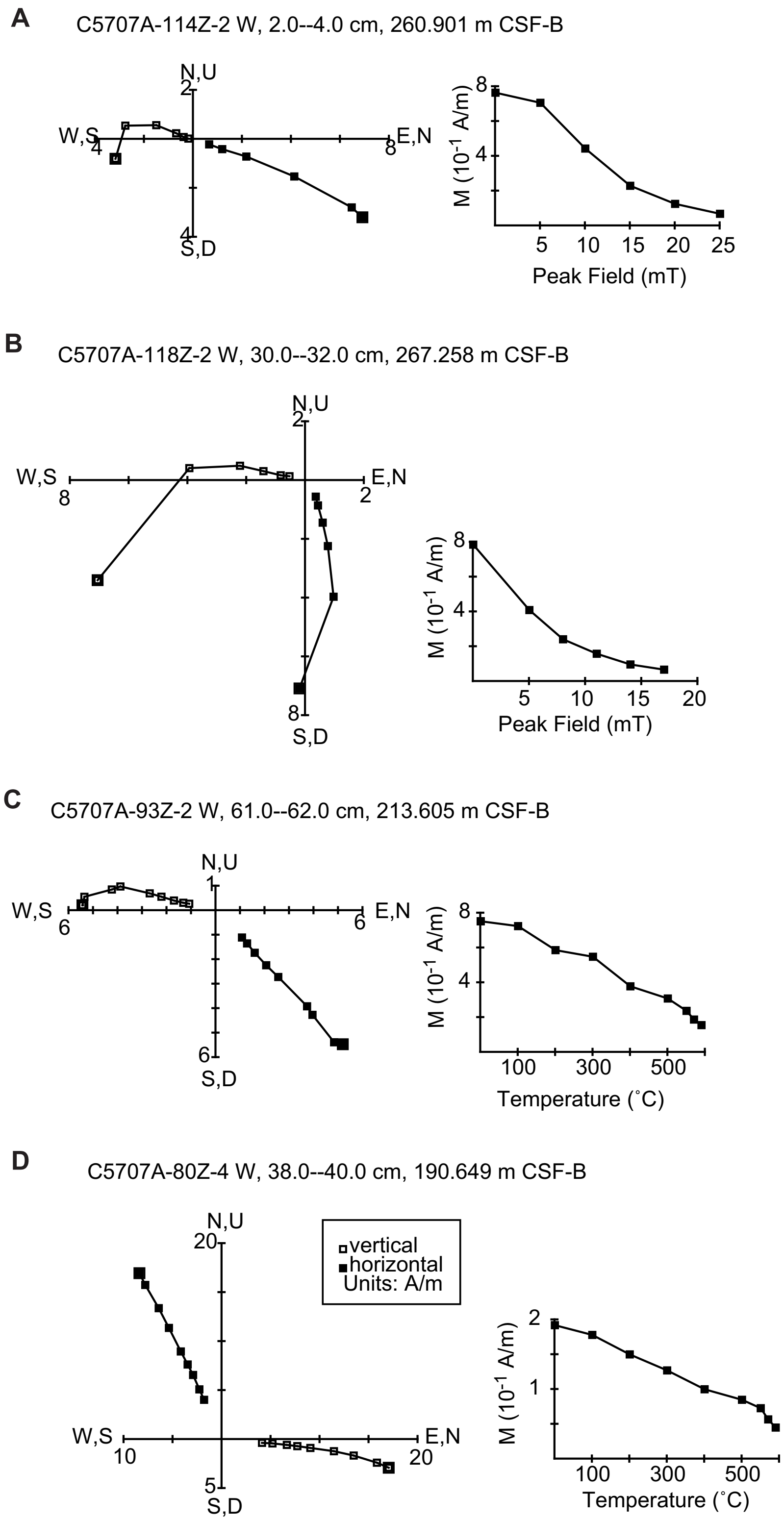

Figure F98. Equal-area plot displaying the ChRM directions for samples from (**A**) the Layered Gabbro Sequence and (**B**) the Crust–Mantle Transition dunite-rich sequences, Hole CM1A. Solid circle = downward facing vector, open circle = upward facing vector.

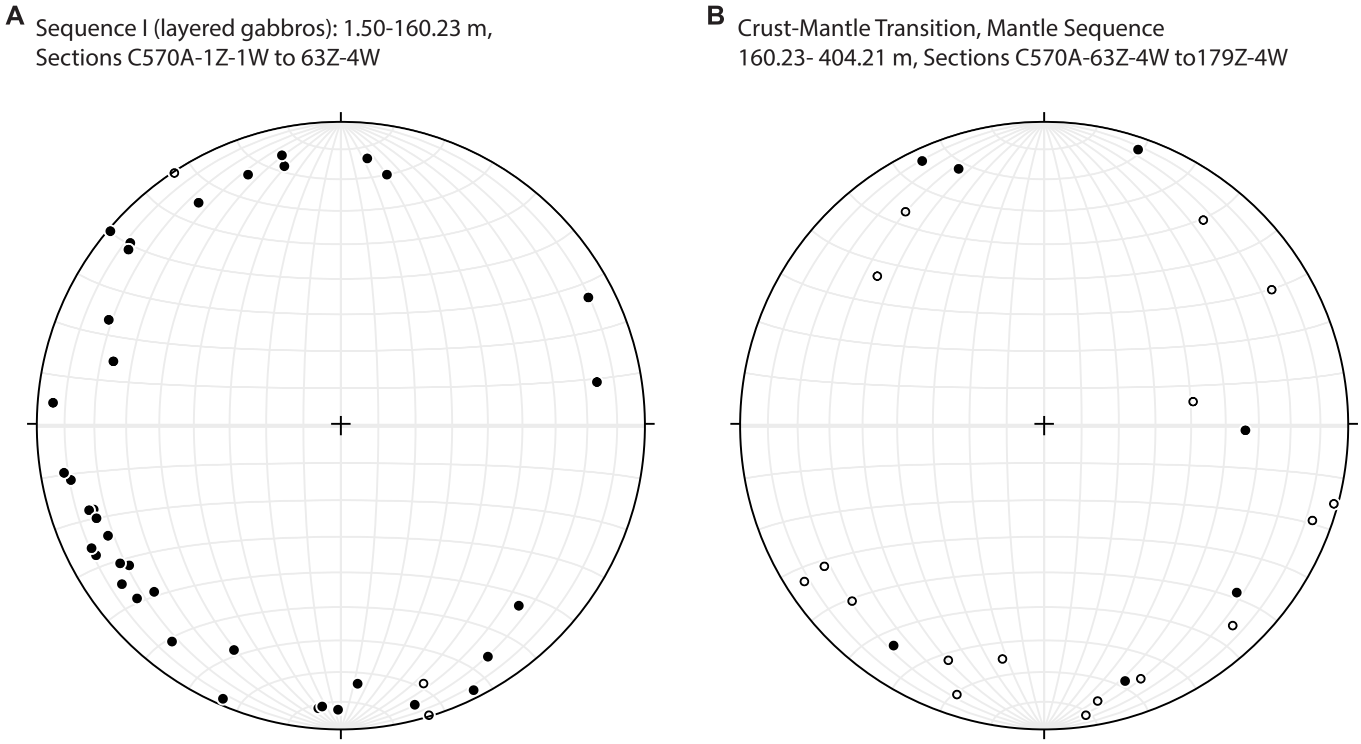

Figure F99. Downhole variations of parameters that describe the magnetic shape anisotropy, including the corrected degree of anisotropy (*P*′), the shape parameter *T*, and the inclinations of the principal axes of magnetic susceptibility K_{min} and K_{max}, Hole CM1A.

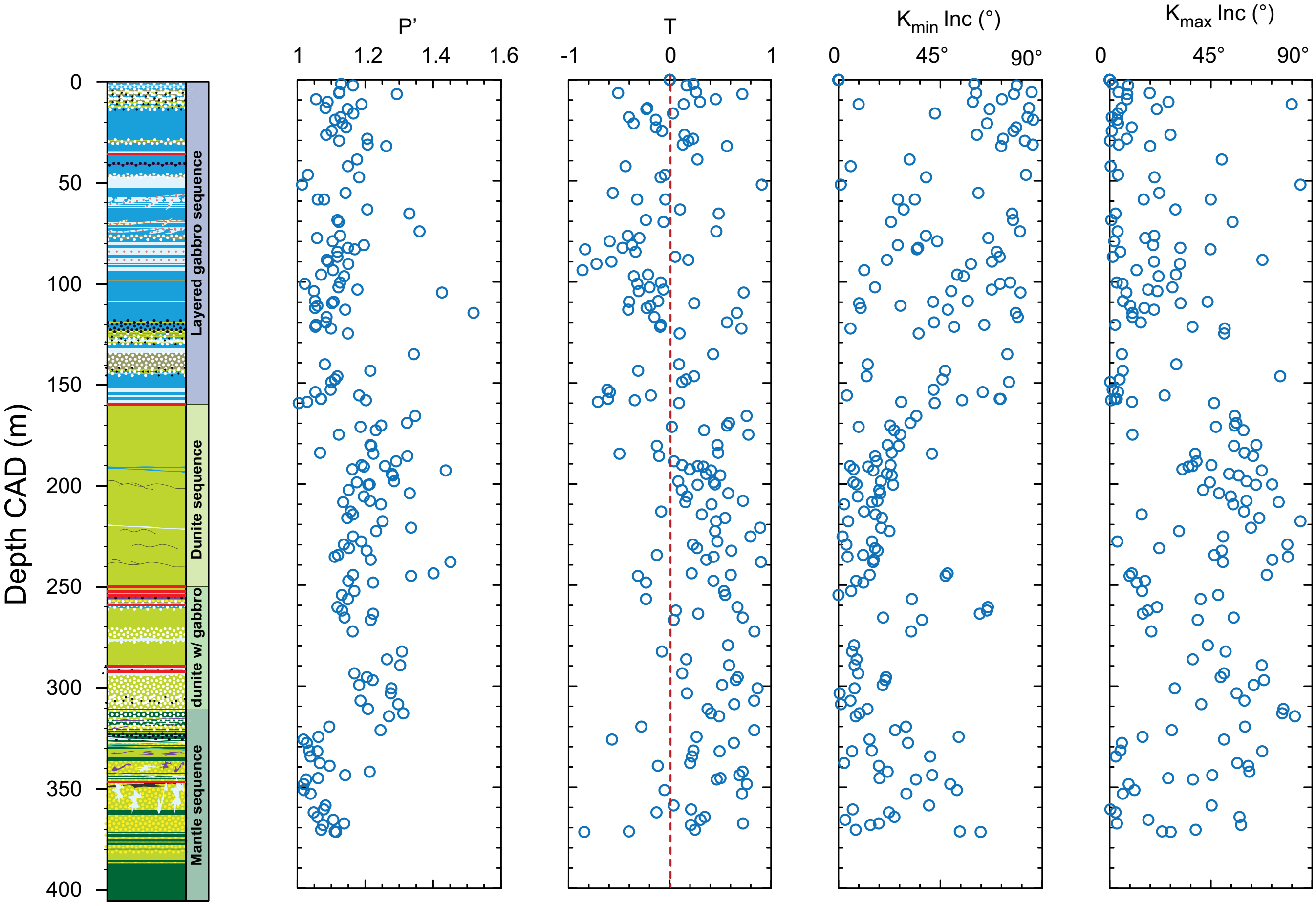

Figure F100. Flinn diagram, displaying magnetic foliation vs. lineation, Hole CM1A. Blue = ratios of magnetic shape anisotropy measured on discrete samples from the Layered Gabbro Sequence, red = serpentinized dunites.

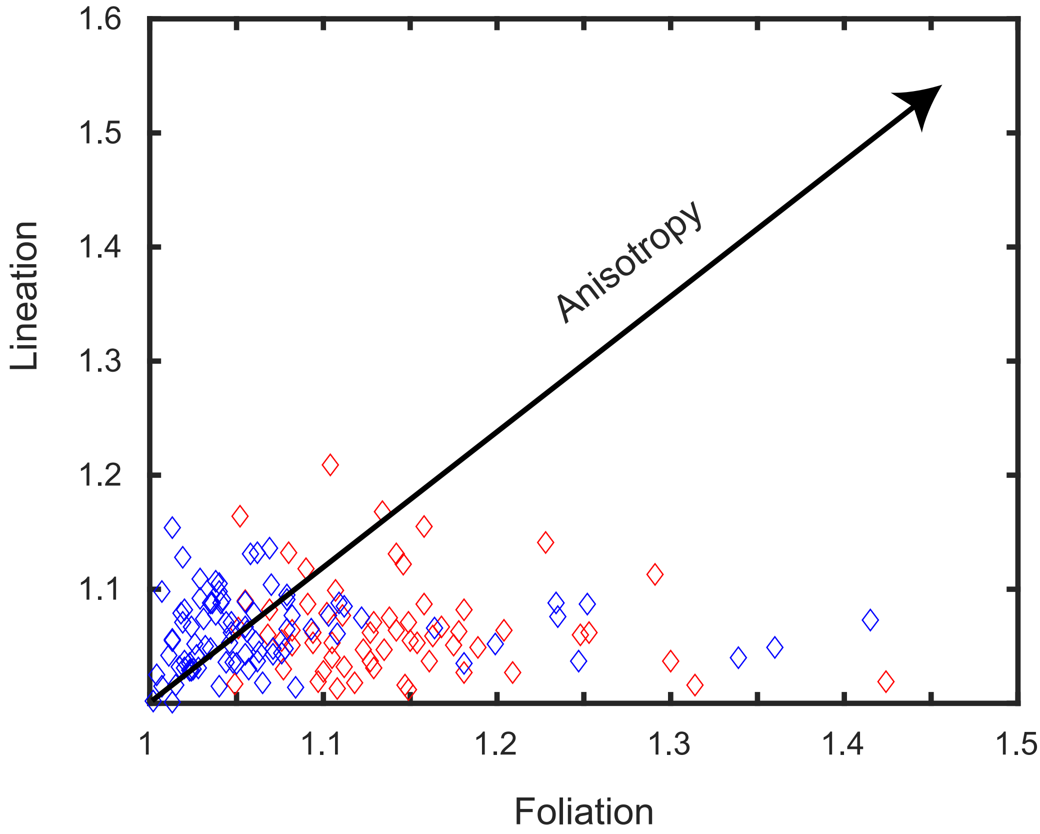

Figure F101. Downhole plots of (**A**) lithology, (**B**) GRA density, (**C**) whole-round magnetic susceptibility, (**D**) *P*-wave velocity, (**E**) electrical resistivity, (**F**) NGR, and (**G**) average and mode of CT values in each section, Hole CM1A.

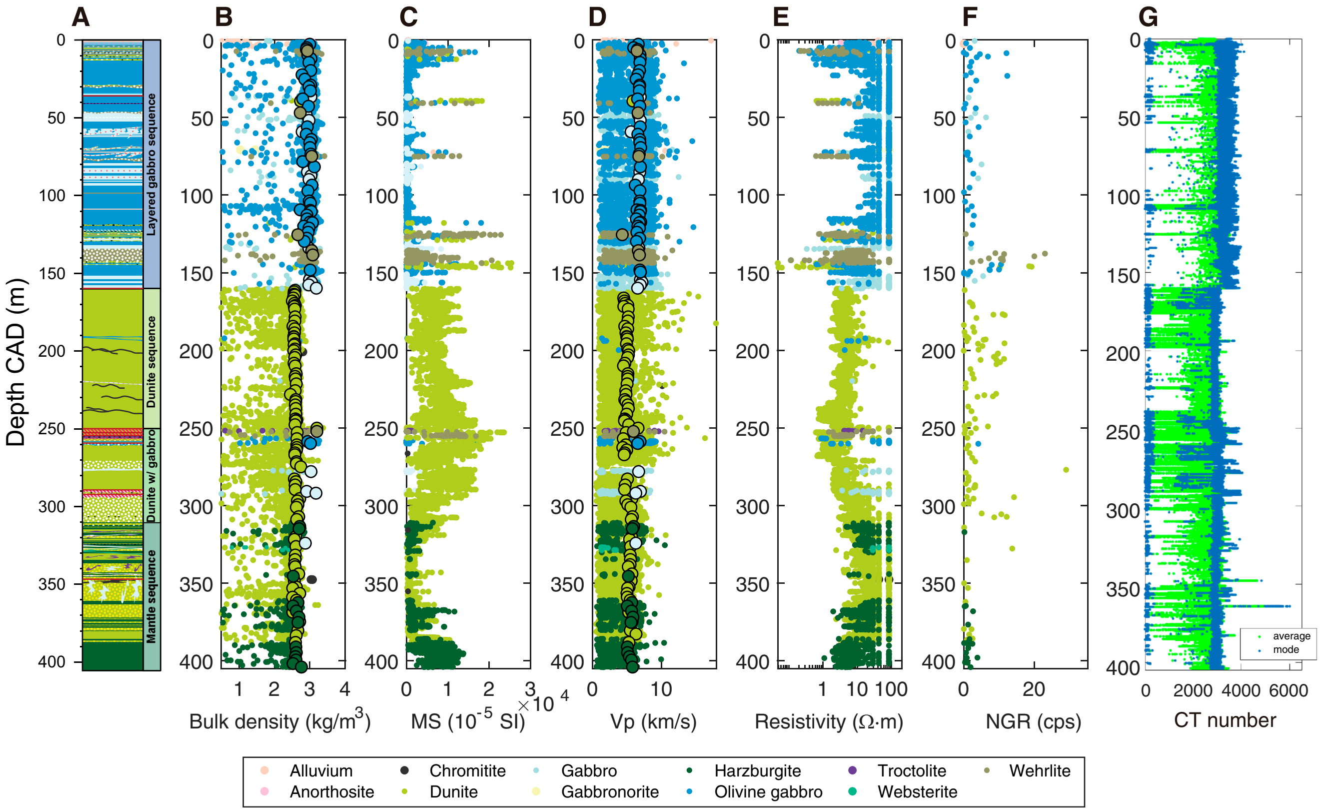

Figure F102. Examples of MSCL-I image, average and mode of CT values, and CT image, Hole CM1A. **A.** Intact gabbro. **B.** Gabbro/dunite (Sequence I/II) boundary. **C.** Intact harzburgite. **D.** Impregnated orthopyroxene-bearing dunite.

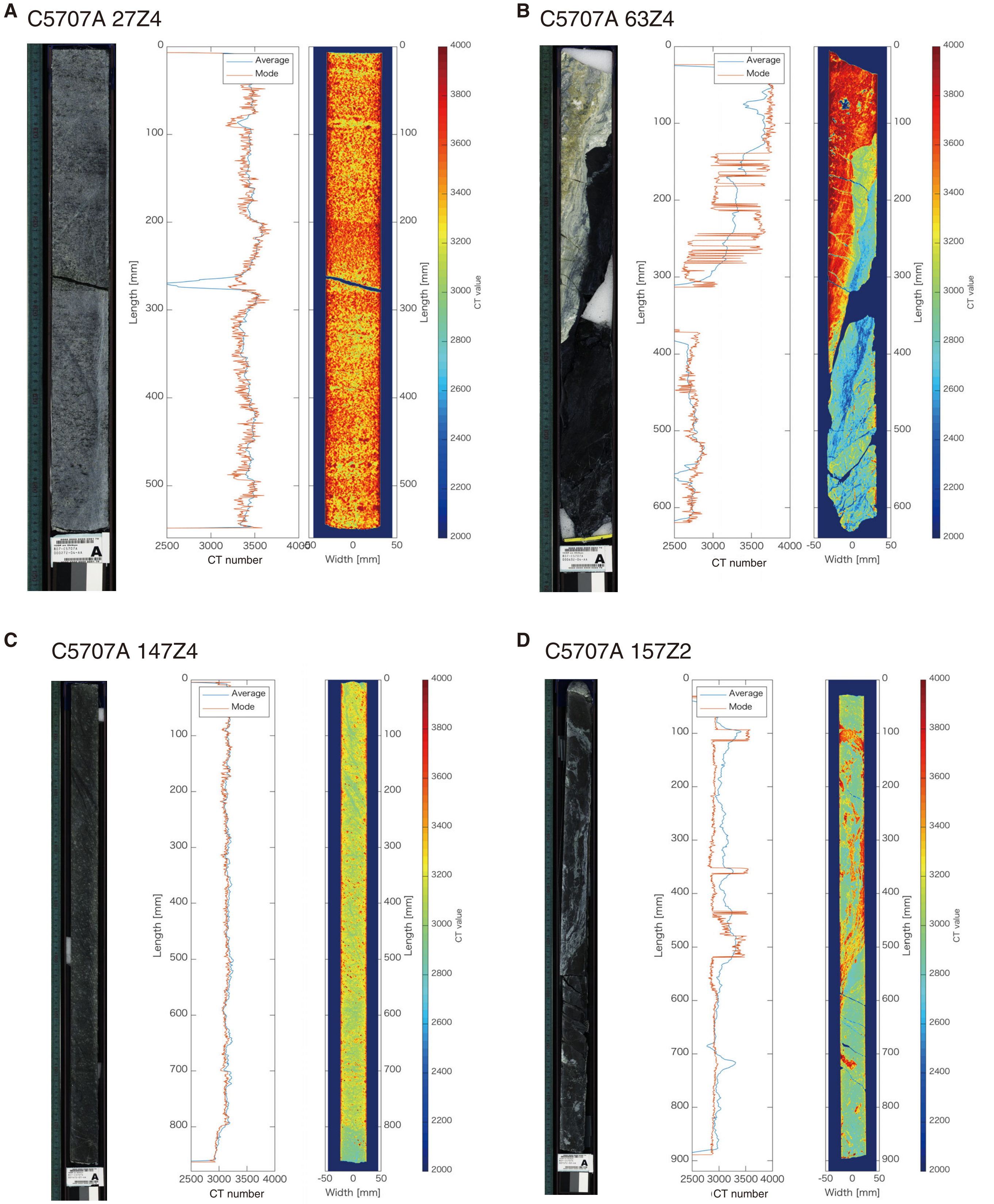

Figure F103. Correlations between XCT number and GRA density of (**A**) gabbro, (**B**) olivine gabbro, (**C**) dunite, (**D**) wehrlite, (**E**) harzburgite, and (**F**) all data from Hole CM1A.

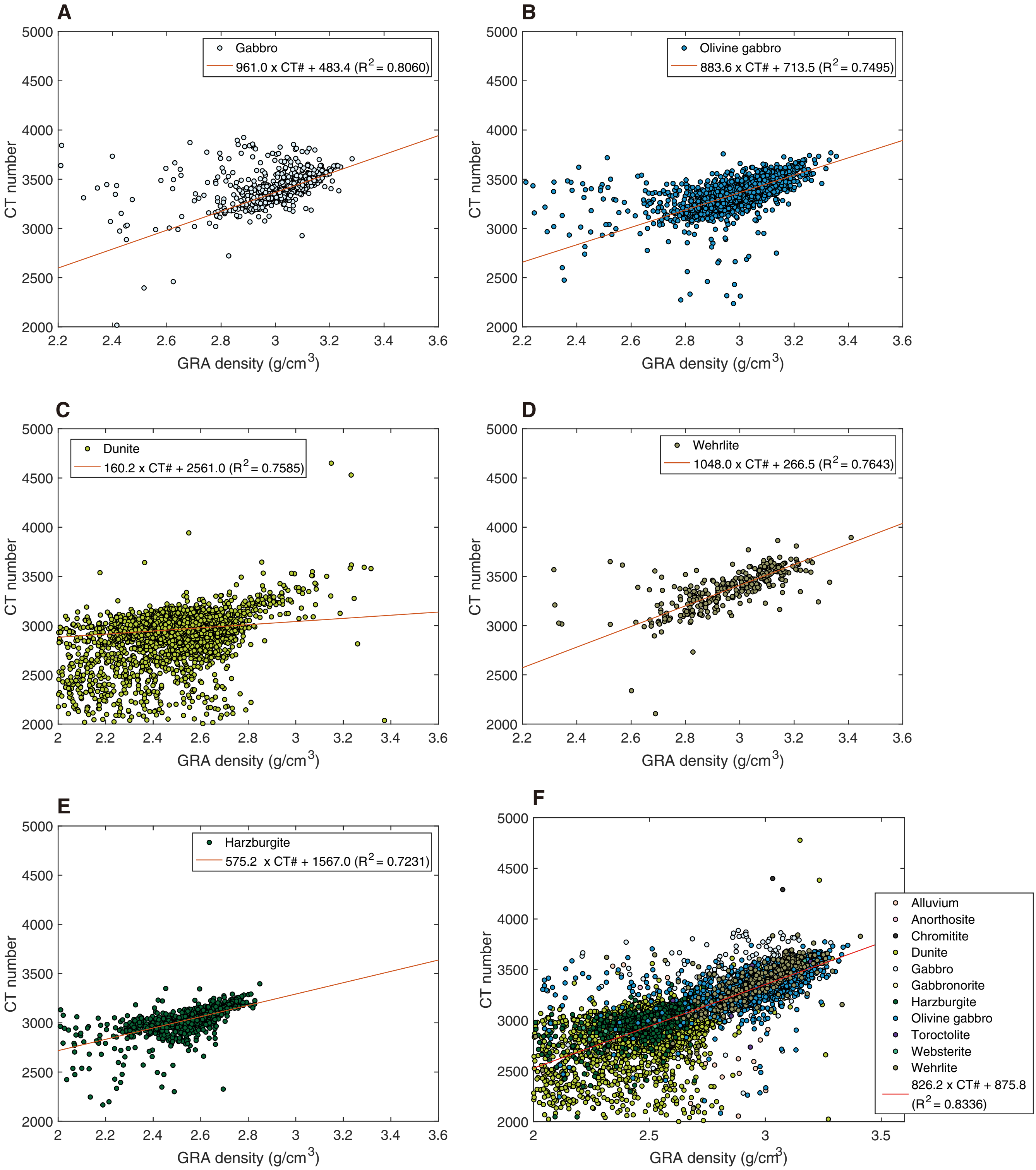

Figure F104. Downhole plot of the half-round core measurements, Hole CM1A. (**A–C**) Color spectrometry (L*, a*, and b*), (**D**) MSP.

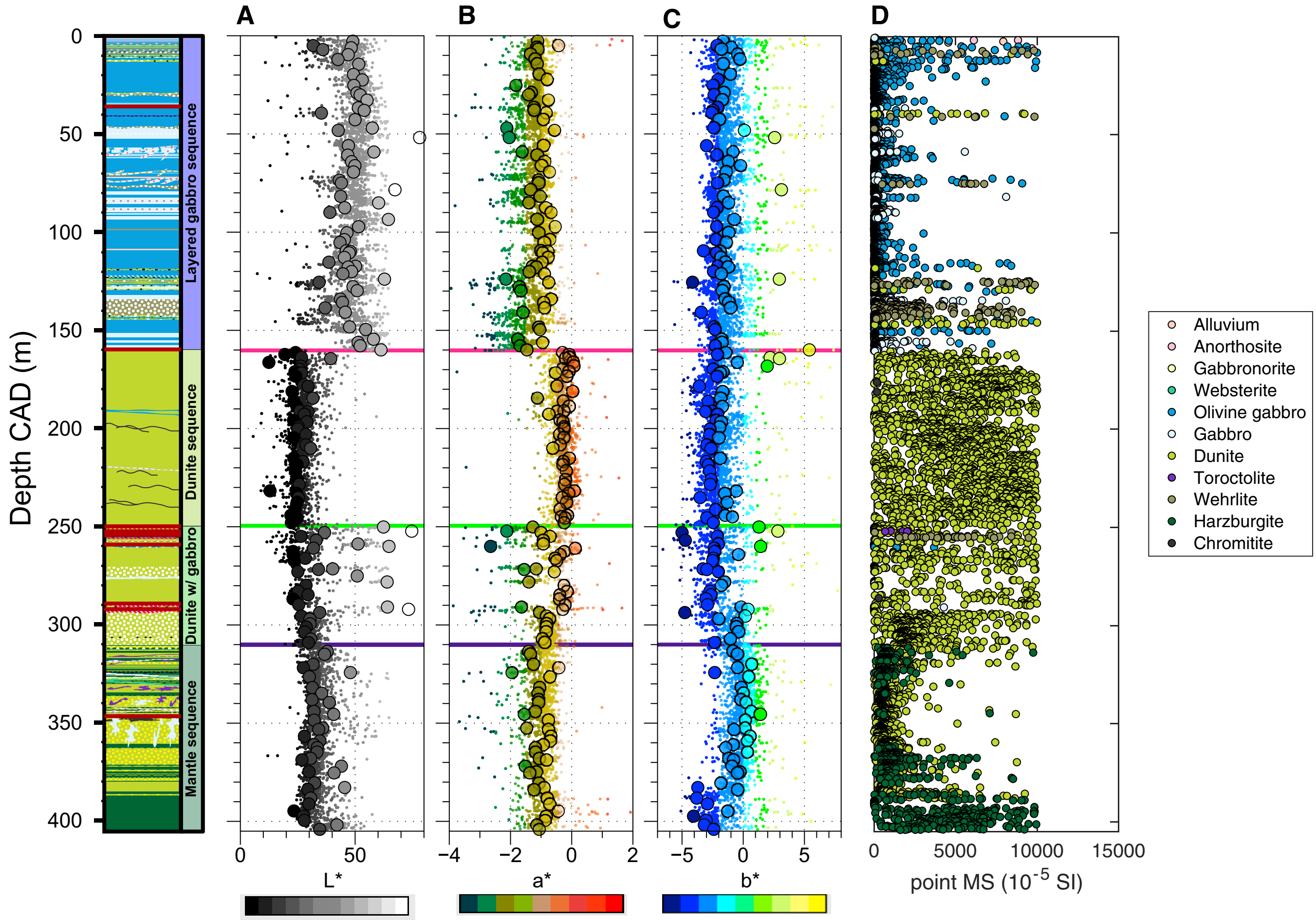

Figure F105. Downhole plots of discrete sample measurements of physical properties, Hole CM1A. (**A**) *P*-wave velocity, (**B**) bulk density, (**C**) grain density, (**D**) porosity, (**E**) electrical resistivity. Horizontal lines are shown at the sequence boundaries.

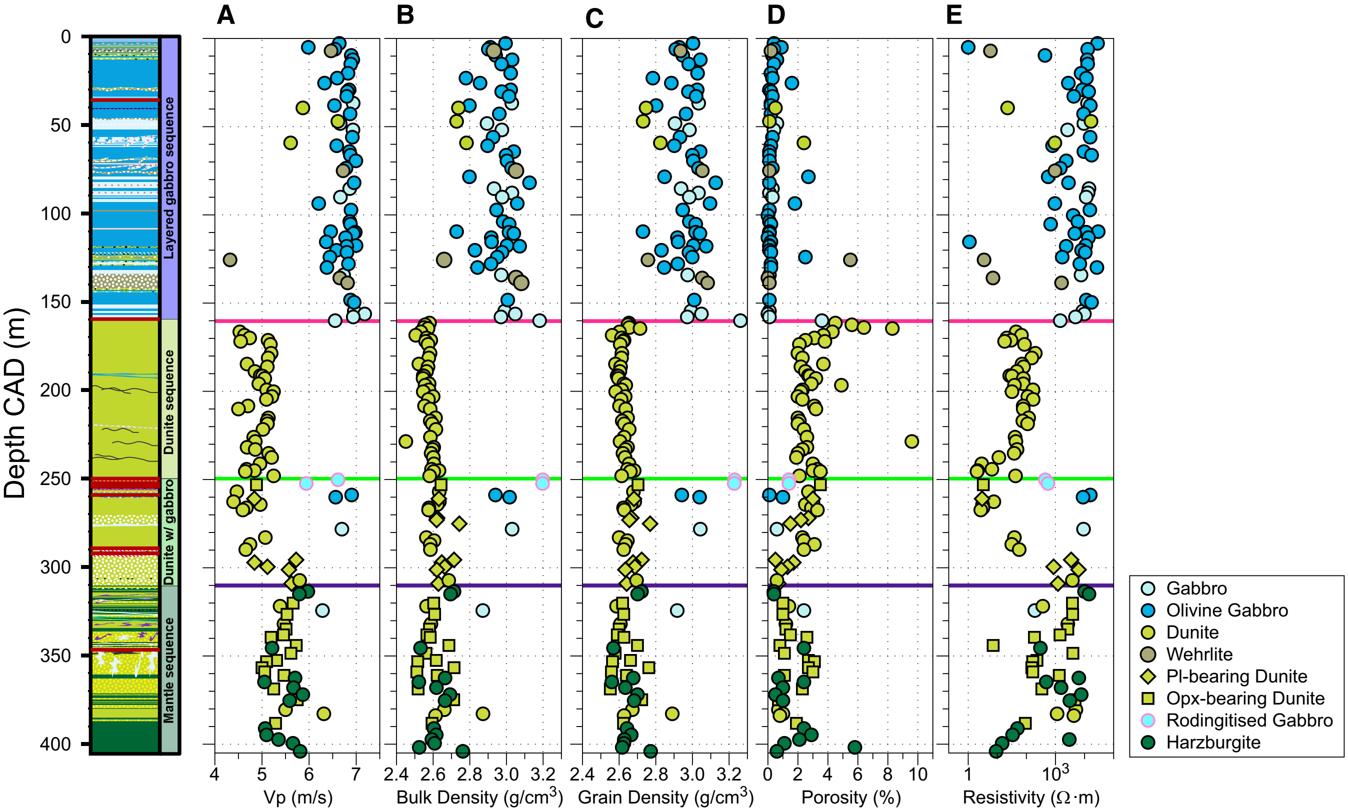

Figure F106. Downhole plot of thermal conductivity data, Hole CM1A.

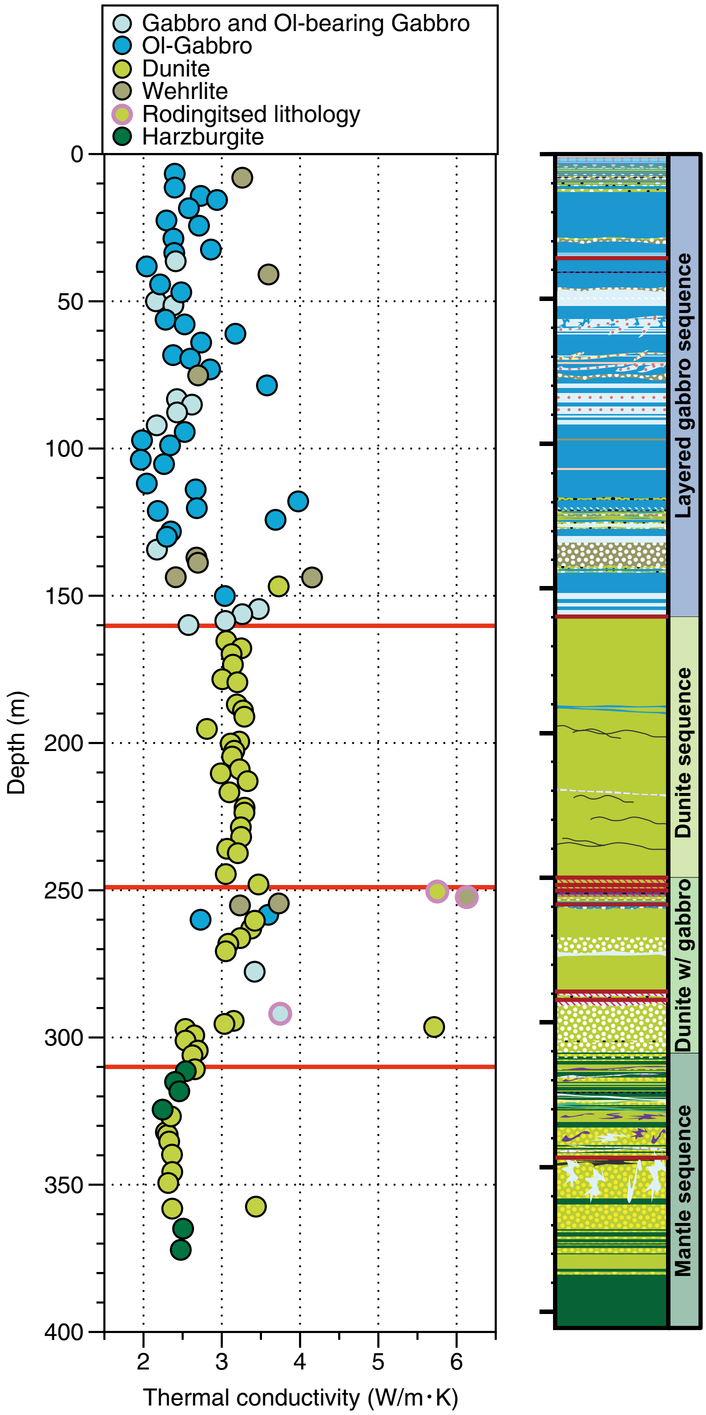

Figure F107. Relationships between porosity and (**A**) bulk density and (**B**) grain density, Hole CM1A. Those data from other OmanDP holes (Holes GT1A, GT2A, and BT1B) are shown in the diagrams for comparison.

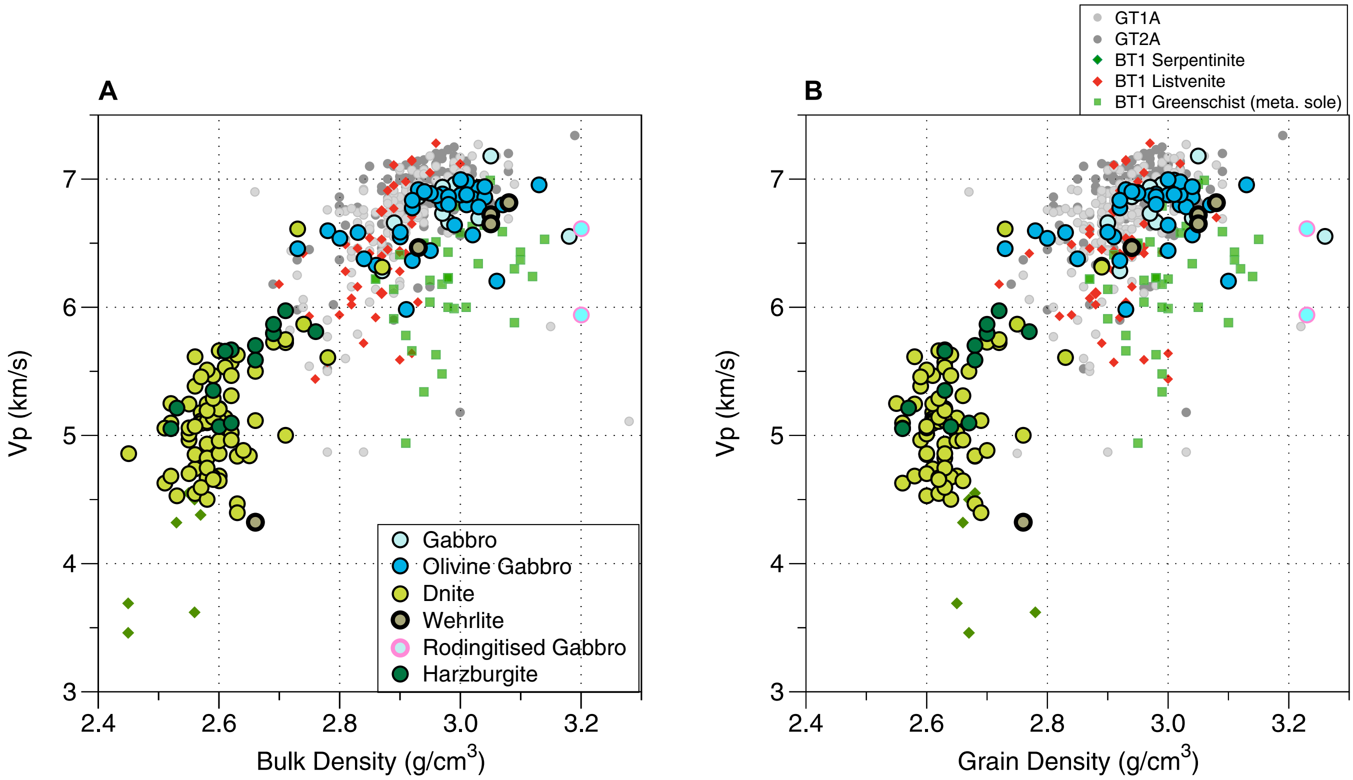

Figure F108. Relationships between *P*-wave velocity and porosity of minicube samples (**A**) linear scale and (**B**) logarithmic scale for the porosity measurements, Hole CM1A.

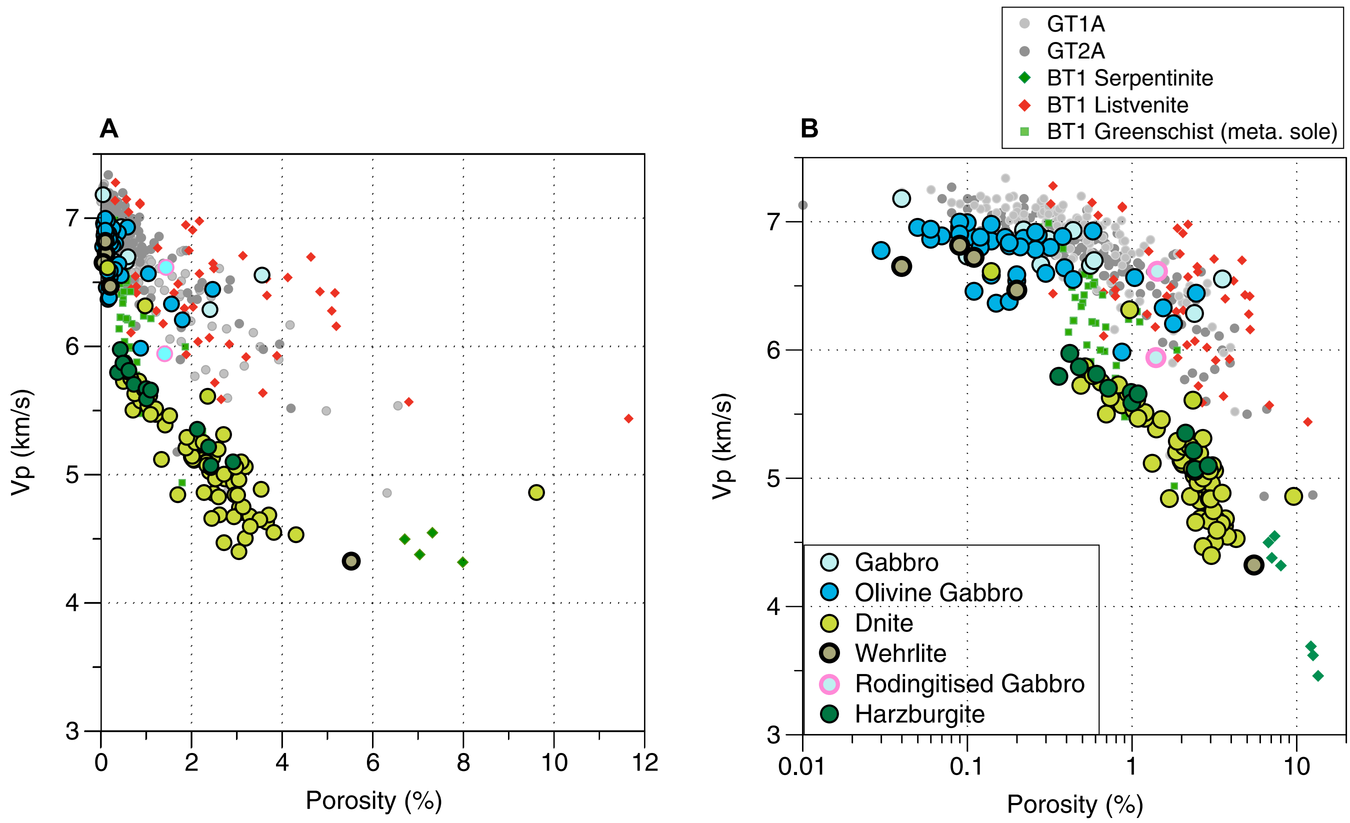

Figure F109. Relationship between *P*-wave velocity and (**A**) bulk density and (**B**) grain density, Hole CM1A.

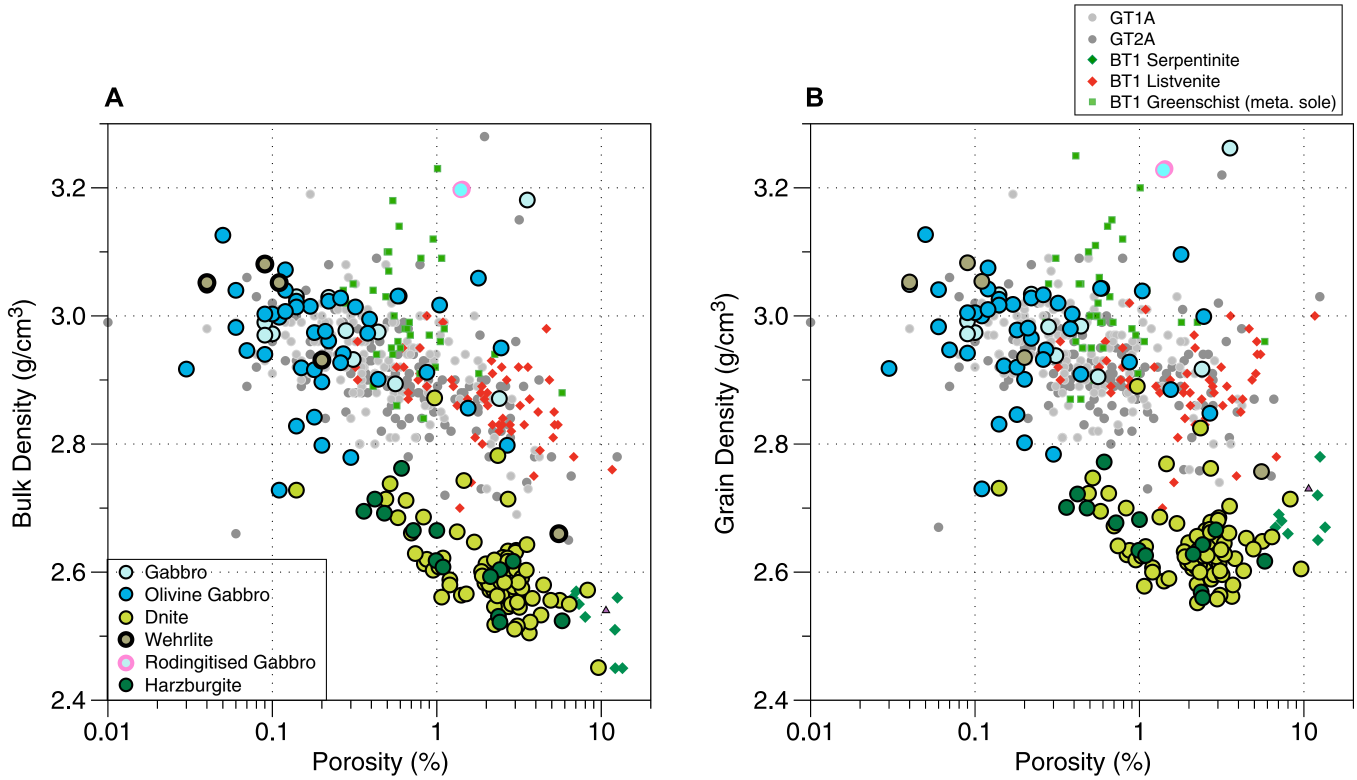

Figure F110. Downhole plot of *P*-wave velocity with color scale of (**A**) bulk density, (**B**) grain density, and (**C**) porosity, Hole CM1A.

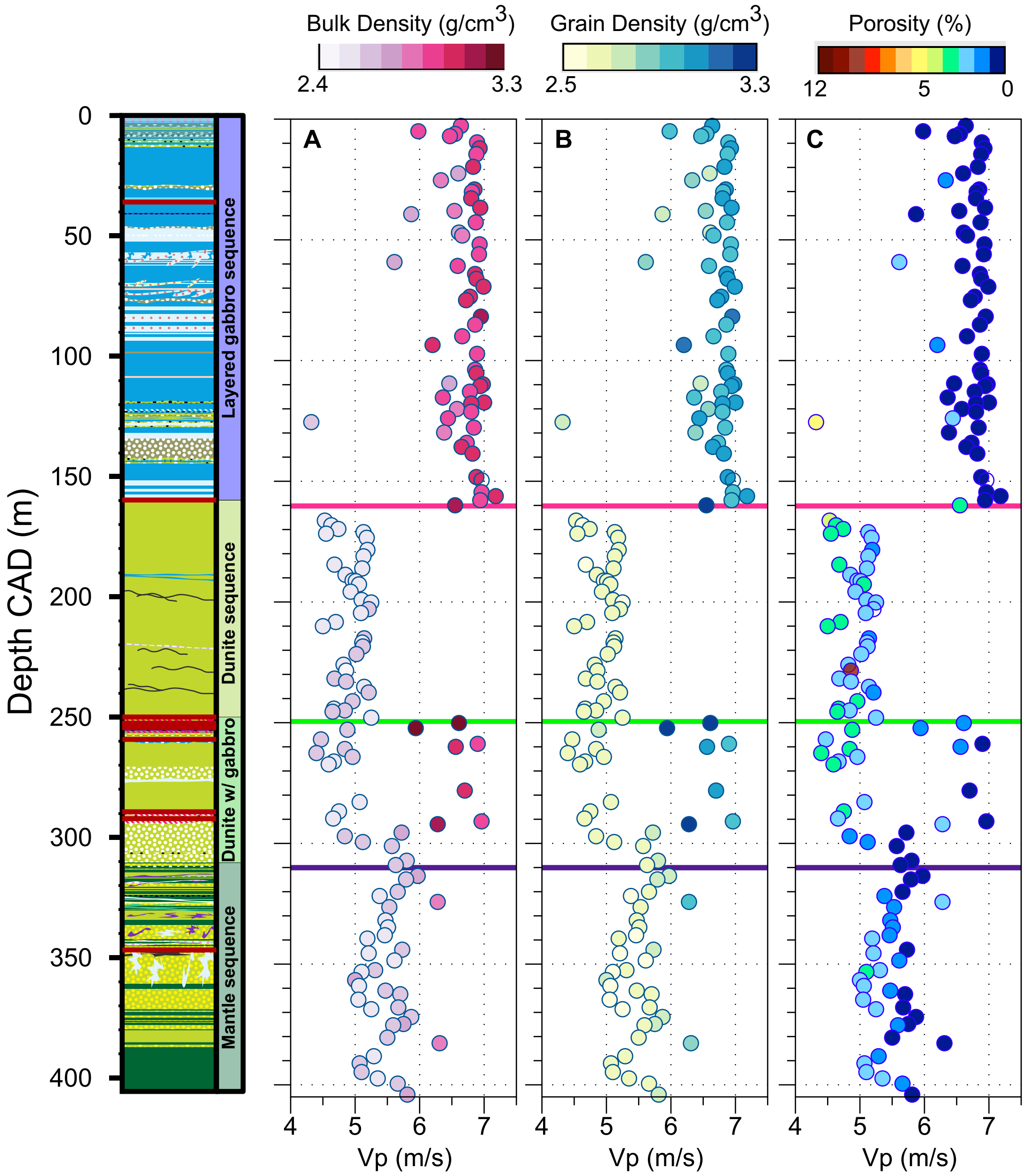

Figure F111. Downhole plot of resistivity with color scale of (A) bulk density, (B) grain density, and (C) porosity, Hole CM1A.

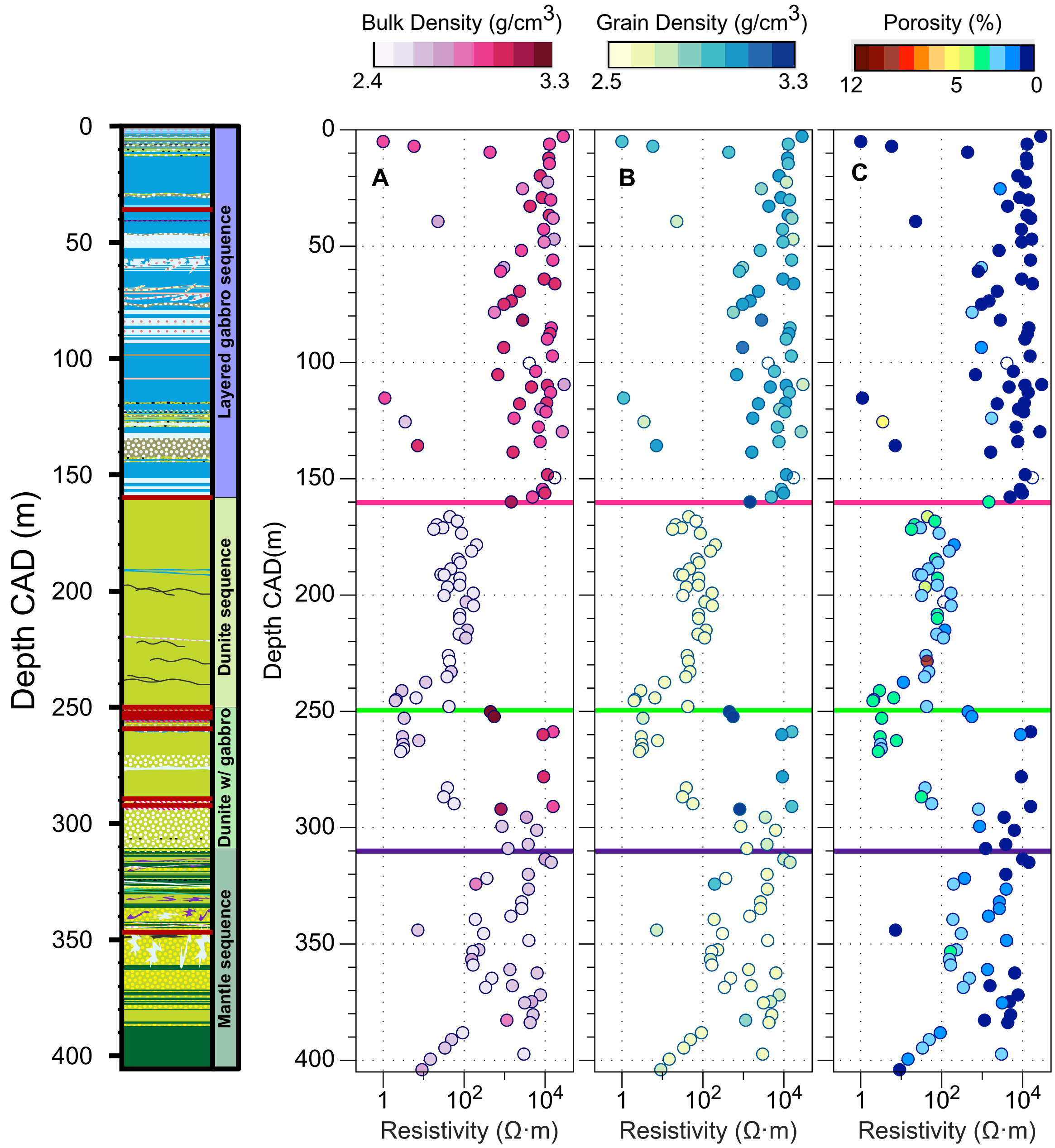

Figure F112. Relationship between *P*-wave velocity and electrical conductivity with color scales of (**A**) bulk density, (**B**) grain density, and (**C**) porosity, Hole CM1A.

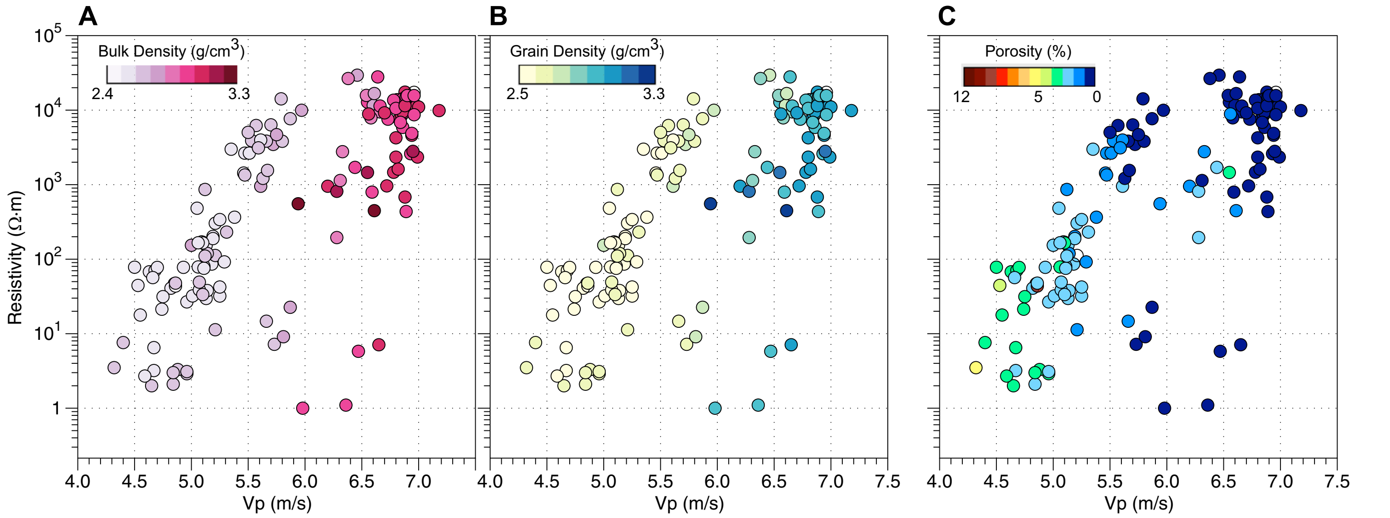

Figure F113. **A.** Intrinsic specific energy (strength) plotted with a strength color coded background from Hole CM1A upper section (134.93–159.9 m). **B.** Profile of ultrasonic velocities V_P (gray) and V_S (red) overlaid on the strength (blue) values.

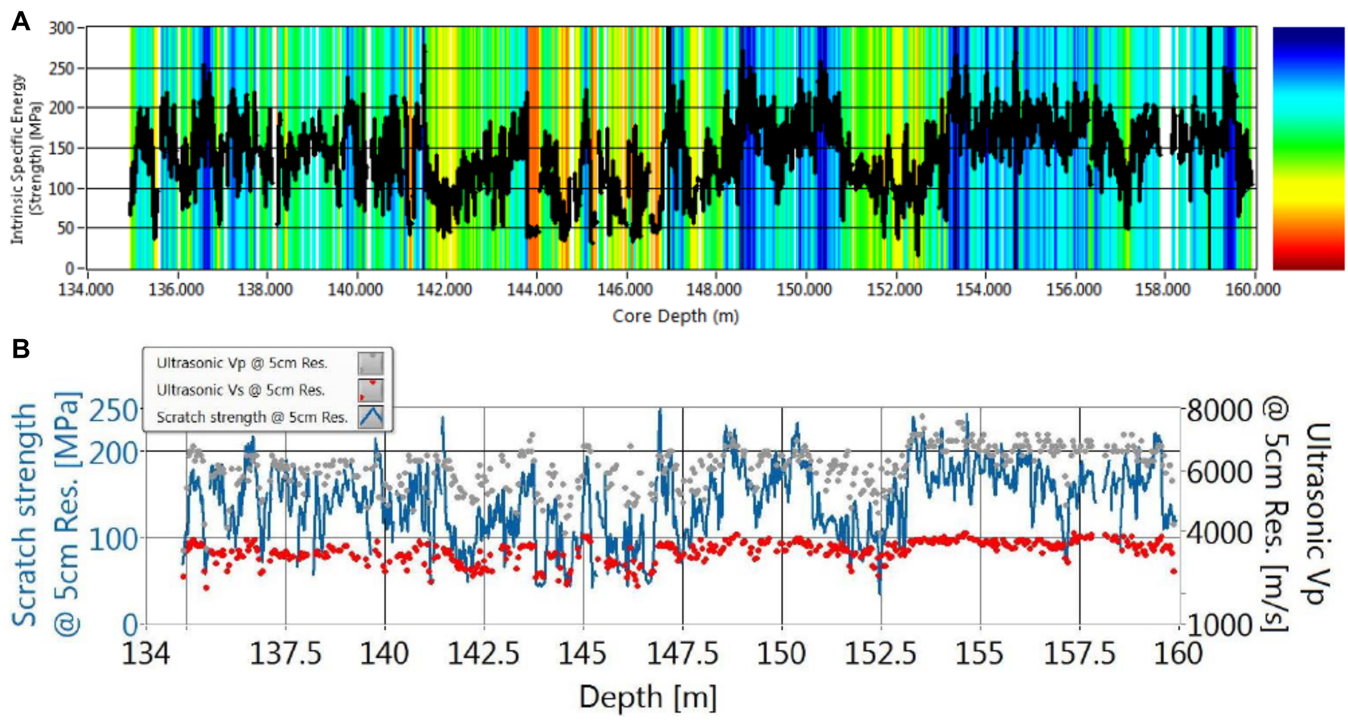

Figure F114. **A.** Intrinsic specific energy (strength) plotted with a strength color coded background from Hole CM1A upper section (159.9–175.89 m). **B.** Profile of ultrasonic velocities V_P (gray) and V_S (red) overlaid on the strength (blue) values.

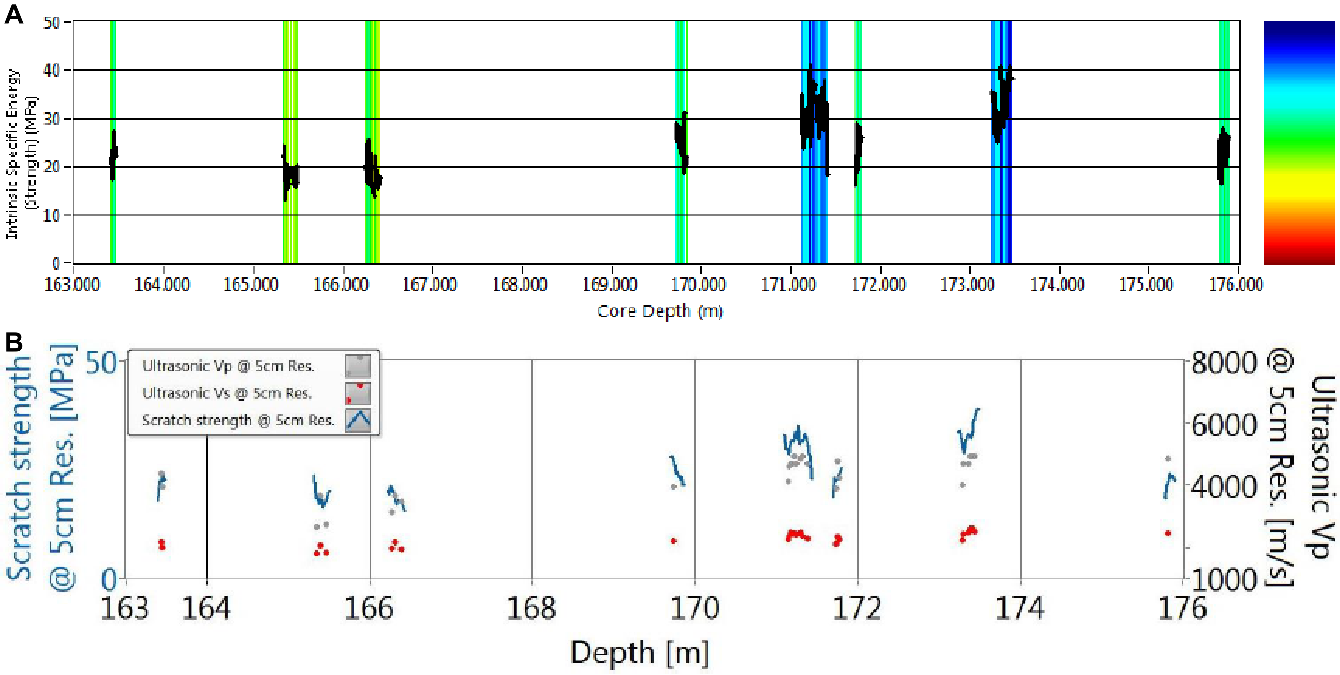

Figure F115. Example of processed imaging spectroscopy data from Hole CM1A. **A.** Lightened MSCL-I image. **B.** Mineral mapping derived using combinations of band depths (Clark and Roush, 1984) and comparison with spectra of pure minerals from the USGS spectral library (Kokaly et al., 2017) to assess the presence and absence of diagnostic mineral features indicative of minerals of interest. Brighter colors indicate deeper absorption features, which often correlates with the abundance of the mineral but can also be influenced by texture and grain size. Other minerals and additional mixing are likely present but are not shown in this view for simplicity.

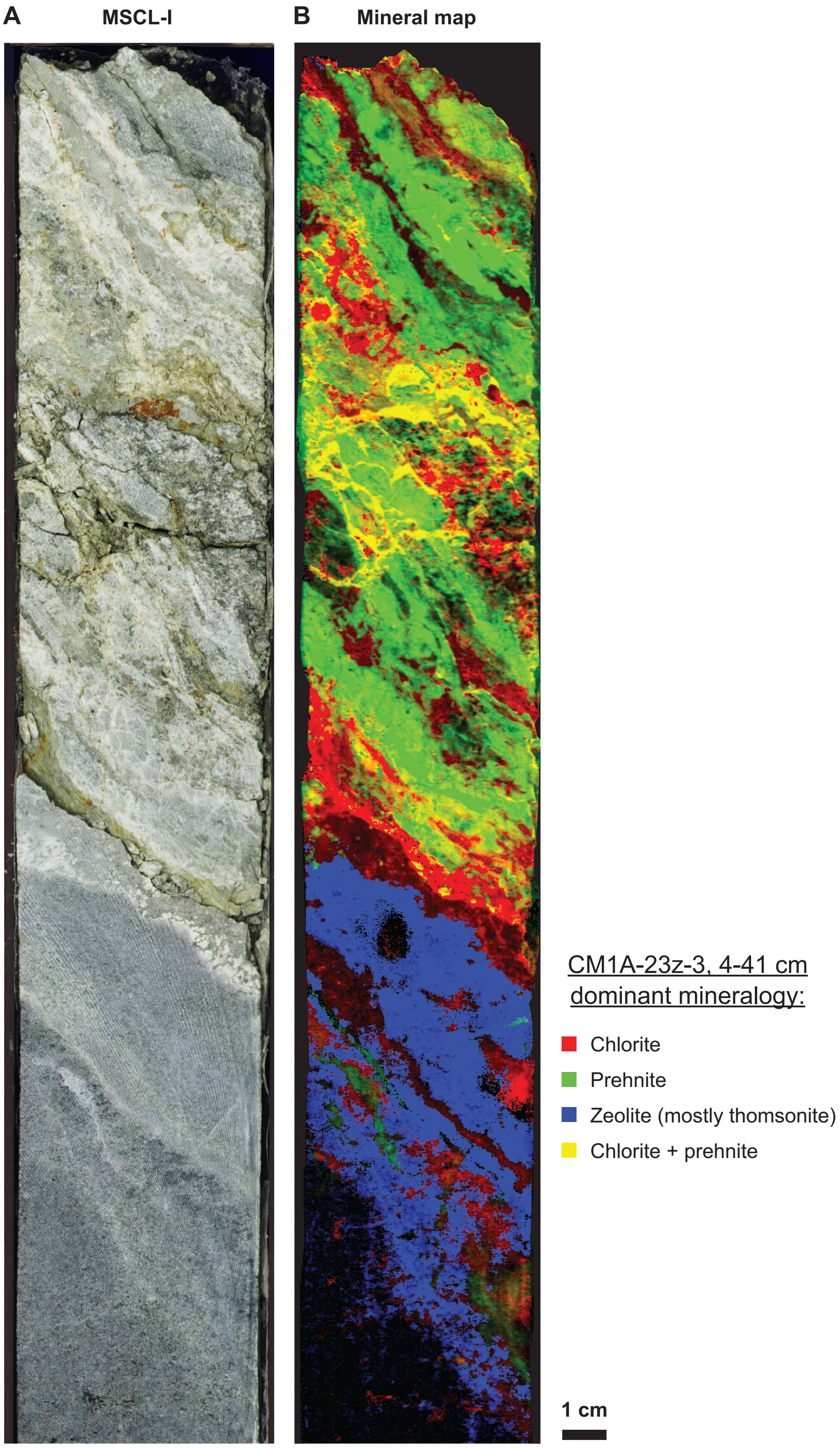

Figure F116. Lithology from core cuttings, Hole CM1B.

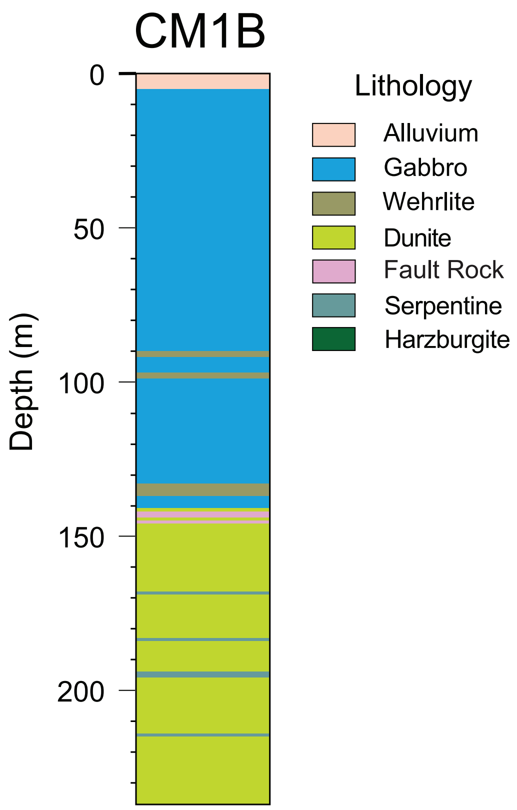

Tables

Table T1. Operations, Site CM1. **This table is available in Microsoft Excel format.**

Table T2. Number and thickness of units/subunits in each principal lithological sequence, Hole CM1A. **This table is available in Microsoft Excel format.**

Table T3. Details of the principal lithologic sequences, Hole CM1A. **This table is available in Microsoft Excel format.**

Table T4. Secondary minerals in selected vein and alteration phases identified by XRD, Hole CM1A. **This table is available in Microsoft Excel format.**

Table T5. Characteristics of vein generations, Hole CM1A. **This table is available in Microsoft Excel format.**

Table T6. Sense of shear indicators, Hole CM1A. **This table is available in Microsoft Excel format.**

Table T7. Gabbro vein dips, Hole CM1A. **This table is available in Microsoft Excel format.**

Table T8. Ultramafic rock vein dips, Hole CM1A. **This table is available in Microsoft Excel format.**

Table T9. Fault zones, Hole CM1A. **This table is available in Microsoft Excel format.**

Table T10. Whole-rock major and trace element, LOI, TC, IC, and H_2O compositions, Hole CM1A. **This table is available in Microsoft Excel format.**

Table T11. Whole-rock trace element compositions of selected pellets by LA-ICP-MS, Hole CM1A. **This table is available in Microsoft Excel format.**

Table T12. Clinopyroxene trace element compositions of selected clinopyroxene mounted plots by LA-ICP-MS, Hole CM1A. **This table is available in Microsoft Excel format.**

Table T13. Orthopyroxene trace element compositions of selected orthopyroxene mounted plots by LA-ICP-MS, Hole CM1A. **This table is available in Microsoft Excel format.**

Table T14. Bulk magnetic susceptibility measurements (relative) conducted during thermal demagnetization experiments, Hole CM1A. **This table is available in Microsoft Excel format.**

Table T15. Magnetic remanence intensities and ChRM directions calculated by PCA, Hole CM1A. **This table is available in Microsoft Excel format.**

Table T16. Summary of whole-round and section half measurements, Hole CM1A. **This table is available in Microsoft Excel format.**

Table T17. Summary of discrete physical properties measurements, Hole CM1A. **This table is available in Microsoft Excel format.**

Table T18. Velocity, density, porosity, and electrical resistivity measurements, Hole CM1A. **This table is available in Microsoft Excel format.**

Table T19. Thermal conductivity measurements, Hole CM1A. **This table is available in Microsoft Excel format.**

Table T20. Cuttings lithology log, Hole CM1B. **This table is available in Microsoft Excel format.**

Supplemental tables

Table ST1. Plutonic log containing all described intervals/units/subunits, Hole CM1A. **This table is available in Microsoft Excel format.**

Table ST2. Summary of all described units and subunits including thickness, Hole CM1A. **This table is available in Microsoft Excel format.**

Table ST3. Alteration log, Hole CM1A. **This table is available in Microsoft Excel format.**

Table ST4. Vein log, Hole CM1A. **This table is available in Microsoft Excel format.**

Table ST5. Bulk XRD on-site sample analyses, Hole CM1A. **This table is available in Microsoft Excel format.**

Table ST6. MSCL-W measurements, Hole CM1A. **This table is available in Microsoft Excel format.**

Table ST7. MSCL-C measurements, Hole CM1B. **This table is available in Microsoft Excel format.**

Supplemental figures

Figure SF1. XRD compilation of Cores CM1A-1Z through 29Z. **This figure is available in PDF format.**

Figure SF2. XRD compilation Cores CM1A-30Z through 59Z. **This figure is available in PDF format.**

Figure SF3. XRD compilation Cores CM1A-60Z through 89Z. **This figure is available in PDF format.**

Figure SF4. XRD compilation Cores CM1A-90Z through 119Z. **This figure is available in PDF format.**

Figure SF5. XRD compilation Cores CM1A-120Z through 149Z. **This figure is available in PDF format.**

Figure SF6. XRD compilation Cores CM1A-150Z through 179Z. **This figure is available in PDF format.**